CRYSTAL GROWTH AND AERODYNAMICS OF DRUG PARTICLES

Hak-Kim Chan

A thesis submitted in fulfilment of the requirement
for the degree of Doctor of Philosophy in the
Department of Pharmacy, Faculty of Science
University of Sydney

March, 1988

Summary

Solid forms of three therapeutic agents were studied for crystal habit modifications and/or aerodynamic properties with the aim to improve the therapeutic efficiency in direct pulmonary administration.

Firstly, cromoglycic acid (CA), characterized by physical and chemical methods, was prepared in forms of elongated fibrous particles suitable for inhalation. The fibres have a geometric standard deviation (σ_g) = 1.88 and a mass median aerodynamic diameter (MMAD) = 0.65μm which is in the respirable range. As compared to the currently used sodium cromoglycate, CA has a much lower aqueous solubility which thus minimizes the hygroscopic growth of the drug particles and favours the pulmonary deposition that may offer a therapeutic advantage. Theoretical calculations of the aerodynamic diameters indicate that the calculated MMAD and σ_g assuming a perpendicular flight orientation of the fibres are in reasonable agreement with the values obtained by cascade impactor.

Secondly, three solid forms of methotrexate (MTX), a widely used chemotherapeutic agent, were found and characterized: tetragonal crystals from hot water crystallization; the original powder with a lower degree of crystallinity from the manufacturer, and an amorphous powder from methanol. Single crystals were prepared with size sufficiently large for the structure to be solved by X-ray diffraction. The results show that conformation of MTX molecules in the crystal is a potential energy minimum and is similar to the proposed structure of dihydrofolate bound to dihydrofolate reductase (DHFR). These results are in disagreement with theoretical studies which suggested that the bound forms of MTX were highly strained, and are therefore of importance to those attempting to design new inhibitors of DHFR. Subsequent habit modification of MTX crystals using various crystallization conditions revealed a similar rounding effect on crystal habit by different additives. The results suggest that rounding of drug particle may be possible simply by using additives during crystallization. This might be useful pharmaceutically for preparing spherical particles to improve the handling and processing characteristics of crystalline solids.

Lastly, mechanistic studies of the formation of 2 distinct crystal habits of hexamethylmelamine (HMM) in different solvents revealed that growth of compact crystals in both polar and non-polar solvents is controlled by volume diffusion. Formation of needle crystals on fast evaporation from polar solvents is the result of diffusion controlled growth along the [0001] direction and surface controlled growth along the [1100] direction. Discrepancies were found between the α-values and the observed growth rates, which may be attributed to volume diffusion. Solute-solvent interactions in solutions are found to be very weak and no statistically

predominant stereospecific interaction can be identified as responsible for the habit modifications in different solvents. A solvate of HMM-hexafluorobenzene was also identified.

SYNOPSIS

The original aims of the thesis were to investigate the crystallisation methods and mechanisms of formation of elongated particles of drugs that could be used for intrapulmonary administration as dispersion of solid in air ('aerosols'). Particles of elongated shape may be of therapeutic advantages in inhalation treatment of diseases of the respiratory tract.

Chapter one is a study of the crystal growth and aerodynamics of respirable particles of cromoglycic acid (CA). Needle-shaped particles of CA were obtained by crystallization from aqueous solutions. The aerodynamic properties of such elongated crystals were then investigated both theoretically and experimentally.

Chapter two is an effort to prepare respirable elongated particles of another therapeutic agent, methotrexate (MTX). Although this goal was unfulfilled, several important findings on the crystal structure and forms of this drug were obtained. Crystal rounding of MTX was found; a hypothesis was put forward explaining it by: i) particle aggregation and ii) non-specific interactions between the various faces of the crystal and the crystallisation medium. The highly anisotropic growth of needle habit along a specific crystallographic direction is precluded in MTX. This is most likely caused by the loose crystal structure which consists of hydrophilic layers alternating with hydrophobic layers.

Chapter three elucidates the mechanisms responsible for crystal habit elongation, using hexamethylmelamine (HMM) as a model compound. Measurements of crystal growth kinetics indicated that the elongated HMM crystals are formed by a combination of (bulk) diffusion controlled growth along the [0001] direction and surface controlled growth along the [1100] direction.

ACKNOWLEDGEMENTS

I wish to express my sincere appreciation to Dr. Igor Gonda for his continued interest, encouragement and helpful counsel during the course of this study and for his critical reading the manuscript.

I would also like to thank Associate Professor Manuel Aroney, Dr. Trevor Hambley, Dr. Emilios Patsalides, and Dr. Ray Pierens of the School of Chemistry for their interest and collaboration.

I am greatly indebted to Dr. Ian Threadgold of the Department of Geology for his counsel on the aspects of crystallography and polarizing microscopy.

Workshop assistance provided by Messrs Ken Luker, Keith Murray and Geoffrey Markwick is gratefully acknowledged. I also thank Messrs Bruce Tattam and Peter Burden for carrying out the Fourier transform NMR and mass spectral analysis; Dr. Andrew Cheung for helping to interpret the NMR data.

Special thanks are given to Dr. D.J.H. Cockayne and staff (in particular Ms. Diana Benson, Messrs. Tony Romeo and Dennis Dwarte) of the Electron Microscope Unit for extending to me the facilities and for their practical help.

Finally, I would like to thank all the members of the Department of Pharmacy who have helped in this project and the University of Sydney for the award of a postgraduate scholarship.

When I consider your heavens,
 the work of your fingers,
the moon and the stars,
 which you have set in place,
What is man that you are mindful
 of him
the son of man that you care for
 him?

Psalm 8: 3,4

Preface

Inhalation aerosols are drug delivery systems which administer the drugs directly to the vicinity of the target tissues in the lung to improve their therapeutic efficiency and to minimize unwanted systemic toxicity. This concentration advantage is retained over a prolonged period if the drug is removed only slowly from its target site and there are efficient mechanisms for elimination of the drug from systemic circulation. Currently, the most common formulations of therapeutic inhalation aerosols are suspensions of solid drug particles in a halocarbon propellant. There are also formulations using dry powders only.

Several advantages exist when using solid drug particles as opposed to solutions in inhalation aerosols. Firstly, solid particles are not diluted and therefore a bigger drug loading can be used. This is important since there are severe limitations on the total aerosol burden that can be administered to a patient (probably not more that about 0.2g per single treatment). Secondly, for sparingly soluble drugs, solid particles will retain both their size and shape during the transit through the respiratory tract as opposed to solution droplets which will exchange water with the environment resulting in growth or shrinkage. Thus, aerodynamic properties of solid particles can be designed to give a much more predictable deposition or targeting in the lung. Thirdly, deposited sparingly soluble drugs will show 'sustained release' characteristics, provided that the site of deposition is sufficiently deep to avoid rapid clearance upwards by coughing. Lastly, solid forms usually are chemically more stable than solutions.

This project is divided into 3 main chapters; each is a study of a specific drug and can be treated independently. The programme of study for each drug is outlined in Fig. i, ii, and iii.

Fig. i

Cromoglycic Acid (CA)

Preparation:

elongated fibrous particles
crystallized from various solvents

Characterization:

SEM, M.p.
Spectroscopy (UV, IR, ^{1}H NMR)
X-ray powder diffraction

Aerodynamics Study:

Fundamental Study:

Geometric measurement
SEM/NPF/IAS*
Theoretical calculation

Aerodynamic Size Measurement:

Aerosol generation:
(glass nebuliser)
Drying: (spray-dried in a drying column)
Particle sizing:
(cascade impactor)

*
SEM: Scanning electron microscopy
NPF: Nuclepore filter
IAS: Image analysis system

Fig. ii

Methotrexate (MTX)

Preparation of MTX crystals:

i) initial studies using a variety of solvents
ii) crystallization in the presence of thymidine

Crystal structure:

single crystal X-ray diffraction

Characterizations:

M.p., spectroscopy (UV, IR, ^{1}H NMR), MS, TLC, optical rotation, X-ray powder diffraction, microscopy

Crystal habit modification:

chemical effects: solvents
additives
dyes
surfactants —

physical effects: supersaturation
rate of cooling
agitation
temperature
substrate growth
gel-growth

Further characterization of various MTX forms: DTA-TG
X-ray powder diffraction
Solubility

Fig. iii

Hexamethylmelamine (HMM)

Mechanistic study of habit modification:

Quantitation of crystal habits in solvents:

i) preparation of crystals: recrystallization from solvent
ii) Quantitation: IAS

Solute-solvent interactions:

spectroscopy (UV, IR, ^{1}H NMR) and molar Kerr effect

HMM/HFB solvate: formation and characterization

Growth kinetics:

growth of individual crystals in stagnant solutions of a growth cell; solubility and supersaturation measurement

Diffusion-controlled growth rate estimation

α-factor:

estimation from ΔH_s, ΔS_s, ΔH_f, solubility and density

List of Content Page

Chapter 1 CROMOGLYCIC ACID (CA)

1.1 Introduction 1

i) Aim of the study 1

ii) Aerodynamic properties of fibres 2

iii) Deposition of aerosol 3

iv) Deposition and interception of fibres 3

v) Theoretical calculation of aerodynamic diameters of fibres 5

1.2 Preparation of CA 9

1.2.1 Materials and Methods 9

1.2.2 Characterization 10

a) Scanning Electron Microscopy (SEM) 10

b) Melting Point (M.P.) Measurement 11

c) UV Spectroscopy 11

d) IR Spectroscopy 11

e) ^{1}H NMR Spectroscopy 12

f) X-Ray Powder Diffraction 12

1.3 Results and Discussion 13

Characterization

a) Scanning Electron Microscopy (SEM) 13

b) Melting Point (M.P.) Measurement 16

c) UV Spectroscopy 16

d) IR Spectroscopy 19

e) ^{1}H NMR Spectroscopy 19

f) X-Ray Powder Diffraction 19

1.4 Drying of CA 24

Design for a drying column 27

Drying efficiency 27

1.5 Aerodynamic Measurement 30

1.5.1 Generation of aerosols 32

1.5.2	Particle sizing-- Cascade impactor	34
	Treatment of glassware and material	38
	Preparation of collection surfaces	39
1.5.3	Chemical assay of CA	39
	i) Determination of the fluorescence emission and excitation spectra	39
	ii) Calibration curve	40
	iii) Quantitative analysis of CA	41
	iv) Recovery of CA from collection surfaces	42
	v) Data treatment	42
1.6	Results and Discussion	43
	Emission and excitation spectra	43
	Calibration curve	46
	Recovery of CA	46
	Quantitative determination of CA	46
	Impactor data treatment	49
1.7	Fundamental Study of Aerodynamics	49
1.7.1	Geometric measurement	50
	i) Collection on Nuclepore filter (NPF)	50
	ii) Scanning electron microscopy	51
	a. Preparation of specimen	51
	b. Random sampling on the NPF	52
	iii) Image analysis system	52
1.7.2	Measurement of particle thickness	55
1.7.3	Data treatment	56
1.8	Results and Discussion	59
	Geometric measurement	59
	Thickness measurement	62
	Data treatment	63
1.9	Conclusions	65
	Future work	67

Chapter 2 METHOTREXATE (MTX)

2.1	Introduction	68
	i) Modifications of crystal habits	68
	ii) Aim of the study	79
2.2	Preliminary Experiments	81
2.2.1	Crystal Habits of MTX in Different Solvents	81
	i) Materials and Methods	81
	ii) Results	81
	iii) Discussion	83
2.2.2	Crystalline Properties of the Original MTX Powder	83
	i) Materials and Methods	83
	ii) Results	85
	iii) Discussion	85
2.2.3	Preparation of MTX Crystals by Sublimation	87
	i) Materials and Methods	87
	ii) Results and Discussion	88
2.3	Experiments to Prepare MTX Crystals: Crystallization of MTX in the Presence of Thymidine	88
2.3.1	Materials and Methods	89
2.3.2	Results	89
2.3.3	Characterization	90
	i) Experimental	90
	ii) Results	93
	iii) Discussion	105
2.4	Crystal Structure of MTX	108
2.4.1	Experimentals	108
2.4.2	Results and Discussion	109
2.5	Habit Modifications of MTX Crystals	113
2.5.1	Materials and Methods	113
	i) Chemical effects	113
	ii) Physical effects	116
2.5.2	Results and Discussion	122
	i) Chemical effects	122

ii) Physical effects 128
2.5.3 Further Characterization of Various MTX Forms 130
i) Experimental 130
ii) Results and Discussion 133

2.6 Discussion 143

2.7 Conclusion 147
Future Work 148

Chapter 3 HEXAMETHYLMELAMINE (HMM)

3.1 Introduction 149
i) Aim of the study 149
ii) Crystal orientation 150
iii) Solute-solvent interactions 152
a) UV absorption spectroscopy 152
b) IR absorption spectroscopy 153
c) ^{1}H NMR spectroscopy 154
d) Electro-optical Kerr effect measurements 155
iv) Growth kinetics and mechanisms 157
v) The surface entropy (α) factor 159

3.2 Crystal Habit Quantitation 162
i) Experimental 162
a) Growing of HMM crystals 162
b) Measurement of crystal dimension 163
Data treatment 164
c) Determination of crystal orientation 165
ii) Results and Discussion 165

3.3 Solute-solvent Interactions 171
i) Experimental 171
a) UV spectroscopy 171
b) IR spectroscopy 171
c) ^{1}H NMR spectroscopy 172
d) Molar Kerr constant measurements 173
ii) Results and Discussion 173

a) UV spectroscopy 173
b) IR spectroscopy 175
c) ^{1}H NMR spectroscopy 175
d) Molar Kerr constant measurements 180
iii) Conclusions 182

3.4 Growth Kinetics and Evaluation of α-factor 185
i) Experimental 185
a) Solubility measurement 185
b) Growth kinetics of single crystals 186
Estimates of errors in the measurements 190
c) Determination of supersaturation 190
d) Estimation of diffusion-controlled growth rate 191
e) α-factor evaluation 193
ii) Results and Discussion 194
a) solubility measurements 194
b) Growth kinetics and supersaturation 195
c) α-factor 218
iii) Conclusions 223

3.5 Hexamethylmelamine-hexafluorobenzene Complex 224
3.5.1 Characterization 224
i) Experimental 224
a) X-ray powder diffraction 224
b) IR spectroscopy 225
c) Hot-stage microscopy 225
d) DTA-TG analysis 225
ii) Results 226
a) X-ray powder diffraction 226
b) IR spectroscopy 226
c) Hot-stage microscopy 226
d) DTA-TG analysis 226
iii) Discussion 231
3.5.2 Solvation study of HMM/HFB solvate 232
i) Experimental and Results 232
ii) Discussion 232

Appendix 1	Publications	234
Appendix 2	Procedure to locate the random fields of view, f.v., on the filter segment	260
Appendix 3	MTX crystal data collection details	265
Appendix 4	Determination of the crystal orientation by polarizing microscopy	266
Appendix 5	Values of C, C_1, C_2, and C_3 in the polynomial equations of dependence of the crystal length (L) and breadth (B) on time	268
References		270

List of Figures

Figure		Page
1.1	Plots of the dimensionless parameter $(\sqrt{\rho_0/\rho})\ D_a/D_f$ versus the axial (aspect) ratio β for fibres using the expressions listed in Table 1.1	8
1.2a	CA from acidic precipitation before crystallization	14
1.2b	CA recrystallized from hot water	14
1.2c	CA recrystallized from methanol	15
1.2d	CA recrystallized from DMSO/H_2O	15
1.3a	UV spectrum of CA	17
1.3b	UV spectrum of CA at different pH	18
1.4a	IR spectrum of CA from hot water	20
1.4b	IR spectrum of CA from DMSO/H_2O	21
1.5a	^1H NMR spectrum of CA from hot water	22
1.5b	^1H NMR spectrum of CA from DMSO/H_2O	23
1.6a	X-ray powder diffraction pattern of CA (crystalized from hot water)	25
1.6b	X-ray powder diffraction pattern of CA (before crystallization from hot water)	26
1.7a	Photograph of the drying column	28
1.7b	Schematic diagram of the drying column	29
1.8a	Photograph of deVilbiss no.40 nebuliser and the baffled adaptor tube connected to the drying column	31
1.8b	Diagram of deVilbiss no. 40 nebuliser	33
1.9a	Photograph of cascade impactor connected to the drying column	36
1.9b	Schematic diagram of DCI-6 cascade impactor showing (a) ideal and (b) non-ideal collection efficiency	37
1.10a	Emission fluorescence spectrum of CA	44
1.10b	Excitation fluorescence spectrum of CA	45
1.11	Calibration curve of CA	47

1.12	Random sampling on the filter	53
1.13	Block diagram of the image analysis system	55
1.14	CA particles collected on the Nuclepore filter	60
2.1a	Scanning electronmicrograph of the original MTX powder	86
2.1b-f	Optical micrographs of MTX	
	b. original powder	86
	c. tetragonal crystals	119
	d. spheres	119
	e. rosettes	120
	f. ellipses	120
2.1g	Concentration dependent rounding effect of MTX crystals by additives	121
2.2	UV spectrum of MTX in 0.1N NaOH	95
2.3a	IR spectrum of the original MTX powder	96
2.3b	IR spectrum of the tetragonal MTX crystal	97
2.4a	^{1}H NMR spectrum of the original MTX powder	98
2.4b	^{1}H NMR spectrum of the tetragonal MTX crystals	99
2.4c	^{1}H NMR spectrum of thymidine	100
2.4d	^{1}H NMR spectrum of MTX: thymidine (10:1)	102
2.5	Mass spectrum of MTX	103
2.6a	X-ray powder diffraction pattern of the original MTX powder	106
2.6b	X-ray powder diffraction pattern of the tetragonal MTX crystals	107
2.7	Stereoview of the unit cell of MTX	110
2.8	Molecular structure and conformation of MTX molecule in the crystal	111
2.9	Molecular structures of the 'tailor-made' additives	115/116
2.10a	TG and DTA curves of various MTX forms	134
2.10b	DTA curves of various MTX forms (under N_2 atmosphere)	135
2.11a	X-ray powder diffraction pattern of MTX obtained from methanol	138

2.11b	X-ray powder diffraction pattern of MTX obtained from ornithine solution	139
2.12	Solubility characteristics of different MTX forms	140
2.13	X-ray powder diffraction pattern of the original MTX powder after stirring in water for 100 hours	142
3.1	Crystallographic diagram of the crystal morphology of HMM	151
3.2	Principle of molar Kerr effect (showing plane polarized light entering an "ordered" system of molecules ($n_{\parallel} = n_{\perp}$)	156
3.3	Photograph of (a) hexagonal compact and (b) needle habits of HMM crystals	167
3.4	- (not included)	
3.5a	IR spectrum of HMM in $CHCl_3$	176
3.5b	IR spectrum of HMM in CCl_4	177
3.6	^1H NMR spectrum of HMM	178
3.7	Stereospecific encounters between HMM and solvating aromatic molecules	183
3.8	The growth cell for crystal growth kinetics measurement	187
3.9	The whole set-up for crystal growth kinetics measurement	188
3.10a-f	Crystal size (length, L and breadth, B) vs time in methanol	
	a: run 1 (4 crystals), L	197
	b: run 1 (4 crystals), B	198
	c: run 2 (5 crystals), L	199
	d: run 2 (5 crystals), B	200
	e: run 3 (3 crystals), L	201
	f: run 3 (3 crystals), B	202
3.10g-h	Crystal size (length, L and breadth, B) vs time in cyclohexane	
	g: 3 runs (4 crystals) L	203
	h: 3 runs (4 crystals) B	204
3.11a	Supersaturation vs time in methanol	208
3.11b	Supersaturation vs time in cyclohexane	209
3.12a-c	Growth rate (R) vs supersaturation (σ) in methanol (a: run 1, b: run 2, c: run 3)	211-213

3.12d	Growth rate (R) vs supersaturation (σ) in cyclohexane (3 runs)	214
3.13	log X (mole fraction of HMM) vs $1/T \times 10^3$	219
3.14	ln X (mole fraction of HMM) vs ln T (temp)	220
3.15	X-ray powder diffraction pattern of HMM recrystallized from hexafluorobenzene	227
3.16a	IR spectrum of HMM recrystallized from hexafluorobenzene	228
3.16b	IR spectrum of original HMM before recrystallization	229
3.17	TG and DTA curves for the HMM/C_6F_6 adduct	230

Lists of Tables

Table		Page
1.1	Summary of various theoretical expressions for calculation of D_a of fibres	8
1.2	Melting temperatures of CA samples	16
1.3	Recovery of CA from impaction slides and filter	48
1.4	% deposition of CA on each stage of the impactor	48
1.5	Mass median aerodynamic diameters (MMAD) and geometric standard deviations (σ_g) of CA particles measured by cascade impactor	49
1.6	Geometric mean (X_g) and geometric standard deviations (σ_g) of 108 and 200 CA fibres in 60 and 100 fields of view	61
1.7	Mass median aerodynamic diameter (MMAD) and geometric standard deviation (σ_g) of CA particles obtained by theoretical calculations	63/64
2.1	Examples of habit modification by solvents	71
2.2	Melting temperature of the original powder and tetragonal crystals of MTX	94
2.3	TLC results of the original powder and tetragonal crystals of MTX	101
2.4	Optical rotation results of the original powder and tetragonal crystals of MTX	104
2.5	Effects of solvents on the crystal habits of MTX	123
2.6	Effects of surfactants on the crystal habits of MTX	124
2.7	Effects of 'tailor-made' additives on the crystal habits of MTX	125
2.8	Effects of dyes on the crystal habits of MTX	126
2.9	Effects of other additives on the crystal habits of MTX	127-128
2.10	Effects of supersaturation on the crystal habits of MTX	128

2.11	Effects of agitation on the crystal habits of MTX	129
2.12	Solubilities of various MTX forms.	141
3.1	Crystal habits of HMM and solvent polarity	170
3.2	The wavelength and the corresponding intensity for the UV absorption maximum of HMM in various solvents	174
3.3a	The chemical shifts of HMM in both polar and non-polar solvents	179
3.3b	Various temperature NMR study of HMM in d^8 - toluene solution	180
3.4	The molar Kerr constants of HMM in various solvents	181
3.5	Solubilities of HMM in methanol and in cyclohexane	194
3.6a-c	Measured growth rates of HMM crystals in methanol a: run 1 b: run 2 c: run 3	205-206
3.6d	Measured growth rates of HMM crystals in cyclohexane	206
3.7a	Supersaturation of HMM in methanol	210
3.7b	Supersaturation of HMM in cyclohexane	210
3.8	Calculated diffusion growth rates (measured growth rates included for comparisons)	215
3.9	Table of T, $1/T \times 10^3$ and mole fraction (X) $\times 10^3$ in methanol and cyclohexane	218
3.10	Table of T, ln T and ln X (mole fraction) in methanol and cyclohexane	221
3.11	Values of α-factors calculated for the (0001) and (1100) faces of HMM crystals in methanol and cyclohexane	221
3.12	The measured growth rates of HMM crystals at the same supersaturation in methanol and cyclohexane	222

CHAPTER ONE

1. CROMOGLYCIC ACID (CA)

1.1 Introduction

i) Aim of the study

Disodium cromoglycate is an anti-allergic agent. It is administered by direct inhalation into the respiratory tract for prophylaxis of asthma. Being a very hygroscopic salt, DSCG will take up varying amounts of water according to the humidity of environment. In the human respiratory tract, the relative humidity is 99.5%, originating from the saturated vapour pressure over isotonic body fluids at body temperature. Therefore, inhaled DSCG particles have the capacity to absorb moisture and change in size. It was found both from experiments and by calculations that more than a 2-fold increase in the aerodynamic diameters of DSCG particles could occur (Gonda et al, 1982), likely to result in a change of deposition of DSCG particles in the lung. Our aims were:

1.) to eliminate such hygroscopic growth of DSCG by preparing non-hygroscopic particles of cromoglycic acid (CA) in forms suitable for inhalation.

2.) to control the aerodynamic diameters by modifying the shape of CA particles. We are particularly interested in elongated shape particles because of their unique aerodynamic properties (see below). For a non-hygroscopic material, the shape would be preserved until the particle

deposits on the respiratory tract.

ii) Aerodynamic properties of fibres

Aerodynamic diameter, Da, is a very important physical parameter in describing the aerodynamics of fibres and their deposition in the respiratory tract of animals. It is defined as the diameter of a sphere with unit density (e.g. 1 g/cm^3) which has the same terminal settling velocity as the particle of interest (Task, 1966). Therefore, this parameter has been standardized with respect to the density, size and shape of the particle. A classical investigation had been reported on the relationship between the free-falling speeds of fibres and their physical dimensions (Timbrell, 1965). The results showed a close dependence of equivalent (aerodynamic) diameter, Da, on the geometric diameter of fibre. As the aspect ratio (i.e. length/diameter), β, increases the ratio of aerodynamic diameter/fibre diameter increases and tends to become a constant at high β (Fig.1.1, Sec.v). In other words, the Da of a fibre is determined predominantly by the geometric diameter, the length being of secondary importance, especially when the fibre has a high β (e.g. $>$ 10). Therefore, elongated particles of varying lengths but with similar short axes will have a narrow range of aerodynamic diameters, as observed e.g. with an anti-cancer drug designed for direct administration into the respiratotry tract (Gonda and Khalik, 1985b).

iii) Deposition of aerosols

Aerosol particles deposit at various sites within the human respiratory tract by 5 fundamental mechanisms (Lippmann et al 1980; Lippmann,1985): Inertial impaction, gravitational sedimentation, diffusion by Brownian motion, electrostatic precipitation and interception. Only the first 3 mechanisms will be important in most cases. However, for elongated particles such as fibres, interception can be significant, especially when the particle size is a significant fraction of the airway diameter. This accounts for deposition of e.g. asbestos fibres 200 µm long in the alveolar regions of human lung (Timbrell, 1965).

iv) Deposition and interception of fibres

Deposition has been found to be closely related to the geometric diameter of fibres (Timbrell, 1965; 1982). Since the human respiratory tract shows a lot of branchings, heavy deposition of long fibres can be expected at the branching site. Sedimentation and impaction operate throughout the respiratory tract to filter out the fibres of high falling speed, that is, the fibres of large diameter. Long fibres which escape such deposition will be subjected to deposition by interception when they reach the smaller airways of about 200 µm in diameter. Interception could account, at least in part, for the enhanced deposition of fibres at the alveolar duct

bifurcation (Lippmann, 1985). Timbrell (1965) considered the possible influence of the elongated shape of fibres on the magnitude of deposition by interception mechanism. Interception, operating either together with or without the other deposition mechanisms, can cause a particle to be deposited. Its significance in relation to the deposition in airways depends on the ratio of the airway diameter to the fibre length, the fibre orientation, and on the location of the fibre centre relative to the airway axis. Deposition of fibres will continue only as long as the diameter of the airway is decreasing. In laminar flow, interception operation alone cannot result in deposition of fibres in an airway of constant diameter with value greater than the fibre length. Timbrell (1965) also obtained indirect evidence for the orientation of fibres in airstream by measuring the orientation of glass fibres and asbestos fibres in an aerosol spectrometer. The results suggested that for fibres with aspect ratio >5, a definite tendency for the fibres to align themselves with the direction of the air streamlines was indicated, and this was more marked for fibres which were highly symmetrical. However, due to the combination of the corrugated nature of airways, and the low symmetry of some fibres, orientations of such objects in airways will tend to be random (Timbrell, 1965). In contrast, the more recent studies by Griffiths et al (1984; 1986) suggested that the motion of a glass fibre falling out due to gravity in the Timbrell spectrometer appeared to be best represented either as a cylinder or a prolate spheroid

sedimenting in a direction perpendicular to its major axis. In summary, if a fibre has a sufficiently small diameter, the falling speed (and hence the aerodynamic diameter, Sec.ii) can be low enough for the fibre to escape deposition by the inertial impaction and sedimentation mechanisms in the upper part of the respiratory tract. The fibre will penetrate deep into the pulmonary region where, if the fibre is sufficiently long, it may be deposited by interception.

v) Theoretical calculation of aerodynamic diameters of fibres

Fundamental study on aerodynamic behaviour of elongated particles such as fibres using mathematical models have been described by Fuchs (1964), Stober (1972), Davies (1979) and Harris and Fraser (1976). Recently, Gonda and Khalik (1985) have briefly reviewed the calculation of aerodynamic diameters of fibres. Starting with the Stokes law,

$$F_s = 3\pi\eta u.\Phi_D \qquad \text{Eqn.(1.1)}$$

F_s: Viscous drag on a particle

η: Viscosity of the medium

u: Velocity of the particle

Φ_D: Diameter of a sphere giving the same viscous drag as the particle in question

which in steady state equals the gravitational force on the particle, F_g,

$$F_g = V\rho g \qquad \text{Eqn.(1.2)}$$

V: Volume of the particle

ρ: Density of the particle

g: Gravitational acceleration

As a result,

$$u = V\rho g / 3\pi\eta\Phi_D \qquad \text{Eqn.(1.3)}$$

Eqn.1.1 and Eqn.1.2 can also be related in terms of Stokes diameter, Φ_{st}:

$$3\pi\eta u.\Phi_{st} = \pi\rho g\Phi_{st}^3/6 \qquad \text{Eqn.(1.4)}$$

By definition, the aerodynamic diameter, Da, equals (neglecting slip):

$$D_a = \Phi_{st}\sqrt{(\rho/\rho_0)} \qquad \text{Eqn.(1.5)}$$

ρ_0: unit density (e.g. $1 g/cm^3$)

From Eqns.1.3, 1.4 and Eqn.1.5

$$D_a = \sqrt{(6V\rho/\pi\rho_0\Phi_D)} \qquad \text{Eqn.(1.6)}$$

Eqn.1.6 forms the basis of most theoretical expressions for D_a. Nevertheless, the actual formulas may differ from each other for the following reasons (Gonda and Khalik, 1985):

1. The shape of the fibrous particles may be approximated by different objects, usually cylinder or prolate spheroids.

2. The selected shape will affect the expressions for V and Φ_D.

3. The assumed orientation of the fibre with repect to the direction of the gas flow will affect the final expression for D_a.

For example, Harris and Fraser (1976) approximated the viscous drag of the fibres by expressions for Φ_D derived for prolate spheroids, but the volume of the fibres was

approximated by cylinders. It should be noted that the volume of a cylinder is 3/2 the volume of a prolate spheroid. Therefore, Gonda and Khalik (1985) later modified Harris and Fraser's expressions by describing the fibre volume by prolate spheroids. A summary of various expressions for theoretical calculations of Da of fibres and the results are presented in Table 1.1 and Fig.1.1 respectively. Most recently, Johnson (1986) and Johnson et al (1987) also presented a new empirical expression for D_a calculation derived from experimental data using prismatic bodies. The expression has been reported to give a maximum error of 10% in drag predictions on non-spherical, prismatic aerosol particles. It was included in the present study. By substituting the expression

$$\Phi_D = Ds/(0.246 + 0.531\Psi + 0.258Ds/Dn - 0.036Dmax/Dn) \quad \text{Eqn.(1.7)}$$

Ψ: Surface sphericity

= area of equivalent volume sphere/area of the body

Ds: Equivalent volume sphere diameter

Dn: Projected area diameter

Dmax: Maximum body dimension along a primary axis

into Eqn.1.6, D_a can be found.

Correction factor has also been developed to improve the accuracy of Johnson's equation for prisms having large length-to-width ratio (Sheaffer, 1987). We also used it in the calculation.

Aerodynamic diameter	Harris and Fraser (H and F)	Modified equation of (H and F) by Gonda and Khalik (G and K)	Modified equation using $\bar{K}$ of Fuchs and Stöber (F and S) by (G and K)
$Da_{\perp}$ =	1a $\frac{1}{2} D_f \sqrt{\frac{\rho}{\rho_o} \frac{\ln 2\beta + 0.5}{2}}$	1d $\sqrt{\frac{1}{2}} D_f \sqrt{\frac{\rho}{\rho_o} \frac{\ln 2\beta + 0.5}{2}}$	———
$Da_{\parallel}$ =	1b $\frac{1}{2} D_f \sqrt{\frac{\rho}{\rho_o} (\ln 2\beta - 0.5)}$	1e $\sqrt{\frac{1}{2}} D_f \sqrt{\frac{\rho}{\rho_o} (\ln 2\beta - 0.5)}$	———
Da_R =	1c $\frac{1}{2} D_f \sqrt{\frac{\rho/\rho_o}{\frac{0.385}{\ln 2\beta - 0.5} + \frac{1.230}{\ln 2\beta + 0.5}}}$	1f $\sqrt{\frac{1}{2}} D_f \sqrt{\frac{\rho/\rho_o}{\frac{0.385}{\ln 2\beta - 0.5} + \frac{1.230}{\ln 2\beta + 0.5}}}$	1g $D_f \sqrt{\frac{\rho}{\rho_o} \frac{1}{\frac{2}{9} \frac{1}{\ln 2\beta - 0.5} + \frac{8}{9} \frac{1}{\ln 2\beta + 0.5}}}$

Table 1.1 Summary of the expressions for calculation of Da of fibres (Expressions numbered at left top corners)
D_f: Geometric diameter of fibres

$Da_{\perp}$, $Da_{\parallel}$ and Da_R correspond to the orientation of the fibre perpendicular, parallel and random to the direction of its motion respectively

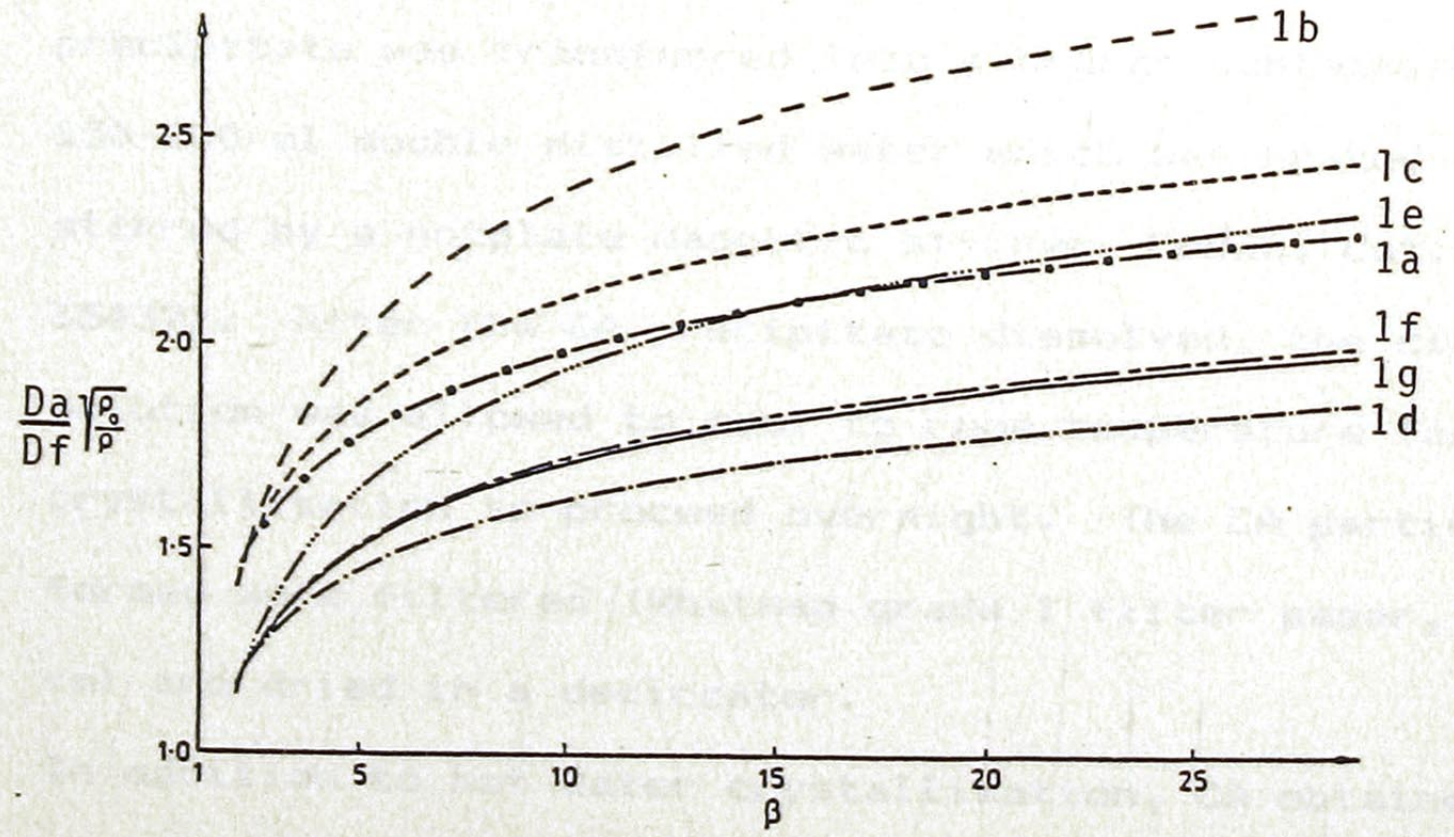

Fig. 1.1 Plots of the dimensionless parameter $Da/Df\sqrt{\rho_o/\rho}$ versus the axial (aspect) ratio β for fibres using the expressions listed in Table 1.1.

1.2 Preparation of CA

1.2.1 Materials and Methods

100 mg of disodium cromoglycate (supplied by Fisons plc, Pharmaceutical Division, England) was dissolved in 30 ml double distilled water. 1 ml conc. HCl (Univar, Ajax Chemicals, Sydney) was slowly added into the solution with stirring to precipitate cromoglycic acid (CA) which was then transferred into a centrifuge tube. The precipitate was washed with double distilled water and centrifuged (Janetzki T22, max. setting, 5 min.). The supernatant was discarded. The washing and centrifuging process was continued until the supernatant showed a pH ~5 on pH paper (14 pH units, Whatman-BDH, Poole, England). At this stage, the CA precipitate was either dried in a desiccator and then further characterised or it was subjected to crystallization from hot water. In the latter case, the precipitate was transferred into a beaker containing 150-200 ml double distilled water which was heated and stirred by a hotplate magnetic stirrer (Cenco, Cat.no. 35432). After the CA precipitate dissolved, the clear solution was allowed to cool to room temperature for crystallisation to proceed overnight. The CA particles formed were filtered (Whatman grade 1 filter paper, 2.0 cm) and dried in a desiccator.

In addition to hot water crystallisation, CA obtained from direct acid precipitation was also crystallised from polar organic solvents such as methanol and dimethylsulfoxide

(DMSO). In 1-2 ml hot methanol (AR, May & Baker, West Footscray, Victoria, Australia), 1 mg CA was dissolved. The solution was allowed to cool for crystallisation. From a DMSO-H_2O system, CA crystals were prepared by adding water dropwise into a solution of CA in DMSO (Univar, Ajax Chemicals, Sydney) to decrease the solubility of the acid until precipitation of CA just occurred. The solution was then heated to redissolve the precipitate and then allowed to stand at room temperature for crystallisation overnight. The CA particles thus formed were filtered and dried as above. Nonpolar solvents such as benzene and cyclohexane were not suitable for crystallisation because CA was practically insoluble in them.

1.2.2 Characterization

Particle morphology was first studied by microscopy on all CA samples. Afterwards, various physical and chemical characterizations were further done on the CA samples prepared from direct acid precipitation before crystallization, and after crystallization from hot water and DMSO/H_2O.

a.) Scanning electron microscopy (SEM)

Cromoglycic acid (CA) particles on a microscope cover slip were mounted onto an SEM sample stub using a double sided sticky tape. After coating with platinum under vacuum,

silver dag was applied to facilitate the electrical contact between the stub and the specimen. The samples were examined under a scanning electron microscope (Jeol JEM 35C). To obtain the image, an electron beam accelerating voltage of 10-25 KV, with both secondary electron and back scattered electron (BSE) detector were used. BSE detector is especially useful for specimens with low degree of contrast such as the flat fibres of CA crystallised from hot water.

b.) Melting point (m.p.) measurement

M.p. was measured both by a melting point apparatus (Townson & Mercer Ltd., England) and a Kofler hot stage microscope (Reichert, Wien, Austria) using a heating rate of 4^0C/min as recommended for substances which decompose on melting (Kuhnert-Brandstatter, 1966).

c.) UV spectroscopy

UV absorption spectra of CA in 0.1N NaOH were determined in a spectrophotometer (Perkin-Elmer Lambda 5 UV/VIS) with a pair of matched 1cm quartz cuvettes. The instrumental settings were: slit 2nm, response 0.5s, and scan speed 60nm/min.

d.) IR spectroscopy

IR spectra were determined in an infra-red

spectrophotometer (Perkin-Elmer double beam 297) by employing the pellet method with KBr as the matrix material and a compression pressure of 2500 lb/in^2 or 10 tons on a 3.375 inches diameter ram of the press (30 ton press H30-1 MK.2, Research and Industrial Instruments Company, England).

e.) ^{1}H-NMR spectroscopy

^{1}H-NMR spectra were determined in a Fourier transform NMR spectrometer (Jeol FX 90Q). Chemical shifts were recorded as δ (ppm) in respect to the internal standard, dioxane or DMSO. 10% sodium deuteroxide was used as the solvent.
The operating conditions were:
Proton irradiation frequency 90 MHz
Deuterium lock signal for tuning
Data points 8K
Spectral width 896 Hz

f.) X-ray powder diffraction

X-ray powder diffraction patterns are chiefly used as a rapid means of identification (Glasser,1977). The condition governing the position of a diffracted X-ray beam from a powder sample is given by Bragg's law:

$n\lambda = 2d_{hkl}.\sin\theta$

n: an integer

λ: wavelength of X-ray

d_{hkl}: interplanar spacing between crystallographic

planes(*hkl*) in the crystal lattice

θ: angle between the crystallographic plane and the X-ray beam

Therefore polymorphs with different crystal lattices can be detected by the differences in their powder patterns. Intensities of the diffraction peaks can also be used to determine the degree of crystallinity of drug powder samples (Black and Lovering, 1977; Scottys et al, 1984; Suryanarayanan and Mitchell, 1985). CA samples in the form of a fine powder were prepared by grinding in an agate mortar with the aims to reduce the particle size and to minimize preferred orientation of the particles. The powder patterns were recorded by an X-ray diffractometer (Rigaku "Miniflex" CN 2005) with Cu target, X-ray tube voltage at 30 KV and a scanning speed of 2^0/min at 50 Hz.

1.3 Results and Discussion

Characterization

a.) Scanning electron microscopy

CA obtained by direct acid precipitation using HCl is shown in Fig.1.2a which shows the amorphous structure and branching system of CA. However, after crystallization from hot water, flat fibres were formed; as shown in Fig.1.2b. CA obtained from methanol was a mixture of amorphous and very fine fibres but from DMSO/H_2O, very well formed rod-shaped fibres were formed which were shown in Fig.1.2c and Fig.1.2d respectively. Therefore, fibres

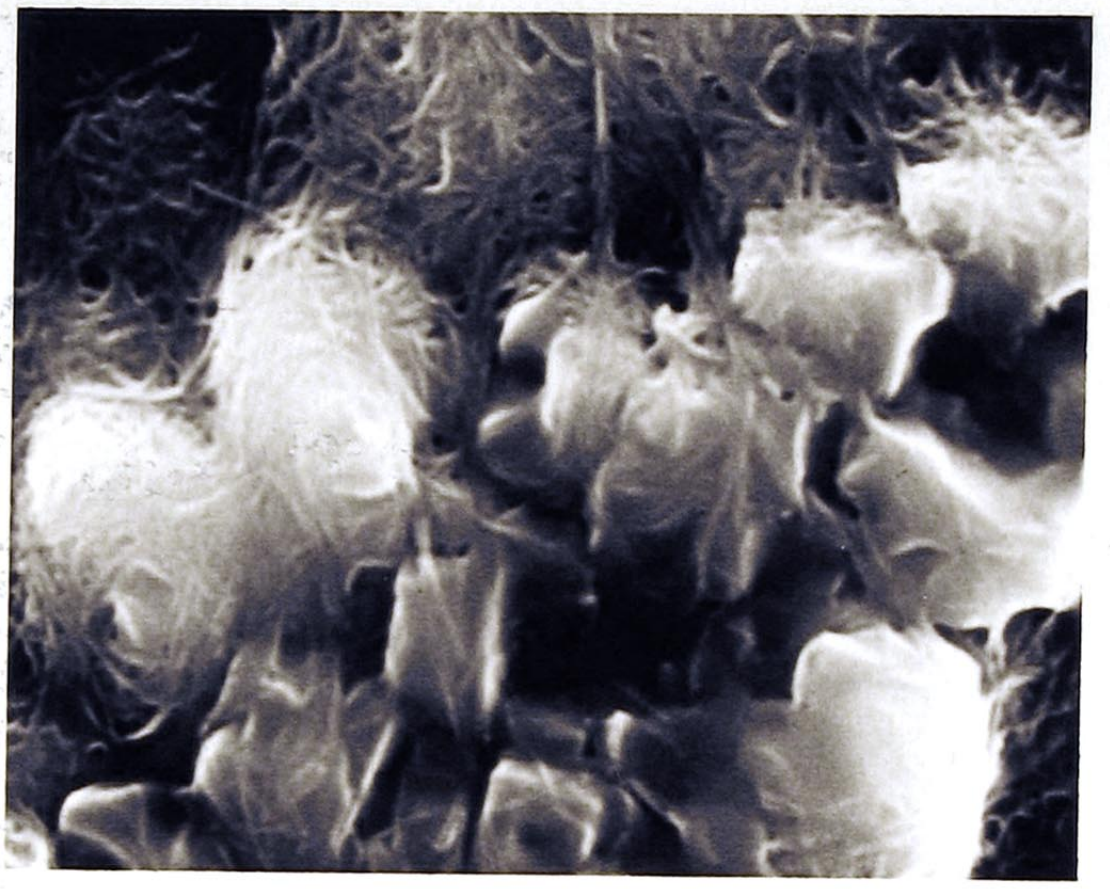

Fig. 1.2a CA from acidic precipitation before crystallization (scale bar: 1μm)



Fig. 1.2b CA recrystallized from hot water (scale bar: 0.5μm)

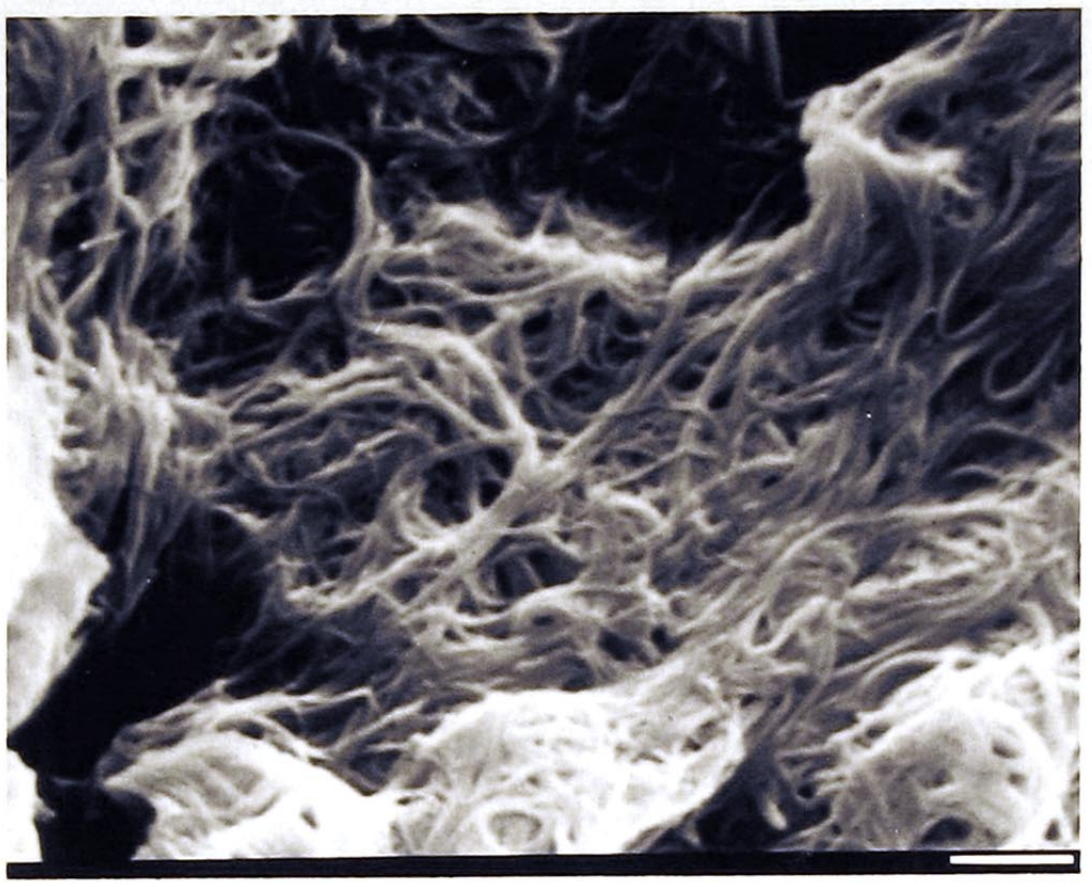

Fig. 1.2c CA recrystallized from methanol
(scale bar: 1μm)

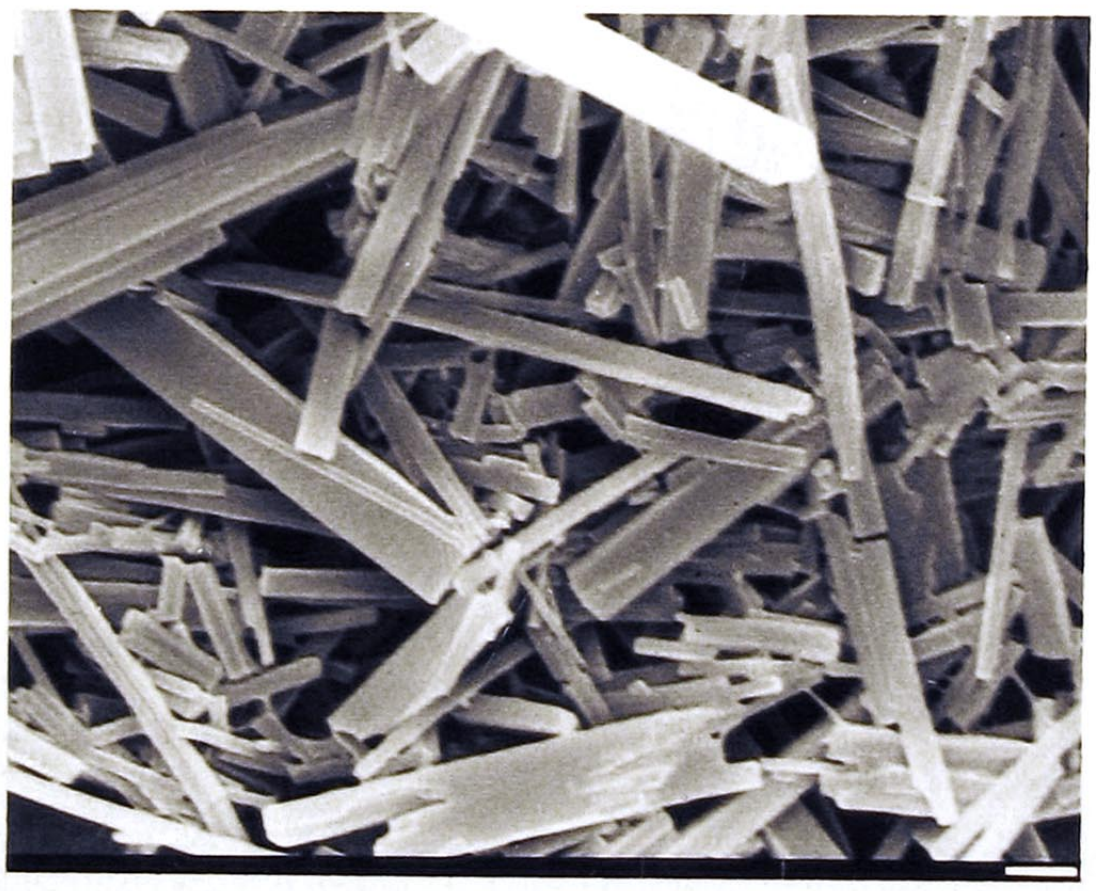

Fig. 1.2d CA recrystallized from DMSO/H_2O
(scale bar: 1μm)

of CA can be obtained from solvents of high polarity such as water and DMSO/H_2O. The CA fibres from hot water were chosen for the aerodynamic study in the later part of the research.

b.) Melting point measurement

Both methods gave similar range of m.p. for CA and the results are shown in Table 1.2. A range of melting temperature instead of a single point obtained was due to the high heating rate plus decomposition of CA on melting.

Table 1.2

samples	melting point (^{0}C)
CA from acid precipitation	239-247
CA crystallised from hot water	242-247
CA crystallised from DMSO	238-244
CA crystallised from DMSO (heated in vacuum and checked by ^{1}H NMR to be free from DMSO)	237-243

c.) UV measurement

The UV spectra of various CA samples are identical (and are the same as the spectrum of sodium cromoglycate in distilled water) with the absorbance maxima λmax at 327.7 and 239.2 nm. A representative spectrum is illustrated in Fig.1.3a (Fig.1.3b shows that the absorption peak at 327 nm is independent of the pH).

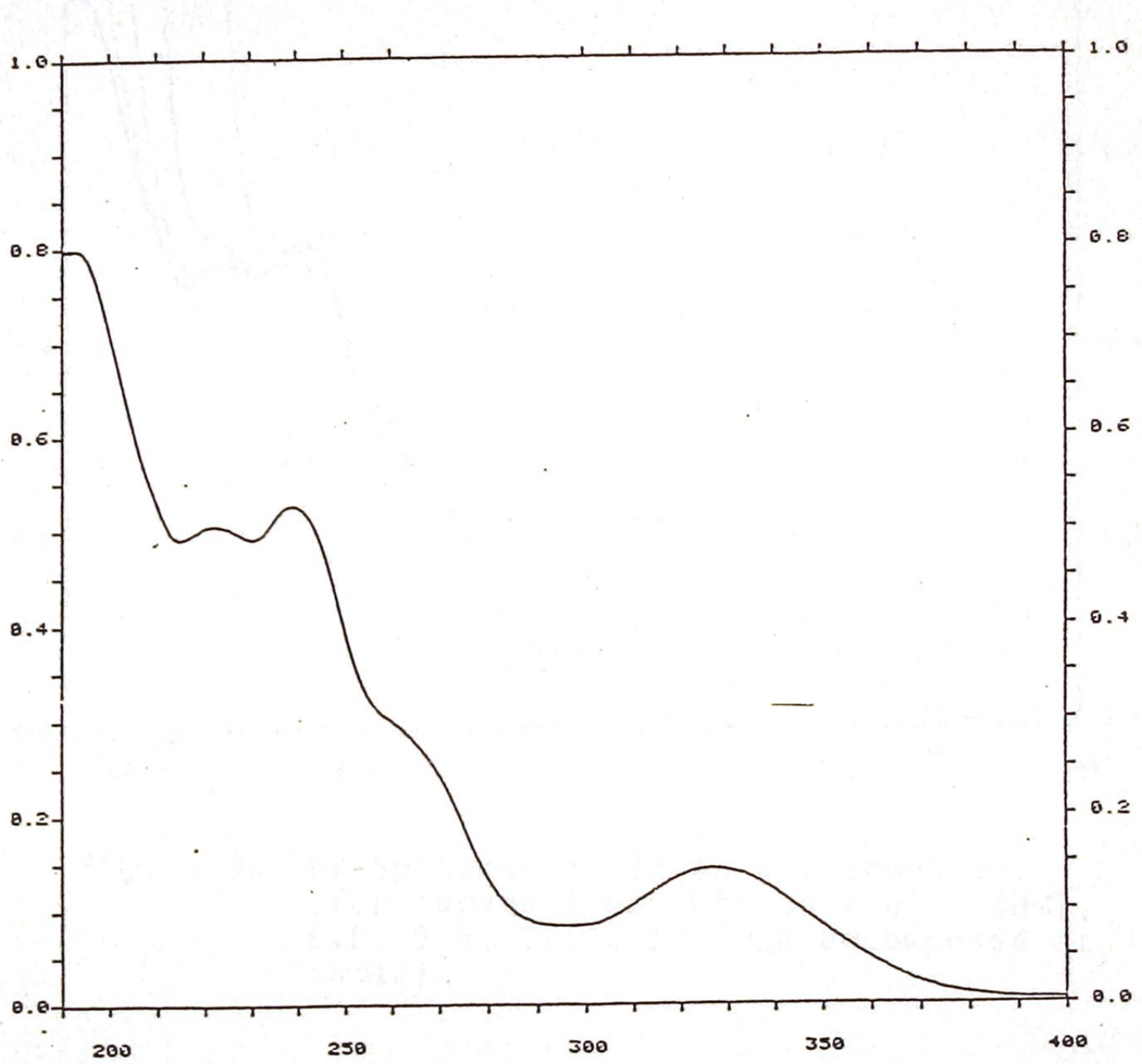

Fig. 1.3a UV Spectrum of CA

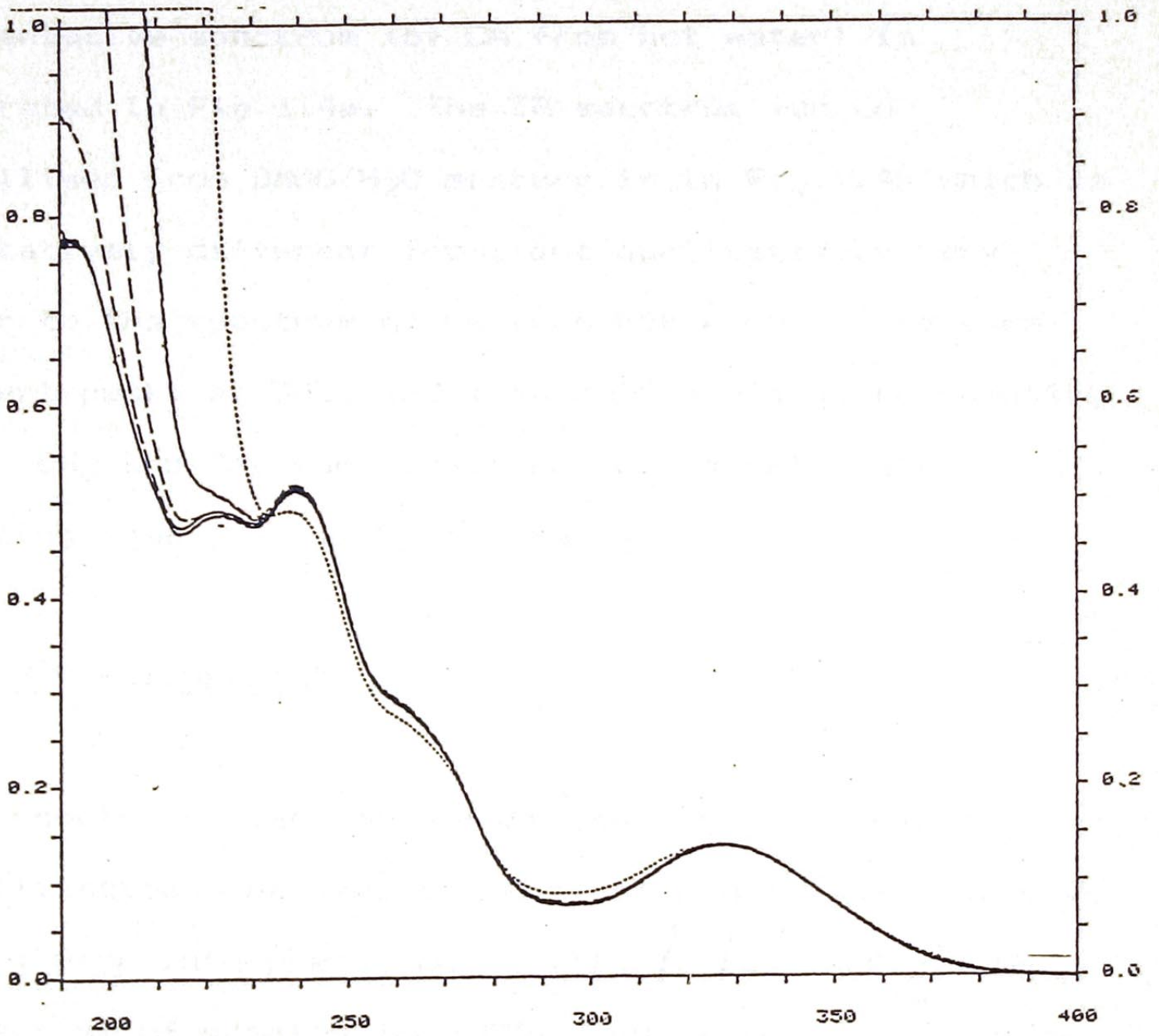

Fig. 1.3b UV Spectrum of CA at different pH. (for curves from left to right: pH<7, 9.0, 9.5, 10.5, >12; CA decomposed at pH>12)

d.) IR measurement

The IR spectra measured for CA before and after crystallisation from hot water are very similar. A representative spectrum (of CA from hot water) is illustrated in Fig.1.4a. The IR spectrum for CA crystallised from DMSO/H_2O mixture is in Fig.1.4b which is quantitatively different from, but qualitatively very similar to the spectrum of CA from hot water. The more prominent peaks at 3050 and 1090 cm^{-1} may be corresponding to the $-CH_3$ and S=O functional groups respectively, suggesting some DMSO might be present.

e.) ^1H NMR measurement

^1H NMR spectra of samples before and after hot water crystallisation are almost identical and a representative spectrum with interpretation is illustrated in Fig.1.5a. The spectrum of samples from DMSO/H_2O gives an extra peak of varying intensity at 2.72 ppm corresponding to DMSO (Fig.1.5b). It has been found that the extra peak can be removed by heating the CA at 170^0 under high vacuum for 24 hours or by washing with distilled water, suggesting surface adsorption of DMSO only.

f.) X-ray powder diffraction

The diffraction patterns of CA obtained both from hot water or DMSO/H_2O are identical, confirming that the 2

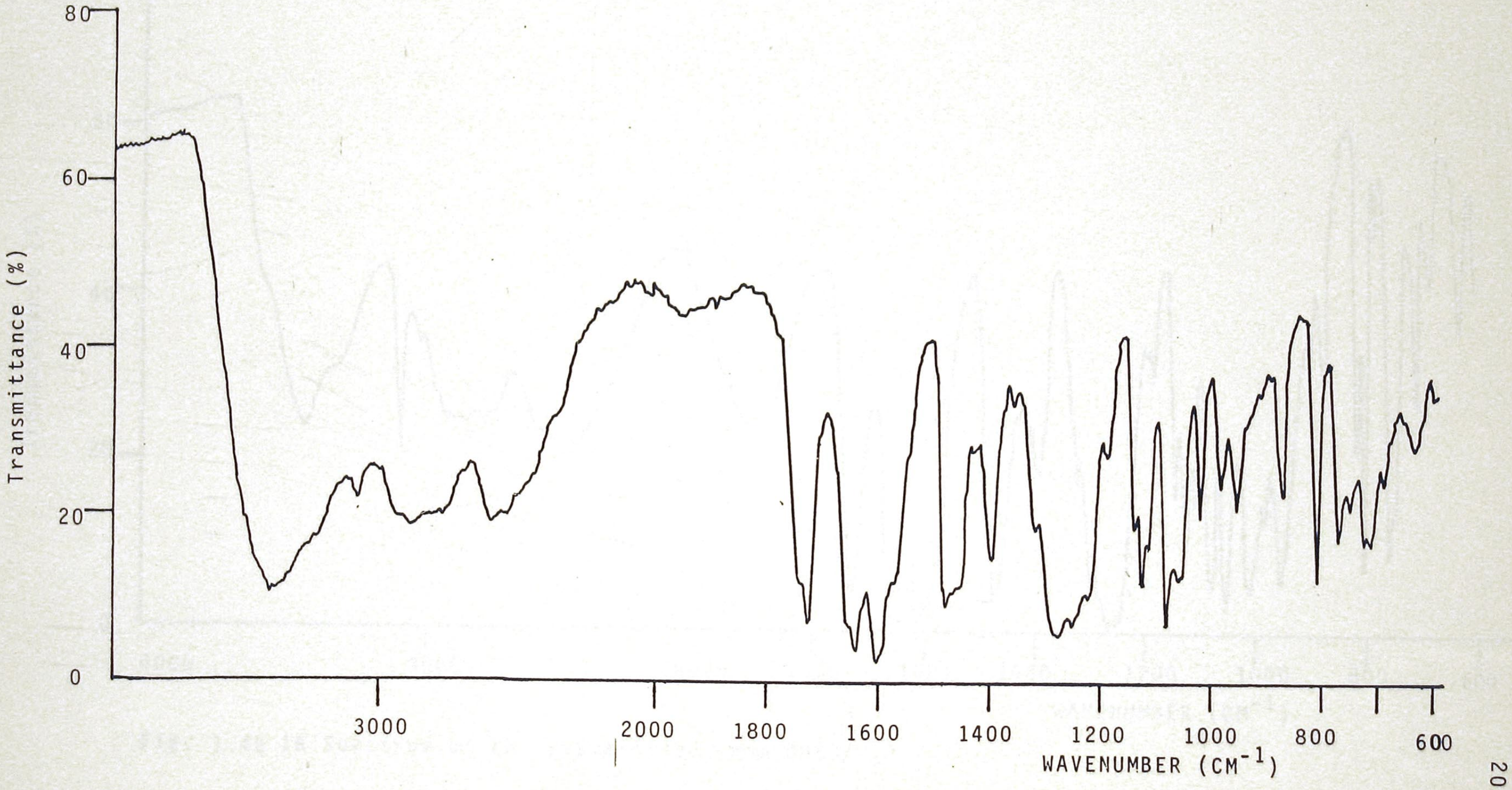

Fig. 1.4a IR Spectrum of CA from hot water

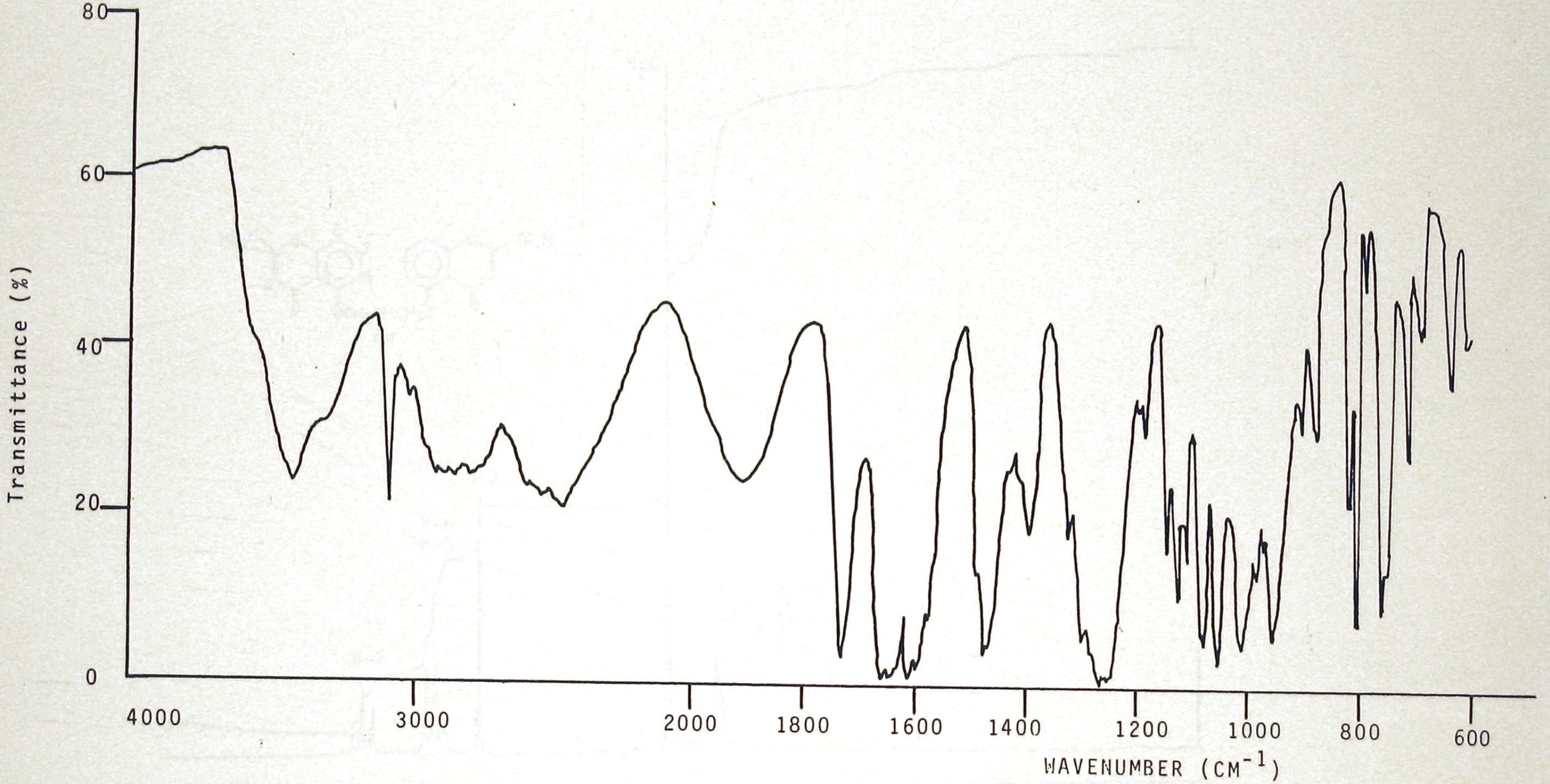

Fig. 1.4b IR Spectrum of CA crystallised from DMSO/H_2O

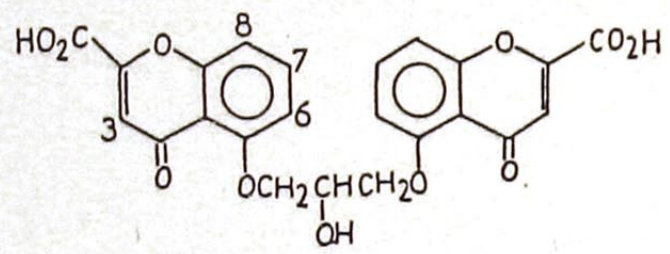

Fig. 1.5a ^{1}H NMR Spectrum of CA from hot water

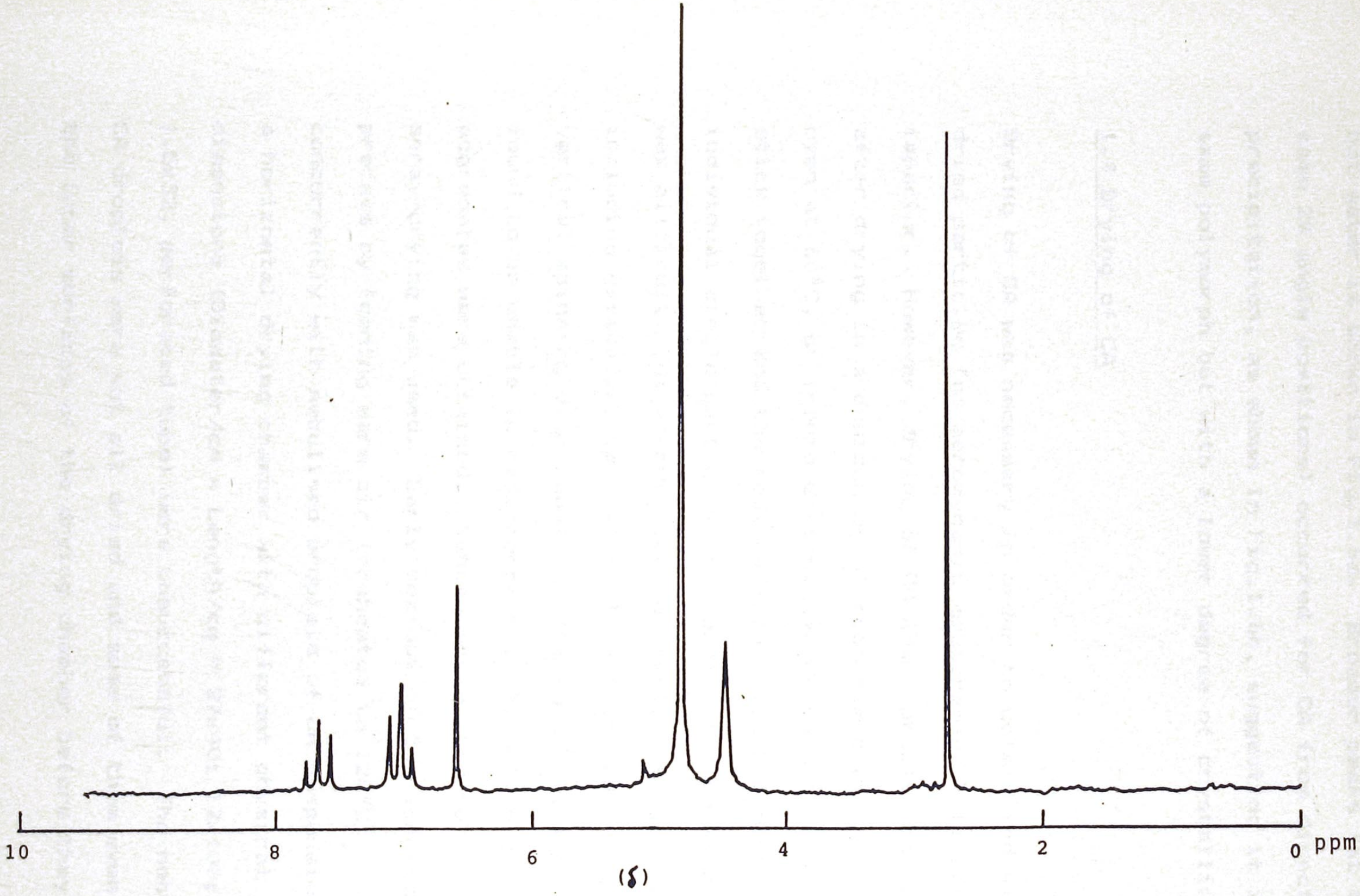

Fig.1.5b ^{1}H NMR Spectrum of CA from DMSO/H_2O

samples are of the same polymorph. The pattern of CA from hot water is shown in Fig.1.6a. Broader peaks (at the same 2θ angle positions) occurred for CA from direct acid precipitation, as shown in Fig.1.6b, suggesting it is the same polymorph but with a lower degree of crystallinity.

1.4 Drying of CA

Drying of CA was necessary in order to obtain individual dried particles for aerodynamic measurement by a cascade impactor. However, drying of CA was a problem because after drying in a desiccator at room temperature, or in an oven at 60^0C, or freeze drying, the CA particles would stick together and the redispersion of such product into individual single particles for aerodynamic measurement was difficult. Different types of redispersing devices including *Rotahaler, Spinhaler, Ingelheim* inhalator and a vertical spinning disc nebuliser (Malem et al, 1981) were found to be unable to redisperse the CA; only big aggregates were obtained. Subsequently, the method of spray-drying was used. Early set-ups of the spray-drying process by feeding warm air (preheated to 120^0C) concurrently with nebulised droplets of CA suspension into a horizontal drying chamber with different physical dimensions (Diameter/cm x Length/cm = 27x40; 12x100; and 1.5x32, perforated tube) were unsuccessful. The nebulised CA droplets were not all dried and some of them even hit the inner surfaces of the drying chamber before they dried.

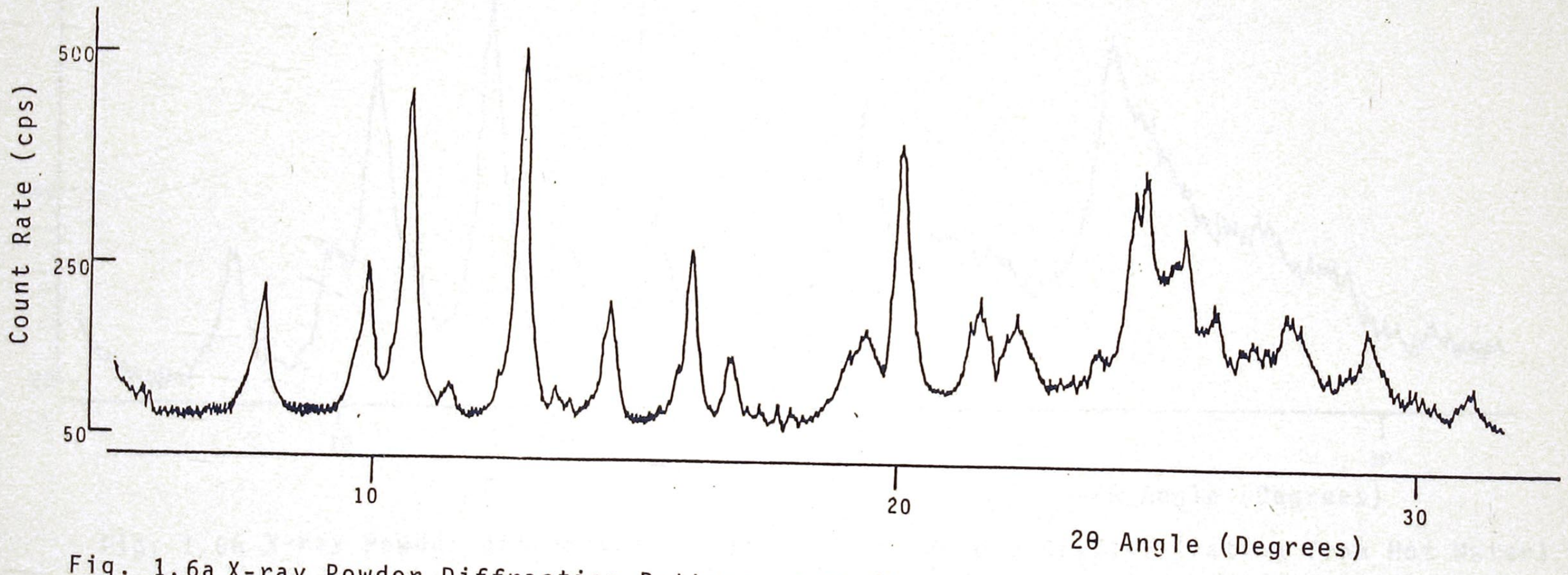

Fig. 1.6a X-ray Powder Diffraction Pattern of CA (Crystallised From Hot Water)

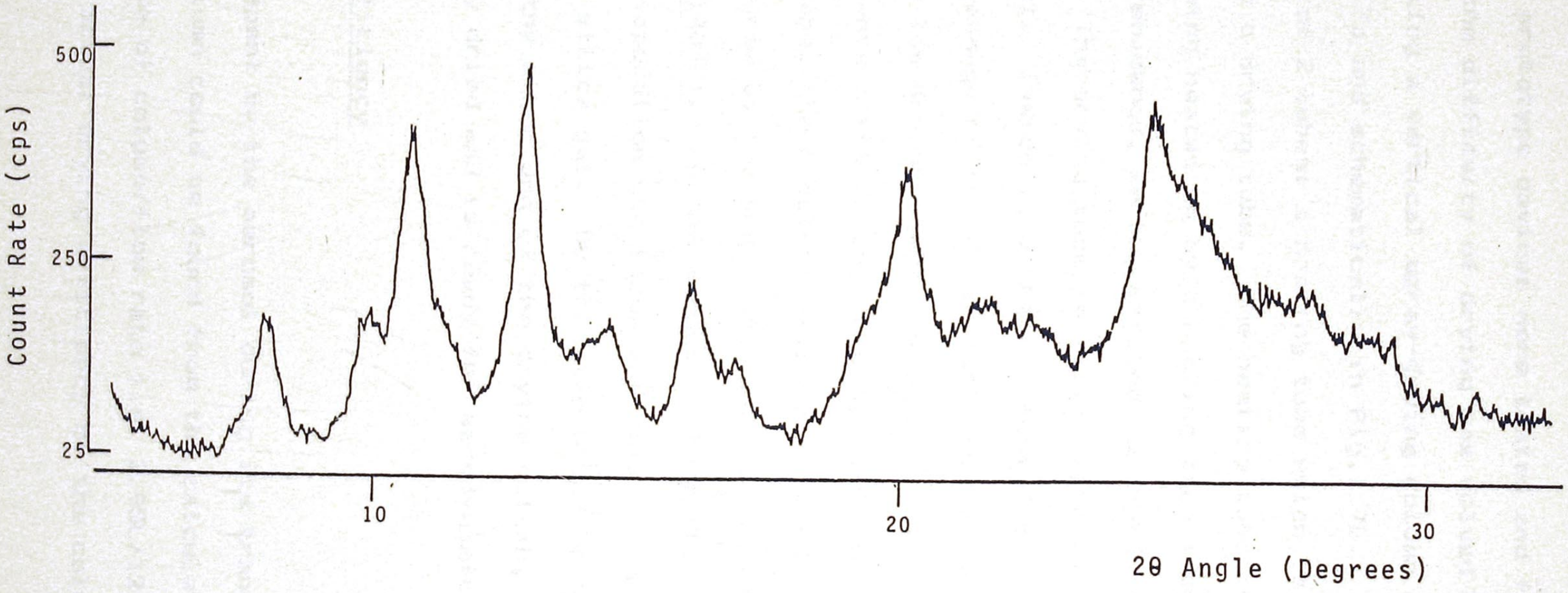

Fig. 1.6b X-ray Powder Diffraction Pattern of CA (Before Crystallization from Hot Water)

Design for a drying column

Numerous prototype devices were tested and failed. Finally the difficulty of drying was solved by constructing a vertical spray-drying column which is shown in Fig.1.7a and schematically in Fig.1.7b. It basically consists of 2 tubes: a heating tube which is connected in series to a drying tube. The heating tube is a copper tubing being heated up by a heating tape (Isotape, Isopad Ltd., Borehamwood, Herts, England) wrapped round on the outside. The drying tube is filled with the drying agent, silica gel. Inside is a channel formed by metal wire mesh for the passage of the CA aerosol and for moisture to gain access to the drying agent. When a stream of aerosolized droplets enters the drying column, at first inside the heating tube, the droplets will evaporate to a greater or lesser degree by the heat (stagnant air temperature inside the tube=140^{0}C). As the aerosol enters the drying tube, further evaporation continues and moisture will be taken up by the silica gel. By the time when the aerosol comes out from the other end of the drying column, it has been completely dried and is ready for aerodynamic measurement.

Drying efficiency

The time spent by the aerosol during its transit in the drying column could be found from the calculation: Time=volume of column/flow rate i.e. 2.95L/12.5L/min or 14 sec. The actual drying efficiency of the column was

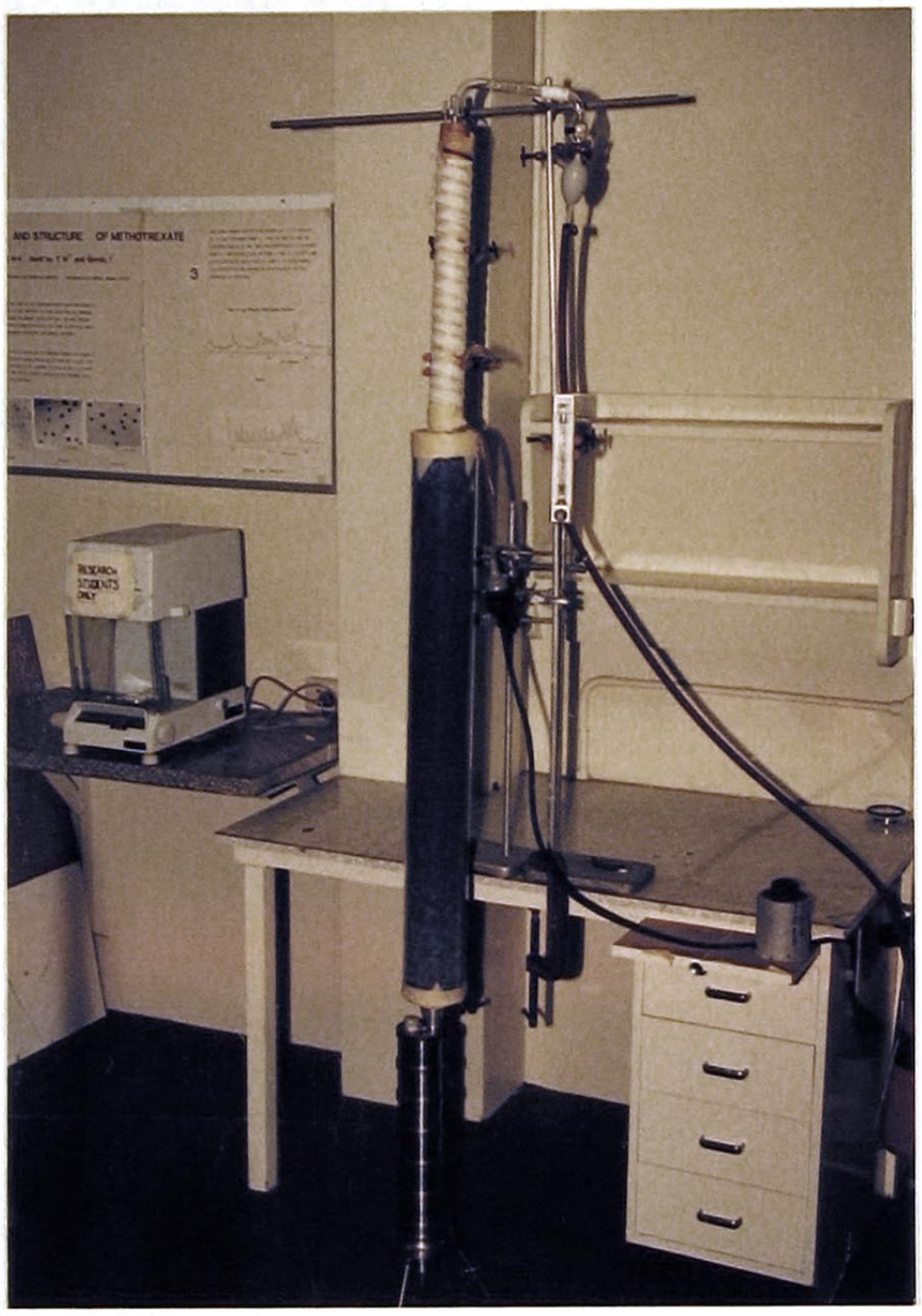

Fig. 1.7a Photograph of the drying column

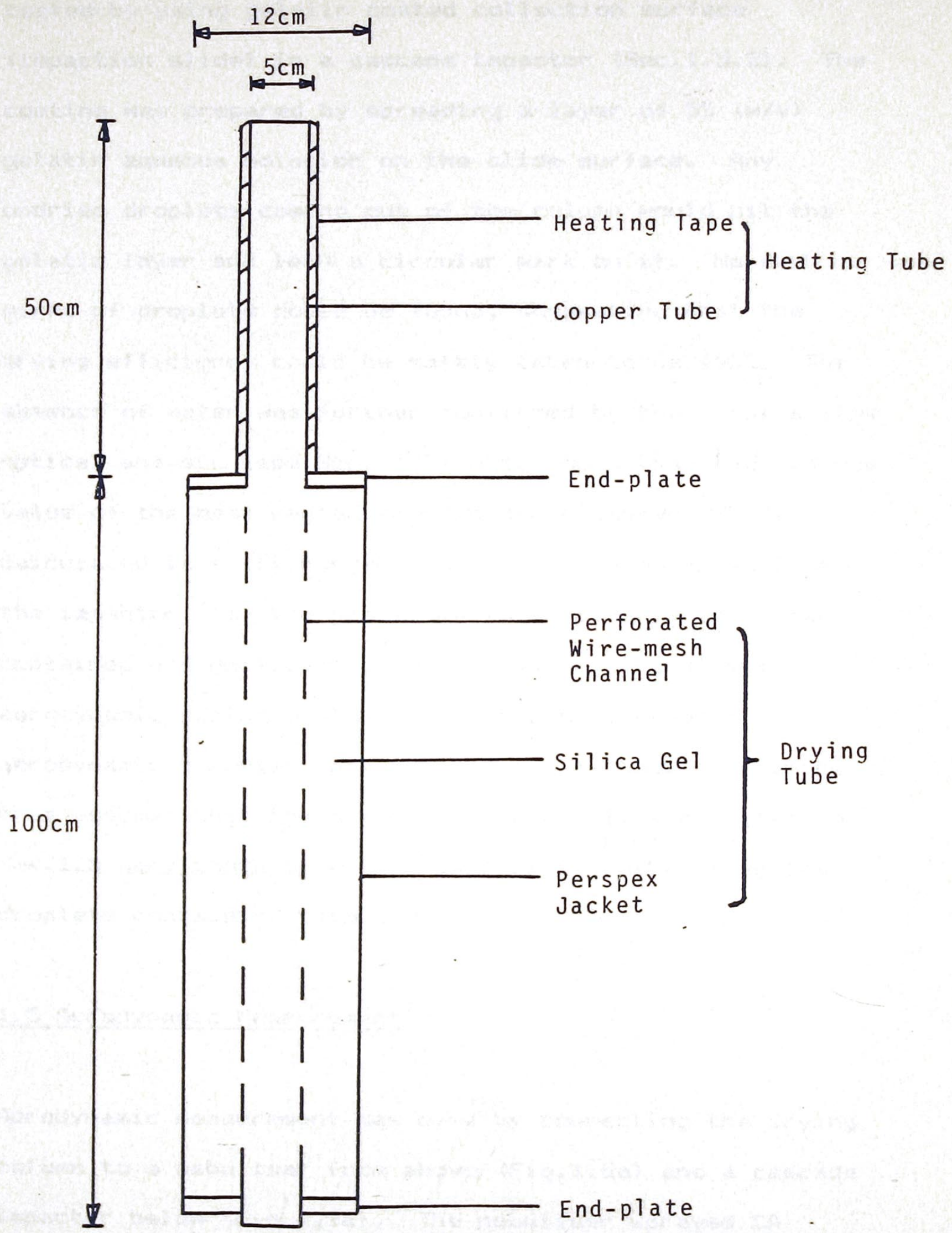

Fig. 1.7b Schematic Diagram of the Drying Column

tested by using gelatin coated collection surface (impaction slide) in a cascade impactor (Sec.1.5.2). The coating was prepared by spreading a layer of 5% (w/v) gelatin aqueous solution on the slide surface. Any undried droplets coming out of the column would hit the gelatin layer and leave a circular mark on it. No such marks of droplets could be found, suggesting that the drying efficiency could be safely taken to be 100%. The absence of water was further confirmed by the results from optical anaysis (see Sec. 1.7) which show that the minimum value of the mass median aerodynamic diameter (MMAD) calculated is still bigger than the value obtained from the impactor. If the particles in the cascade impactor had contained a significant amount of water, the direct aerodynamic sizing would have indicated a greater aerodynamic diameter than the optical method. It can be thus assumed that the aerodynamic properties measured in Sec.1.5 were those of dry CA particles, rather than the droplets containing them.

1.5 Aerodynamic Measurement

Aerodynamic measurement was carried out by connecting the drying column to a nebuliser from above (Fig.1.8a) and a cascade impactor below (Fig.1.9a). The nebuliser sprayed CA suspension into droplets which, after drying in the column, would be measured by the impactor aerodynamically. In this way, the procedure of collecting and redispersing the powder was avoided.

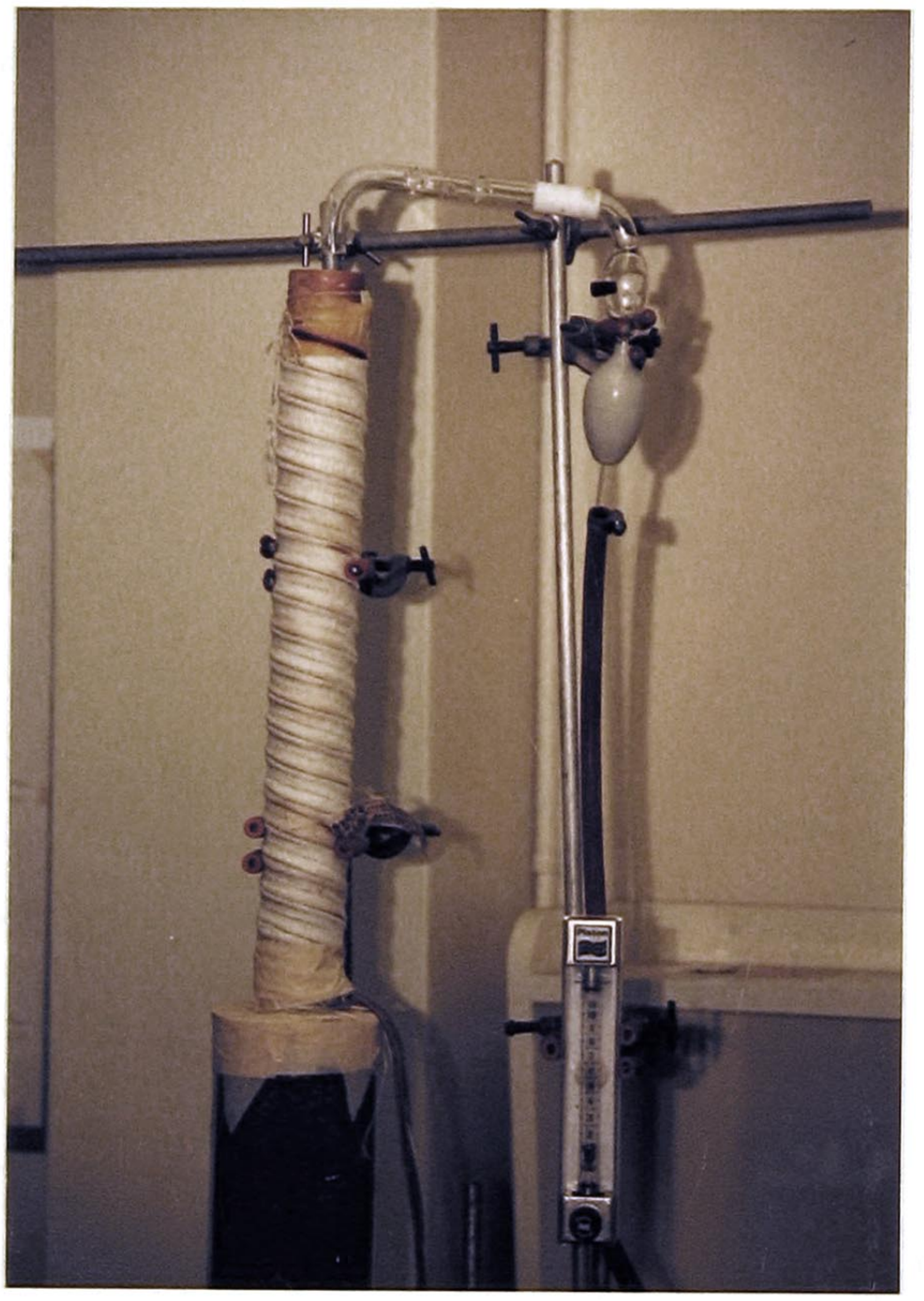

Fig. 1.8a Photograph of deVilbiss no. 40 nebuliser and the baffled adaptor tube connected to the drying column

1.5.1 Generation of Aerosols

CA aerosols were generated by a deVilbiss no. 40 glass nebuliser (The Devilbiss Company, Somerset, Pennsylvania) which is an air-blast type nebuliser operating by the Venturi tube principle (Fig.1.8b). Compressed air enters the nebuliser through a narrow tube immersed in the liquid to be aerosolised. The air mass flow rate depends chiefly on the diameter of the tube orifice and the pressure drop across it. On emerging from the tube, the air expands, more or less adiabatically, in a roughly conical airstream, causing a drop in pressure which draws liquid into the airstream. As a result, the liquid breaks up into droplets whose size distribution depends on the air velocity, and the density, viscosity and surface tension of the liquid (Davis, 1978; Davis et al, 1978). The coarse droplets are removed by imparting on the upper wall of nebuliser and return to the bulk liquid while fine droplets leave the nebuliser. In suspension systems, the fundamental relationship between the primary particle size distribution of the suspension and the ultimate particle size distribution of the dried products has been studied extensively in Appendix 1.

Experimental Conditions

Volume of CA suspension in nebuliser: 2 ml

Concentration of suspension: 0.05% w/v

Compressed air flow rate: 8.5 L/min, controlled by a flowmeter (Platon, tube B6, Hants, U.K.).

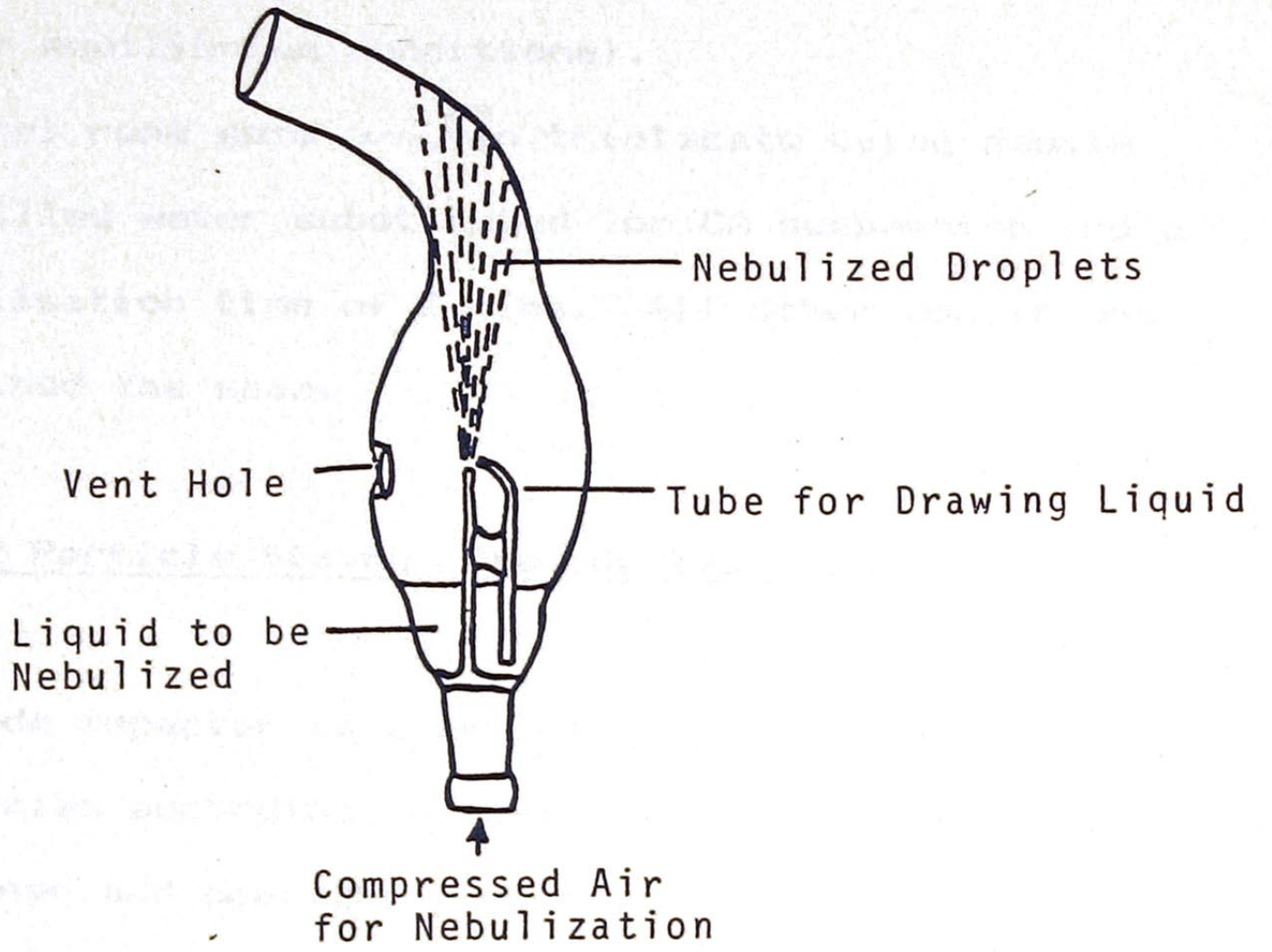

Fig. 1.8b Diagram of DeVilbiss No. 40 Nebulizer

Nebuliser: vent hole closed to prevent the output airflow rate (8.5 L/min) from exceeding the sampling airflow rate of the impactor (12.5 L/min).

Nebulisation time: 1.5 - 5 mins (to confirm deposition under equilibrium conditions).

Control runs were carried out in triplicate using double distilled water substituted for CA suspension and a nebulisation time of 2 mins. All other conditions remained the same.

1.5.2 Particle Sizing- Cascade Impactor

The cascade impactor is a device which measures the size of particles according to their aerodynamic diameters. If designed and operated properly and with special precautions, impactors can provide sharp size cut-off characteristics with reliable and accurate particle size distribution data. Some of the important factors affecting the reliability of impactor data are wall loss or interstage loss, particle bounce and blow off, deagglomeration or break-up, electrostatic attraction and the nature of collection surface (Rao & Whitby, 1978 a&b; Groom & Gonda, 1980) as illustrated in Fig.1.9b.

Wall loss can be substantially reduced to less than 6% by proper design and operation (Mitchell and Pilcher, 1959). Particle bounce and blow off can be minmized using collection surface with high collection efficiency such as silicone fluid (Groom and Gonda, 1980). The Battelle cascade impactor (DCI-6, Delron Research Company, Powell,

Ohio) in this study has been calibrated by Groom (1981). It is shown in Fig.1.9a and schematically in Fig.1.9b. It is basically made up of 6 stages and a final stage which contains an 'absolute' filter (Gelman, Type A-E glass, 76mm). The impactor operates at a constant flow rate of 12.5L/min which is achieved by a Speedivac vacuum pump (Edwards High Vacuum, Sussex, England) attached to the critical orifice at the exit from the impactor. Inside each stage is a jet sitting directly above a round glass impaction slide (4 cm diameter, Quartz Grinding, U.K.) which acts as the collection surface for the aerosol particles. When the aerosol enters the impactor at stage 1, those big particles which have a higher inertial momentum would be caught on the collection surface by impaction force. Those small particles which have a lower inertial momentum would escape the impaction and travel to the next stage where the same impaction process would occur again: particles with higher momentum get caught and those with lower momentum escape to next stage. Such a process would be contined until finally those small particles which have escaped impaction from all previous 6 stages would now be collected on the 'absolute filter' in the last stage. The amount of samples deposited on different stages can be found by chemical assay. It is noteworthy that in this nebuliser-drying column-cascade impactor system, the sampling rate of the impactor always exceeded the gas volume output from the generator so that very little, if any, aerosol escaped into the atmosphere and also turbulent flow was avoided. The latter was

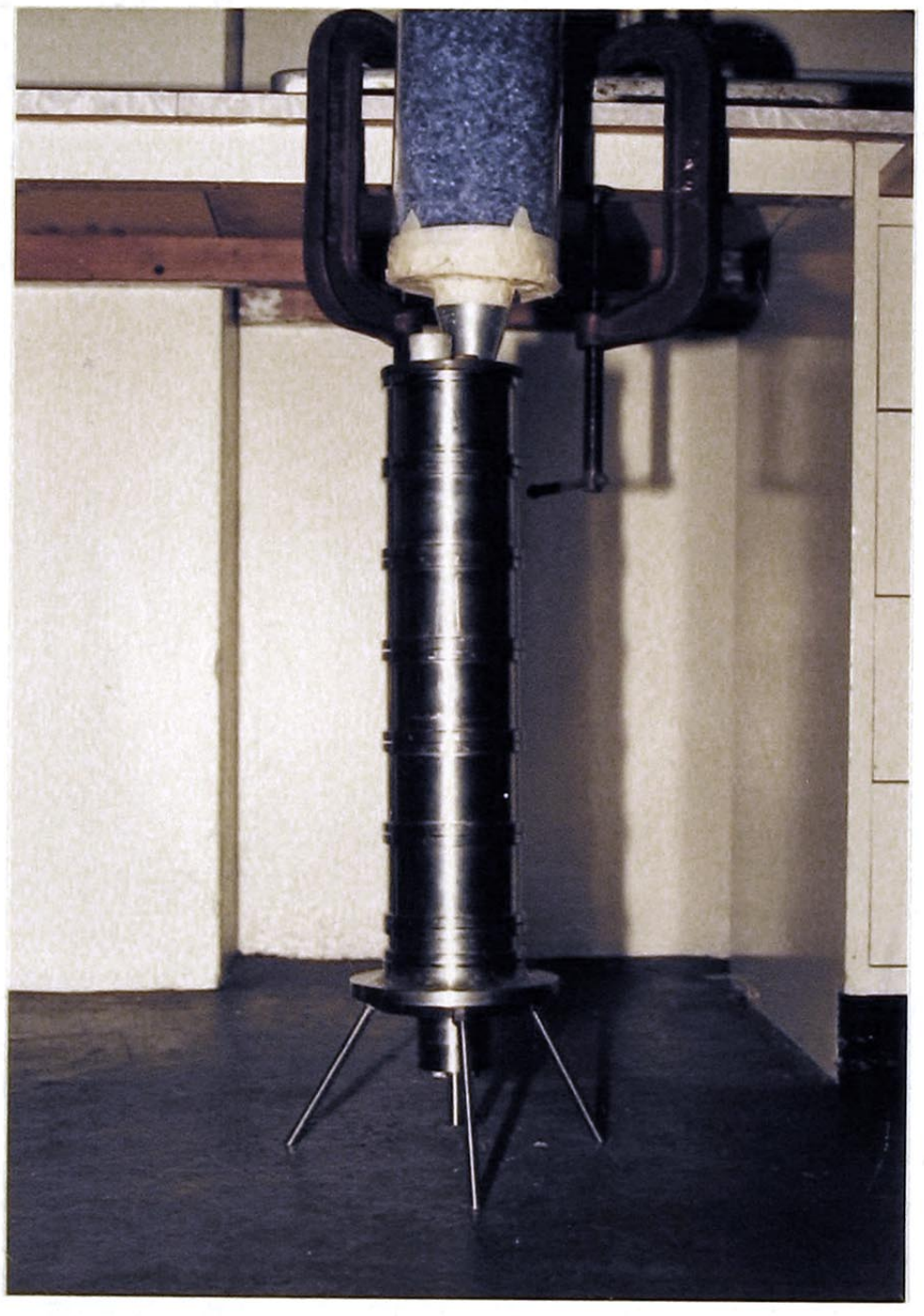

Fig. 1.9a Photograph of cascade impactor connected to the drying column

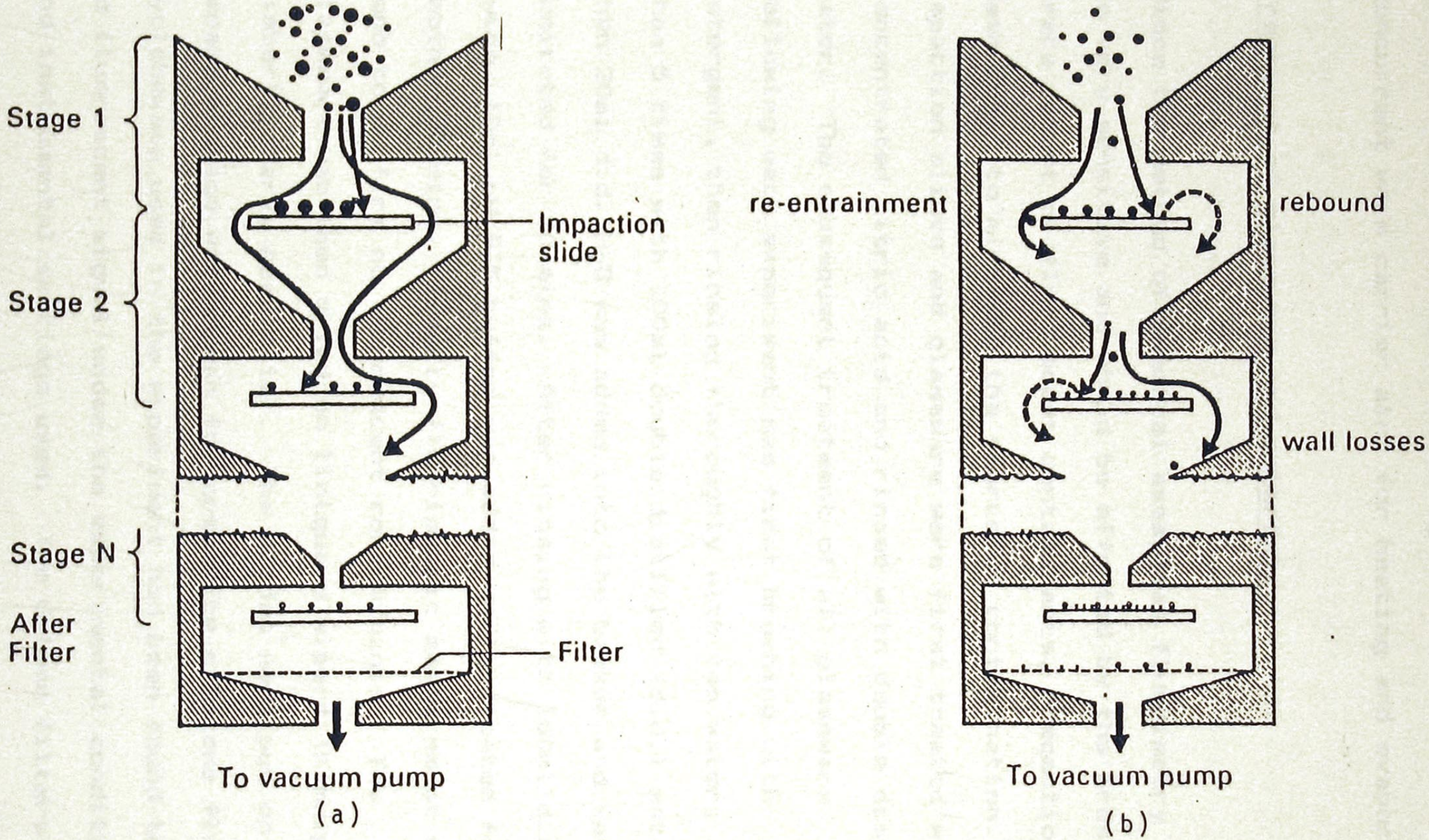

Fig. 1.9b Schematic Diagram of DCI-6 Cascade Impactor showing (a) ideal and (b) non-ideal collection efficiency.

further reduced using the heating tube (instead of concurrent warm carrier air) for heating and evaporation.

Treatment of glassware and materials:

Since the method of chemical assay was fluorimetry which is very sensitive and would be affected by the presence of trace amount of fluorescent contaminants, precautions had been taken to minimize the source of contamination. All impaction slides and glassware were first treated with concentrated nitric acid and rinsed with double distilled water. The subsequent treatment of all glassware following each experiment was first brushing with detergent, then rinsing thoroughly with tap water, and then 5 times with 100ml double distilled (d.d.) water. Then 20ml d.d. H_2O was added into the beaker and was sonicated for 20 mins. After rinsing with 100ml d.d. H_2O twice, 10ml pH $\overline{6.5}$ buffer was added and sonicated for another 20 mins. Finally fluorimetric measurement was done to confirm no fluorescent contaminants. The glassware was then dried on lintguard wipers (Kimwipes, Kimberly-Clark, Australia). The slides were put on the impactor stage with clean forceps. The silicone fluid and cyclohexane used in the experiment had been found to give no fluorescent signal under the experimental conditions and instrumental settings used. The Gelman filters had been washed 5 times with ~300ml d.d. H_2O until they gave no fluorescent signal. They were dried on wipers before use.

Preparation of collection surface:

10% (w/v) silicone fluid (200 fluid/60000 cs, Dow Corning, Blacktown, NSW, Australia) in cyclohexane (Univar, Ajax Chemicals, Sydney) was freshly prepared. 0.4ml of the solution was pipetted (Pipetman P1000) on to the pre-cleaned impaction slide. After evaporation of the cyclohexane, a smooth layer of silicone fluid resulted on the slide surface.

1.5.3 Chemical assay of CA:

Disodium cromoglycate is fluorescent in aqueous solutions with pH greater than 2 (Moss et al, 1971). Quantitative determination of CA was done by measuring the fluorescence of CA in pH 6.5 phosphate buffer on a fluorescence spectrofluorimeter (Perkin-Elmer model MFP-44B).

i) Determination of the fluorescence emission and excitation spectra

The emission wavelength maximum was found by setting the absorption wavelength at 350nm (Moss et al, 1971) and manually scanning the emission wavelength from 350nm to 600nm. The emission wavelength, $E\lambda_1$, which gave the maximum fluorescence signal was noticed. Similarly, the absorption wavelength maximum was found by setting the emission wavelength at $E\lambda_1$ while manually scanning the absorption wavelength from 295nm to 450nm, again the

wavelength $A\lambda_1$ which gave the maximum fluorescence signal was noticed. The wavelengths were refined by repeating the whole process using the new wavelengths $E\lambda_1$ and $A\lambda_1$. Finally the emission and absorption spectra were plotted out by a recorder (Perkin-Elmer Hitachi 057 X-Y Recorder).

Experimental conditions:

The following instrument settings were used in the determination of fluorescence emission and absorption spectra:

Emission wavelength	480nm
Excitation wavelength	330nm
Emission slit	15nm
Excitation slit	5nm
Ratio	3
Signal gain coarse adjustment	3X
fine adjustment	fully anticlockwise

The same experimental conditions were used in preparing the calibration curve and in the quantitative determination of CA.

ii) Calibration curve

A series of different concentrations of CA in pH 6.5 phosphate buffer ranging from 0.2µg/ml to 3.5µg/ml were freshly prepared and measured fluorimetrically under the stated experimental conditions in Sec.i). Each concentration was done in duplicate or triplicate. In this way, a calibration curve was prepared to establish the rectilinear range between the relative fluorescence

intensity and concentration of CA.

iii) Quantitative analysis of CA

The CA deposited on the impaction slides was first subjected to extraction and then analysed by spectrofluorimetry.

The method of double extraction similar to that employed by Hering et al (1979) was used. Briefly, the slides with CA deposited on them were ultrasonically extracted for 20 mins with 5.0ml cyclohexane in a 100ml beaker. To the cyclohexane solution, 5.0ml pH 6.5 phosphate buffer was added and then the ultrasonic extraction was repeated for an additional 20 mins. The cyclohexane served to dissolve the silicone fluid, while the CA was soluble in the phosphate buffer. Before analysis, the extracts were centrifuged for 5 mins (Janetzki T22, max. setting) to separate the 2 immiscible solvents, and to remove any suspended particles. The buffer layer was then analysed by spectrofluorimetry under the experimental conditions stated in Sec.i). The filter samples were ultrasonically extracted with 15ml pH 6.5 phosphate buffer in a 500ml beaker for 20 mins. After passing through a 0.22µm Millipore (Millex-GS, Millipore Corp., Bedford, U.S.A.) to remove any particles given off from the filter sample, CA in the buffer solutions was then analysed with the impaction slide samples.

iv) Recovery of CA from collection surface

Impaction slides coated with silicone fluid were placed in 100ml beakers and were spiked with 2.0µg and 50.0µg CA, using 0.2ml of 10µg/ml aqueous solution of CA and 250µg/ml suspension of CA in 0.1N HCl, respectively.

Likewise, Gelman filters were spiked with about 5, 20 and 40µg CA accurately.

After drying in desiccator, CA was recovered by the extraction and analytical methods described in Sec.iii) and i).

Each concentration was done in triplicate and blank control was also done in triplicate.

v) Data treatment

Inversion of particle-sizing experimental data into aerosol size distribution was done by the well-documented procedure of indirect least mean square fitting (Raabe, 1968; Gonda and Groom, 1981) of an assumed size distribution function (normal or/and log-normal) to the experimental data. The theoretical amounts deposited on each stage of the impactor were calculated after the user decided upon a certain type of size distribution which can be described adequately by 2 parameters (eg. the mass median aerodynamic diameter and the geometric standard deviation in log-normal distribution).

A range of parameter values of 10 mass median diameters and 10 geometric standard deviations was selected. A 2-dimensional "error map" of the sums of the squares of

residues (differences between the theoretical and experimental results) for each stage was computed and printed on a grid whose axes are the assumed values of the 2 parameters (Gonda and Groom, 1981; Gonda et al., 1982). A minimum (i.e., the best fit) is easily identified from the error map. In practice, a wider range of values of the 2 parameters were at first chosen so as to approximately identify the minimum and to avoid overlooking of multiple minima due to potentially ambiguously assigned distributions (Huang et al 1970, Gonda & Groom 1981). A narrower range of parameters was then chosen to obtain the accurate optimum fit. For the best fit the residue values are shown to ascertain the random nature of errors. A systematic trend in errors indicates that a different type of size distribution should be attempted. All the computations were carried out by a Cyber 830 computer in the University Computer Centre of the University of Sydney.

1.6 Results and Discussion

Emission and excitation fluorescence spectra

The emission and excitation fluorescence spectra of CA are shown in Fig.1.10a and Fig.1.10b respectively. The excitation spectrum is in close resemblance to the UV absorption spectrum as expected with an absorption peak at around 330nm. The emission spectrum has the maximum fluorescence peak at around 480nm.

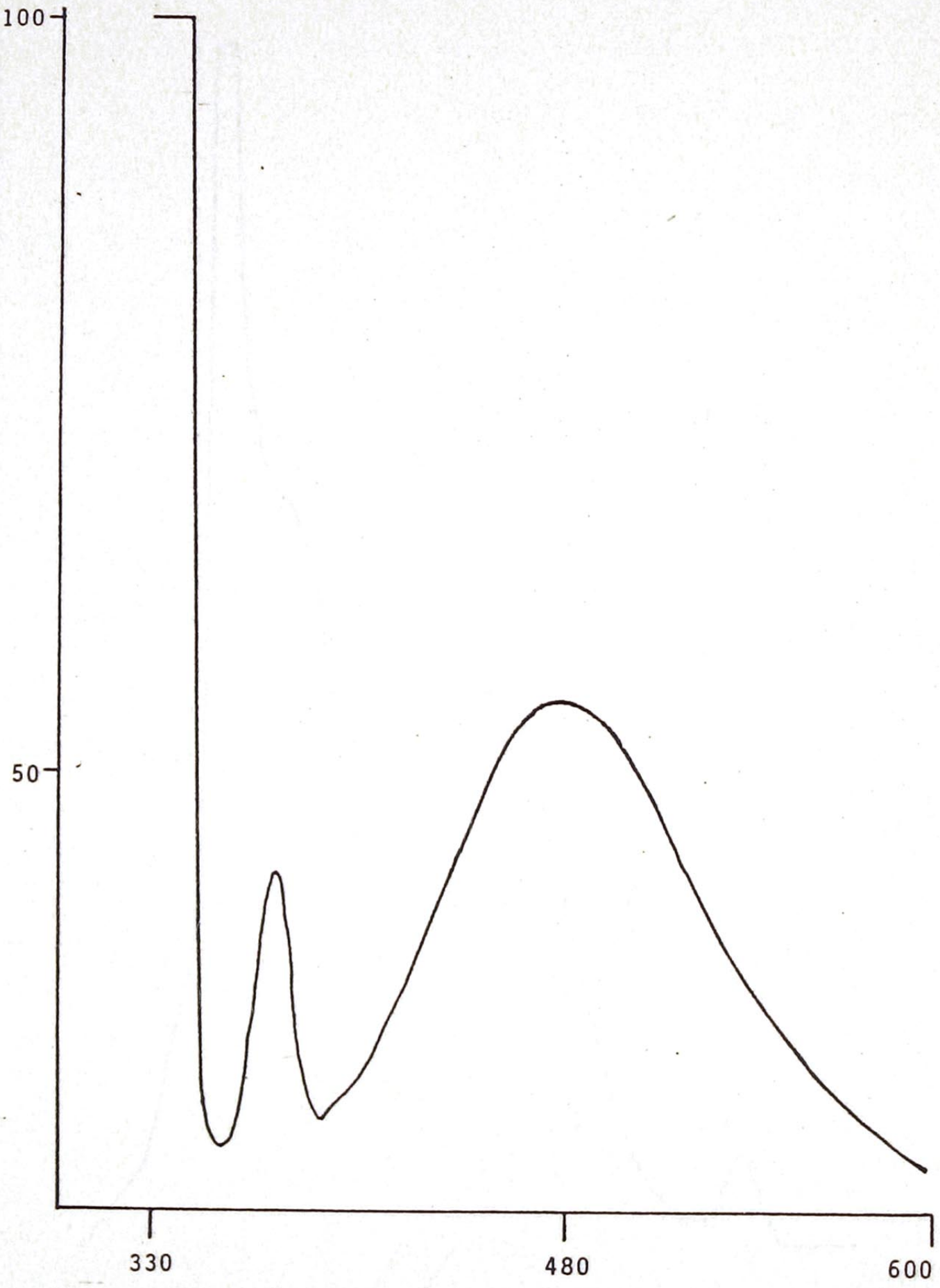

Fig. 1.10a Emission Flourescence Spectrum of CA (Uncorrected)

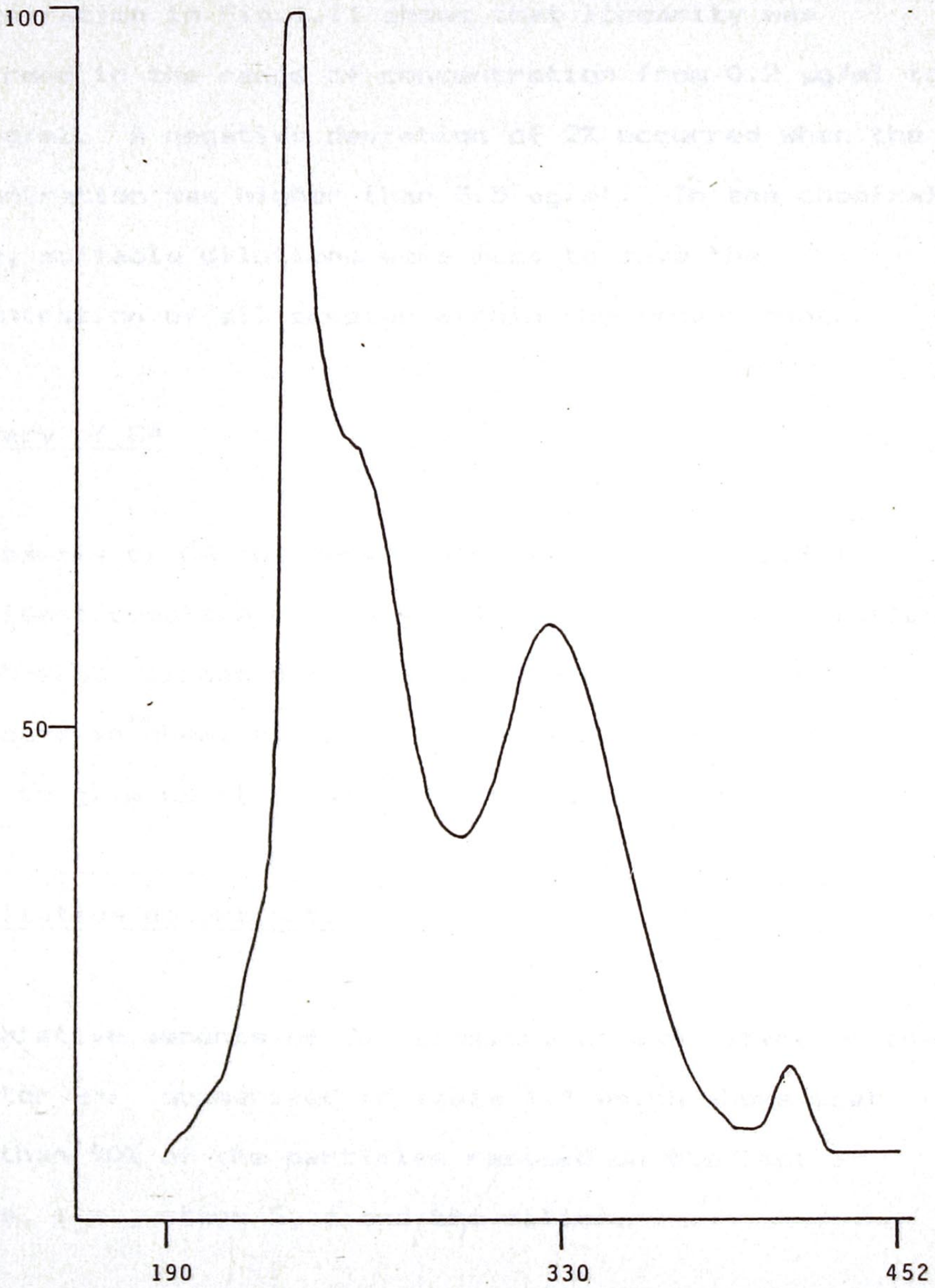

FIG. 1.10b Excitation Fluorescence Spectrum of CA (Uncorrected)

Calibration curve

The calibration curve of fluorescence intensity against CA concentration in Fig.1.11 shows that linearity was confirmed in the range of concentration from 0.2 µg/ml to 2.0 µg/ml. A negative deviation of 2% occurred when the concentration was higher than 3.5 µg/ml. In the chemical assay, suitable dilutions were made to make the concentration of all samples within the linear range.

Recovery of CA

The results of CA recovery are summarized in Table 1.3. The almost complete recovery (99.5-102%) with a variation of 0.5-4.3% validated the use of a double extraction procedure in the chemical assay. The blank controls were found to give no fluorescence signals.

Quantitative determination

The relative amounts of CA deposited on each stage of the impactor are summarized in Table 1.4 which shows that more than 90% of the particles resided on the last 3 stages, i.e., stage 5, 6 and the filter.

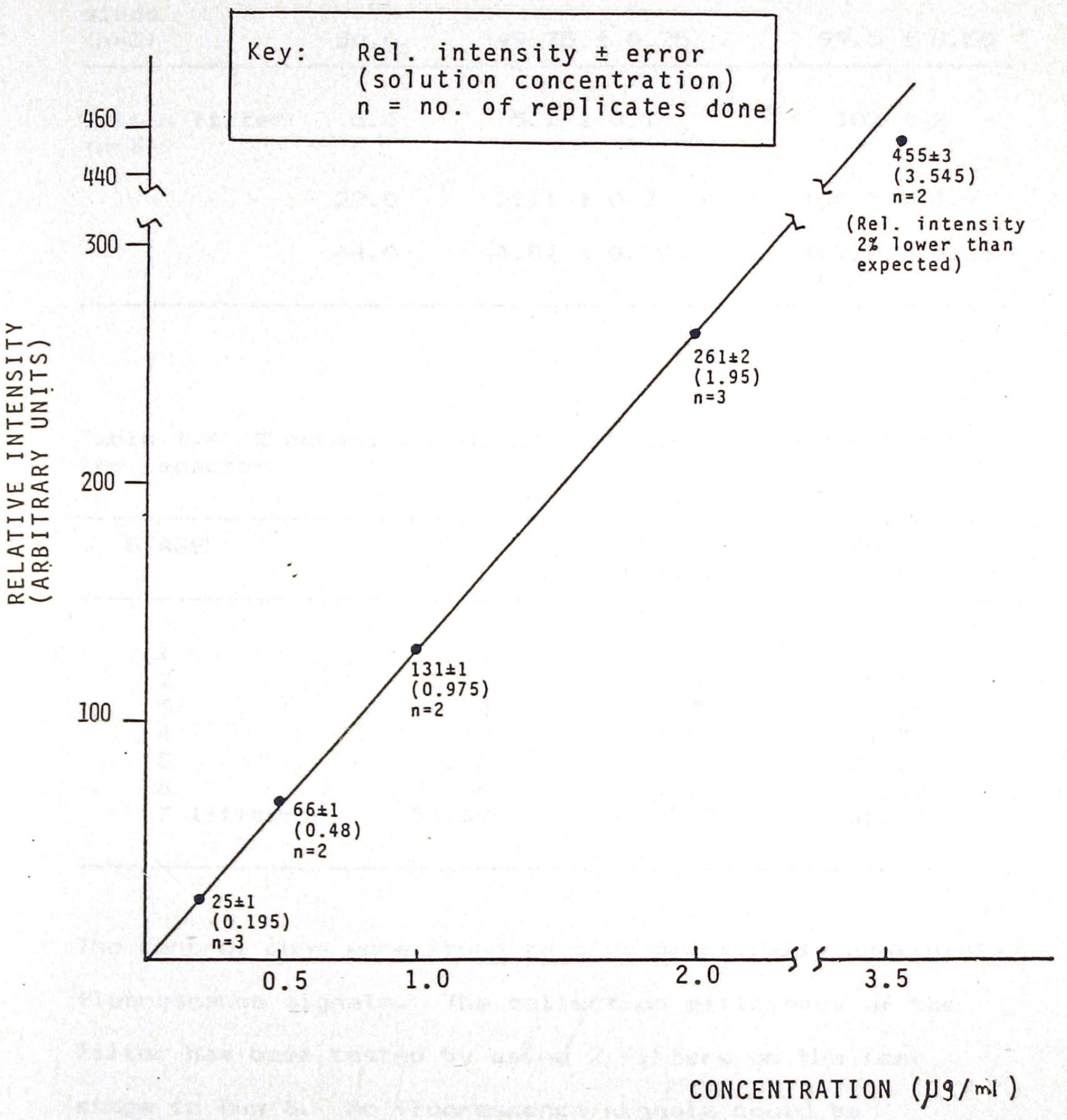

FIG. 1.11 CALIBRATION CURVE OF CA

Table 1.3

Collection surface	Amount added(µg)	Amount recovered (µg)	% recovery
impaction slide (n=3)	2.0	1.99 ± 0.085	99.5 ± 4.25
	50.0	49.75 ± 0.25	99.5 ± 0.50
Gelman filter (n=3)	5.0	5.1 ± 0.1	102 ± 2
	22.0	22.1 ± 0.2	100.5 ± 0.9
	44.0	44.87 ± 0.38	102.0 ± 0.86

Table 1.4 % deposition of CA particles on each stage of the impactor

STAGE	RUN1 (1.5 mins)	RUN2 (5 mins)	RUN3 (3 mins)
1	0.91	o	o
2	0.46	o	0.13
3	1.14	0.23	0.13
4	3.19	1.89	2.35
5	29.16	28.41	28.50
6	31.66	32.19	32.42
7 (filter)	33.49	37.29	36.47

The control runs were found to give practically negligible fluorescence signals. The collection efficiency of the filter has been tested by using 2 filters on the last stage in Run 3. No fluorescence signals could be registered for a buffer solution in which the second filter had been extracted ultrasonically by the procedure described in Sec.1.5.3 iii), suggesting that the collection of CA particles by the filter was complete.

Impactor data treatment

Least mean square fitting showed that the data were best represented by a log-normal particle size distribution with a mass median aerodynamic diameter (MMAD) of 0.65μm and geometric standard deviation (σ_g) of 1.88 as shown in Table 1.5.

Table 1.5

	MMAD (μm)	σ_g
RUN 1	0.68± 0.02	1.88± 0.05
RUN 2	0.64± 0.02	1.88± 0.05
RUN 3	0.64± 0.02	1.88± 0.05
Mean=	0.65± 0.02	1.88± 0.05

Particles with MMAD of 0.65μm are definitely respirable. However, the σ_g showed that the particle size distribution was polydisperse. Such increased polydispersity is likely due to the presence of small particles and fragments which formed during the process of nebulisation and spray drying (see Sec.1.8). This is confirmed by the results of theoretical calculations in Table 1.7. When the fragments or small particles were eliminated in the calculation, the σ_g dropped to 1.55 which corresponds to mild polydispersity in terms of deviations from regional deposition of truly monodisperse aerosols in the human respiratory tract (Gonda, 1981).

1.7 Fundamental study of aerodynamics

A fundamental study of the relationship between the

particle shape and the aerodynamic diameter was done by geometric measurements of the physical dimensions of particles followed by calculations of aerodynamic diameter using theoretical expressions discussed in Sec.1.1 v)

1.7.1 Geometric measurement

Geometric measurement could not be done by optical microscopy for the important reason that the breadth of the fibres was about 0.2-0.5 microns, that is very close to the resolution limit of optical microscope, therefore electron microscope had to be used. Scanning electron microscopy (SEM) was used because of several advantages:

1. higher resolution (*c.a.* 10nm *c.f.* 0.5μm in optical microscopy).
2. large depth of field.
3. more surface details.
4. greater contrast between particles and background.

However, SEM could not be employed directly to the CA particles deposited on the impaction slides because the particles were embedded totally inside the silicone fluid coating, therefore they would not be visible under the electron beam in the SEM. To solve the problem, a technique of Nuclepore filter/Scanning electron microscopy (NPF/SEM) was used (Beckett, 1973; Altree-Williams and Preston, 1985) as follows:

i.) Collection on Nuclepore filter:

All the particles after spray-drying (spray time 3 mins.) were collected on a Nuclepore filter (Nuclepore Corporation, California) using only the first and the last stage of the cascade impactor. Nuclepore filters are manufactured by etching the tracks of high energy particles through polycarbonates. The filter was chosen because of its excellent flat and smooth surface giving a uniform background on which the fibres can be easily distinguished, and was thus very suitable both for SEM and for semi-automatic evaluation by a particle image analysis system. The Nuclepore filter (0.2 µm pore size, diameter 62mm cut from a 8 x 10 inch sheet) was used with the shiny side up as recommended by Beckett (1973) and the manufacturer.

ii.) Scanning Electron Microscopy

a. Preparation of specimen:

A sector was cut by a razor blade from the Nuclepore filter (NPF) on which the CA particles were collected, and mounted on two SEM specimen stubs by division into 2 transverse parts. As described in Sec.1.2.2 a), after mounting and coating, the specimen was viewed on the SEM (Jeol JEM 35C, Japan) under the same experimental conditions. Polystyrene latex spheres (0.48µm diameter, Dow Chemical Company, Midland, Michigan) were used as the internal calibration standard for magnification.

b. Random sampling on the NPF:

Measuring all the fibres on the filter sector was practically impossible because enormous number of fields of view and thus photographs would have to be taken. Instead, random sampling on the NPF was done. There are several possible ways to do random sampling on the filter sector if the particles are randomly distributed as shown in Fig.1.12 a-d. Since particles collected on the filter in the impactor were not randomly distributed, but were more densely distributed towards the centre under the impactor jet, sampling methods in Fig.1.12 a-c are not suitable because all of them will give a bias in sampling towards the centre. Random sampling was therefore done as in Fig.1.12d by dividing an area of segment into 100,000 quasi-rectangular fields of view (f.V) and by taking pictures on pre-determined random fields of view. A total of 100 fields were taken according to the first 100 numbers in a table of 2,500 five digit random numbers (Abramowitz and Stegun, 1970). The procedure taken to locate the fields on the filter segment was described in Appendix 2.

iii.) Image Analysis System

The schematic diagram showing the image analysis system (Dapple Systems, Sunnyvale, CA, USA) is shown in Fig.1.13. The SEM picture was put under the TV camera which projected the image onto the TV monitor (and onto



a.) Fields of view taken along radial traverses.



b.) Equal band width (basically same as Fig. a except that, instead of continuous sampling along the radius, discrete points or areas are taken for sampling).



c.) Band width decreasing outwardly to keep the sampling areas equal.



d.) Random fields of view taken over the whole filter sector.

Fig. 1.12 Random Sampling On The Filter (Sampling areas shaded)

the computer screen as a grey-scale image). This video image was then digitized into a 254x192 point array (on the computer screen) and the brightness of each picture point (pixel) was measured with a resolution of 64 grey levels. By specifying the grey level range (using a pair of upper and lower level discriminators), the features of interest could be separated from the unwanted features and from the surrounding background. This binary image was displayed on the computer screen and could be edited manually by drawing on a Koala pad. Image editing included direct drawing, erasure or selection of feature, and filling of holes. As a result, by choosing the appropriate level of grey and by image editing, the ultimate binary image is an idealized version of the 'raw' video image on the screen. This is facilitated by use of the video mixer which will superimpose the grey-scale image and binary image on the computer screen for comparison. The program will then measure the features according to their physical dimensions including the length, breadth, area, perimeter and angle. New variables may be added in the measurement, if desired, (e.g. the volume, axial ratio) by either using in-built variables in the program or by creating new variables using standard BASIC language. The data of measurements were stored in a hard disk for data treatment.

Fig. 1.13 Schematic Diagram of the Image Analysis System:

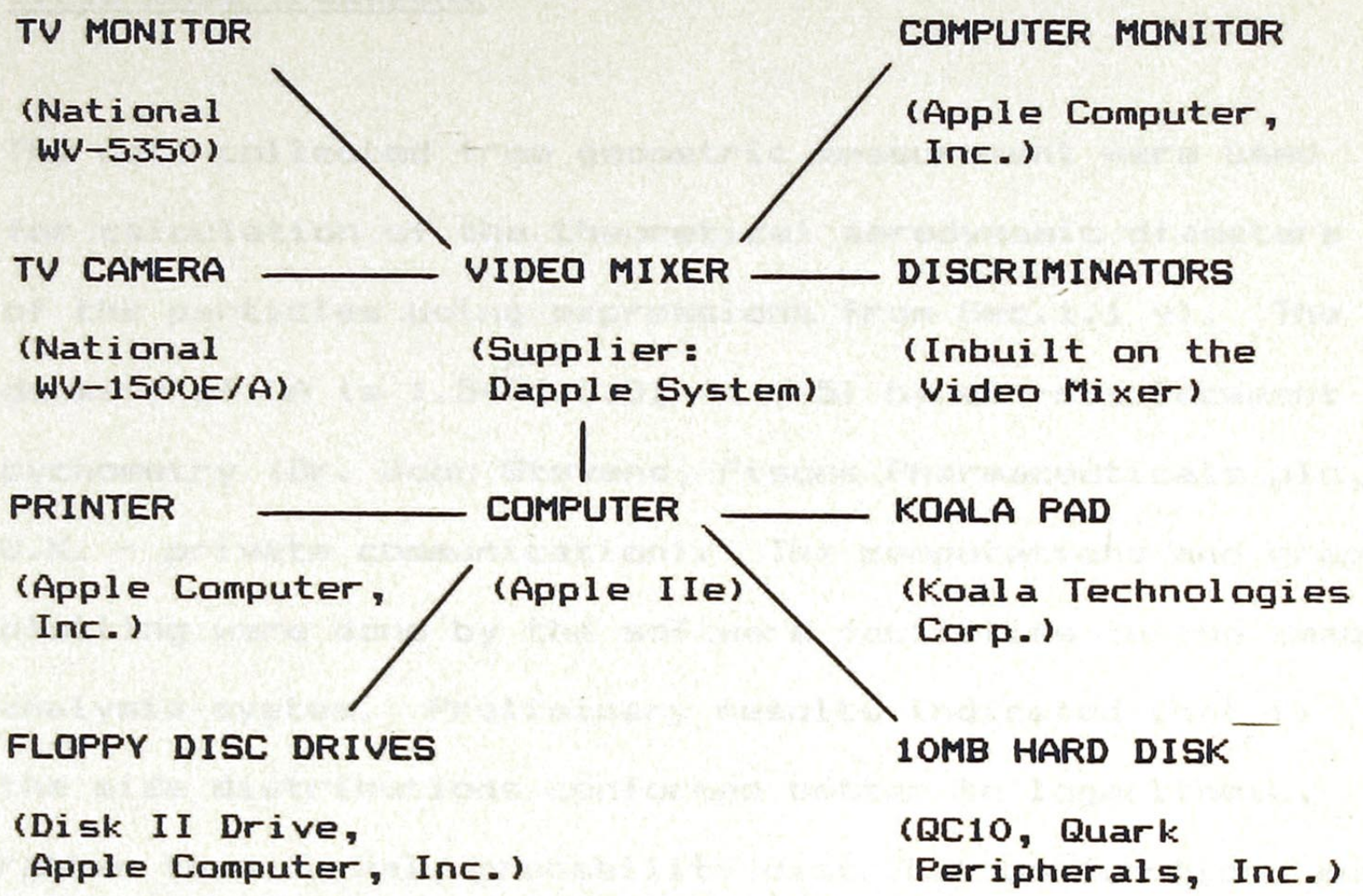

1.7.2 Measurement of particle thickness

The thickness of particles can be estimated using SEM by the technique of specimen shadowing. Particles on the filter were shadowed with a thin coat of platinum (~2.5nm) at an angle of 20-30^0. The particle thickness was found by measuring the 'length' of the shadows of the particles cast onto the filter. The exact angle of shadowing was obtained using latex spheres with known dimensions (0.234μm diameter, Dow Chemical Company, Midland, Michigan) as a calibration standard. The shadowed samples revealed that some of the fibres were slightly tilting up at an angle with the filter. For reliable thickness measurement, only those fibres lying flat with their long

axis normal to the shadowing direction were chosen.

1.7.3 Data treatment

The data collected from geometric measurement were used for calculation of the theoretical aerodynamic diameters of the particles using expressions from Sec.1.1 v). The density of CA is 1.54 g/cm^3 ± 0.01 (n = 5) by air-displacement pycnometry (Dr. John Stevens, Fisons Pharmaceuticals plc, U.K. - private communication). The computations and graph plotting were done by the software facilities in the image analysis system. Preliminary results indicated that i) the size distributions conformed better to logarithmic, rather than normal, probability distribution functions and ii) these calculations yielded values somewhat higher than the cascade impaction method. Therefore, only those equations were used which assume that the objects are positioned to give the maximum viscous resistance, i.e., with their long axis perpendicular to the direction of motion [This orientation gives lower aerodynamic diameters than equations assuming parallel or random orientation (Fuchs, 1964)]. The calculation procedures are summarized in the following (Method I used only the information from the apparent two-dimensional images of the particles; methods II and III made use of the thickness obtained from the shadowing as well):

Calculation of Da by Harris & Fraser's expression modified by Gonda & Khalik (method I):

(i) Calculation of volume of each particle assuming prolate spheroid.

Volume = $M.B.^2 * L * \pi/6$

M.B.= mean breadth of the particle

L = length of the particle

(ii) Mean Breadth and Axial ratio (β) of each particle

Mean Breadth= projected area/length

β = length/mean breadth

or $\beta = length^2$ /projected area.

(iii) Calculation of the aerodynamic diameter of each particle using

Exp.1d in Table 1.1., i.e.

$$Da = \sqrt{3/2} * M.B. * \sqrt{\rho\ (\ln 2\beta + 0.5)/(2\rho_0)}$$

ρ = density of CA

ρ_0= unit density (i.e. 1 g/cm^3)

(iv) Plot cumulative % volume vs Da on a log-probability graph to obtain MMAD and σ_g.

Calculation of D_a by the expression for Φ_D derived for elongated prolate spheroids (Harris and Fraser, 1976), Φ_D = 4 L/ 3(ln 2β + 0.5) (method II):

(i) Calculation of the volume of each particle

Volume (V) = projected area (A) * thickness (T)

(ii) Calculation of Da

$$Da = \sqrt{6\ V\ \rho/(\rho_0\ \pi\ \Phi_D)}$$

Substituting the above expressions for V and Φ_D,

$$Da = \sqrt{6\ A\ T\ \rho/(\pi\ \rho_0) * 3\ (\ln 2\beta + 0.5)/(4\ L)}$$

(iii) The particle size distribution (MMAD and σ_g) was obtained from a cumulative % volume vs Da plot

assuming log-normal distribution.

Calculation of Da by Johnson's empirical expression (method III):

(i) Calculation of the volume of each particle (V)

Volume = projected area * thickness

(ii) Equivalent volume sphere diameter (Ds)

$Ds = (6*V/\pi)^{1/3}$

(iii) Projected area diameter (Dn)

$Dn = (4*A/\pi)^{1/2}$ A: projected area of the fibre

(iv) Total area of the (fibre) body (Ab)

$Ab = 2*(M.B.*L + M.B.*T + L*T)$ M.B.: Mean breadth of fibre

L: Length

T: Thickness

(v) Surface sphericity (Ψ)

$\Psi = \pi * Ds^2/Ab$

(vi) Calculation of the diameter of a sphere with the same viscous drag as the particle in question (Φ_D)

$\Phi_D = Ds/(0.246 + 0.531\Psi + 0.258Ds/Dn - 0.036L/Dn)$

(vii) Calculation of the aerodynamic diameter (Da) of each particle

$Da = \sqrt{(6\rho V/\pi\Phi_D)}$

(viii) Plot cumulative % volume (from (i)) vs Da (from(vii)) on a log-probability graph to get MMAD and σ_g.

1.8 Results and Discussion

Geometric Measurement

Particles collected on the Nuclepore filter are shown on the SEM photograph in Fig.1.14. Examination of the electronmicrograph showed that there were very clearly two classes of particles in the samples: small, almost symmetric looking particles with axial ratios not more than about 2.5, and distinct elongated particles with much higher axial ratios. Such small particles could have originated from i) the evaporated droplets which did not contain initially any solid CA particles but had small quantities of nonvolatile soluble material in them (dissolved CA plus contaminants) and ii) mechanical fragmentation of the long CA fibres during nebulisation. Size characteristics were subsequently analyzed for the elongated particles separately as well as for all the particles together. Since more than 50 particles were present in 1 field of view (f.v.), only the left-top quadrant in each photograph (f.v.) was measured. For edge particles, they would be recorded as belonging to the field area if they lie on the 2 adjacent sides of the upper and left hand boundary lines. (SEM photos were taken for these particles as well). Since the Da of fibres depends primarily on the breadth and the aspect ratio, and is relatively insensitive to the length, criteria were chosen (Gonda et al, 1985c) to avoid measuring more than enough particles but to assure that

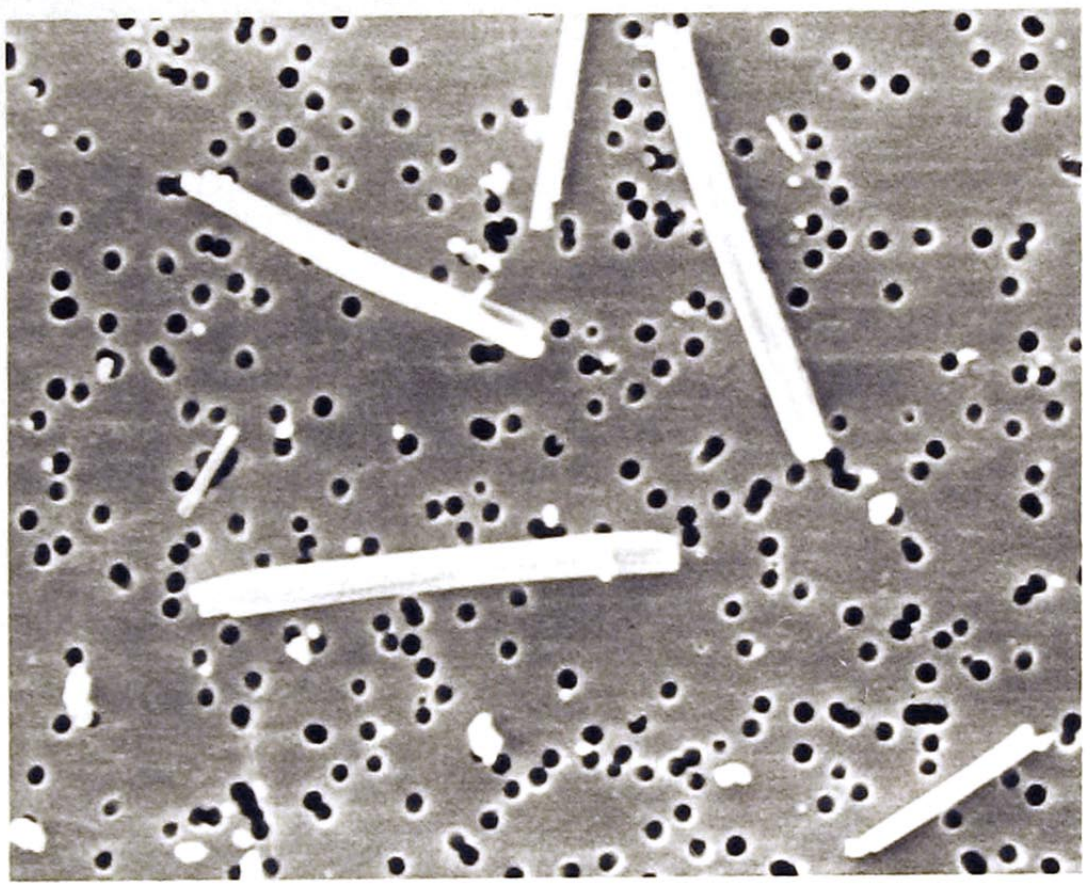

Fig. 1.14 CA particles collected on the Nuclepore filter
(pore size: 0.2μm)

sufficient numbers of particles were measured:

$$\frac{X_g(n_2)-X_g(n_1)}{X_g(n_1)} *100\% \quad < 5\% \text{ for mean breadth and } \beta$$

$$< 10\% \text{ for Length}$$

X_g: geometric mean of the length, β and mean breadth

n_1&n_2: number of particles measured in 60 and 100 f.v. respectively.

$$\frac{\sigma_g(n_2)-\sigma_g(n_1)}{\sigma_g(n_1)} *100\% \quad < 5\% \text{ for mean breadth, length, and } \beta$$

σ_g: geometric standard deviation of X_g

A total of 60 and eventually 100 f.v. were measured and the results are summarized in Table 1.6 which demonstrates that the criteria are satisfied. In order to reduce the time of computation and to avoid overflowing of the computer storage system, the measurements of 60 f.v. were used in the theoretical calculation of Da.

Table 1.6. Geometric mean (X_g) and geometric standard deviation (σ_g) of 108 and 200 CA fibres in 60 and 100 f.v. respectively. (Total number of particles including fragments in 60 f.v. is 1050)

	No. of f.v.				% Increment	
	60		100			
	X_g	σ_g	X_g	σ_g	X_g	σ_g
Length (L)	1.997	1.799	2.090	1.826	4.63	1.50
Mean breadth (M.B.)	0.196	1.551	0.203	1.584	3.47	2.14
Axial ratio (β)	10.185	1.507	10.360	1.527	1.72	1.31

Thickness measurement

A total of 28 fibres and 27 'fragment' particles were measured in 50 and 6 fields of view respectively. The thickness (T) was best expressed by multiple regression equations:

For fibres:

$$T = (0.59657*M.B. + 0.114658*L + 0.044379) * \tan\theta$$

$$(r^2 = 0.69)$$

M.B.=Mean breadth

L=Length

For fragment particles:

$$T = (0.29687*L + 1.49724*B + 0.0728) * \tan\theta$$

$$(r^2 = 0.69)$$

B=Breadth

tanθ =thickness of a standard /shadow length of the

latex sphere standard latex sphere

= 0.2318/0.5227

The thickness was then calculated for all evaluations according to the above equations from ordinary 2-dimensional image analysis of mean breadth and length.

Data treatment

The mass median aerodynamic diameters MMAD calculated according to the three theoretical methods from the planar (P) images were all greater than the experimental MMAD obtained by cascade impaction (Table 1.7). The difference between the latter result and methods I and III is well within the expected level of uncertainty of the techniques used especially since the size distributions are not perfectly log-normal. These theoretical calculations were based on the assumption that the particles are oriented to give maximum viscous drag; calculations based on random, or parallel orientation to the direction of motion, would have yielded even higher aerodynamic diameters (Gonda & Khalik, 1985). Method I which utilizes only the apparent two-dimensional images (i.e., no use is made of the thickness obtained from the shadowing technique) gives surprisingly good agreement with the experimental result both for MMAD and σ_g. Incorporation of the thickness measurement into the calculation of aerodynamic diameter and the volume for prolate spheriods (Method II) gives still higher MMAD. Method III (Johnson 1986; Johnson et al., 1987) is closer to the experimental MMAD and σ_g than Method II; Sheaffer (1987) suggested a correction to the Johnson equation (Method III). However, no difference was found in the results of the calculation with Sheaffer's correction, the reason being that it only becomes significant for very high axial ratios. The theoretical calculations were repeated for 'Fibres only' (Table 1.7)

TABLE 1.7

METHOD [a]		I		II		III		EXPERIMENTALLY BY CASCADE IMPACTION	
		MMAD (μm)	σ_g	MMAD (μm)	σ_g	MMAD (μm)	σ_g	MMAD (μm)	σ_g
ALL PARTICLES	P [b]	0.74	1.81	0.87	1.66	0.79	1.70	0.65 S.D. 0.02	1.88 S.D. 0.05
	T [c]	0.78	1.80	0.96	1.64	-	-		
FIBERS ONLY [d]	P	0.73	1.55	0.98	1.55	0.93	1.56	-	-
	T	0.78	1.55	1.05	1.55	-	-		

a. Methods I, II and III are based on theoretical calculations which utilize the geometric measurements of the electronmicrograph images of the particles as explained in Sec. 1.7.3

b. P - planar images

c. T - image dimensions corrected for tilt (see Sec. 1.7.2 and Sec. 1.8 under 'Data treatment')

d. Calculations which exclude small compact ($\beta < 2.5$) particles of CA.

by excluding small particles with axial ratio less than about 2.5 (subjectively, these particles looked very different from the much bigger well-formed elongated CA crystals). These calculations showed that the fibres still had a low MMAD, making them suitable for pulmonary drug delivery especially in conjunction with breath holding (Palmes et al, 1973). Interestingly, the calculated σ_g for aerodynamic diameters of the fibres is reflected quite well by the σ_g for the mean breadth and β. Uncertainty in the theoretical calculations may arise from the fact that the deposited particles may not be parallel to the impaction surface. If we assume 54.7^0 as the statistical mean angle of particles with respect to the direction of motion (i.e. perpendicular to the image) (Fuchs, 1964) then a correction for the tilt (T) can be made (Table 1.7); this correction makes MMAD a little higher but it does not affect σ_g.

It has to be mentioned that the perpendicular flight orientation of the fibres as suggested by the results of the theoretical calculations is in contrast to previous work. Kasper and Shaw (1983) obtained evidence for a significant parallel component for the orientation in a nine-stage impactor. They used chain aggregates of iron oxide (density = 4.9 g/cm^3) and a flow rate of 30 L/min. A later work by Gonda and Klalik (1985b) on the aerodynamics of particles of different crystal habits of hexamethymelamine (HMM) (density = 1.1 g/cm^3) showed data which did not enable them to make any definite statements about the particle orientation in the cascade impactor.

However, they suggested that by assuming the orientation at low Da was parallel and at high Da was perpendicular to the flow, the calculated Da results correlated better with the experimental data. In other words, perpendicular orientation was suggested only for large particles. The cascade impactor they used was the same as in the present study with a flow rate of 12.5 L/min. However, there were some major differences between the two studies: the particles of HMM were more like cylinders rather than the flat and rod needles of CA. Khalik and Gonda's 'geometric' method was less reliable than the current one because the aerodynamic diameters were calculated from the average dimensions of all particles on an impactor slide. Also, they tried to correlate the average aerodynamic diameter of each impactor slide with these average theoretical Da. Such averaging leads to results with poor accuracy. Therefore, it seems that more experimental data are yet to be collected before a definite generalization on flight orientation could be made. It is possible that the difference in the flight orientation inside an impactor among different studies may be due to a combination of factors including the differences in particle shape, density, size, geometric and mass uniformity of the fibres [as have been observed for particles under gravitational sedimentation (Timbrell, 1965; 1972)] and the flow rate of the impactor.

1.9 Conclusions:

CA fibres, characterized by chemical and physical methods,

have been prepared in respirable form suitable for direct pulmonary administration. The CA particles were dried by a vertical drying column and measured aerodynamically by a cascade impactor. Experimental results showed that the CA particles have a MMAD = 0.65μm with σ_g = 1.88 and axial ratio (geometric mean for fibres)=10.2. Theoretical calculations of Da using geometric data obtained from electronmicrographs were also attempted. The calculated MMAD and σ_g assuming perpendicular orientation of the elongated particles with respect to the direction of motion were in reasonable agreement with the values obtained by cascade impactor.

[Currently, the most common formulation of therapeutic inhalation aerosols are suspensions of solid drug particles in a halocarbon propellant. It has been known that the size distribution of the particles after generation from the nebuliser will shift to larger sizes (Polli et al, 1969). Apart from the reasons of the presence of non-volatile excipients in the formulation and aggregate formation in the suspension (e.g. due to poor physical stability), a more general reason for the shift is that the aerosol droplets contain more than 1 particle which will form aggregates after they are dried. The aerodynamic properties of the aggregates will be different from the primary particles because of the increase in size and likely a change in shape. As a result, deposition of the aggregates in the respiratory tract will be different from that of the primary particles and this may be undesirable. Such modification of aerodynamic properties

of solid particles by aggregation from aerosol droplets has been modelled for system of monodisperse particles in monodisperse droplets (Gonda, 1985). Extension of the system to monodisperse particles in polydisperse droplets was also attempted (in Appendix 1). The results elucidate the effects of various controlling physical parameters (such as the suspension concentration, droplet/particle size ratio) which can be used to find the deviations from the aerodynamic diameter of a single particle. The study is also relevant to the spray drying process of e.g. CA in Sec.1.4 if individual particles are desired.

Finally, when aerosols are used as aqueous suspensions, bronchospasm may be evoked in asthmatic patients if the suspension tonicity is significantly non-isotonic and the volume nebulised is large (millilitre quantitites) (Schoeffel et al, 1984; Anonymous, 1984). Study of tonicity of some commonly used drug preparations for nebulisation was therefore undertaken. The results are discussed in Appendix 1.]

Future work

The drying column was definitely a solution to solve the problem of drying CA particles for aerodynamic measurements. However, it would be most inconvenient for use with patients. Obtaining sufficient amount of dry particles and testing their redispersibility are therefore studies to be done in future.

CHAPTER TWO

2. METHOTREXATE (MTX)

2.1 Introduction

i) Modifications of crystal habits

[Note that habit modification due to polymorphism is not considered here until the end of this section]. The external shape of a crystal is determined by the relative development of the various crystallographic faces governed by their growth kinetics (Mullin, 1972). Certain growth directions in growing crystals may be preferred to others. If the crystal grows mainly in one direction it assumes an elongated shape. Crystals growing mainly along one plane become plate-like. Furthermore, crystals which grow nearly uniformly in all three dimensions are isometric (Tarjan and Matrai, 1972). The habit of a crystal is therefore bound by the dominant crystallographic faces which are the ones with the slowest growth rate. Hartman (1969) summarized the various factors affecting the growth habit of a crystal into 2 main types, internal and external. The internal or structural factors include (i) the crystal lattice which is governed by the intermolecular interactions like hydrogen bonds, dipolar and van der Waals forces and (ii) the presence of crystal lattice defects such as dislocations. Basically, theoretical equilibrium and growth habits of a crystal can be obtained by structural

consideration using the periodic (strong) bond chain approach (Hartman, 1969; 1973) and by energy consideration using the attachment energy approach (Hartman, 1973; Hartman and Bennema, 1980; Saska and Myerson, 1983; Aquilano et al, 1986). However, crystal habits also depend on the external or environmental factors which account for the deviation of the growth habit from the theoretical habit. Wells (1946; 1949) has found that the external form of a crystal is the expression not only of its internal structure but also of the interaction between solute and solvent. External factors are all the physicochemical parameters of the crystallization conditions which generally include:

1) the presence of foreign materials (solvents and additives or impuritites).

2) the degree of disequilibrium (supersaturation, undercooling and rate of cooling).

3) the supply of solute (stirring and viscosity).

4) others (temperature, pH, etc.)

(Wells, 1946; Hartman, 1969; Mullin, 1972; Haleblian, 1975; Boistelle, 1976; Khamskii, 1976). For classification, the external factors can be divided into physical and chemical ones.

A. Chemical factors:

a) Solvents

Solvents can be very powerful in changing the growth

habits of crystals. Some examples are listed in Table 2.1. The mechanisms of crystal habit modification in solvents have been considered (Wells, 1946; 1949; Davey, 1982; Berkovitch-Yellin, 1985; Addadi et al, 1985). The basic steps of the process of crystal growth from solution include (Mullin, 1972):

1) Volume diffusion of solvated solute molecules towards the crystal surface.

2) Desolvation of both the solute molecules and the growth sites on the crystal surfaces.

3) Incorporation of solute molecules into the crystal lattice which includes surface kinetics processes such as adsorption, surface diffusion, and incorporation at kinks.

It is clear that the activation energies associated with step 1) and 2) are dependent on the strength of the intermolecular interactions between the solute and solvent molecules, which therefore play an important role in the solvent effects on crystal habit. In fact, solute-solvent interaction have been proposed and generally accepted as the mechanism responsible for habit modification of crystals in solvents (Wells, 1946; 1949; Davey, 1982; Berkovitch-Yellin, 1985; Addadi et al, 1985). Indirect quantitative evidence has been put forward by Berkovitch-Yellin (1985) and Addadi et al (1985) by theoretical modelling of the solvent effects on crystal habit (via adsorption) using electrostatic potential energy mapping along various crystal faces of the compound resorcinol. Their results support the previous theory by Wells (1946; 1949) that the growth of a crystal face is

Table 2.1
Examples of Habit Modification by Solvents

Compound	Habit	Solvent	Reference
Iodoform	hexagonal bipyramids hexagonal prism	aniline cyclohexane	Wells (1946)
Resorcinol	compact very fine needles	water benzene and CCl_4	Wells (1946)
Adipic acid	needle hexagonal plate	vapour or non-polar water	Michaels and Colville (1960)
Salol	compact or plate (1) only plate	alcohols benzene, CCl_4, acetone	Kleber and Raidt (1963)
Phthalic acid	various	polar solvents	Davey (1982)
Oxalic acid	prismatic tabular	acetone-water water	Torgesen and Strassburger (1964)
Nitrofurantoin	tabular to needle plate (2)	formic acid formic acid/H_2O or ethanol	Garti and Tibika (1980)
Succinic acid	plate needle	water isopropanol	Davey et al (1982)
Acetanilide	long needle less elongated	benzene alcohols, DMSO, acetone	Etter et al (1986)

(1) also depending on supersaturation and temperature.

(2) also depending on solvent vol. ratio, stirring etc.

inhibited by strong adsorption of solvent. When solvent molecules adsorb preferentially on certain crystal faces due to favoured solute-solvent interaction, it is necessary to remove the solvent layer prior to the deposition of solute. As a result, the growth rate of these faces decrease and consequently a change of the growth habit occurs. In addition to solvent adsorption, Bourne and Davey (1976) and Davey (1982; 1986) also proposed a parameter called surface entropy factor or α-factor to quantify the roughness of an interface between a solid and a fluid phase for explaining the solvent effects. This α-factor is a function of the crystal and the solvent. It defines the enthalpy changes which take place when a flat interface is roughened. The value of α can be related to the expected growth mechanism of a face (Davey, 1979):

$\alpha < 3.0$ Surface inherently rough, no barrier to surface nucleation at any supersaturation.

$3.0 < \alpha < 4.0$ Surface smoother, surface nucleation still possible at low supersaturation.

$\alpha > 4.0$ Surface smooth, growth at low supersaturation only possible if screw dislocations are available.

It is clear that growth of a rough interface can proceed easier and faster than a smooth interface. As different crystal faces will have different values of α, therefore the crystal habit may well be dependent on α (and hence on the solvent). Solution structure, although not much discussed in literature, has also been found to affect crystal growth. Watson (1954) reported the surface morphology (growth steps on crystal faces) of

n-pentacontanol-1 crystals depended on the association of solute and solvent in solution. Ananikyan et al (1985) found that the best crystals of potassium iodate and pentaborate were grown from the least associated solutions.

b) Additives (impurities)

Hundreds of reports have been published on the effects of additives on the growth kinetics, surface morphology and growth habit of crystals, especially in industrial crystallization (Mullin, 1972; 1976; deJong and Jancic, 1979; Jancic and deJong, 1982; 1984). In pharmaceutics, the research team headed by Grant recently published several papers on modification of drug crystals and excipients and on their physicochemical properties using additives (Chow et al, 1985; Chow et al 1985). An additive is a system-specific compound which adsorbs on the surface of the crystal, and modifies the growth characteristics of the crystallizing solute (Davey, 1979). Additives incorporated into the crystal (Go and Grant, 1985; Addadi et al, 1985) may also affect crystal habits in addition to other physicochemical properties. In industrial crystallization, the effective additive concentration can be as low as 10^{-3} - 10^{-8} mole fraction (Davey, 1979). Various models have been proposed for the adsorption of additives onto crystal surfaces. Three surface sites are possible for adsorption: kink, step and ledge or terrace (Davey, 1979). Weijnen et al (1987) found that both models of preferential adsorption at the

kink sites (or at the steps), or of random adsorption upon the terraces between the steps agreed quite well with the experimental adsorption data. Grant's group (York and Grant, 1985; Grant and York 1985; 1986) explained the influence of additive on drug crystals from a thermodynamic view point using enthalpy and entropy concepts.

(a) 'Tailor-made' additives

Lately, a series of papers on the growth of organic crystals in the presence of so called 'tailor-made' additives has been reported by Berkovitch-Yellin et al (1982; 1985), Addadi et al (1982; 1985), Addadi and Weiner (1986), and Weissbuch et al (1985 a & b; 1987) from the Weizmann Institute of Science in Israel. Using 'tailor-made' inhibitors with molecular structures very similar to those of the corresponding substrate molecules comprising the crystal, Berkovitch-Yellin et al successfully engineered amino acid crystals with desired morphology. From the results, they established a stereochemical correlation between the structure of the crystal, its modified morphology and the molecular structure of the inhibitors. Their work suggested that crystal habit can be modified in a controlled way by use of appropriate crystal growth inhibitors.

(b) Surfactants

Surfactants were used in crystal habit modification because being surface-active, they tend to be physically and/or chemically adsorbed onto the crystal surface (ionic surfactants may interact with the charged functional groups of the solute molecules as well), and thus affect the nucleation and incorporation of solute molecules onto the crystal faces. This results in the change of growth rate along certain directions, and hence the growth shape. In the classical example of crystal habit modification of adipic acid (Michaels and Colville, 1960), addition of trace quantities (50-100 ppm) of anionic or cationic surfactant caused reduction of the growth rate of all faces, but to different extent. The anionic surfactant retarded the growth on the (110) and (010) faces more than on the (001) face, thus favouring formation of prismatic or needle crystals; this was related to the hydroxyl density on the crystal faces. The cationic surfactant had the opposite effect, favouring growth of thin plates. Surfactants have also been reported to affect the habits of inorganic crystal such as gypsum (Schroeder et al, 1976) and polymorphic modifications of stearic acid (Garti et al, 1982).

B. Physical factors:

a) Supersaturation

The growth kinetics of individual face of a crystal usually depends to a different extent on supersaturation.

By raising or lowering the supersaturation level it is therefore possible to exert a considerable control over the crystal habit (Mullin, 1972). When salol was crystallized from methanol, the change of symmetry of the crystals was most pronounced at low supersaturation (Kleber and Raidt, 1963). In adipic acid, the growth rate of each face of the crystal in water was increased with increasing supersaturation, very rapidly at low supersaturations and more slowly as the supersaturation increased, with the hexagonal plate crystal changed from a thick, elongated shape to a thinner, more regular shape (Michaels and Colville, 1960). Empirical equation has been proposed to describe the dependence of the length to breadth ratio (y/x) of crystals to the supersaturation level (Δc),

$$y/x = k\ (\Delta c)^n$$

k: a constant depending on the crystallization conditions, especially on diffusion.

n: a number bigger than 1, depending on the crystallizing substance.

suggesting that a change of habit to needle like when the supersaturation is increased (Haleblian, 1975). Experimentally, Garti and Tibika (1980) found that such relationship could be applied to the crystallization of nitrofurantoin in a formic acid solvent system.

b) Rate of cooling

Rapid cooling of a melt or solution, or during sublimation often causes extreme developments, leading to the formation of needles, dendrites or thin plates instead of compact crystals due to rapid crystal growth. It is because such habits permit a more rapid dissipation of the heat of crystallization from the solid phase (Mullin, 1972). For example, rapid cooling of naphthalene solution in ethanol gives very thin plates while in cyclohexane it forms needles (Wells, 1946). Similarly, thin square plates of pentaerythritol were obtained from a solution in β-ethoxyethanol on rapid cooling but compact bipyramid habit on slow growth. Moreover, Garti and Tibika (1980) found that an increase in the cooling rate of crystallization of nitrofurantoin in a quiescent solution of formic acid-ethanol (2:1) caused an increase in the supersaturation values and more elongated, needle-like crystals were collected. However, it should be noted that too rapid a cooling rate may cause excessive nucleation which will deplete the solute necessary for further crystal growth, resulting in small crystals or dendrites, or even amorphous form in the extreme case.

c) Temperature

Although temperature has often been found to have a prominent effect on the crystal habits of different polymorphic modifications, e.g. of paraffin wax (Edwards, 1957) and stearic acid (Sato and Boistelle, 1984), it has been suggested by Boistelle (1976) that there are no

important habit changes due to the sole effect of the crystallization temperature if phase transformations are excluded. Nevertheless, Khamskii (1976) reported that high temperature appeared to promote non-isometric forms of inorganic crystals such as ammonium chloride. It is noteworthy that temperature may co-operate with impurities to produce a habit change, since it is evident that impurity adsorption depends largely on temperature (Boistelle, 1976).

d) Agitation

Generally, agitation promotes mass transfer on and around nuclei and crystal surfaces, and enhances interfacial supersaturation and nucleation, and consequently leads to a less non-isometric crystal growth. Thus, smaller and less elongated nitrofurantoin crystals (Garti & Tibika, 1980), and isometric inorganic crystals of ammonium chloride (Khamskii, 1976) were promoted in an agitated system.

e) Others: e.g. pH, substrate, gel-growth.

Inorganic halides can grow in forms of whiskers (long needles) on porous substrates such as cellophane membrane and ceramics (Tarjan and Matrai, 1972). The growth habit of organic crystals such as cytosine monohydrate is very sensitive to pH. The rod like crystals at low pH change to prisms and finally plates as the pH is increased above

neutral (Davey, 1986).

Habit Modification due to Polymorphism

While the above discussion has been confined to crystal habit modifications of the same polymorph of a compound, it should be included here that different crystal habits may result by polymorphic transformations. Similar to habit modifications, polymorphic transformation can be affected by the crystallization conditions such as solvents, supersaturation and agitation e.g. stearic acid (Garti et al, 1980; Sato and Boistelle, 1984). However, in pharmaceuticals, polymorphism and phase transition are most commonly mediated by solvents and temperature change. Thermally induced transition can be detected by thermal analysis, such as differential thermal analysis and differential scanning calorimetry. A detailed summary of various pharmaceutical substances showing polymorphism has been given by Byrn (1982) and Wollmann and Braun (1983).

ii) Aim of the study

Methotrexate (MTX) is an antitumour agent for the treatment of cancer and it is active in lung tumours including small cell type (Comis, 1981). Our objective was to prepare MTX in a respirable form suitable for direct administration into the lung. It might be an advantage if MTX could achieve a higher concentration in

the lung and a lower concentration systemically. Then it might achieve a better therapeutic index. We wanted to modify the shape of the particles to an elongated one so as to control the aerodynamic diameter and the deposition in the lung (see Chapter 1, Introduction).

Modification of crystal habits of MTX could be studied systematically by considering the physico-chemical properties of various faces in the crystal. By choosing suitable physico-chemical conditions of crystallization, the growth rate of certain crystal faces might be altered with the result of a change in the final growth forms of the crystal. For example, by encouraging the growth along a specific crystallographic direction or alternatively by inhibiting the growth in other directions may result in an elongated shape.

The greatest difficulty in this project was the inability to prepare MTX crystals for 9 months using many different crystallization conditions. All we could obtain were just small anhedral particles. We realized then that no one has ever succeeded in obtaining single crystals of MTX with size big enough for X-ray single crystal diffraction study, although it has been discovered more than 30 years ago. At this stage, we changed our original goal and tried to prepare a complex of MTX with a desirable aerodynamic shape. Thymidine was chosen because it has been used concurrently with MTX administration to reduce the toxic effect of the latter (Ensminger, 1984). We were then pleased to obtain our first crop of what we expected to be crystals of an MTX-thymidine complex. But, after a

series of chemical analyses (UV-visible, IR and NMR spectroscopy, Mass spectrometry and TLC), to our surprise, the crystals thus obtained were MTX itself without any trace of thymidine.

2.2 Preliminary Experiments

2.2.1 Crystal Habits of MTX in Different Solvents

i) Materials and Methods

2 mg MTX (supplied by the American Cyanamid Company, Pearl River, N.Y.) was dissolved in 1ml of solvents and heated up if necessary. The volume of the solvent was increased up to 10ml if dissolution was difficult. The solutions were allowed to cool and evaporate at room temperature for crystallization. The solvents used were double distilled water, methanol, ethanol, butanol, octanol, cyclohexane, carbon tetrachloride, benzene, DMSO and 0.1N HCl. All solvents were of analytical grade.

ii) Results

The results of crystallization in various solvents are summarized as follows:

a. Water:

The solubililty of MTX in cold water is low but increases significantly at elevated temperature. On cooling a

heated supersaturated solution or on evaporating an unsaturated solution, MTX crystallized out. Both cases gave aggregates of anhedral particles. No well-formed individual crystals formed.

b. Methanol:

Similar to water.

c. Ethanol:

Also similar to water but the solubility is apparently lower.

d. Butanol, octanol:

MTX is practically insoluble.

e. Cyclohexane, carbon tetrachloride, benzene:

MTX is practically insoluble.

f. DMSO:

MTX is extremely soluble in DMSO and forms a viscous solution. However, due to the very low volatility of DMSO, no MTX crystals were formed after leaving an unsaturated solution standing for 1 month to evaporate. When water was added into the solution, MTX was precipitated out as aggregates of tiny particles. The same aggregates were obtained on cooling a heated supersatured solution of MTX in DMSO. No well-shaped crystals were observed.

g. 0.1N HCl

MTX is extremely soluble in 0.1N HCl. On evaporation, the solution would not form crystals readily but rather turned into a highly viscous liquid which later solidified as all the water evaporated. The resulting solids appeared as dendritic forms under the optical microscope. However, on adding a drop of water, a brown mass formed immediately.

h. 0.1N HCl/methanol solution

MTX is extremely soluble in the solution which after evaporation gave yellow aggregates that turned brown on addition of a drop of water.

iii) Discussion

No well-defined single crystals of MTX could be found at this stage. The aggregates formed under acidic condition were most probably the unstable HCl salt of MTX. Turning brown may be due to decomposition. The inability to form individual crystals led us to investigate the crystalline properties of the original MTX powder from the manufacturer.

2.2.2 Crystalline Properties of the Original MTX Powder

i) Materials and Methods

a. Polarizing microscopy

The MTX powder was observed in an immersion oil (n=1.53) using a petrological polarizing microscope (Leitz).

b. X-ray powder diffraction

X-ray powder diffraction pattern was recorded on an X-ray diffractometer (Philips) fitted with a graphite monochromator and connected to an X-ray generator (Philips PW 1730, 2KV) using: slit $1/2^0$, range 10^3, time constant 1, scan rate 2^0/min and Cu target.

c. Scanning electron microscopy (SEM)

MTX powder samples were mounted on an EM sample stub by double-sided sticky tape. After platinum coating, the samples were viewed under a scanning electron microscope (Jeol JEM 35C) using an electron beam voltage of 15KV and a back scattered electron detector.

d. Transmission electron microscopy (TEM)

This work was carried out by Dr. David Cockayne, director of the Electron Microscope Unit, University of Sydney. MTX powder was directly adhered onto the surface of an EM grid which was then observed under a transmission electron microscope (Philips 300). TEM provided a complementary study (to X-ray diffraction) of the crystallinity of the powder by observing the diffraction pattern of the electron beam.

ii) Results

a. Polarizing microscopy

The powder appeared as bright yellow aggregates between cross polars under the polarizing microscope.

b. X-ray powder diffraction

Broad but prominent peaks occurred from 2θ values of about $3^0 - 30^0$ in the diffraction pattern (see Fig. 2.6a).

c. Scanning electron microscopy

Spherical aggregates with irregular platy surface texture were observed. No sharp edges or flat surfaces characteristic of well-formed crystals could be found. (see Fig. 2.1a)

d. Transmission electron microscopy

No electron diffraction pattern could be obtained.

iii) Discussion

It is difficult to determine whether the MTX powder is crystalline or amorphous by ordinary optical microscopy (Fig.2.1b). However, X-ray powder diffraction revealed that the powder was crystalline, althought with a low

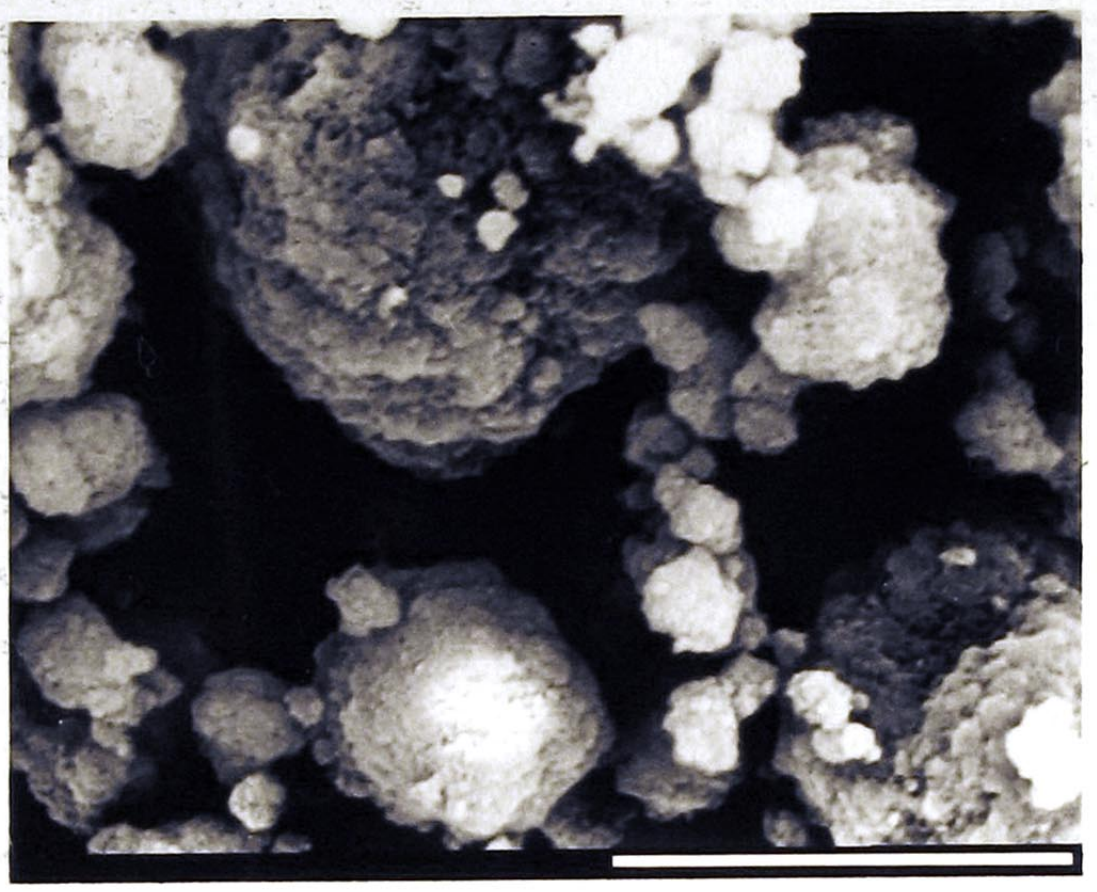

(a)

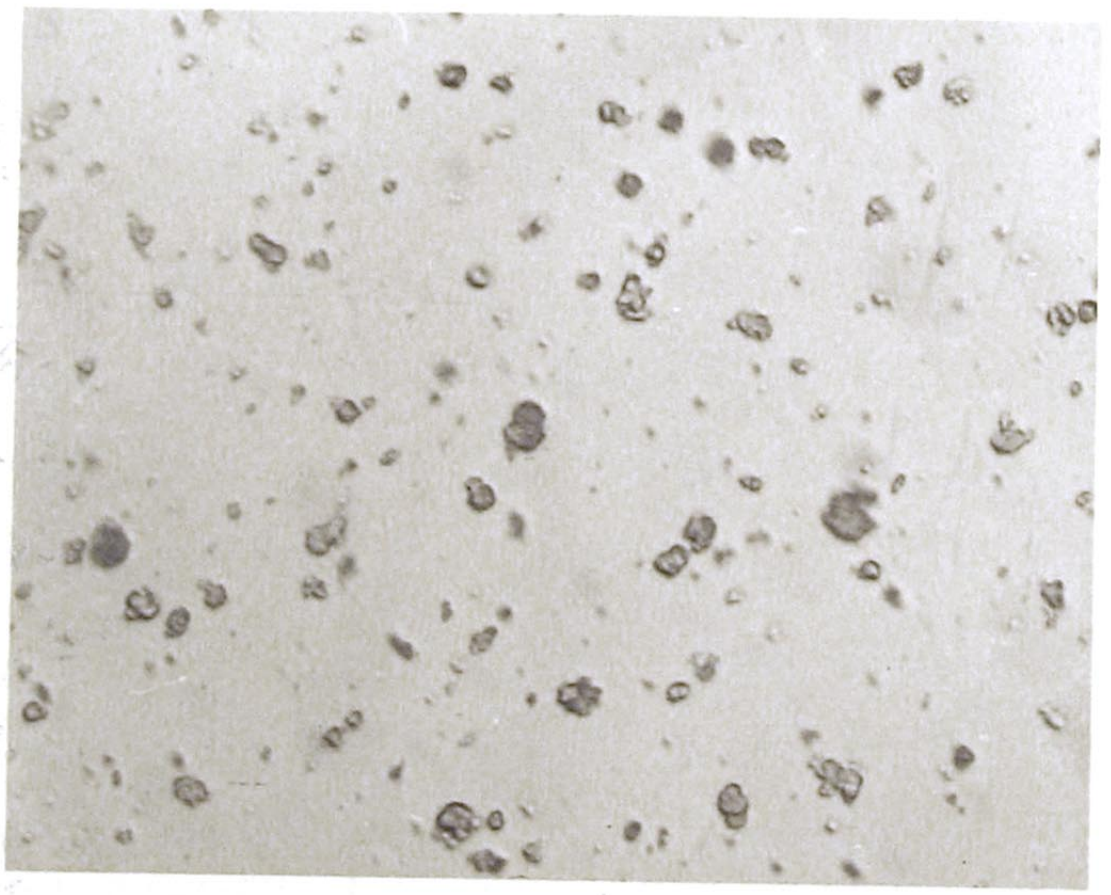

(b)

Fig. 2.1 Original MTX powder

a) Scanning electronmicrograph
b) Optical micrograph
(scale bars: 10μm)

degree of crystallinity. Polarizing microscopy showed that the crystalline structure was anisotropic, suggesting that it could not be amorphous or cubic crystalline form (which is isotropic because of its high degree of symmetry, and will appear black, i.e. extinct, between cross polars), but belongs to other symmetry class. Furthermore, SEM showed that these crystalline powders appeared as aggregates with platy surface texture. Nevertheless, TEM failed to give an electron diffraction pattern of the crystalline solid. This may be due to (i) collapse of the crystal structure because the water of crystallization might be lost under the high vacuum inside the microscope, and (ii) the physical or/and chemical instability of MTX under the electron beam. (i) has been tested by putting MTX under high vacuum (1-100 micron mercury) for 24 hours and then kept in a desiccator. On doing the X-ray powder diffraction again, however, the same diffraction pattern was obtained (re-hydration of the crystal structure might probably take place as the powder is exposed to the atmosphere). The possibility of (ii) is likely to be low because the MTX powder should be able to reveal its electron diffraction pattern even at least for a very short time before it decomposes (unless the rate of decomposition or change in the structure is too quick to be detected).

2.2.3 Preparation of MTX Crystals by Sublimation

i) Materials and Methods

MTX in a round-bottom flask was heated in an oil-bath. The flask was connected to a vertical condenser tube circulating with cold water to allow condensation of any vapour evolved. The system was under vacuum (~50μm Hg). Temperature of the bath was increased gradually and the condenser was observed carefully for sublimation. No sublimates were formed. The temperature was then fixed at 150^0 - 160^0C for 1 hour. Afterwards, temperature was further increased until the MTX melted with decomposition at >200^0C. Any sublimates formed were collected and dissolved in 0.1 N NaOH for characterization by UV-visible spectroscopy.

ii) Results and Discussion

No sublimation took place at temperature ≤ 150-160^0C. On melting, white sublimates were formed and condensed on the neck of the flask. However, the UV-visible spectroscopy showed a different spectrum from that characteristic of MTX, suggesting that it was not MTX (most probably a decomposition product of MTX).

2.3 Experiments to Prepare MTX Crystals:

Crystallization of MTX in the Presence of Thymidine

Thus far we could not obtain any MTX crystals. As mentioned in Sec.2.1 ii), we changed our original goal at

this stage and tried to prepare a MTX-thymidine complex with desirable crystal shape.

2.3.1 Materials and Methods

Methotrexate (supplied by the American Cyanamid Company, Pearl River, N.Y., U.S.A.) was crystallized from aqueous solutions containing different amounts of thymidine (Calbiochem, Calbiochem-Behring Corp., La Jolla, CA, USA)) as follows:

2mg of MTX powder was weighed into a specimen tube (2" x 1"). 1 ml of double distilled water and thymidine (see below) were added and heated in a 90-100^{0}C water bath to dissolve the MTX. The weight ratios of MTX/thymidine were 1:0.5, 1:1 and 1:5. The hot solutions were then allowed to cool to room temperature for spontaneous nucleation and crystallization. Afterwards (overnight), drops of solution containing some crystals were observed under an ordinary optical microscope. Later, a zoom stereomicroscope (Kyowa, trinocular, model SDZ-Tr-P) was used to observe the crystals inside the specimen tubes *in-situ*.

2.3.2 Results

Small crystals floating on the top of the solutions observed in the ordinary microscopy were found to be well-shaped yellow colour tetragonal crystals. Later results by the zoom stereomicroscope revealed that most of

the crystals were twins or aggregates consisting of more than 1 individual crystal. Nevertheless well-formed single crystals could also be found (Fig.2.1c). Interestingly, some crystals were round with irregular surface which is more prominent in the 1:1 and 1:5 solution i.e. as the amount of thymidine increased. At this stage we thought that the crystals were most likely a complex of MTX with thymidine. The crystals were then subjected to further characterization.

2.3.3. Characterization

Two samples were used in the characterization: the original MTX powder from the manufacturer and the MTX obtained from crystallization in thymidine solution (25mg of crystals were obtained from 20ml solution containing 40mg MTX powder and 20mg thymidine).

i) Experimental

a.) Melting point (m.p.) measurement

M.p. was measured by a melting point apparatus (Townson & Mercer Ltd., England) and a Kofler hot stage microscope using a heating rate of 4^0C/min as recommended for substances which decompose on melting (Kuhnert-Brandstatter, 1966).

b.) UV spectroscopy

UV absorption spectra were recorded using a spectrophotometer (Perkin-Elmer Lambda 5 UV/VIS) with instrumental settings: slit 2nm, scan speed 60 nm/min, response 0.5s and peak threshold 0.02A. A pair of matched 1cm quartz curvettes was used. The solvent was 0.1N NaOH in all runs.

c.) IR spectroscopy

IR spectra were determined in an infrared spectrophotometer (Perkin-Elmer double beam 297) by employing the KBr pellet method with a compression pressure of 2500 lb/in^2.

d.) ^1H NMR spectroscopy

^1H NMR spectra were determined by a Fourier transform NMR spectrometer (Jeol FX 90Q) operating at proton irradiation frequency 90 MHz with deuterium lock signal for tuning, data points 8K, and spectral width 896 Hz. Tetramethylsilane (TMS) and d_6-DMSO were used as the internal standard and solvent respectively. Additional spectra of thymidine and of a physical mixture of MTX with thymidine (approximately weight ratio 10:1) were also compared under the same experimental condition.

e.) Mass spectrometry

The [redacted] method of mass spectrometry [redacted] used by Cheung et al (1985) for the characterization of analogues of MTX was employed. Chemical ionization (CI) mass spectra were recorded on a quadrupole mass spectrometer (Finnigan 3200) on-line to a data system (Finnigan 6100). Ammonia (Metheson anhydrous, 99.9%) was used as reactant gas at a pressure of 1 Torr. The source temperature was 90^0C. The ammonia CI spectra were collected using a solids insertion probe (Finnigan) for thermal desorption from a platinum wire (Cheung et al, 1985). Samples of 1-5 µg of MTX were used.

f.) Thin-layer chromatography (TLC)

The TLC method of assay of MTX in the U.S.P. XIX edition was used. MTX sample solutions were prepared and then applied onto the TLC plate as described in the U.S.P. XIX. The chromatography system was as follows:

TLC plate: cellulose-coated glass plate (Merck);
length 12cm

Developing solvent: citric acid monohydrate aqueous solution (10g/200ml) was adjusted to pH 8 with NH_4OH. 10 volumes of this solution were shaked with 1 volume of amyl alcohol and allowed to stand for 30 minutes, afterward the lower phase was used.

Visualisation: UV lamp (both short and long wavelength light).

After development, drying, and visualisation, both the fluorescent and non-fluorescent (yellow colour) bands were

scraped separately into centrfuge tubes containing 0.1N NaOH. After shaking and centrifuging, the supernatant MTX solutions were diluted and analysed by UV spectroscopy as described in this section, b.).

g.) Optical rotation

Since MTX molecule has a chiral centre (α-carbon in the glutamate moiety) and is therefore optically active, it is possible that during crystallization in hot water, racemic modification might have been formed by thermal racemization or ion formation (Eliel, 1962). In order to find out this, optical rotation of MTX in 0.1N NaOH was measured using a polarimeter (Hilger and Watts) with a 2 dm sample tube and a sodium lamp as the light source.

h.) X-ray powder diffraction

X-ray powder diffractions of MTX samples were carried out as described in Chapter 1, Sec.1.2.2 f.

ii) Results

a) M.p. measurement

Both methods of measurement gave similar results. Although there is some overlapping, it appears from Table 2.2 that the tetragonal crystal has a higher melting temperature than the original MTX powder.

Table 2.2.

Sample	M.P. (^{0}C)
Original MTX powder	193-199
Tetragonal crystal	196-210

b) UV spectroscopy

The UV spectra of different samples of MTX in 0.1N NaOH are identical with the characteristic maxima at 371.9, 303.1 and 258.7 nm (Chamberlin et al, 1976). A representative spectrum is illustrated in Fig.2.2.

c) IR spectroscopy

There are some differences in the IR spectra measured for the 2 MTX samples as shown in Fig.2.3 a & b. In comparison, Fig.2.3 b shows the absence of an absorption band at 1300cm^{-1} (tetragon crystal sample) but the presence of more prominent bands at 1100, 1020 and 860cm^{-1}.

d) ^{1}H NMR spectroscopy

The 2 spectra obtained were basically similar as illustrated with interpretation in Fig.2.4a & b. Some peaks were shifted simply due to the exchangeable proton(s) contained in some functional groups (amine, amide, and hydroxyl including water) of the structure. The spectrum for thymidine is shown in Fig.2.4c.

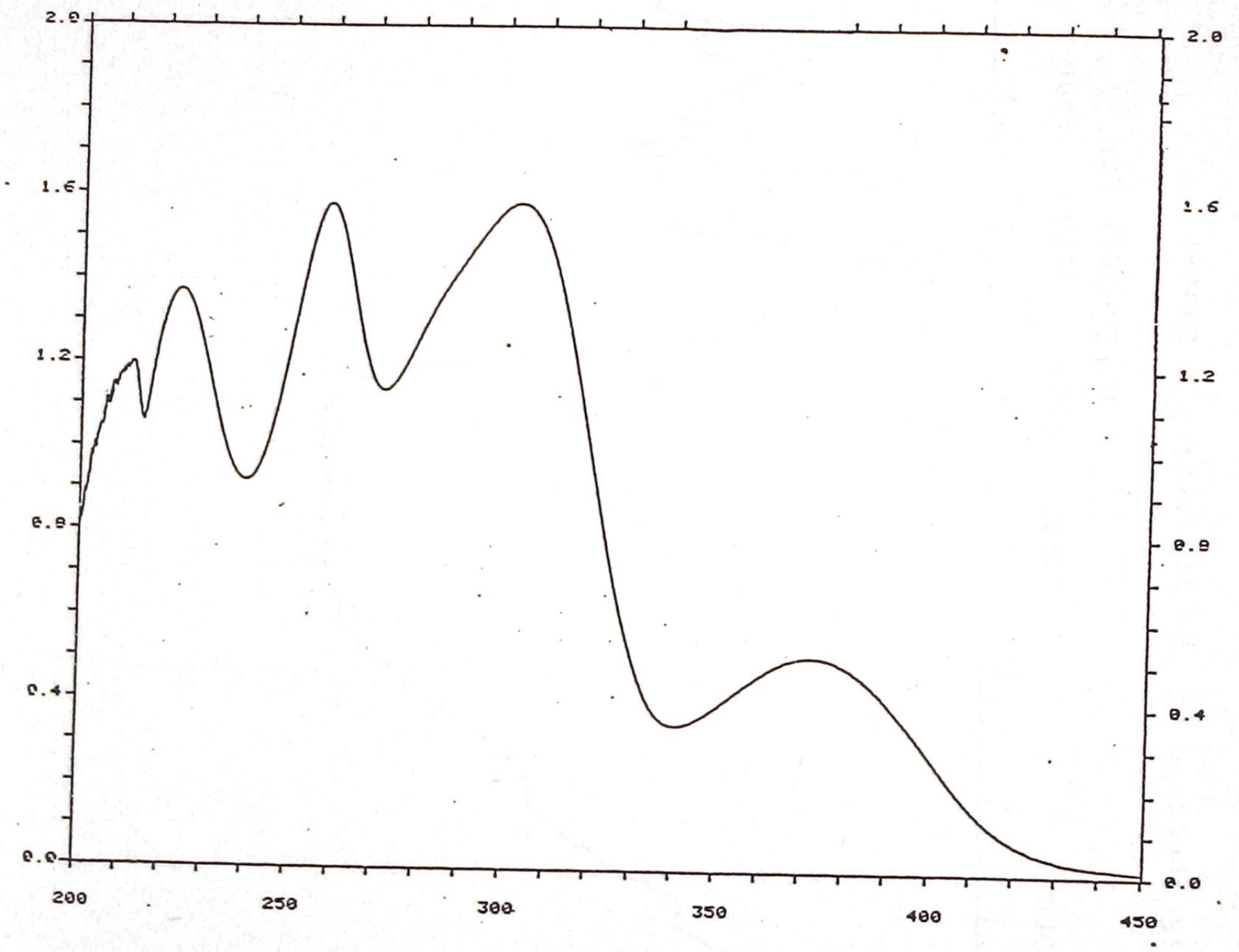

Fig. 2.2 UV Spectrum of MTX in 0.1N NaOH

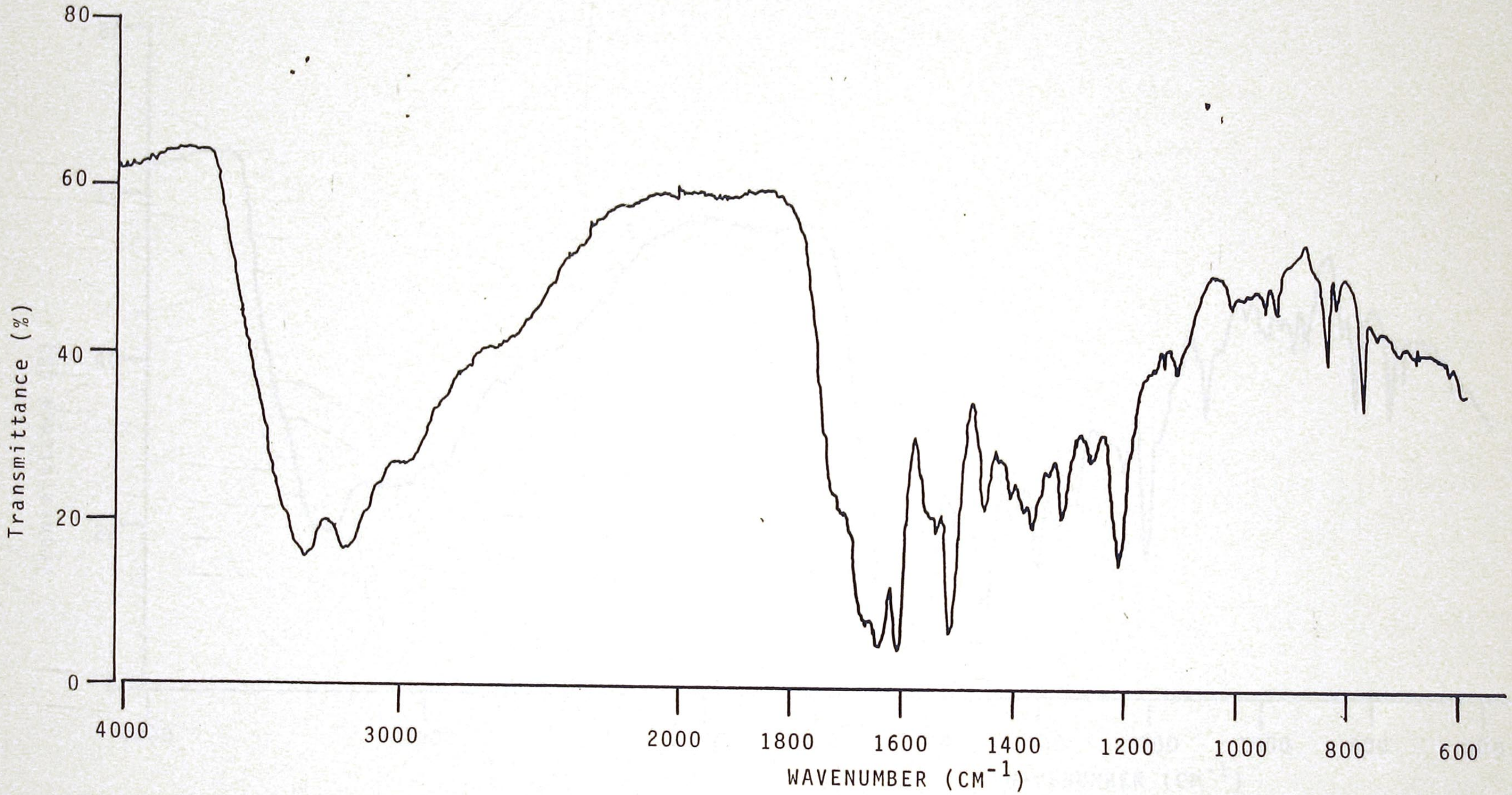

Fig. 2.3a IR Spectrum of the original MTX powder

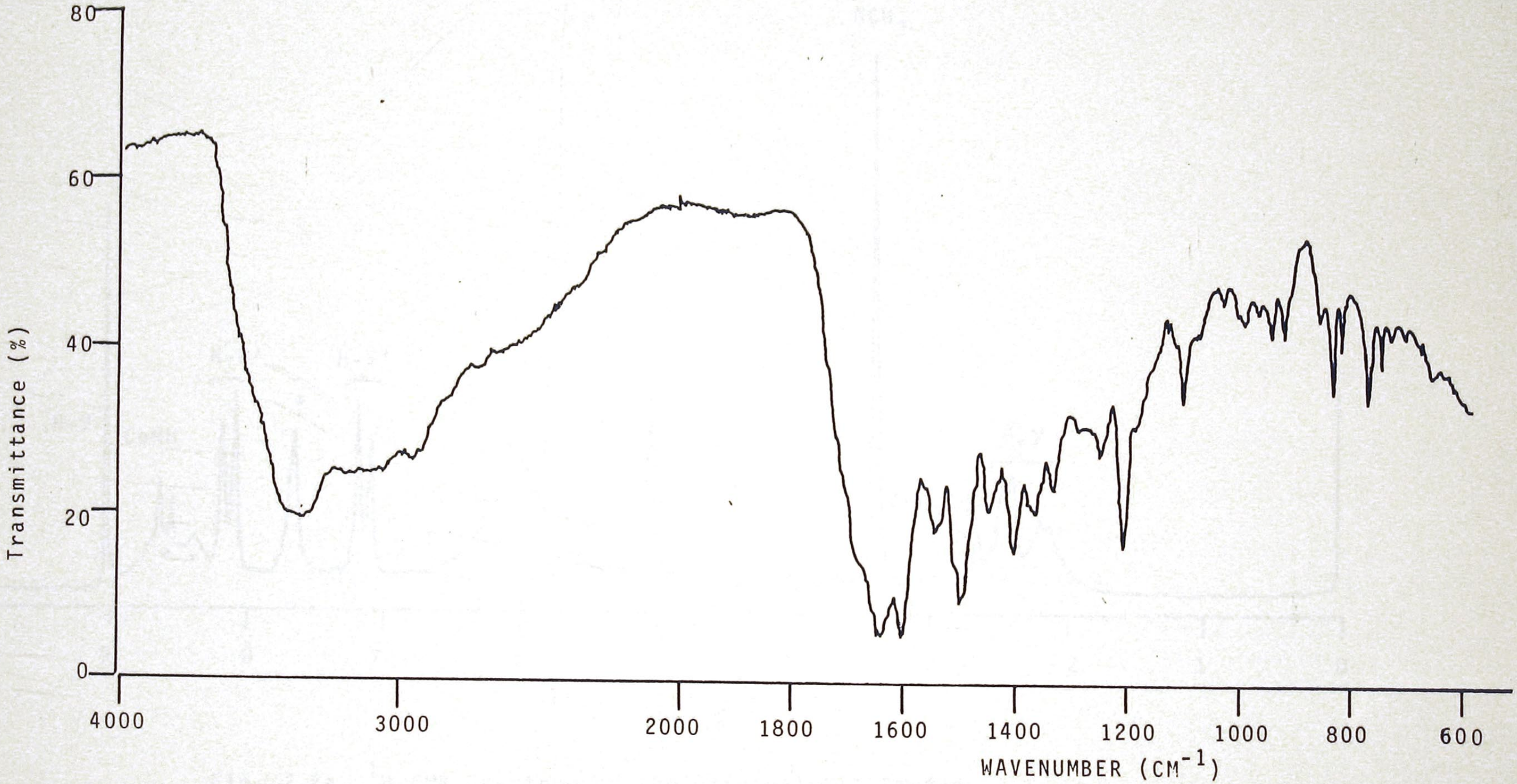

Fig. 2.3b IR Spectrum of the Tetragonal MTX Crystals

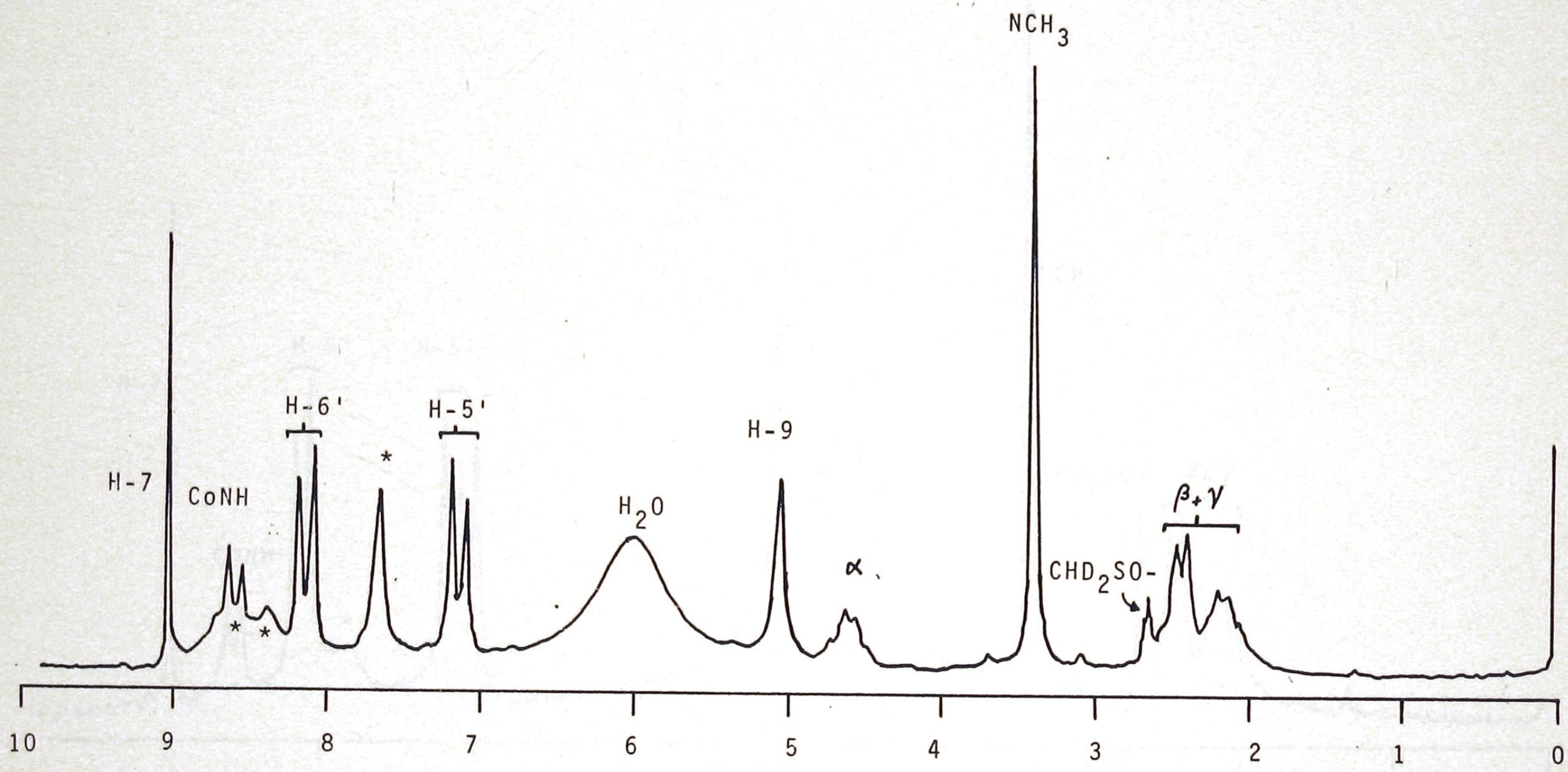

Fig. 2.4a ^{1}H NMR Spectrum of the Original MTX Powder
(*exchangeable proton(s))

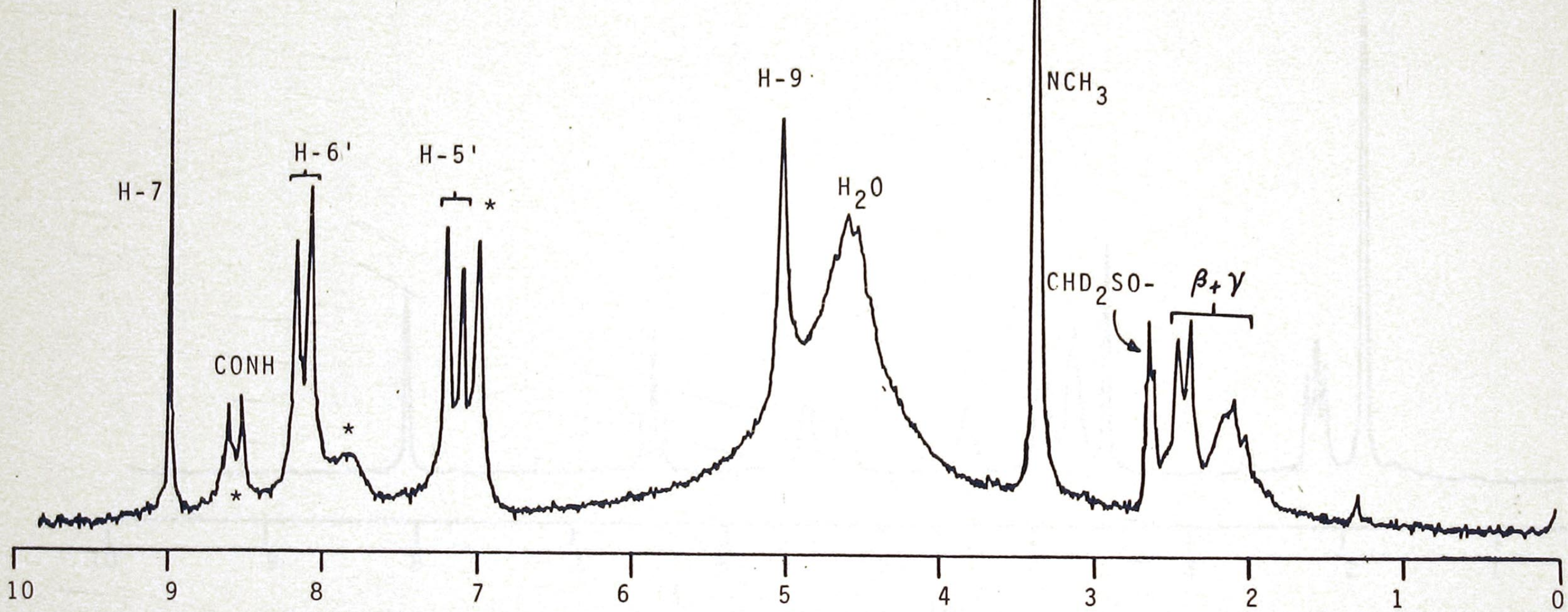

Fig. 2.4b ^1H NMR Spectrum of the Tetragonal MTX Crystals
(*exchangeable proton(s))

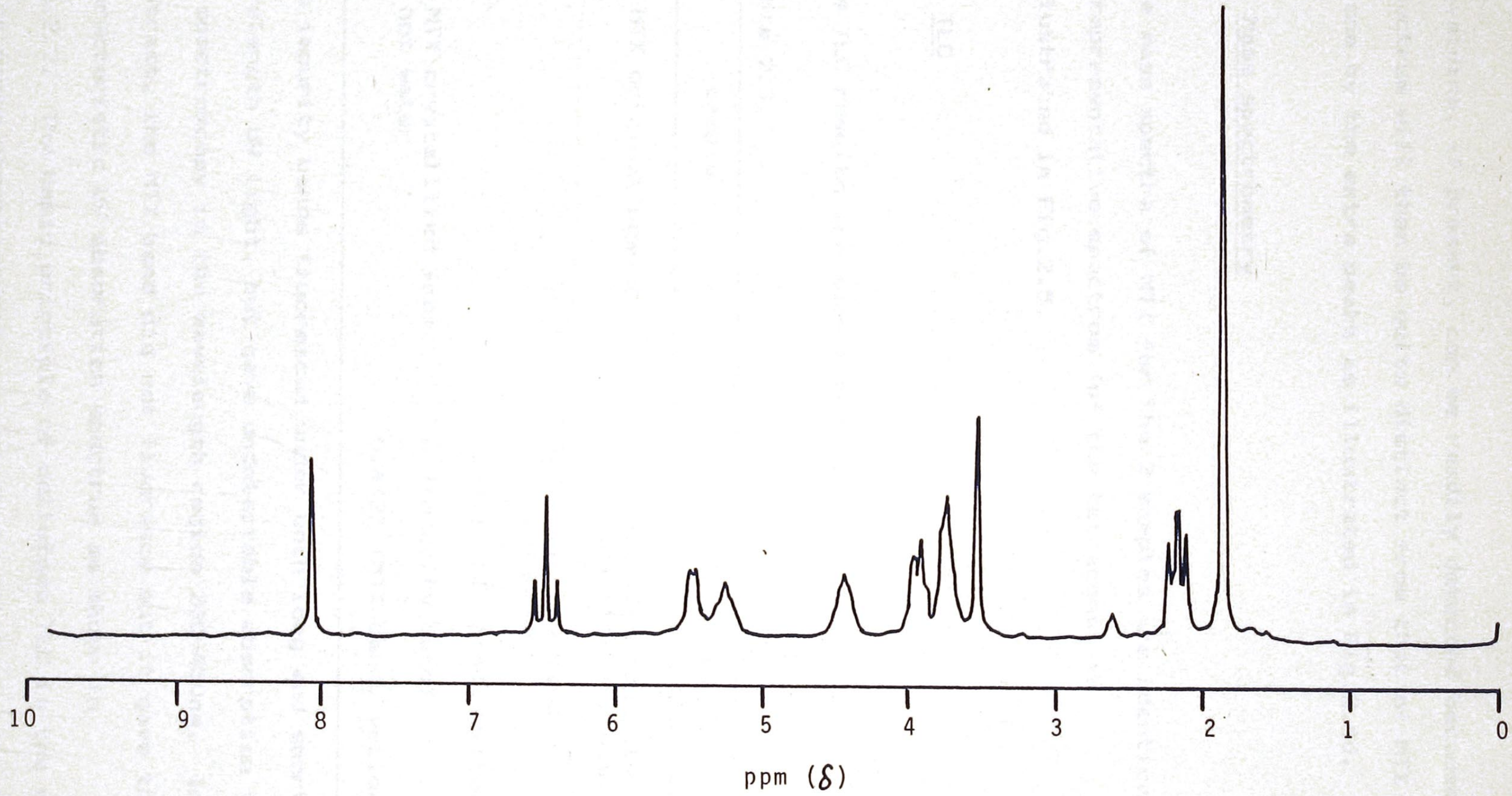

Fig. 2.4c ^{1}H NMR Spectrum of Thymidine

Thymidine, if present, can be readily detected because the spectrum will then be quite distinct from that of MTX alone by the extra peaks as illustrated in Fig.2.4d.

e) Mass spectrometry

The mass spectra of MTX for the 2 samples are identical. A representative spectrum (of the tetragons) is illustrated in Fig.2.5.

f) TLC

The TLC results are summarized in Table 2.3.

Table 2.3.

sample	Rf Value
MTX original powder	0 (colourless impurity band at the starting position)
	0.2 (impurity band, colourless)
	0.4(4) (MTX band, yellowish)
MTX crystallized from hot water	0 (impurity band)
	0.4(2) (MTX band, yellowish)

The impurity bands fluoresced under both long and short wavelength UV light, but gave undetectable absorption in UV spectroscopy in the wavelength region 200-450nm. In contrast, the MTX band did not fluoresce but it gave the characteristic UV absorption spectrum as shown in Fig.2.2. The basic principle of cellulose TLC is the same as of paper chromatography, namely by partitioning of the

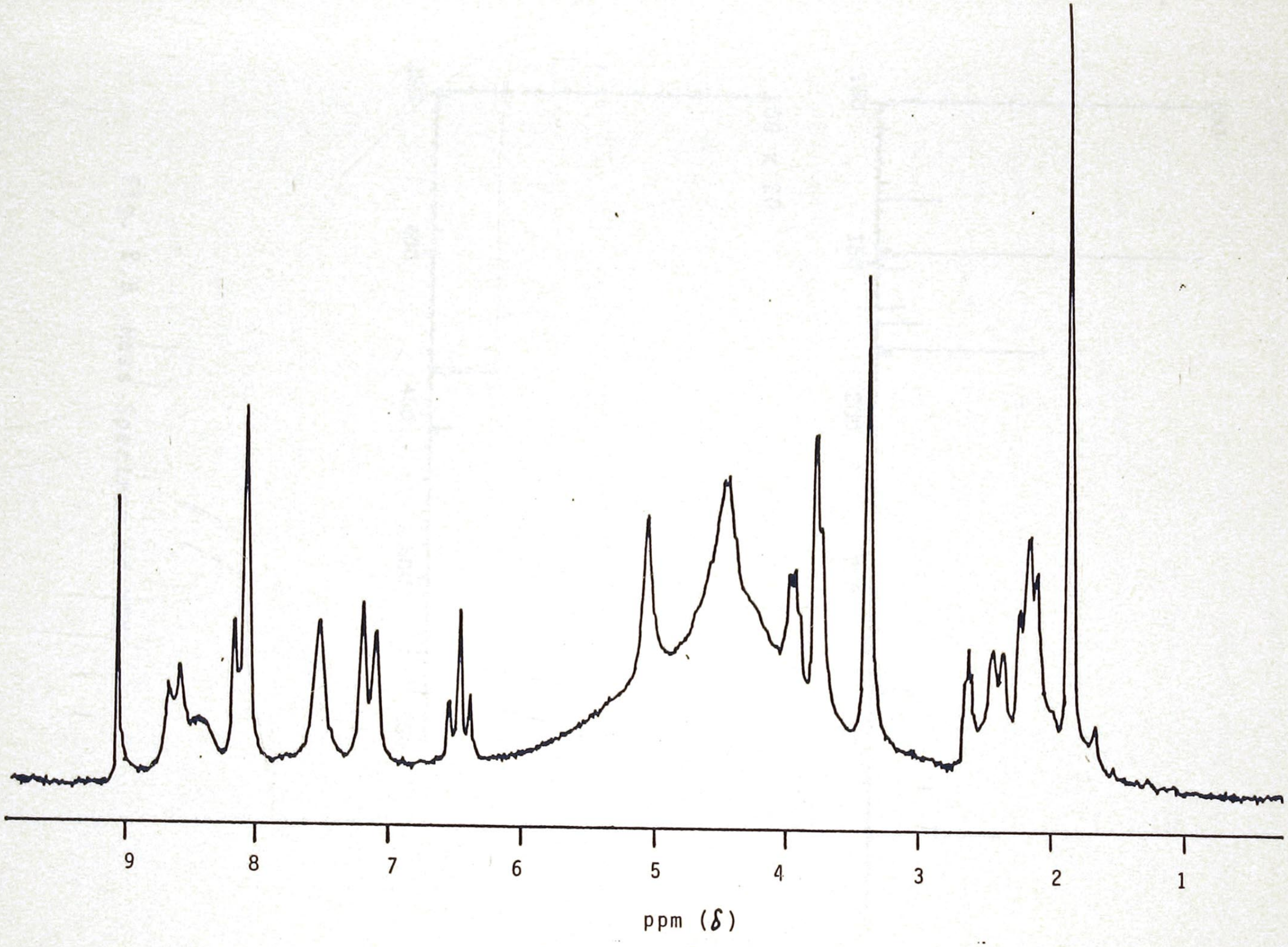

Fig. 2.4d ^{1}H NMR Spectrum of MTX:Thymidine (approximate wt. ratio 10:1)

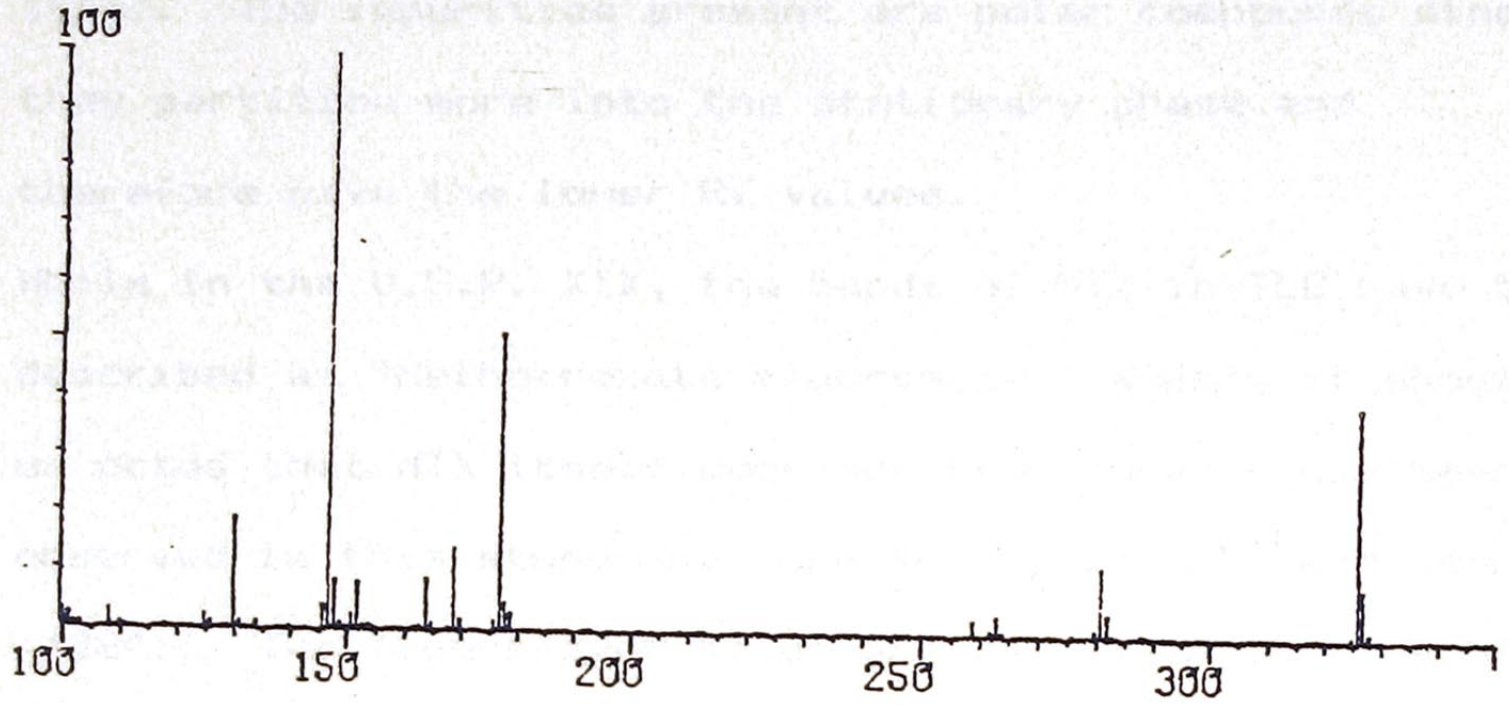

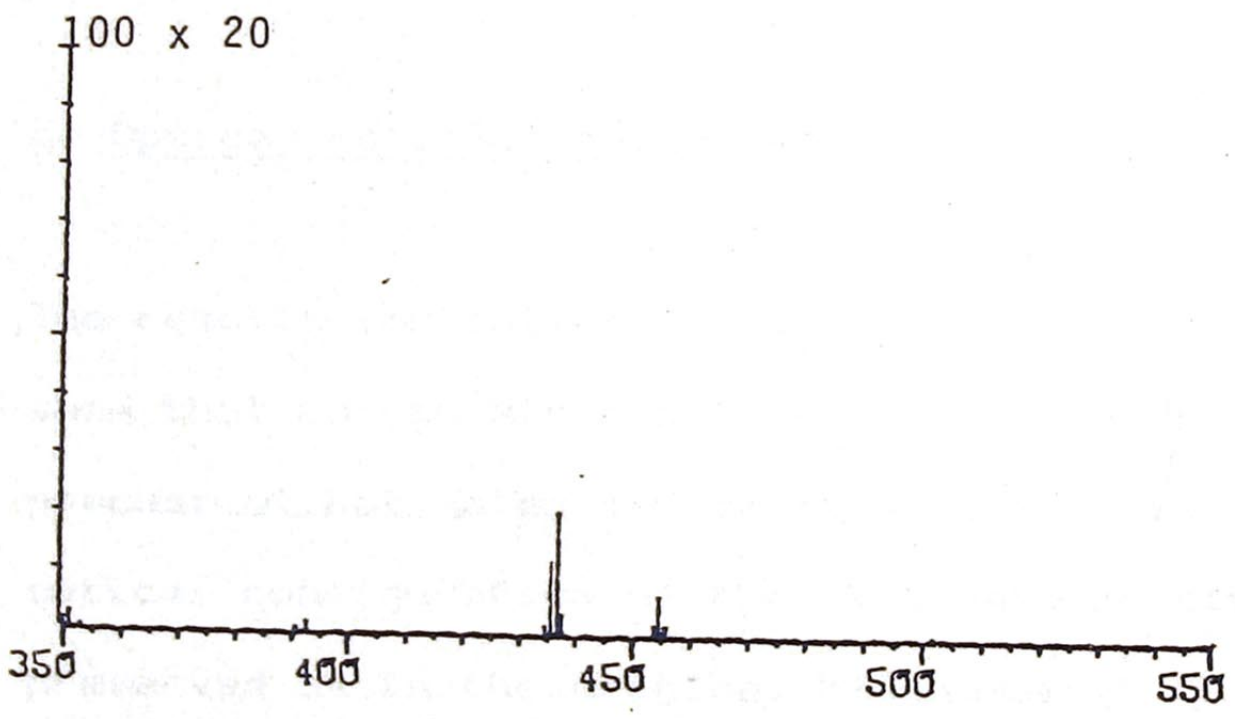

Fig. 2.5 Mass Spectrum of MTX

solutes to be separated in the mobile phase (developing solvents) and the stationary phase; the latter is the polar hydration shell of the cellulose fibres (Randerath, 1966). The impurities present are polar compounds since they partition more into the stationary phase and therefore have the lower Rf values.

While in the U.S.P. XIX, the bands of MTX in TLC have been described as "Methotrexate fluorescent bands", it should be noted that MTX itself does not fluoresce as has been observed in this study and reported by Zaharko and Dedrick (1984). The fluorescent bands are the impurities of MTX, most likely the pteridine derivatives.

g) Optical rotation measurement

The results for optical rotation measurement in Table 2.4 show that no racemic modification formed during the process of hot water crystallization. Thus the same optical configuration of the glutamate moiety was preserved as in the original MTX powder.

Table 2.4.

sample	optical rotation $[\alpha]_D^{19}$
MTX original powder	18±2
crystallized from H_2O	19±3
Literature (Chamberlin et al)	21.4±0.6 at 21^{0}C

h) X-ray powder diffraction

The diffraction patterns for the 2 samples are very different, as illustrated in Fig.2.6a and b. The broad peaks of the pattern of the original powder also revealed a low degree of crystallinity.

iii) Discussion

At first it was thought that the crystals we obtained were a complex of MTX-thymidine as suggested by the IR and X-ray powder diffraction results which are distinct from that of the original MTX powder. However, the UV spectrum is identical to that of MTX alone, suggesting that the crystal is MTX only and not a complex. This was confirmed by the results of ^{1}H NMR and mass spectrometry which showed the characteristic spectra of MTX without the presence of any extra peaks due to thymidine. TLC showed one less impurity in the MTX crystals. Optical rotation measurement revealed that the crystals retain the same optical configuration of the glutamate moiety as the original powder. Therefore, it is clear that the distinct IR spectrum and X-ray diffraction pattern are the result of different polymorphs. The M.P. and solubility measurements [(Sec.2.5.3 ii) d)] further suggested that the crystal is a lower energy form than the original powder.

The explanation for the success of formation of MTX crystals in thymidine solution is still not known. At the beginning, it was thought that the effects of thymidine might be possibly (i) due to the sugar moiety (ribose)

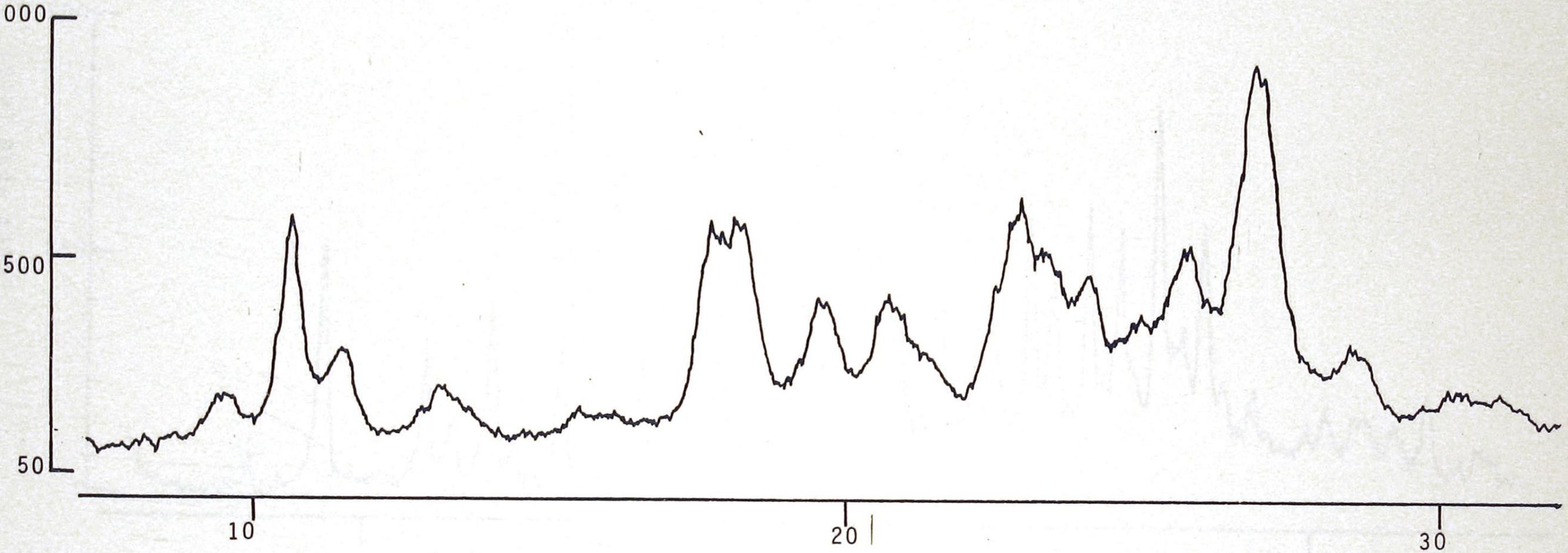

Fig. 2.6a X-Ray Powder Diffraction Pattern of the Original MTX Powder

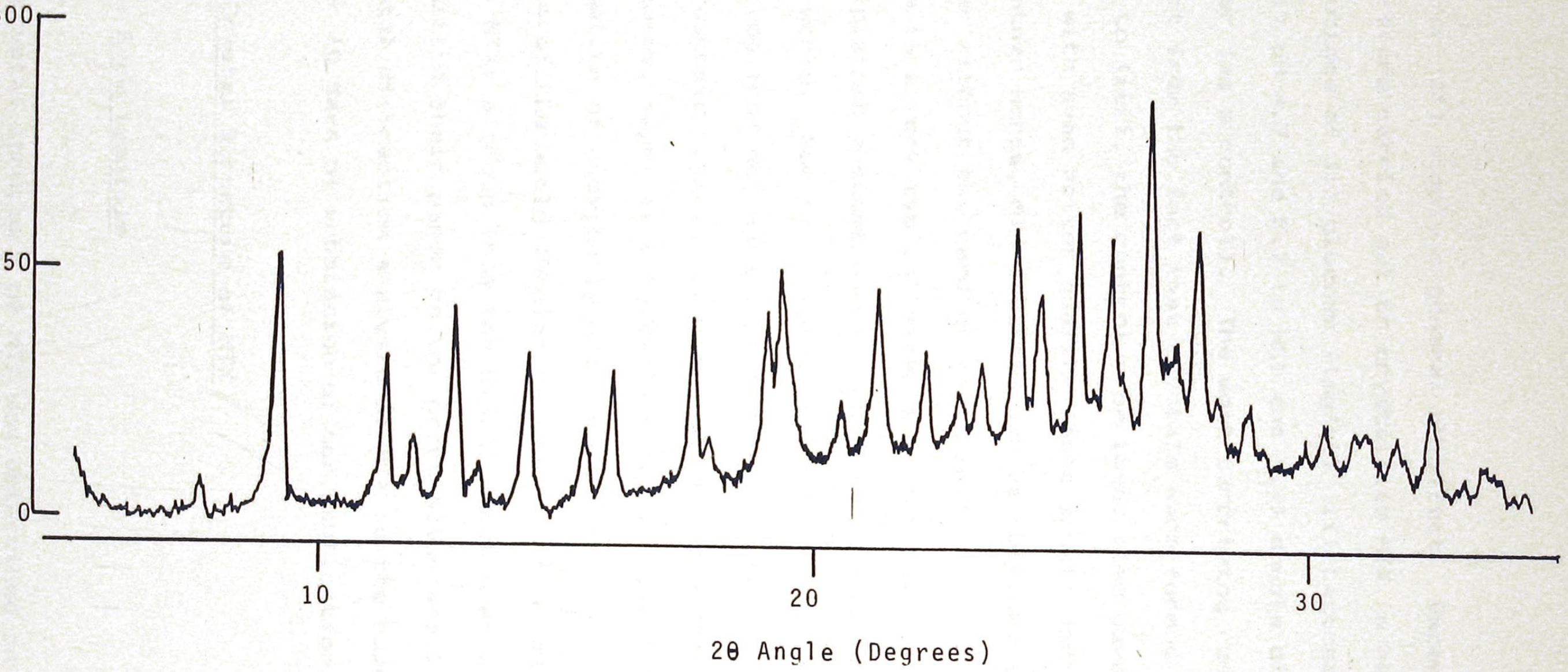

Fig. 2.6b X-Ray Powder Diffraction Pattern of the Tetragonal MTX Crystals

and/or (ii) simply a general pH effect. Experiments were therefore carried out to crystallize MTX in heated aqueous solutions of (i) glucose (1mg/ml) (ii) Lactose (1mg/ml) (iii) pH 4.7 and 5.7 in HCl and (iv) double distilled water (as a control). The most surprising result was, apart from the fact that crystals were formed in solution (i) to (iii), the control experiment also gave crystals of MTX with even better quality (more single and less twins). In other words, MTX crystals can be obtained simply from water without the need of thymidine!

This is a very typical example of the well-known but unexplained phenomenon of sudden appearance of crystals in the world. Now MTX crystals can be obtained simply by cooling from hot water, presumably due to the presence of microscopic nuclei. However, other explanations have been proposed, especially to explain nearly simultaneous formation of previously unobtainable crystals in distant parts of the world (Sheldrake,1981). This has happened with MTX: a group from the U.S.A. (Sutton et al, 1986) submitted their paper on the preparation and X-ray single crystal diffraction analysis of MTX to the same journal after 10 days of submission of our publication.

2.4 Crystal Structure of MTX

2.4.1 Experimentals

The crystal structure of MTX was determined on a X-ray diffractometer (Enraf-Nonius CAD4-F). This part of the

work was carried out by Dr. Trevor Hambley from the School of Chemistry, University of Sydney (Hambley et al., 1986). The structure was solved by direct methods, extended by subsequent difference Fourier synthesis, and refined by full-matrix least-squares methods. Initially a data set was collected from a crystal using MoKα radiation. This data set was of limited extent because of a small crystal size (0.20 x 0.10 x0.10 mm). Subsequently, when a larger crystal (0.30 x 0.15 x0.10) was obtained, a more complete data set was collected, using CuKα radiation. Data collection details are listed in Appendix 3. The crystal used in the study was obtained from a 1% Tween solution during the work on the habit modification using additives (Sec.2.5.1 i) b). Same series of analysis as described in Sec. 2.3.3 i) (except the optical rotation) have been done to confirm the identity of these crystals, for which identical set of result was found as before (Sec.2.3.3 ii).

2.4.2 Results and Discussion

Crystal Structure of MTX

The crystal was found to be tetragonal, space group $P4_12_12$ with unit cell dimensions a= b= 10.355(3), c= 45.712 (5)A^0. In the structure, the MTX molecules pack in such a way that alternating hydrophobic and hydrophilic layers lying roughly perpendicular to the c-axis result (Fig.2.7). The hydrophobic layers accomodate the

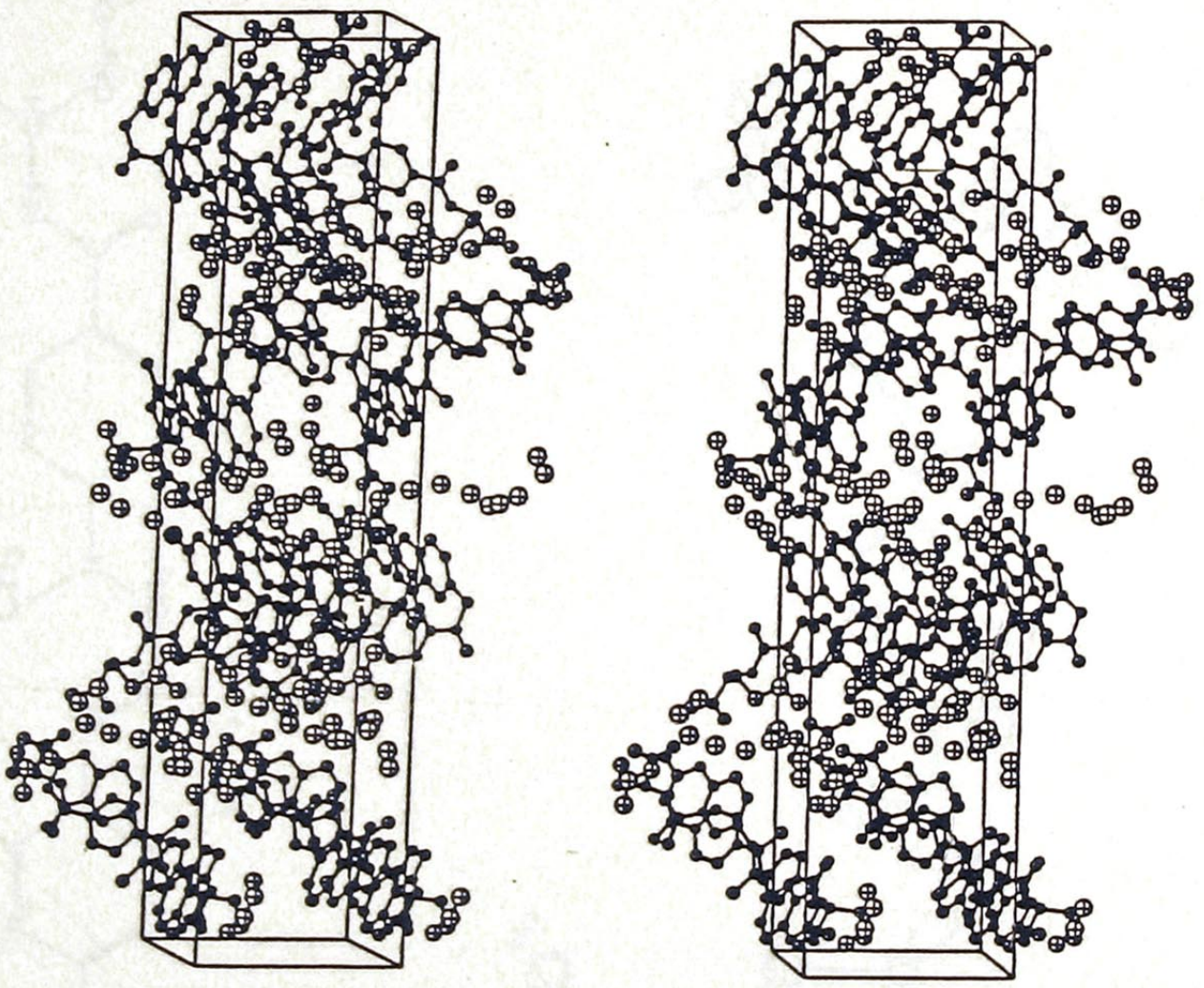

Fig. 2.7 Stereoview of the Unit Cell of MTX

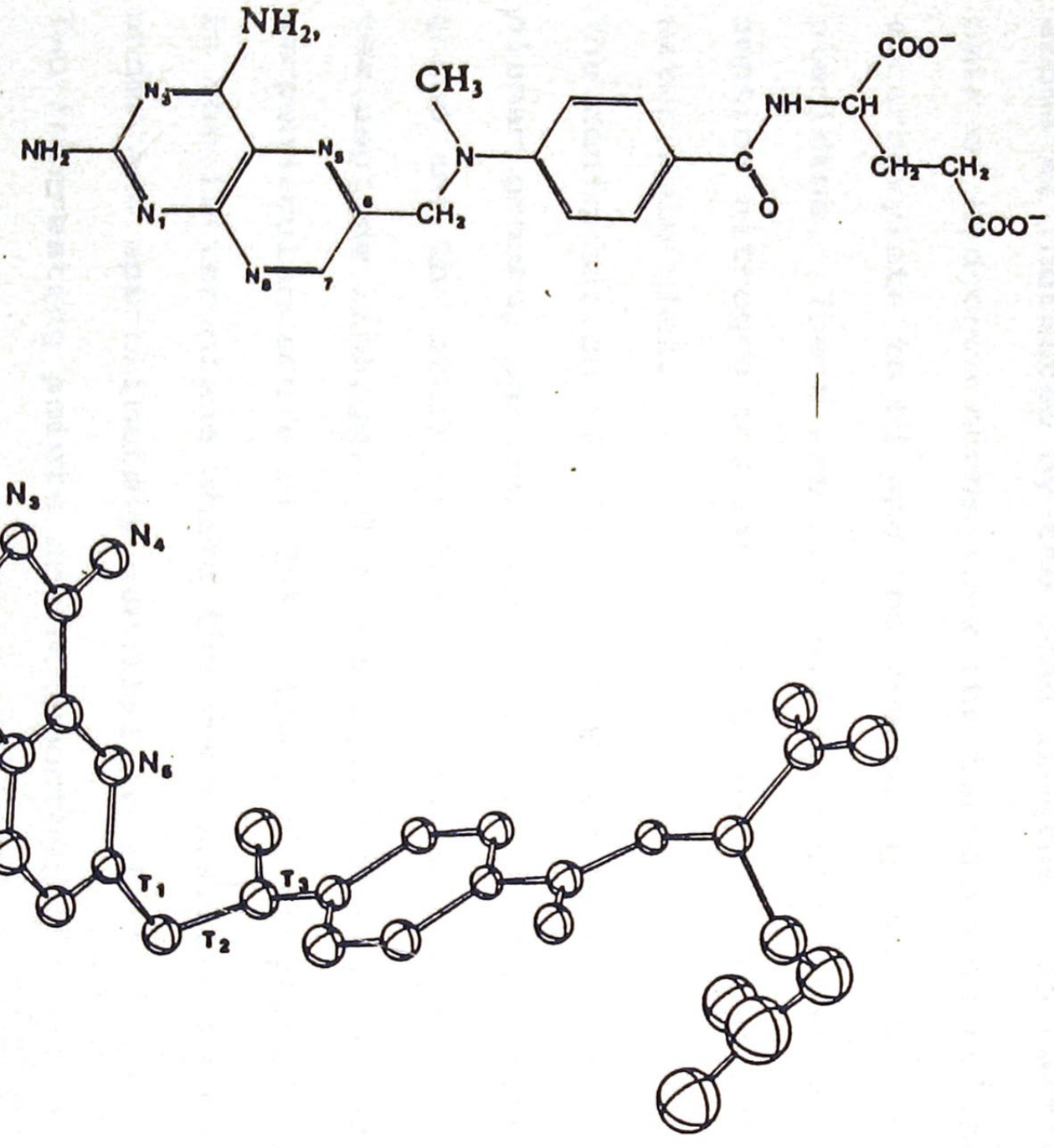

Fig. 2.8 Molecular Structure and Conformation of MTX Molecule in the crystal

pteridine and benzoyl groups stacked so that they overlay benzoyl and pteridine groups, respectively, of adjacent molecules apparently through π-π interactions. The hydrophilic layers accomodate the amine groups of the pteridine, the carboxylate groups of the glutamate and the water molecules. The adjacent layers are linked by a number of very strong hydrogen bonds between the amine hydrogen atoms of the pteridine and carboxylate oxygen atoms as indicated by the bond lengths. In particular a pair of hydrogen bonds link the two oxygens of the α-carboxylate to N1 and the 2-amino group (N2) of the pteridine. There are also hydrogen bonds between the peptide nitrogen and carboxylate oxygen atoms and the water molecules.

The conformation of MTX (Fig.2.8) is best described as 2 planar groups; one made up of the 2, 4-diaminopteridine group and the other of the p-methylamino benzoyl group and the peptide linkage. The 2 planes meet at the nearly perpendicular angle of 84^0. The α-carboxylate lies nearly in the latter plane while the γ-carboxylate is folded back under and approximately parallel to it.

Two interesting points are noteworthy:

1.) Pteridine nitrogen N1 is protonated.

Protonation of N1, which does not occur for dihydrofolate, appears to be a major factor in the binding of methotrexate to the enzyme dihydrofolate reductase (DHFR).

2.) The conformation for MTX in the crystal structure is similar to that suggested for bound dihydrofolate that is, with the pteridine ring flipped over (Bolin, 1982).

Although this conformation of the pteridine is different approximately 180^0 from that observed for MTX bound to DHFR, molecular mechanics calculations showed that 2 orientations of the pteridine each correspond to a potential energy minimum (Dr.Trevor Hambley, School of Chemistry, University of Sydney - private communication). Thus, previous suggestions that bound MTX (Spark et al, 1982; Dauber et al, 1982) is highly strained are not supported by the present study. It may be then that a favourable conformation is an important determinant of binding strength because very little energy is required to distort the bound substrate.

2.5 Habit Modifications of MTX Crystals

After single crystals of MTX were obtained, habit modification was attempted under various crystallization conditions as described in Sec.2.1, Introduction. Crystallization was carried out by slow cooling of 1ml of a hot supersaturated solution of MTX (~2mg/1ml) in the crystallizing medium as described in Sec.2.3.1, or otherwise stated. The resulting crystal habits were then observed using a zoom stereomicroscope (Kyowa Trinocular, Model SDZ-Tr-P). Photographs were taken by the camera attachment (Olympus PM-10M) of the microscope.

2.5.1 Materials and Methods

i) Chemical effects

a) Solvents

In preliminary experiments, MTX was found insoluble in non-polar solvents. Therefore only polar solvents were used. They were chosen on the basis of their similarities in the values of dipole moment and dielectric constant to water as listed below:

Solvent	ε	μ(debyes)	B.P.
water	87.7	1.8	100
methanol	32.6	1.7	65
ethanol	24.5	1.66	78.5
DMSO	45	3.96	189
DMF	-	3.82	153
acetone	20.7	2.88	56
acetonitrile	37.5	3.82	81.6
glycerol	42.5	2.76	290
propylene glycol	32.0	2.25	188

Mixtures of water and polar solvents such as DMSO, DMF, glycerol and methanol were also used. The volume of solvents was increased to 10 ml when dissolution was difficult. The hot solutions of MTX were allowed to cool to room temperature for crystallization.

b) Surfactants

Cationic, anionic and non-ionic surfactants were all used as listed in the following table. According to their molecular weight and critical micelle concentration (cmc), a series of surfactant solutions of different dilutions (10^{-5} - 2.5 g/l) were prepared in which crystallization of MTX was carried out.

Surfactant	mol. wt.	cmc(g/l)
Cetrimide	364	1.06
Cetylpyridinium chloride (CPC)	340	0.17
Dodecylpyridinium chloride (DPC)	284	0.80-8.26
Sodium lauryl sulfate (SLS)	288	2.36
Tween 80	1240	0.014

c) 'Tailor-made' additives

Additives with chemical structure similar to MTX were used (Fig.2.9). They included folic acid (Hopkin and Williams Ltd., Essex, England), 1-deaza-7, 8- dihydropteridines (NSC 181928 and 350386, supplied by the Pharmaceutical Chemistry Division Southern Research Institute, Alabama), trimetrexate isethionic acid (supplied by the Pharmaceutical Research Division, Warner-Lambert Company, Michigan) and methotrexate ethylacetate (synthesed by acidic esterification of MTX in ethanol). From a series of solutions containing $2.0-2\times10^{-4}$ g/L additives, MTX was allowed to crystallize as described in Sec.2.3.1. The aqueous solubility of the additive NSC 181928 is very low, therefore in addition to its saturated aqueous solution, different dilutions in water were also prepared from a DMF solution (1mg/ml).

d) Dyes

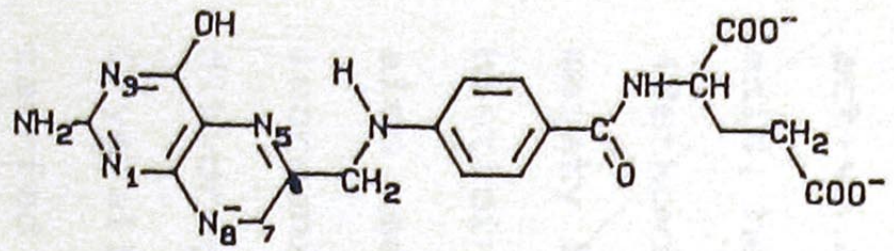

Dihydrofolate: C_7 and N_8 positions hydrogenated

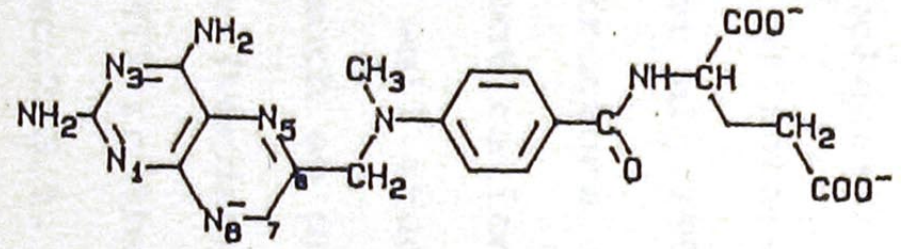

Methotrexate (MTX)

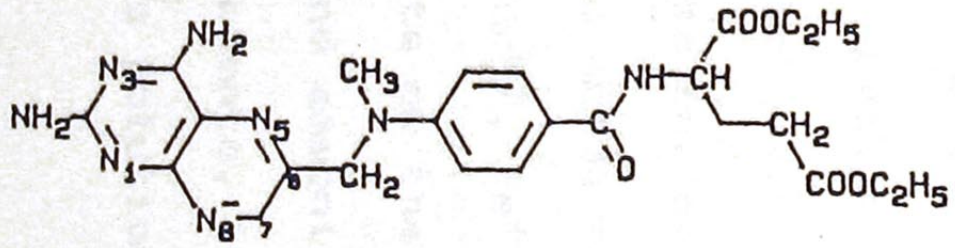

MTX - ethyl acetate

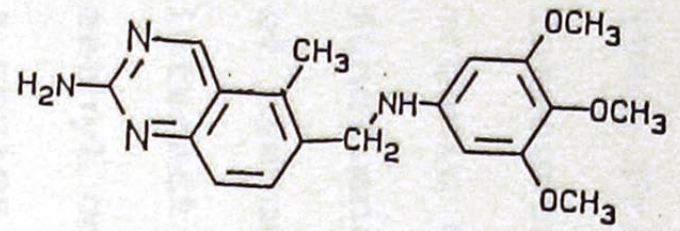

Trimétrexate

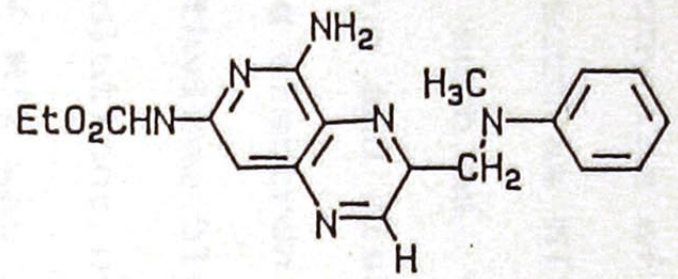

NSC 181928

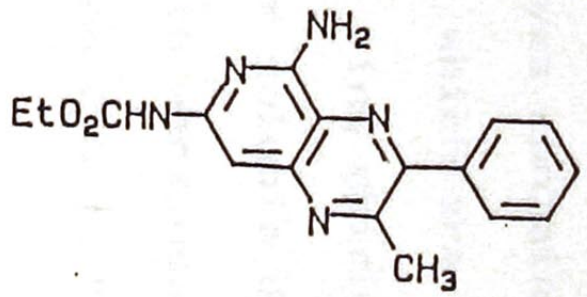

NSC 350386

Fig. 2.9 Molecular structures of the 'tailor-made' additives

It is well-known that dyes have a great effect on the habits of many inorganic crystals by adsorption (Frondel, 1940; France, 1944; Buckley, 1952). It is therefore interesting to study the effects of dyes on the habits of organic crystals such as MTX as well. Dyes contain functional groups such as -OH and $-SO_3H$ which are capable of hydrogen bonding and also the benzene ring which may interact via the π electron cloud. Water soluble dyes methyl orange, methylene blue and amaranth were used. In a series of dye solutions of concentration $2.0-10^{-4}$ g/L, crystallization of MTX was done as in Sec.2.3.1.

e) Other additives

Other additives (see below) were chosen because they are capable of hydrogen bonding (e.g. urea), forming inclusion compounds [e.g. β-cyclodextrin (β-CD)], or being optically active and bearing molecular structure similar to glutamic acid, hence capable of interacting selectively (Berkovitch-Yellin et al, 1982) with the chiral glutamate moiety in the MTX structure (e.g. amino acids such as histidine). Trivalent cations (Al^{+3}, Cr^{+3}, Fe^{+3}) were also used for their well studied effects on the habits of inorganic crystals such as potassium and ammonium dihydrogen phosphate (Verdaguer and Clemente, 1986). Crystallization of MTX in the additives solutions was carried out as in Sec.2.3.1.

ii) Physical effects

a) Supersaturation

MTX solutions with different levels of supersaturation were prepared as follows:

2 mg of MTX was dissolved in 1ml hot water at ~90^{0}C (2mg/ml is the approximate saturation solubility of MTX in hot water). 0.5, 0.25, 0.15 and 0.1ml of the saturated MTX solution was taken and diluted with hot water to 1ml. The table below shows the concentration of the resulting solutions:

Vol. of saturated MTX solution (ml)	Resulting concentration of MTX (mg/ml)
0.5	1
0.25	0.5
0.15	0.3
0.1	0.2

The solutions were allowed to cool to room temperature for crystallization.

b) Rate of cooling

Hot saturated MTX solution was prepared by dissolving 2mg MTX in 1ml water in a 15ml specimen tube at 90^{0}C. Instead of slow cooling to room temperature, a rapid cooling rate was achieved by an ice-bath. Nuclei formed immediately and were allowed to grow in the bath for several hours.

c) Agitation

Hot saturated solution of MTX was prepared as in b). After being stirred by a magnetic bar for various length

of time (<1/2 ~ 3 mins), the suspension was allowed to stand undisturbed for crystallization.

d) Temperature

Crystallization of MTX at elevated temperature was done by keeping specimen tubes containing 5ml hot saturated solution [as prepared in b)] in an oil bath at 50^{0}C and 70^{0}C. The specimen tubes were sealed to lower evaporation of the solutions.

e) Substrate growth

Substrate surface induced growth of MTX was attempted by crystallization (slow cooling of a hot saturated solution to room temperature) in the presence of various substrates: cellophane sheet, dialysis membrane, sintered glass, porcelain and paraffin wax.

f) Gel-growth

Growth of MTX crystals in gelatin was done by transferring 1ml of saturated aqueous MTX solution [as prepared in b)] onto the top of a layer of congealed gelatin in a specimen tube and allowed to crystallize spontaneously.

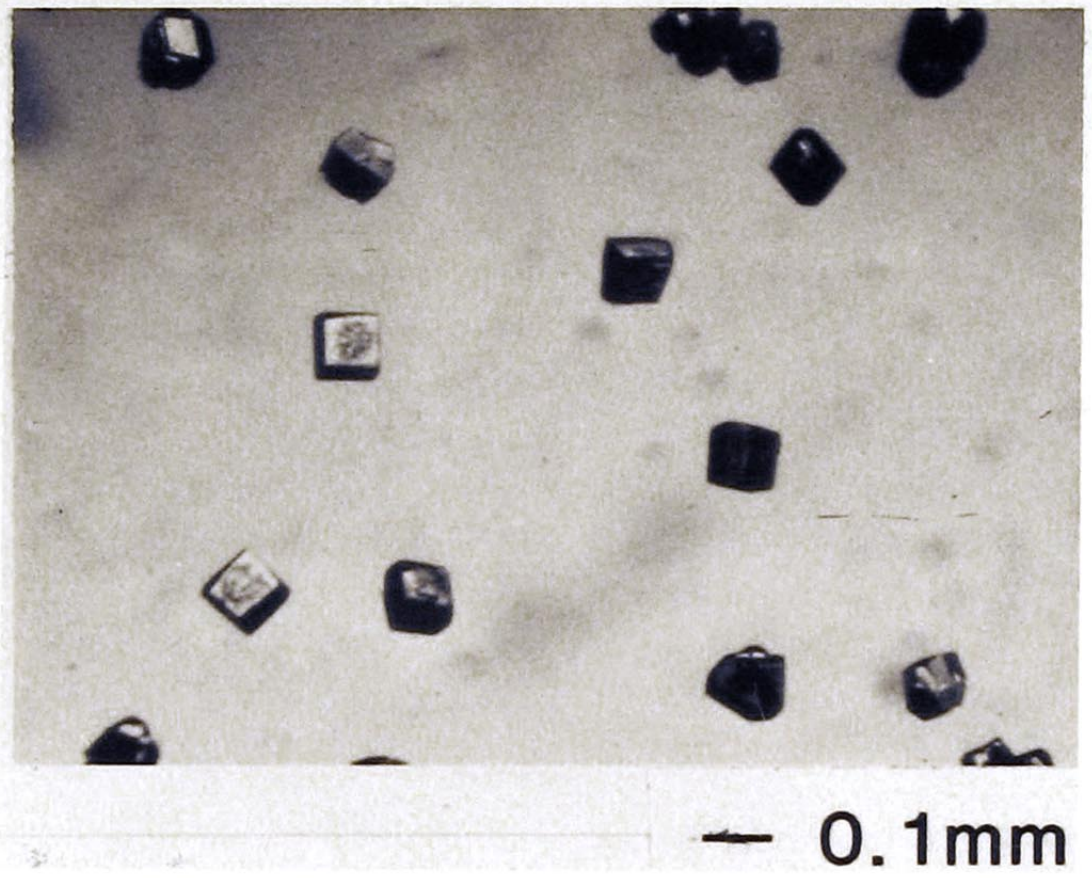

Fig. 2.1c Micrograph of MTX tetragonal crystals

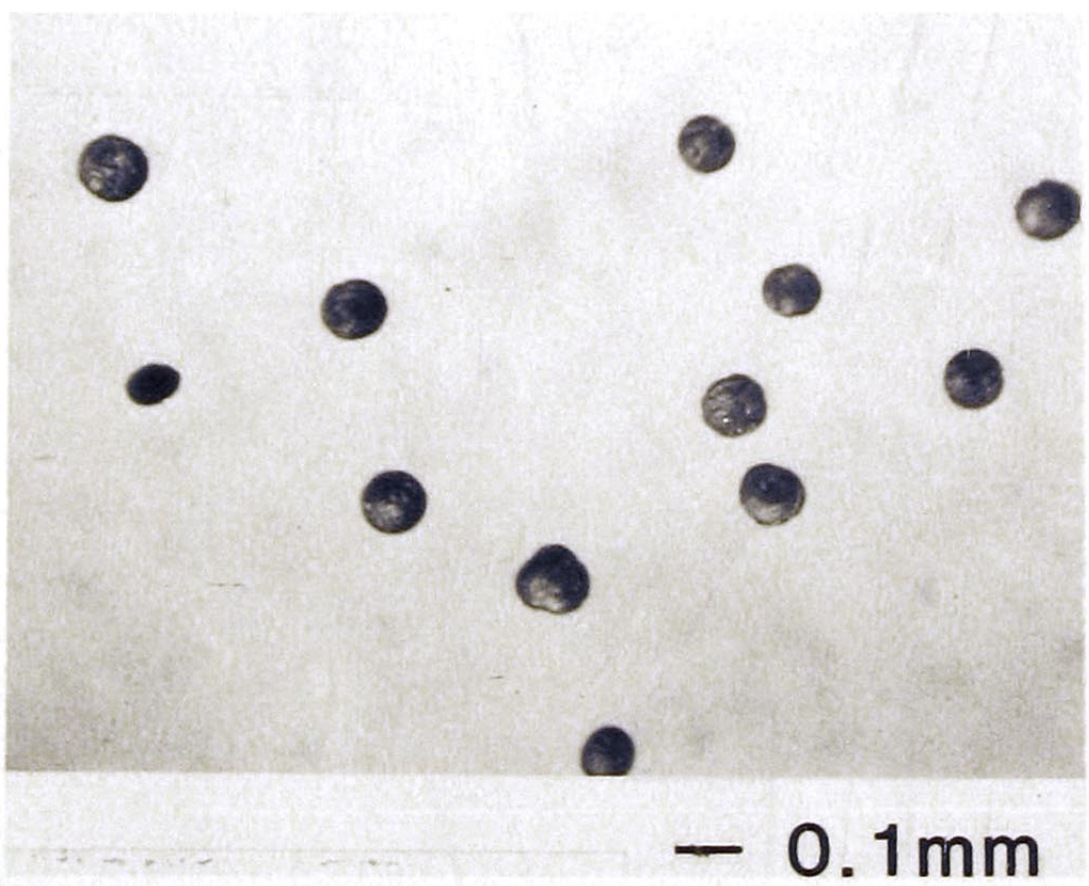

Fig. 2.1d Micrograph of MTX spheres

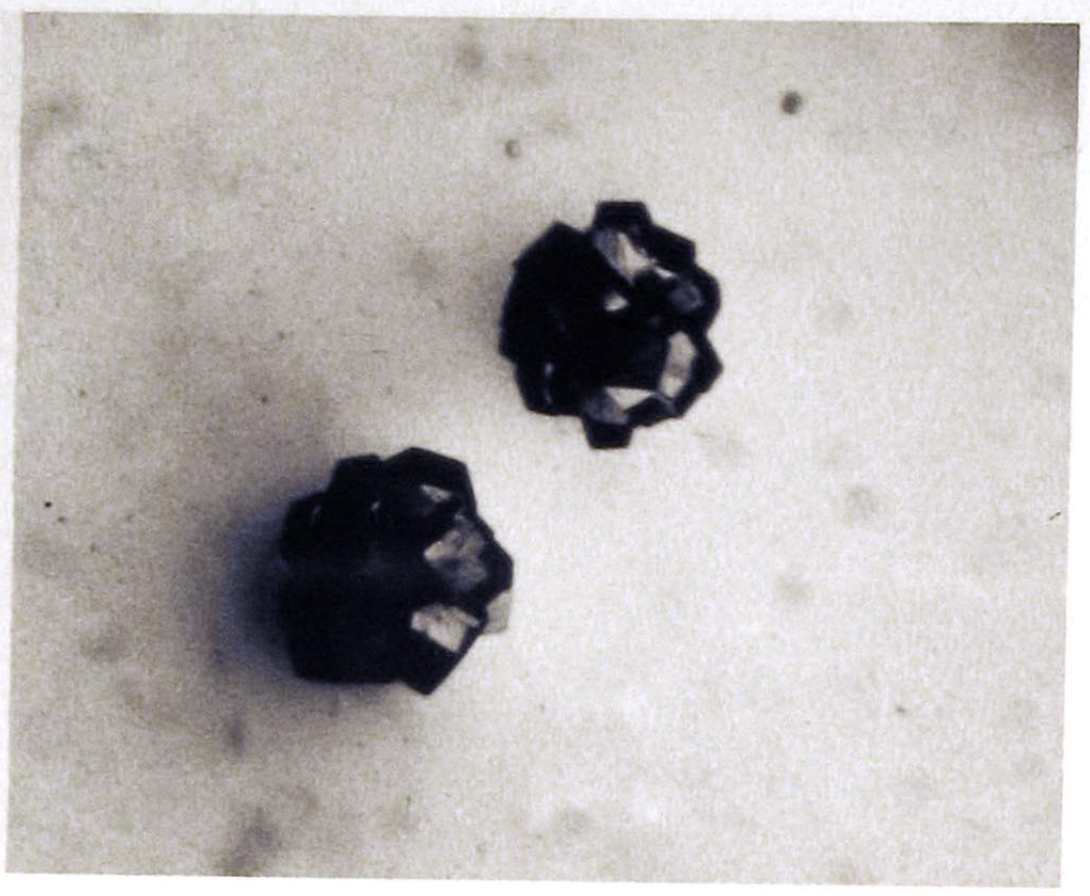

Fig. 2.1e Micrograph of MTX rosettes
(scale bar: 0.1mm)

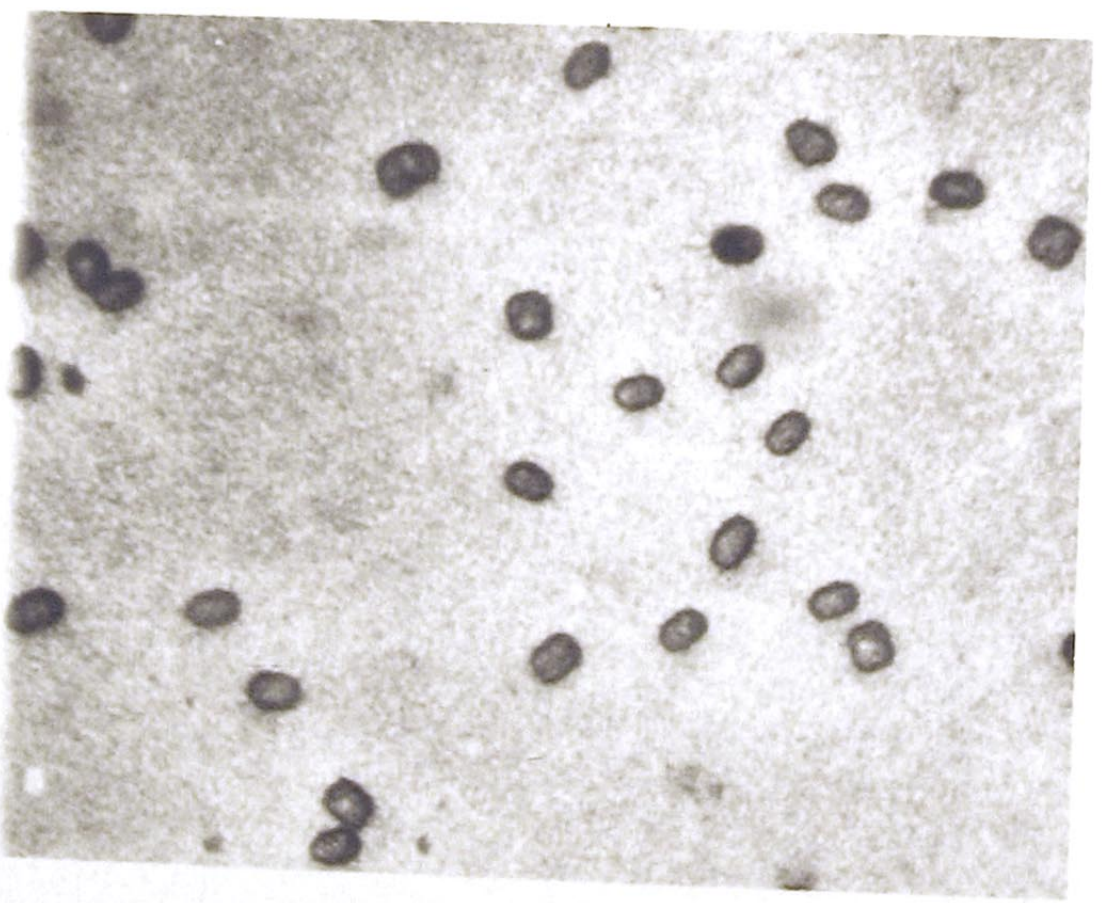

Fig. 2.1f Micrograph of MTX ellipses
(scale bar: 0.1mm)

Fig. 2.1g (next page) Concentration dependent rounding effect of MTX crystals by additives
Top: absence of additives
Middle: low concentration additives
Bottom: increased concentration of additives

Scale bars: 10 μm



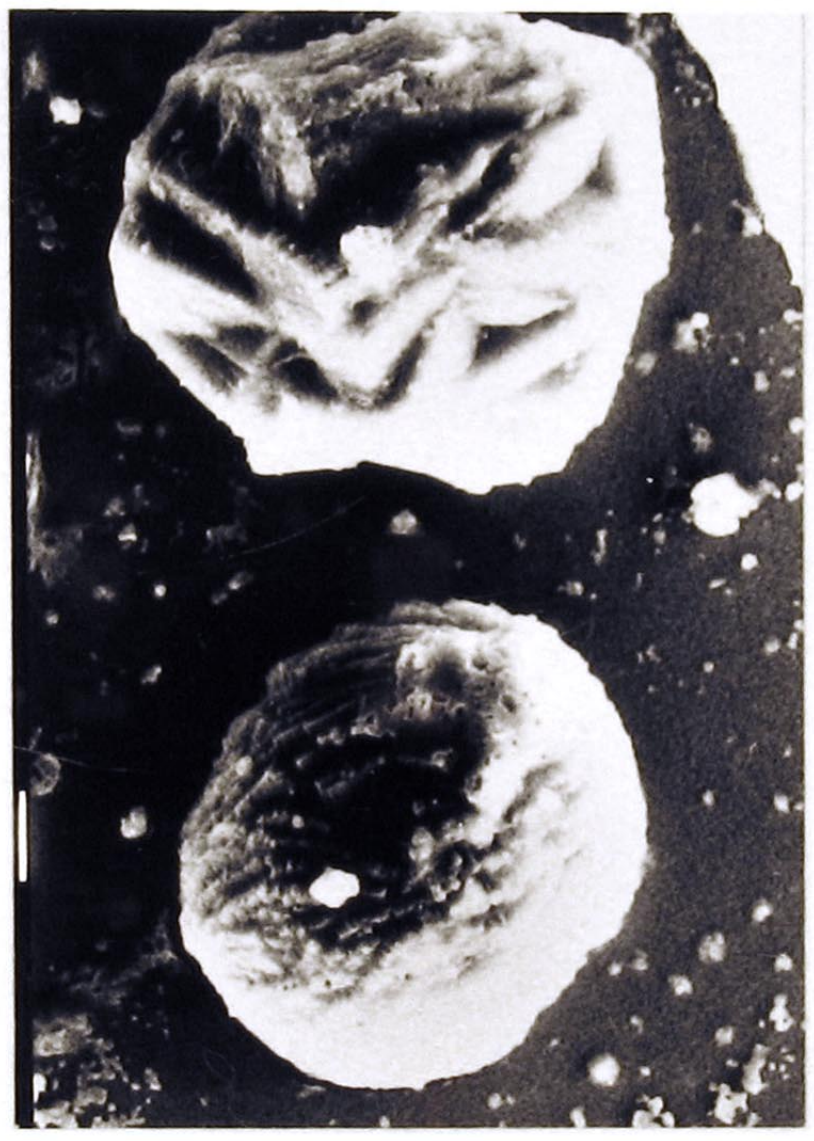

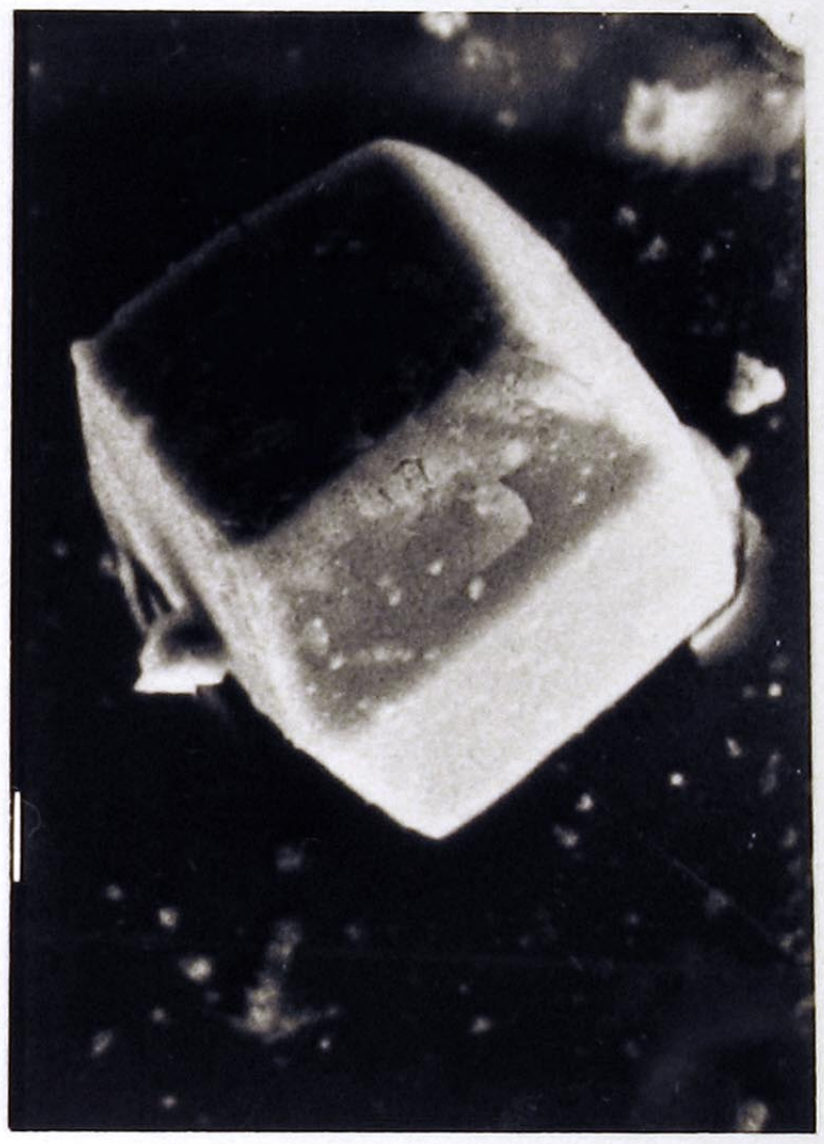

2.5.2 Results and Discussion

For all the following results, spheres (smooth and stepped respectively) refer to the spherical crystals of MTX as shown in Fig.2.1d and 2.1g (last picture), and Fig.2.1g (middle picture) respectively.

i) Chemical effects

a) Solvents

The effects of solvent on the crystal habits of MTX are shown in Table 2.5.

When polar solvents were used alone, no crystals of MTX were formed. In most cases, only anhedral particles could be obtained. Therefore, water appears to be an essential part in the formation of the crystals as the crystal structure of MTX contains water molecules as the solvent of crystallisation.

In solvent mixtures with water, glycerol and methanol tend to round the tetragon off at low concentration but enhance nucleation and/or inhibit crystal formation at high concentration.

b) Surfactants

The effects of surfactants on the crystal habits of MTX are shown in Table 2.6.

Generally, at low concentration (10^{-2} - 10^{-5} g/L),

surfactants have no effect on the habit. As concentration increased (0.2-0.5 g/L), they tended to round the tetragons off. At high concentration (2.0 g/L), they inhibited the formation of crystals. Only tiny particles were formed from the nuclei.

Table 2.5.

Solvents	Habits
DMSO DMF DMF/H_2O DMSO/H_2O	anhedral particles only no crystals formed
Glycerol	very small particles with size smaller than the original powder
Glycerol: H_2O(ml) 50: 50	very fine particles, no crystals
20: 80	very fine particles, plus some stepped spheres
10: 90	well-formed smooth and stepped spheres
Glycerol 3.5×10^{-2} g/l	single and twin tetragons
Propylene glycol	tiny spherical particles
Acetone Acetonitrile	particles are almost identical to the original powder as MTX is insoluble
Ethanol Methanol	anhedral particles
Methanol: H_2O (ml) 6.0: 6.0	no crystals formed at first, but spheres appeared 2 days later
5.5: 6.0	spheres
5.0: 6.0 4.5: 6.0 4.0: 6.0	rosette of tetragons (Fig. 2.1e), and spheres
3.5: 6.0	tetragon twins

Table 2.6.

Surfactants	Conc. (g/L)	Habits
Cetrimide	2-3.5	spherical particles (no crystals)
	0.2	smooth spheres
	1.34×10^{-2} 1.34×10^{-3} 1.34×10^{-4} 1.34×10^{-5}	single and twin tetragons
CPC	2.5	spherical particles
	0.5	not well-shaped spheres
	0.11 1.25×10^{-2} 1.25×10^{-3} 1.25×10^{-4} 1.25×10^{-5}	single and twin tetragons
DPC	2.0	tetragons and spheres
	1.10×10^{-2} 1.10×10^{-3} 1.10×10^{-4} 1.10×10^{-5}	single and twin tetragons
SLS	1.0 -2.0	very tiny particles
	0.5	mostly spheres with some tetragons
	1.21×10^{-2} 1.21×10^{-3} 1.21×10^{-4} 1.21×10^{-5}	single and twin tetragons
Tween 80	2.0	smooth spheres
	0.2	stepped spheres
	1.0×10^{-2} 1.0×10^{-3} 1.0×10^{-4} 1.0×10^{-5}	single and twin tetragons

c) 'Tailor-made' additives

The effects of 'tailor-made' additives are shown in Table 2.7 below.

Table 2.7.

Additives	Conc.(g/L)	Habits
Folic acid	0.2	spheres and aggregates of spheres
	2×10^{-2} 2×10^{-3} 2×10^{-4}	single and twin tetragons
NSC-350386	2.0 0.2 2×10^{-2}	rounding increased with additive concentration, spheres with smooth instead of stepped surface
	2×10^{-3}	tetragons with stepped surface and rounding
NSC-181928*	0.5	no crystals formed
	0.1	rosettes
	0.01	spheres
	sat'd H_2O sol'n	sphere aggregates
MTX-ethyl acetate	1-2	very fine particles, no crystals
	0.4	spheres of various sizes with aggregates
	0.2	single spheres
Trimetrexate	1.0	smooth spheres
	0.2	stepped spheres
	0.01	single and twin tetragons

(*: prepared from DMF solutions)

Similar to surfactants, the results show a concentration dependent effect of the additives on the habits. Again, rounding effect was noted.

d) Dyes

The effects of dyes on the crystal habit of MTX are shown in Table 2.8.

Table 2.8.

Dyes	Conc.(g/L)	Habits
methyl orange	2.0	coloured, amorphous particles similar to the original powder
	2.2×10^{-2}	orange-coloured, mainly spheres; some not well-shaped and some aggregates
	2.2×10^{-4}	single and twin tetragons
methyl blue	3.89×10^{-2}	green coloured, mainly spheres some still retain the tetragonal shape
	3.89×10^{-4}	single and twin tetragons
amaranth	2.0	irregularly-shaped aggregates deep-red coloured
	6.7×10^{-2}	red-coloured spheres
	6.7×10^{-4}	single and twin tetragons

Similarly, a general concentration dependent effect including rounding was shown.

e) Other additives

The results of other additives are shown in Table 2.9. Again, a concentration dependent effect of the additives on the habit is shown which is similar to that of the other additives. Also similar rounding effect was noted.

Table 2.9.

Additives	Conc. (g/L)	Habit
urea	1.5	stepped spheres
	$5.0x10^{-3}$	single and twin tetragons
	$5.0x10^{-5}$	single tetragons highly favoured
β-Cyclo-dextrin (β-CD)	50	solubilization
	5.0	spheres
	0.5 $5x10^{-2}$ $5x10^{-3}$ $5x10^{-4}$	single and twin tetragons
dl Histidine	20 (5mg MTX used)	solubilization
	2.5 (5mg MTX used)	a few smooth spheres
	1.0 0.2	spheres and tetragons
L-ornithine	20	very fine particles
	2-0.5	stepped spheres
	0.2	single tetragons with a few spheres
L-Lysine	2.0	single and twin tetragons
D-Glutamic acid	6.5	very fine particles, no crystals
	2.0 1.0	stepped spheres
	0.65	single and twin tetragons
	$6.5x10^{-2}$ $6.5x10^{-3}$	single tetragons

continued on next page

L-Glutamic acid	10	very fine particles
	5.5 2.5	both stepped and smooth spheres
	2.0 0.67 6.7×10^{-2}	tetragons, some round and some twins
Gelatin	1.2	spheres and ellipses (Fig. 2.1f)
	0.5 0.2	mostly ellipses with a few spheres
	0.1	spheres
$AlCl_3$ $CrCl_3$ $FeCl_3$	0.1	fine particles only, no crystals (MTX not fully dissolved as solubility in solutions is low)
	1×10^{-3} 1×10^{-4}	single and twin tetragons in $AlCl_3$; twin tetragons and stepped spheres in $CrCl_3$; stepped and smooth spheres in $FeCl_3$

ii) Physical effects

a) Supersaturation

Table 2.10.

Concentration level (mg/ml)	Habits
1 0.5 0.3 0.2	single and twin tetragons, with the number of crystals formed decreasing with the concentration level

In the range of supersaturation used, the results suggested that suspersaturation has no effects on the habit of MTX crystals.

b) Cooling rate

No MTX crystals were formed by rapid cooling of the supersaturated solution in ice. Anhedral particles similar to the original powder were obtained. This is most likely due to the excessive nucleation (by rapid cooling) which depleted the solute necessary for further crystal growth.

c) Agitation

Table 2.11.

Stirring Time (mins)	Habits
3	very fine particles
2	very fine particles with some small tetragons
1 1/2 stirred until MTX just precipitated (<1/2 mins)	the number and size of tetragons increased with decreasing stirring time

The results suggested that stirring will affect nucleation and the size but not the shape of the MTX crystals. When stirring time was more than 2-3 mins, excessive nucleation depleted the solute necessary for further crystal growth.

d) Temperature

At 50^{0}C, single and twin tetragons were formed in the solution. At 70^{0}C, no MTX crystals formed after 3 days. The seal was then punctured to allow crystallization by evaporation. The crystals obtained were not well-formed

tetragons but bigger in size. The results suggested that elevated temperature has no noticeable effect on the growth habit of MTX crystals.

e) Substrate growth

Almost all of the crystals (mostly tetragons) were found on the bottom of the specimen tube. As a whole, MTX did not grow on the substrate surfaces. Even when growth occurred (e.g. on the sintered glass surface), there were just a few tetragons found.

f) Gel-growth

MTX crystals did not form at the beginning. After 1 week, spheres were found on the bottom of the gelatin layer which may be due to the chemical effect of gelatin instead of physical influence.

2.5.3 Further Characterization of Various MTX Forms

In order to establish the identity of the solid forms, the smooth spheres and the anhedral fine particles were further characterized.

i) Experimental

a) ^{1}H NMR

The analysis was done as described in Sec. 2.3.3 i) d). MTX spherical crystals obtained from aqueous solution containing β-Cyclodextrin (β-CD) were chosen for this analysis because presence of trace amounts of β-CD can be readily detected due to the presence of numerous hydrogens in this macromolecule.

b) Thermal analysis

Thermoanalysis was carried out on a combined DTA-TG instrument (Rigaku, Thermoflex 8075). 4 representative samples were analysed: original powder from the manufacturer (sample O), anhedral particles from methanol (sample A), tetragonal crystals from water (sample T), and spheres from β-CD solutions (sample S). The samples were heated from room temperature to approximately 250^0C at 10^0C/min in air. Sensitivity was ±100μV and an empty sample pan was used as the reference standard. DTA was also repeated under N_2 saturated atmosphere.

c) X-ray powder diffraction

The X-ray diffraction was carried out as described in Chapter 1, Sec. 1.2.2 f. The samples used for this analysis include:

(a) spherical crystals from solutions of β-CD, thymidine, Tween 80 and dye amaranth.

(b) small particles from methanol and ornithine solutions.

d) Solubility measurement

The solubility characteristics of the 4 representative samples O, A, T, and S as in b) above were studied as follows: 100 mg of the sample were put into a glass tube (i.d. 60mm) containing 200ml double distilled water (pH = 6.2 ± 0.3) which was kept in a thermostatically controlled water bath at 20^{0}C (YS1 proportional temperature controller, model 72, Yellow Springs Instrument Co., Ohio, USA). The solutions were stirred continuously by a magnetic stirrer (Dynamax, Ainsworth consolidated Industries Ltd., Sydney, Australia).

At fixed times, 10ml portions were removed and filtered by pushing through a membrane filter (0.2µm, Metrical, Gelman Sciences, Ann Arbor, Michigan, USA) fitted to a syringe, both of which had been equilibrated at the bath temperature of 20^{0}C. Preliminary experiments showed that in order to minimize surface adsorption onto the filter of MTX to less than 1%, the first 5ml portion of filtrate have to be discarded so as to saturate the filter. The subsequent filtrate was diluted appropriately with 0.1N NaOH and the MTX concentrations were determined spectrophotometrically at 303nm (635 UV-VIS spectrophotometer, Varian Techtron, Melb., Australia). The calibration line of UV absorbance against concentration of MTX in 0.1N NaOH was found to be : [Absorbance = $-3.5170 \times 10^{-3} + 0.0496 \times$ concentration (µg/ml), $r^2 = 0.9999$, n = 8] from which the solubilities were calculated. Since MTX is photosensitive, the whole

experiment was carried out in darkness (except during sampling and absorbance determination which were done under subdued light) to minimize possible decomposition of MTX. The solubility measurement was terminated after more than 48 hours. Each of the samples was transferred to a porcelain dish with the supernatant discarded and then dried in a desiccator at room temperature in darkness. After drying, all the samples were analysed by X-ray powder diffraction to detect any polymorphic transformation during stirring in water.

ii) Results and Discussion

a) ^{1}H NMR

The ^{1}H NMR spectrum of MTX spheres from β-CD solution was the same as the MTX tetragons and the orginal MTX powder as in Sec. 2.3.3 ii) d). No extra peaks due to β-CD could be detected. The absence of β-CD suggested that the MTX spheres are not complexed with additives.

b) DTA-TG

The DTA-TG curves (in air) are shown in Fig. 2.10a; DTA curves (in N_2) are shown in Fig. 2.10b. Samples T and S give very similar DTA-TG curves, indicating that they are the same polymorph. The gradual weight loss from room temperature to ~120^{0}C could be attributed to loss of water of crystallization. In fact the % of weight change was

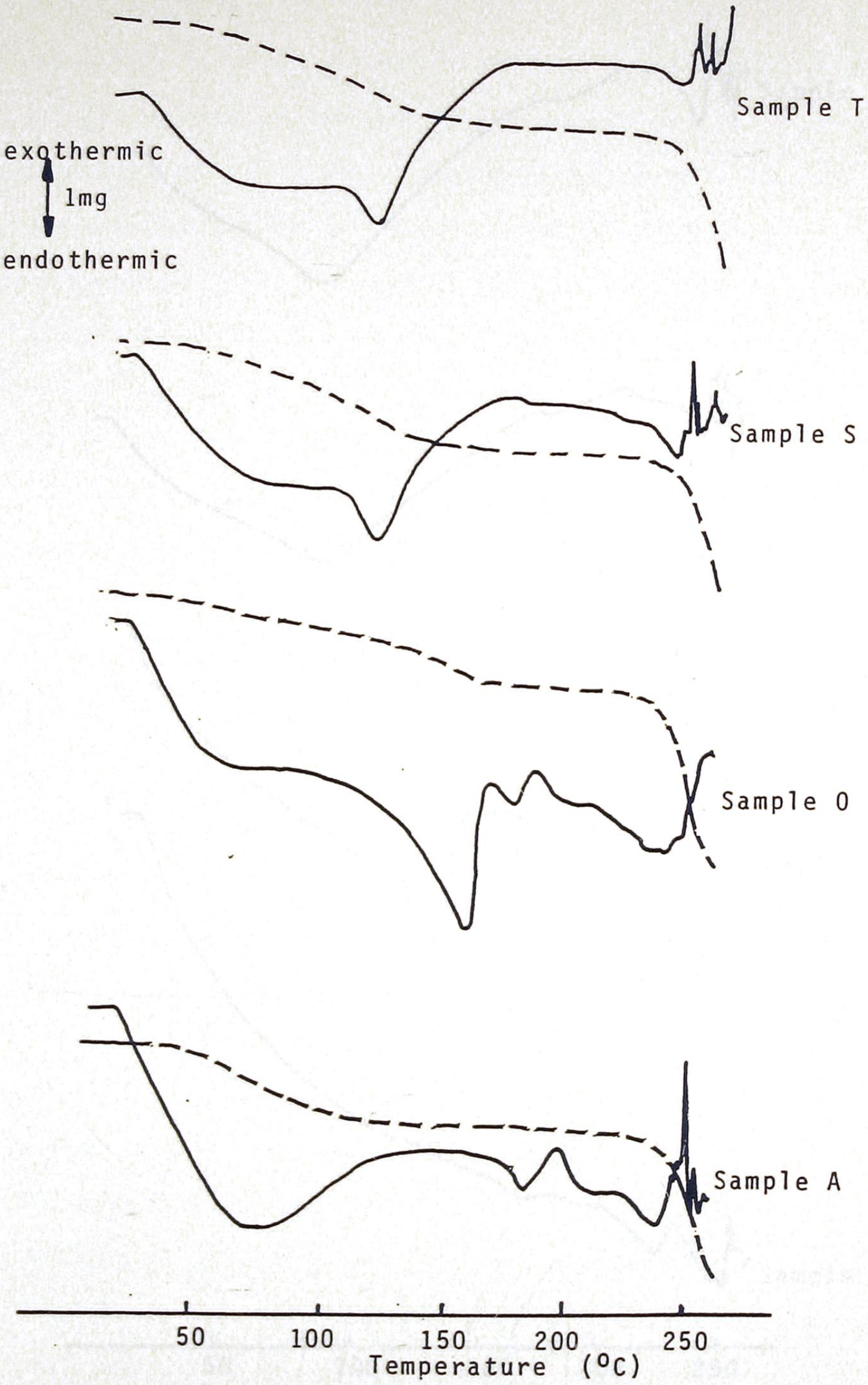

Fig. 2.10a
TG curves (- - -) and DTA curves(———) of various MTX forms
Sample starting weights: 7.03mg (Sample T), 7.54mg (Sample S), 8.24mg (Sample O), 8.40mg (Sample A).

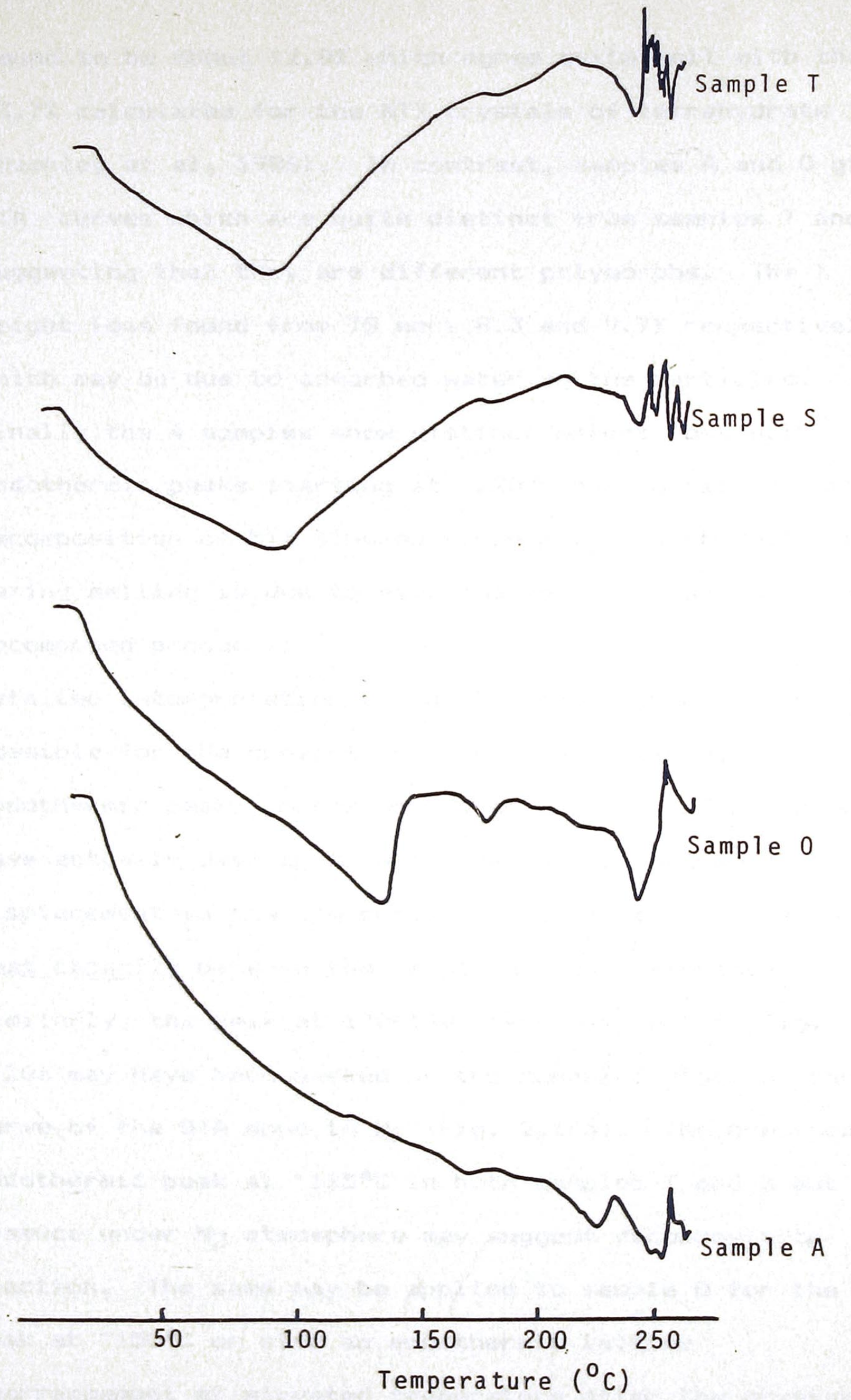

Fig. 2.10b DTA curves of various MTX forms (under N_2 atmosphere)

found to be about 12.8% which agree quite well with the 13.7% calculated for the MTX crystals of tetrahydrate (Hambley et al, 1986). In contrast, samples A and O give DTA curves which are quite distinct from samples T and S, suggesting that they are different polymorphs. The % weight loss found from TG were 8.3 and 9.7% respectively which may be due to adsorbed water on the particles. Finally the 4 samples show distinct weight loss with endothermic peaks starting at ~220^{0}C due to melting with decomposition of MTX (The multiple peaks on the DTA curve during melting is due to vigorous volume expansion of the decomposed product).

Detailed interpretation of the DTA thermograms may not be possible for the present results. For example, endothermic peaks corresponding to the loss of water may have actually overlapped with the initial downward displacement in the DTA curve due to the difference in the heat capacity between the sample and the reference. Similarly, the peak at 170-180^{0}C for sample A in Fig. 2.10a may have been masked by the downward slope of the curve of the DTA done in N_2 (Fig. 2.10b). The presence of endothermic peak at ~115^{0}C in both samples T and S but absence under N_2 atmosphere may suggest decomposition reaction. The same may be applied to sample O for the peak at ~150^{0}C or else an endothermic lattice rearrangement at elevated temperature after the crystals lost water of crystallization occurred. All these details may be clarified in future work by doing DTA under N_2 atmosphere (to minimize possible decompositions) at

different heat rates (slow heating rate promotes solid-solid transformation while high heating rate minimize it) using a better matched heat capacity reference standard (to optimize the baseline). Alternatively, DSC could be used since it measures the power difference, not the temperature difference, it does not require the thermal masses of the sample and reference to be closely matched (Daniels, 1973).

c) X-ray powder diffraction

(a) All samples of spheres (S) gave identical diffraction to that of the tetragons (T), thus confirming the thermoanalytical results that the spheres are the same polymorph as the tetragons.

(b) Samples from methanol (A) gave diffraction patterns of one single broad hump only (Fig. 2.11a), indicating that these MTX particles are in fact amorphous. Samples from ornithine solution gave patterns similar to that of the original powder (O) from the manufacturer but with even broader peaks (Fig. 2.11b), suggesting lower crystallinity.

d) Solubility measurement

The solubility characteristics of the 4 samples of MTX are shown in Fig. 2.12. Solubility data at 1 and 48 hours are shown in Table 2.12.

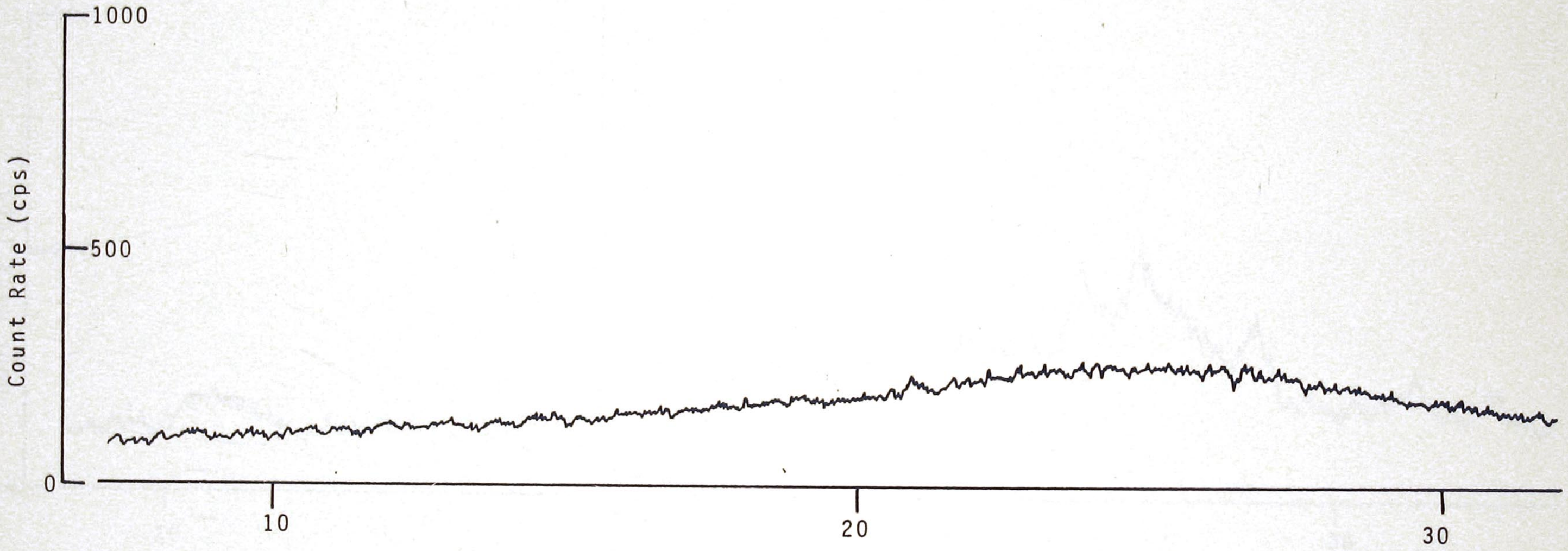

Fig. 2.11a X-Ray Powder Diffraction Pattern of MTX obtained from Methanol

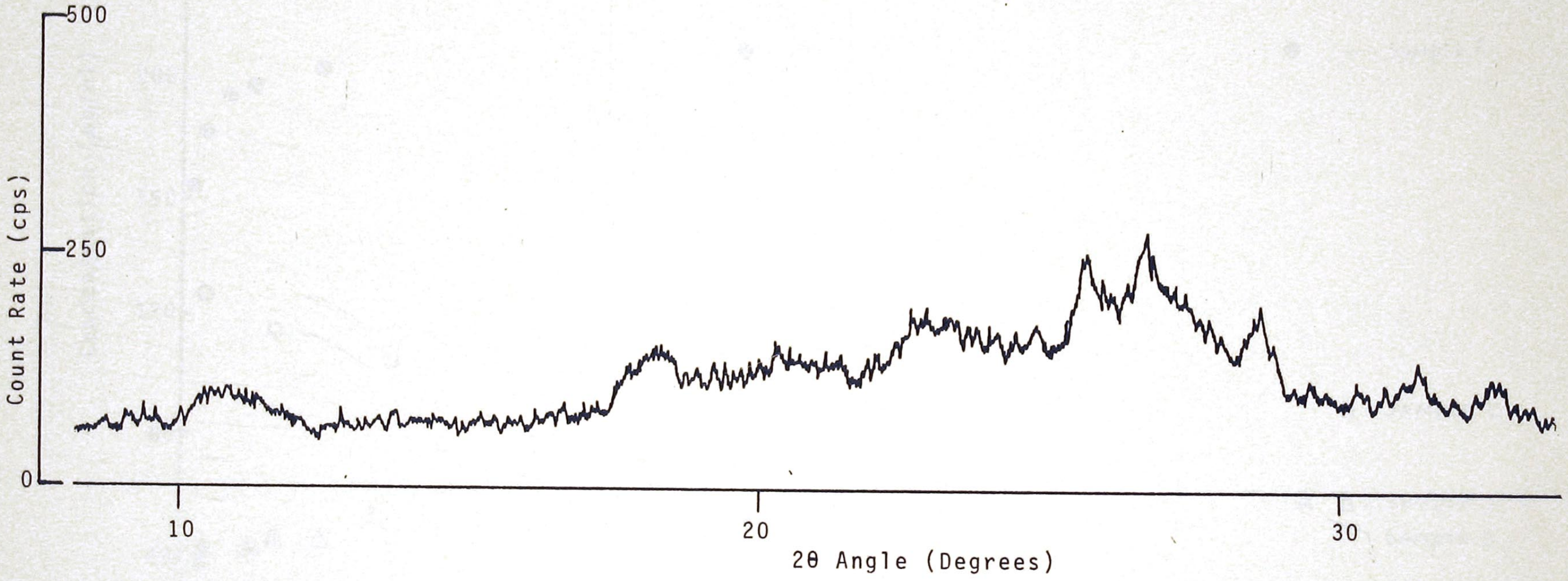

Fig. 2.11b X-Ray Powder Diffraction Pattern of MTX obtained from Ornithine Solution

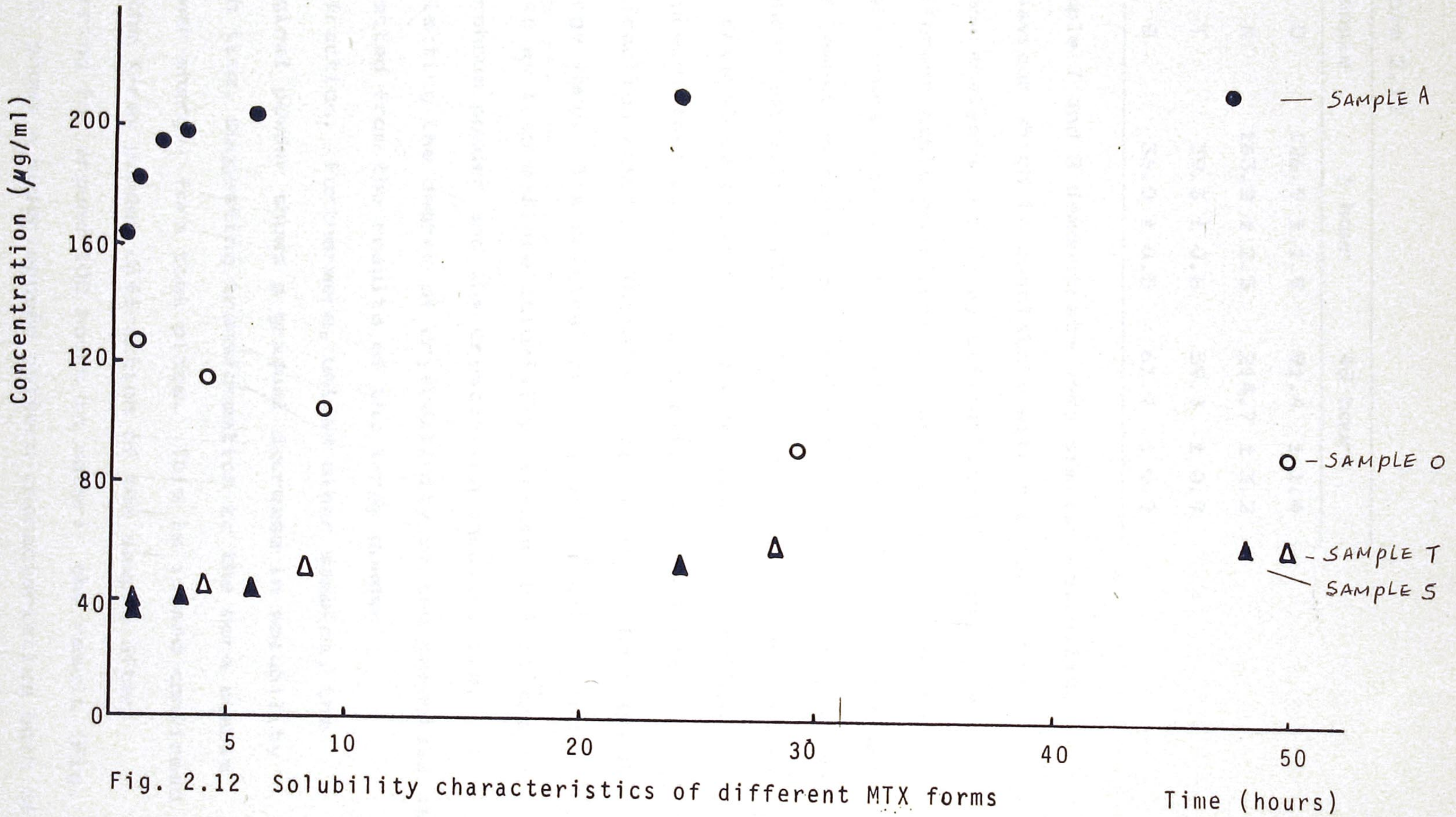

Fig. 2.12 Solubility characteristics of different MTX forms

Table 2.12

Sample	1 hour	48 hours
O	126.9 ± 1.9	91.4 ± 1.4
A	163.2 ± 2.5	214.7 ± 3.2
T	39.3 ± 0.6	59.3 ± 0.9
S	36.0 ± 0.5	61.7 ± 0.9

Sample T and S demonstrate very similar solubility behaviour which is consistent with the results of thermal analysis and X-ray diffraction that they are different habit modifications of the same polymorph. Their lowest solubility indicates that the crystals are the lowest energy form. Sample A in contrast shows the highest solubility (3.5 - 4.0 times higher than that of the crystal samples) which agrees with the amorphous nature of the sample as illustrated by the X-ray diffraction result. Therefore, sample A is the highest energy form. The original powder, on the other hand, gives an intermediate solubility between that of the amorphous powder and the crystalline samples, i.e. reflecting the degree of crystallinity of the materials as expected from the results of the X-ray powder diffraction. Furthermore, unlike other samples, the original powder shows a gradual decrease in solubility with time, suggesting transformation to the more stable (lower energy) form took place. This is indeed confirmed by the X-ray powder diffraction of the sample after stirring for around 100 hours in water: the result (Fig. 2.13) shows a superimposed pattern characteristics both of the original powder and the tetragonal crystals. The

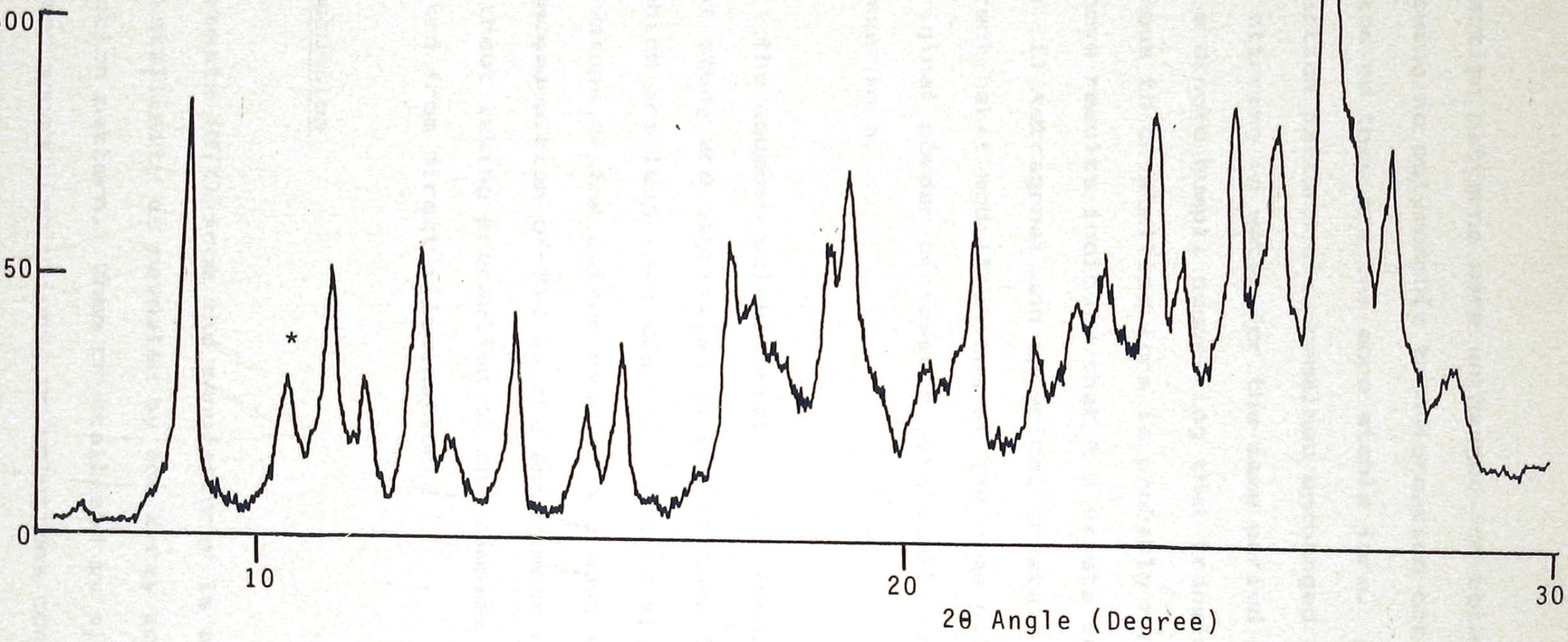

Fig. 2.13 X-Ray powder diffraction pattern of the original MTX powder after stirring in water for 100 hours

(*: this peak is characteristic of the original powder)

diffraction patterns were unchanged for both samples T and S, showing no polymorphic transformation occurred which is expected as they are the more stable form. However, diffraction pattern also remained unchanged for sample A after stirring in water for the same period of time (i.e. still a single hump), suggesting that transformation from amorphous to crystalline form is probably rather slow.

The above results indicate that MTX exists in 3 solid forms: i) tetragonal and spherical crystals which are different habit modifications of the same polymorph, ii) the original powder of lower crystallinity and iii) an amorphous form.

[Note: the aqueous solubilities of MTX found in the present study are significantly higher than the previous data which are less than 20μg/ml (Chan et al, 1986). The lower values of the latter results are most likely due to photodecomposition of MTX as the experiment was carried out without taking precaution of the samples being protected from direct illumination.]

2.6 Discussion

Methotrexate (MTX) from the manufacturer is a powder of low crystallinity as revealed by the X-ray powder diffraction pattern. When crystallized by slow cooling of saturated aqueous solutions, or solutions containing only low concentrations of additives, single and twin tetragonal crystals are mostly obtained. As the

concentration of the additives increased, the tetragonal crystals were rounded off to spheres. At high concentration, no crystals but small particles mostly anhedral, were formed. Unlike water, organic polar solvents such as methanol, ethanol, DMF, DMSO and glycerol are unable to give the crystals, neither tetragons nor spheres. Again, only small particles resulted. Solvent mixtures like water/methanol and water/glycerol have effects similar to additives. In the less polar or nonpolar solvents, e.g. butanol, octanol, CCl_4, cyclohexane and benzene, MTX is essentially insoluble, hence crystallization could not be done.

The most interesting result is the rounding effect of the aditives. Rounding of inorganic crystals of ammonium sulphate was reported by Broul (1976) using Mn^{2+} ion as the additives under the conditions of high rate of agitation and/or supersaturation. Furthermore, rounding of drug crystals has been reported by Kawashima et al (1982; 1984) by direct spherical agglomeration of needle-like salicyclic acid crystals during crystallization in a strongly agitated system of solvent mixtures. They have also applied this spherical crystallization technique to other systems such as phenytoin (1986 a & b) and tolbutamide (Sano et al, 1987). Moreover, McCarthy et al (1983) have described the rounding of sparingly soluble drugs like sulphonamides by periodic temperature cycling. The results in the present study furthermore suggest that rounding of drug particles may be possible simply by using additives during

crystallization. Spherical particles were of no special interest in this project aimed at shape modification for aerodynamic purposes but is of great interest in solid dosage form development. Spherical particles have been made for improving flowability of powders and for various physicochemical properties such as compressibility of tablet excipients (Staniforth, 1984). Therefore the rounding effect might be utilized in particle engineering in future.

The simplest explanation for the concentration dependent effect of additives and solvents (Fig.2.1g) might be related to crystal growth inhibition via intermolecular interactions including solute-solute, solute-solvent and solute-additive types. At low concentration, additives are not present in sufficient amount to affect crystal growth. As concentration increased, additives inhibited growth of the nuclei into large single crystals; instead, many small crystals formed which then coagulated into spheres so as to minimize the surface energy. At high concentration, inhibition caused by intermolecular interaction was so extensive that crystal growth was almost hindered. The result was a loss of crystallinity as shown in Sec.2.5.3 ii c) (b) and Fig.2.11.

We may still go one step further to consider the rounding mechanism by intermolecular interaction. Since additives with very different chemical structures (e.g. urea, surfactants, β-CD) have very similar rounding effect, this suggests that the interaction is non-specific regarding the crystal faces. The crystal structure of MTX consists

of both hydrophilic and hydrophobic groups projecting out of all faces of the tetragonal form along the crystallographic c and a(=b) axes. Considering solute-solvent or solute-additive interactions, in order to obtain an acicular habit of MTX crystal we must decrease the growth velocity in either 2 directions along the a, b,or c-axis in the crystal, or alternatively, increase the growth velocity in one direction. In the MTX molecule, the hydrophilic groups (which include $-NH_2$ in the pteridine and -COOH in the glutamate) can interact to certain extent with the additives through H-bonding or other dipolar interactions. However, since almost all the additives used are water soluble and contain hydrophilic groups that are capable of H-bonding, and all the faces of MTX crystals bear both polar and non-polar groups, the hydrophilic interactions would tend to be all-around or non-selective. Similarly, non-polar groups in the additives such as the benzene or heterocyclic ring may interact isotropically with the benzoyl and pteridine ring on all faces of the crystal. Such all around isotropic interaction would lead to isotropic growth of the MTX crystal, resulting in a sphere. This explains why even the 'tailor-made' additive e.g. folic acid which has a chemical structure very similar to MTX, has no effects on selective growth of MTX along a specific direction. Folic acid has an -OH or =O group instead of a $-NH_2$ group at N_4 in the pteridine (Fig. 2.9), therefore is expected to interfere with the growth along the c-axis since there is a strong hydrogen bond between the N_4-amino group and the benzoyl

oxygen linking the 2 layers in the MTX structure. However, due to the non-selective interaction, folic acid will also interact with other faces, leading to non-specific growth into a sphere.

In addition, the effect of solvent on inhibition of crystal growth can also be understood from the viewpoint that in the crystal structure, the hydrophilic layers partly consist of water molecules which also form hydrogen bonds between the peptide nitrogen and carboxylate oxygen atoms. Substitution of water molecules by other polar solvent molecules may be energetically and/or stereochemically unfavourable, resulting in the failure of formation of crystals. Therefore, water appears to be an essential part in the formation of the crystals.

Finally, for the physical factors, all of them have effects only on nucleation or/and crystal size but not at all on the shape.

2.7 Conclusion

The original objective of the research of preparing acicular crystals has not been fulfilled but the study has been extremely rewarding. There are 3 important accidental findings:

1. The crystal structure of MTX has been solved. The results support that a favourable conformation of the MTX molecule corresponding to a potential energy minimum is an important determinant of MTX–DHFR binding. This is in disagreement with theoretical studies (Spark et al, 1982;

Dauber et al, 1982) which indicated that the bound forms of MTX were highly strained. Our findings therefore shed light on the future design of antitumour drugs bound to the enzyme DHFR.

2. Rounding of drug particles may be possible simply by using additives during crystallization. This might be useful pharmaceutically for preparing spherical particles to improve the handling and processing characteristics of crystalline solids.

3. MTX exists in 3 polymorphic forms: a highly crystalline polymorph with 2 distinct habits, a second polymorph with a lower degree of crystallinity and lastly an amorphous form.

Future work

Rounding of particles using additives could be further exploited in other drugs in future.

CHAPTER THREE

3 HEXAMETHYLMELAMINE (HMM)

3.1 Introduction

i) Aim of the study

Hexamethylmelamine (HMM) is a chemotherapeutic agent which is active against small-cell lung carcinoma when administered orally (Hahn, 1983). Recently, with the aim to prepare HMM in forms suitable for direct administration into human airways, Khalik (1984) and Gonda et al (1985 a&b) reported 2 main crystal habit modifications of HMM from different organic solvents. Crystallization of HMM from polar solvents (methanol, acetone, dichloromethane) yielded predominantly acicular crystals. In contrast, non-polar solvents (cyclohexane, benzene) produced mainly compact hexagonal crystals. It was reported that the crystal habit of HMM is not dependent on kinetic factors such as the rate of cooling or supersaturation which were found to determine the size of the crystal only. Neither does it depend on the habit of the crystal seed. Khalik (1984) concluded that (1) the habit is "thermodynamically" controlled, i.e. it is an equilibrium property of the HMM-solvent system and (2) solvent polarity (i.e. the dielectric constant and the dipole moment) are the most likely parameters affecting the solute-solvent interaction and consequently the crystal habit.

The aims of the present study were:

1. To further quantify the effect of solvent polarity on

HMM crystal habit as Khalik (1984) and Gonda et al (1985 a&b) only presented a qualitative relationship.

2. To elucidate the mechanisms of habit modification of HMM crystals in different solvents by studying:

a) solute-solvent interactions.

b) growth kinetics

c) interfacial roughness or α-factor.

ii) Crystal Orientation

Hexamethylmelamine (HMM) in this study is optically uniaxial, anisotropic (birefringence: 0.266, N_o=1.692 ± 0.003; N_e=1.430 ± 0.003) and belongs to the hexagonal crystal symmetry system. Its habit is hexagonal bipyramidal (Winchell, 1954) (Fig.3.1). But the actual shapes may vary according to differences in growth rates along different crystallographic axes. Briefly, HMM crystals elongated along the c-axis form needle-like habits while growth along the [1100] direction gives hexagonal compact habits or plates.

However, elongation along the other axis (other than the c-axis) may also result in habits so similar to a needle that it will lead to uncertainties about the growth direction of the crystal if the analysis is based on the shapes only. For these reasons, polarizing microscopy was employed to characterize the relationship between the habits and crystallographic axes in the crystals. The method used in the study has been described in details by Bloss (1961) and is summarized in Appendix 4.

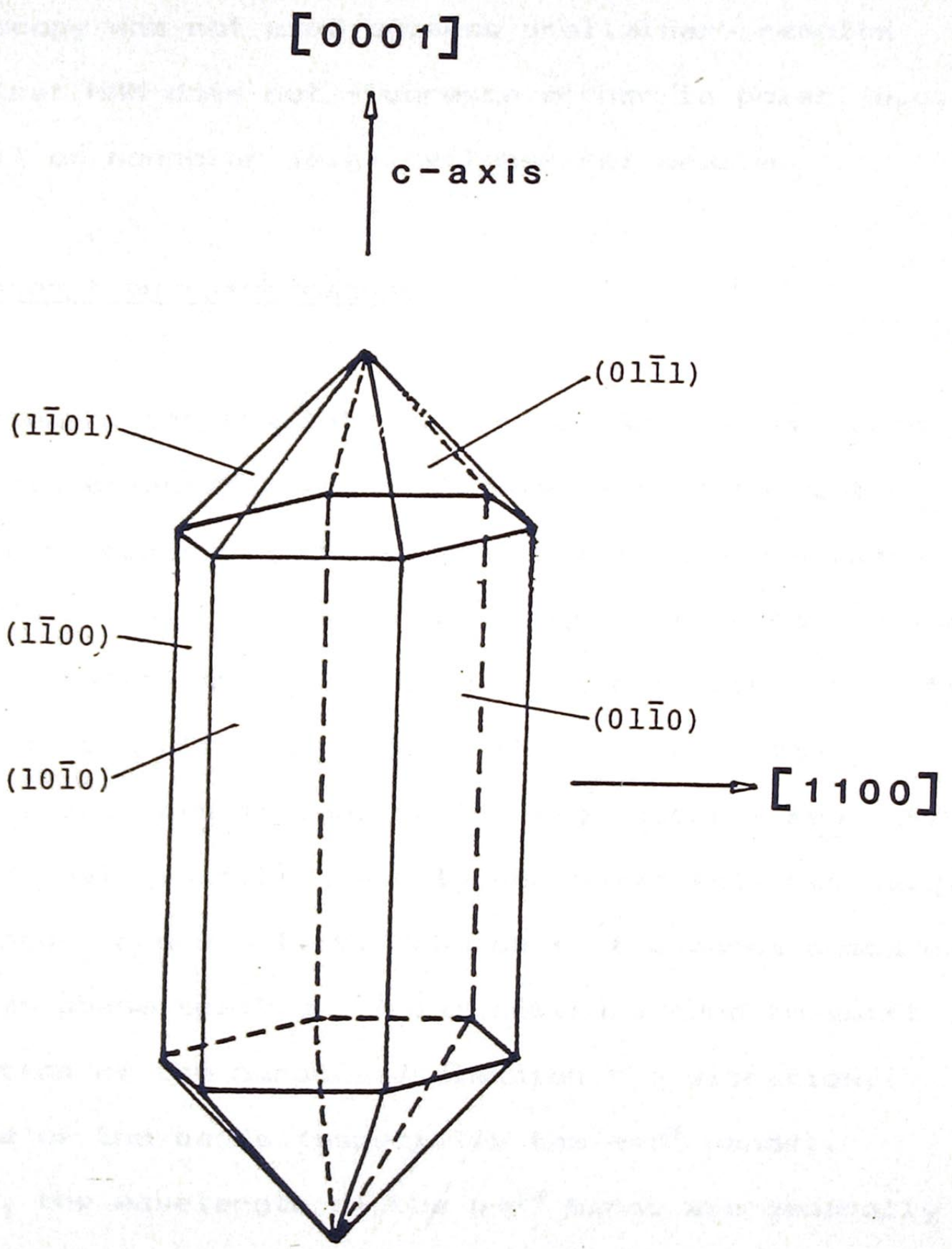

Fig. 3.1 Crystallographic diagram of HMM crystal morphology

iii) Solute-solvent Interactions

Solute-solvent interactions of HMM in solutions were investigated by spectroscopy (UV, IR, and ^{1}H NMR) and electro-optical Kerr effect measurement. Fluorescence spectroscopy was not used because preliminary results showed that HMM does not fluoresce either in polar (e.g. methanol) or nonpolar (e.g. cyclohexane) medium.

a) UV absorption spectroscopy

The wavelength and the intensity of UV absorption bands can be both affected when a molecule is in a solvent environment compared with its spectrum in the gas phase (Rao, 1975). This is due to the unequal perturbation (or stabilization) of the ground and excited electronic states of the molecule which depends on the nature of the solute-solvent interactions in the two states. Rao (1975) described that generally, highly non-polar solvents (e.g. hydrocarbons) produce little change in the bands compared to the gas phase spectra. Polar solvents tend to shift the position of the bands and diminish the vibrational structure of the bands (especially the $n\rightarrow\pi^*$ bands). Moreover, the wavelength of the $n\rightarrow\pi^*$ bands are generally found to decrease (blue-shift) with the increase in the polarity of the solvent. Polar solvents often but not always shift the $\pi\rightarrow\pi^*$ transition to longer wavelengths (red-shift). Theoretical expressions for the solvent-induced frequency shift have

been derived by McRae (1957) in terms of the dielectric constant and refractive index of the solvent and dipole moment of the solute. Several applications have been also discussed by McRae (1957). On the other hand, a simple expression for the solvent effects on the intensity of UV absorption band was derived by Myers and Birge (1980) in terms of the refractive index of the solvent and a solute geometric factor. In selected experimental examples, Myers and Birge's theory appeared to predict better than the previous theories of Chako (1934) and Abe (1970) [see Myers and Birge, 1980].

b) IR absorption spectroscopy

IR studies of solute-solvent complexation in solutions of pharmaceuticals have been reported by James and co-workers (James, 1986). Solvent-induced change in vibrational frequency of a solute dipole can be explained by 2 major factors (Rao, 1963): general electrostatic interaction and specific localized interaction.

The relative frequency shift given by the former is a function of the dielectric constant of the solvent and a constant characteristic of the solute. However, this theory is only applicable to nonpolar solvents. Also, it does not take into account the more specific localized interactions. The latter includes dipolar interaction, dimerization, hydrogen bonding and interaction with the π-cloud of aromatic solvents, and has been extensively studied by Bellamy (1975). In explaining the solvent

effect on IR, both the electrostatic and localized interaction are important. Their relative significance varies and depends on both the solute and the solvent. Solvent effects on IR intensity have not been studied as extensively as on frequencies and will not be considered here.

c) ^{1}H NMR spectroscopy

The environment of the protons in a molecule can be affected markedly by solvents and consequently changes in the position of the chemical shifts can be observed in different solvents. The measurement of these spectral changes due to solvents may throw some light on the intermolecular interactions. Solvent effects on the chemical shift are most notable when there are specific solute-solvent interactions. For example, Williams and Fleming (1966) reported that when a proton is hydrogen bonded, then the effect is to cause a downfield shift relative to the unbonded state and such paramagnetic shift can be quite large. Furthermore, aromatic solvents (e.g. benzene) frequently cause chemical shift of up to 0.5 ppm (relative to CCl_4 or $CDCl_3$) even for C-H protons (Williams and Fleming, 1966). Such aromatic solvent-induced shifts (ASIS) were further described by Brown and Stark (1965) and Armstrong et al (1973) with application to stereospecific solute-benzene interaction and solvent orientation in solvation. A general review on solvent effects and NMR has been detailed by Laszlo (1967). NMR

relaxation studies of solute-solvent interactions were published also by Bryant (1978).

d) Electro-optical Kerr effect measurements

Birefringence induced in a material by application of an electric field is known as the Kerr effect. The general principle of the Kerr effect measurement has been given by Aroney (1977). Briefly, when plane polarized light passes through a solution in the absence of an electric field, the emergent light is still plane polarized because the orientation of the molecules in the solution is random. However, when an electric field is applied, there will be a partial ordering of molecules due to the induced (dipole) moment (Fig.3.2). The result is that the molecular system in the field becomes optically anisotropic. Consequently, the refractive index measured in the direction of the field ($n_{\parallel}$) differs from that perpendicular to the field ($n_{\perp}$) and the solution becomes birefringent. If, e.g. $n_{\parallel} > n_{\perp}$, then the light in the direction parallel to the field will be retarded more than the light in the perpendicular direction, resulting in the emergent light being elliptically polarized. This ellipticity (or electric birefringence) is usually expressed as the molar Kerr constant, mk. It is a function of the solute dipole moment μ (if there is any) and the polarizabilities along the principal axes of the solute molecule. The kerr effect is very sensitive to variation of molecular geometry and environment, and is

Fig. 3.2 Principle of the Kerr effect
(showing plane polarized light entering an "ordered" system of molecules ($n_{\parallel} \neq n_{\perp}$)
E: applied electric field

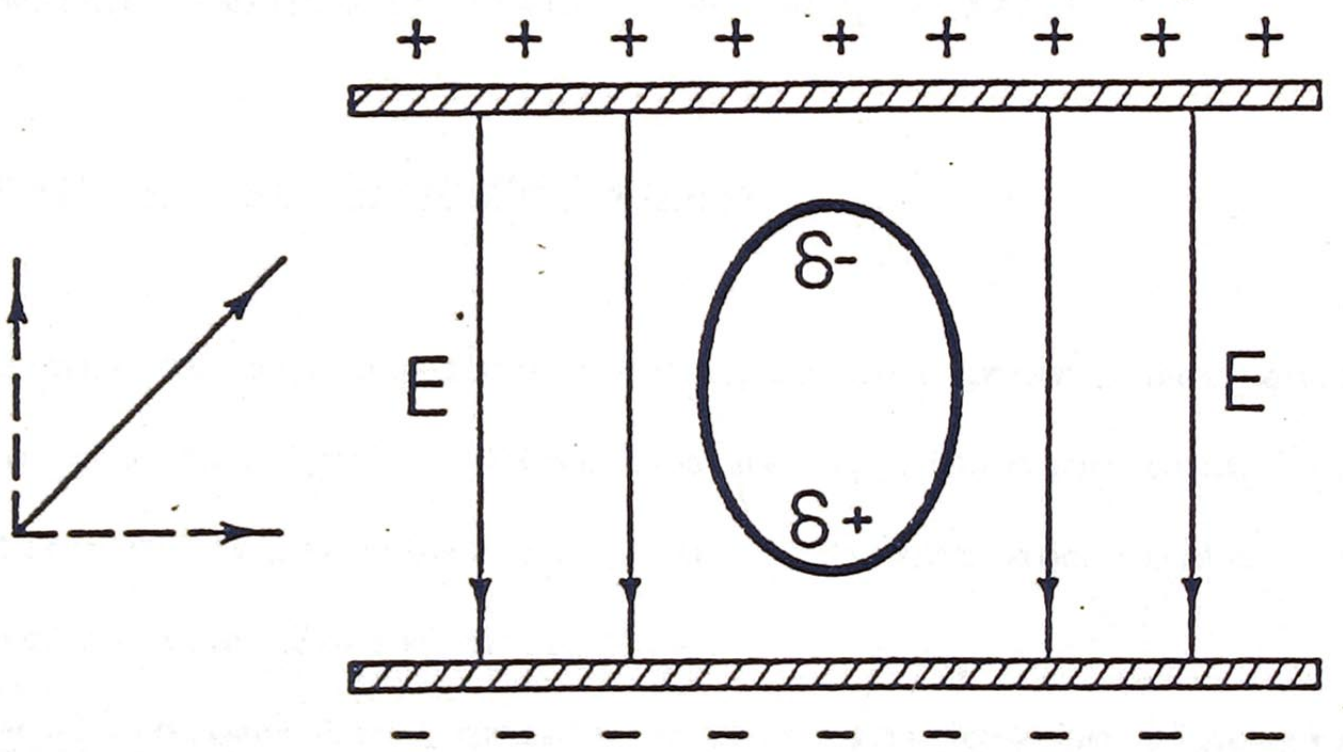

therefore a potent method for studying the conformations of molecules. It has been applied to investigations of solute-solvent interactions such as the solute aggregation and the geometry of solvation (Aroney, 1977). However, a major limitation in molar Kerr measurement is that normally only nonpolar or near-isotropically polarizable solvents can be used. In polar solvents, although pulsed-voltage techniques can be used, interpretation of the measured data will be difficult due to the inadequacy of existing dielectric theory (Aroney, 1977).

iv) Growth Kinetics and Mechanisms

It is a standard procedure to deduce the growth mechanisms from the crystal growth kinetics data, although such evaluation of mechanisms could be indirect and quite speculative (van Enckevort, 1984).

In general, elementary growth mechanisms may be classified according to the rate law resulting when they are, one at a time, fully responsible for the growth rate. The classes are: linear, parabolic and exponential rate law. The rate expressions are, respectively

(1) $R = k_1 \sigma$

(2) $R = k_2 (\sigma^2/\sigma_1)\tanh(\sigma_1/\sigma)$

when σ_1 is small,

$$R = k_2 \sigma^2$$

(3) $$R = k_e(1+\sigma)^{7/6} \sigma^{2/3} \cdot x [\ln(1+\sigma)]^{1/6} \exp [-K_e/\ln (1+\sigma)]$$

when $\sigma \ll 1$, $\ln(1+\sigma) \simeq \sigma$, $1+\sigma \simeq 1$,

$$R = k_e \sigma^{5/6} \exp [-K_e/\ln (1+\sigma)]$$

R is the growth rate, σ is the supersaturation, $(C-C_s)/C$, C is the solute concentration, C_s is the solute equilibrium solubility, k_1, k_2, σ_1, k_e, and K_e are characteristic constants in terms of the equilibrium solubility, solute concentration in the adsorption layer of the crystal, molecular diameter and volume, temperature, frequency of integration of molecules in kink sites on crystal surface, and interfacial tension, as given by Bennema and Gilmer (1973) and Nielsen (1984). The three kinds of kinetics are explained by the following rate-determining mechanisms, respectively: (1) volume transport or adsorption, (2) surface spiral growth (dislocation), and (3) surface nucleation (polynuclear) (Davey, 1982; Nielsen, 1984). Therefore, if the growth is controlled by (1), a plot of R vs σ should give a straight line. On the other hand, a $R-\sigma^2$ plot will give a straight line in (2) while plotting $\ln (R/\sigma^{5/6})$ vs $1/\ln (1+\sigma)$ will yield a straight line in (3).

v) The Surface Entropy Factor (α)

The use of α-factor [see also Chapter 2, Sec.2.1 i) A) a)] has become increasingly popular in characterizing crystal growth from solution (Davey, 1982; 1986). As described by Bourne and Davey (1976), generally α-factor can be estimated from the heat of solution (ΔH_s), or the entropy of solution (ΔS_s), or the edge energy (Υ):

$\alpha = \xi\ \Delta H_s/RT$ eqn.(3.1)

or $= \xi\ \Delta S_s/R$ eqn.(3.2)

or $= 4\Upsilon/kt$ eqn.(3.3)

R = Gas constant

k = Boltzmann constant

ξ = the crystallographic factor describing the anisotropy of the particular surface under consideration, approximated by n_s/n_t, which is the ratio of the number of nearest neighbours in the surface to that in the bulk of the crystal.

Υ = the edge energy which may be calculated from the surface energy (F) using the relationship (Bourne and Davey, 1976 b):

$$\Upsilon = F \times H \times L$$

H = height of a growth step on the crystal surface

L = length of step occupied by one molecule

In addition, Human et al (1981) also used the expression

$\alpha = \xi\ [\Delta H_f/RT_m - \ln X_{seq}\ (T)]$ eqn.(3.4)

to calculate α for biphenyl crystal growth.

$X_{seq}(T)$ is defined as the ratio of the solubility to the density of the solute at temperature T. T_m is the melting

point of the solute. The expression predicts that α will decrease with increasing solubility. Thus when a substance crystallizes from different solvents, high solubilities will lead to low α and increased growth rate. The same prediction can be obtained from eqn.(3.3) since Υ is inversely proportional to solubility (Davey et al, 1982) but not from eqn.(3.1) and eqn.(3.2) because solubility is not directly related to either ΔH_s or ΔS_s but is rather a combination of both.

Although in some systems of solution crystal growth studied (Bourne and Davey, 1976; 1978), it seems likely that the most reliable estimate of α for solution growth is obtained from the edge energies, nevertheless the question remains as to which method of calculation in general estimates best the α-factor which predicts successfully the growth rate (Bourne and Davey, 1978). Today (10 years after the 'classic' papers by Bourne and Davey) the issue is still not clarified. It thus appears that α calculation is still system specific. The use of eqn.(3.1) to calculate α can fail when the dissolution is either exothermic or athermal because the former would lead to a negative value of α which is meaningless while the latter would result in a constant value of α which fails to account for the differences in crystal growth (Davey, 1982). Moreover, in some cases the failure of the α values based on heats and entropies of solution to predict the crystal growth rates could be rationalised if the rate determining step in the mechanism were steric in origin e.g. molecular orientation at the surface or entry

into a kink site (Bourne and Davey, 1978). This has been substantiated recently by Elwenspoek et al (1987) on the studies of growth forms of naphthalene crystals in various solutions.

Since

$$\Delta H_s = \Delta H_f + \Delta H_m$$

in non-ideal solutions, $\Delta H_m \neq 0$. Strong solvent-solute interactions causing negative deviation from ideality ($\Delta H_m < 0$) lead to a reduction in ΔH_s, and therefore a reduction in α. This should result in an increase in crystal growth rate due to the roughening of the surface. However, if the solvent interacts strongly also with the solute incorporated into the crystal (i.e. the case of strong adsorption), then this would in fact inhibit the rate of growth. Such solvent adsorption has been used to explain the discrepancy between the calculated α values and the observed experimental results (Davey, 1982).

Lastly, it is very important to note that the growth mechanism predicted by α is only related to those processes occurring at the crystal surface; volume diffusion is not considered (Bourne and Davey, 1976). Thus, the measurements are usually carried out under well-stirred condition with rapid bulk diffusion (Bourne et al, 1978). It is obvious that direct application of α to growth from stagnant solution may be irrelevant as the growth mechanism could be diffusion controlled, although such application did occur in literature (Borecka et al, 1983).

3.2 Crystal Habit Quantitation

i) Experimentals

a) Growing of HMM crystals

Nearly saturated solutions (~15ml) were prepared by dissolving sufficient amount of HMM (NSC no. 13875-NI, supplied by the NIH, USA) according to the solubilities at room temperature in various solvents (Khalik, 1984). When the solubility was unknown, a slight excess of solute was used. The solutions were sonicated (Bransonic 52, Branson cleaning equipment Co., Shelton, Conn., USA) and heated (~60^{0}C) for about 30 sec. to facilitate dissolution. After slow cooling to the room temperature (~20^{0}C), the solutions were filtered (Whatman no.1, Whatman Ltd., England) and transferred to three 100 ml beakers; each thus contained 4-5 ml solution. For those solvents with high volatility, e.g. acetone, 1 ml excess solvent was added to the solution prior to filtration to make it unsaturated so as to avoid possible crystallization in the filtrate as evaporation took place. The beakers were then covered with a sheet of aluminium foil, sealed with plastic sticky tape and allowed to equilibrate in an oil bath thermostatically controlled at 20^{0}C (Thermomix 1441, B. Braun, West Germany). Spontaneous nucleation and subsequent crystal growth were achieved in the beakers by slow evaporation of the solvents through 1-3 small holes (made by a pin) in the covering foil. In an attempt to

minimize the kinetic effect of growth on the equilibrium crystal habits (due to rapid crystallization), the evaporation rate was kept low such that it took at least one week for the growth to complete.

Since crystal growth can be very sensitive to the presence of impurities [see Chapter 2, Sec.2.1 i) A) b)], precautions were taken to minimize possible contamination: The beakers used in the experiment had been cleaned thoroughly by washing with concentrated nitric acid (Univar, Ajax Chemicals, Sydney, Australia.), brushed with detergent and rinsed with double distilled water; the filter papers were washed with the respective solvents before use. All the solvents were at least of analytical or spectroscopic grades.

b) Measurement of the crystal dimensions and habits

The crystal dimensions and parameters of habits were measured *in-situ* on the bottom of the beaker using the image analysis system of which the basic principle has been described in Chapter 1, Sec.1.7.1 iii). The images of the crystals were obtained by the TV camera using either a TV lens (16mm, 1:1.6) or a trinocular stereomicroscope (Olympus 214971) for the crystal size (dimension 1-10 mm) and the appropriate magnification required. Basically, all the crystals were measured except for the tiny particles and the extremely thin needles (diameter < 0.1-0.2mm) which contribute very little to the total mass, and for those crystals grown on

the side wall or with the crystallographic c-axis normal to the bottom of the beaker (as the solvents evaporate, the solution level will fall below the crystals and the growth along the c-axis will be artificially terminated).

Data Treatment

The habit of the HMM crystals was expressed by the aspect or axial ratio (β) which is the length (L) divided by the mean breadth (MB) of the particle. Length is measured as the longest perpendicular distance (longest Feret's diameter) by the image analysis system and the mean breadth is calculated as the projected area (A) of the particle divided by its length.

$$\beta = L/MB = \frac{L}{A/L} = L^2/A$$

The volume (V) of the crystal was calculated using the equation for a cylindrical particle.

$$V = \pi r^2 * L$$

$$= \pi (MB/2)^2 * L \quad \text{(taking } r = MB/2\text{)}$$

$$= \pi/4 \times A^2/L$$

The β and V for each crystal were thus calculated by substituting the appropriate values. Preliminary measurements show that most of the data (β) could be represented better by log-normal rather than normal distribution. Therefore, from the cumulative V vs β relationship assuming a log-normal distribution of β, the mass or volume median aspect ratio β_m was obtained as the interpolated β value corresponding to the 50% cumulative

volume. β_m based on the mass rather than on count was used because (i) it reflects how the mass of the sample behaves without giving undue importance to a large number of small crystals (ii) the large crystals reflect better the equilibrium shape.

c) Determination of the crystal orientation

Elongated crystals were carefully removed from the beakers with a spatula, placed on a microsope slide and then observed under a petrological microscope (Vikers Instruments) using the extinction position method or the interference figures as described in the Appendix 4.

ii) Results and Discussion

Crystal Growth (Habit)

Elongation has been confirmed by the polarizing microscopy to be along the optical c-axis rather than the other axis. Table 3.1 summarizes the results of the solvent polarity (dipole moment μ and dielectric constant ϵ) and the crystal habits of HMM (in terms of the mass median aspect raio, MMAR). Correlation between MMAR and μ or MMAR and ϵ, and multiple regression of MMAR on μ and ϵ were attempted. All of them gave r^2 values smaller than 0.4, suggesting very weak quantitative relationship between the crystal habit and solvent polarity. This is in contrast to the previous findings of Gonda et al (1986) which

showed a fairly high correlation (r^2 = 0.7). There are a number of reasons for the discrepancy between the previous report and this one: i) two of the dipole moment values in the previous study (for methanol and acetonitrile) were later found to be erroneously quoted from literature, ii) the count median aspect ratio (CMAR) was used previously rather than the MMAR at present, and also iii) faster evaporation and growth rates were used previously.

However, qualitatively it is still obvious that polar solvents (e.g. acetone, methanol) give needles while nonpolar solvents (benzene, cyclohexane) yield compact crystals as reported before (Khalik, 1984; Gonda et al, 1985 a&b; 1986) (Fig.3.3). It should be mentioned that while in some of the polar solvents (e.g. 1-propanol) compact crystals were obtained, yet in the same beakers there were numerous very thin needles formed as well which did not occur in the non-polar solvents. Such thin needles were not counted because: (i) the small magnitude of their diameter (<0.1-0.2mm) which makes simultaneous accurate measurement with their length difficult, (ii) the mass contribution is negligible (estimated ≤ 10%). These thin needles were presumably formed at the later stage of the evaporation when the growth rate may be faster and/or the growth interface (solvent/air/glass) may be different from that of the initial stage. This is confirmed by the results with unsealed beakers where spontaneous (fast) evaporation of the HMM solution in polar solvents would predominantly form needles. Alternatively, fast crystallization of a drop of the polar solution on a microscope slide would



(a)

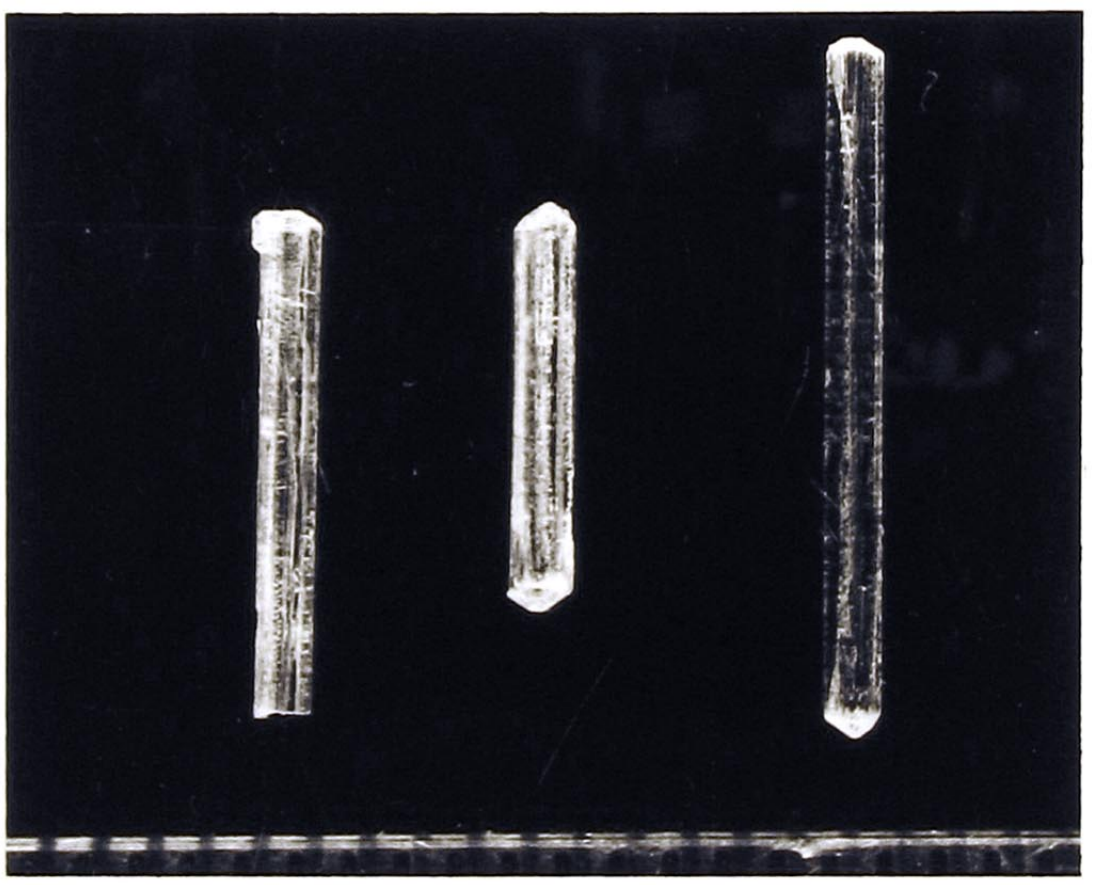

(b)

Fig. 3.3 Photograph of (a) hexagonal compact and (b) needle habits of HMM crystals (scale bars: 2mm)

again favour needle formation as observed under a microscope. In the original work by Khalik (1984) on habit modification of HMM crystal, 'slow' evaporation from polar solvents would yield needles. It should be noted that Khalik (1984) carried out the evaporation in a fume cupboard or in a desiccator using open beakers which would in fact give 'fast' evaporation and growth as compared to the sealed beakers in the present study.

Therefore, similar to that reported by Khalik (1984), the present study confirmed that in nonpolar solvents the crystal habit of HMM is independent of the supersaturation and growth rate, and the equilibrium form is hexagonal compact. However, on the other hand, our study also suggested that in polar solvents, the crystal habit of HMM could be affected by the rate of growth and probably supersaturation as well, and the equilibrium form may be again compact which is in contrast to the previous findings (Khalik, 1984). The formation of needles in polar solvents may therefore be kinetically but not thermodynamically controlled.

Table 3.1

solvent	μ(D)	ϵ	no. of crystals	β_m	σ_g
methanol	1.70	32.7	51	7.44	2.21
			79	9.77	1.84
			18	2.42	1.25
acetone	2.88	20.7	30	9.00	1.72
			50	6.94	1.68
			24	12.57	1.86
1-propanol	1.68	20.1	33	1.92	2.86
			7	2.07	1.15
			24	2.23	1.46
2-propanol	1.66	18.3	31	13.34	2.00
			5	1.90	–
			15	1.86	–
1-butanol	1.66	17.1	54	4.16	1.67
			48	2.86	1.61
			59	2.49	1.67
thiophene	0.54	2.76	17	2.08	–
			42	2.14	1.22
acetonitrile	3.37	37.5	61	3.37	1.36
ethanol	1.68	24.3	29	7.26	1.76
triethylamine	0.77	2.42	22	1.86	1.49
ethylacetate	1.81	6.02	11	2.03	–
furan	0.67	2.95	53	1.97	1.30
toluene	0.39	2.38	19	2.21	1.20
hexane	0.1	1.89	35	1.91	1.39
decane	0.1	1.99	21	2.06	–
heptane	0.1	1.92	46	2.03	1.27
			36	1.92	1.28
CCl_4	0.0	2.24	19	1.94	–
benzene	0.0	2.28	32	1.96	1.12
cyclohexane	0.0	2.02	12	1.82	–
CH_2Cl_2+	1.60	9.08	–	>5-10	–
chloroform+	1.01	4.81	–	>5-10	–

σ_g : Geometric standard deviation of β

+ : Quantitative measurements were not done because of extensive interlinking among the crystals

For the first 5 solvents (from methanol to 1-butanol):
$\beta_m = 4.435\mu + 0.172\epsilon - 6.832$ ($r^2 = .33$, $n = 15$)

For the first 5 solvents using weighted mean of β_m in each solvent:
$\beta_m = 2.925\mu + 0.205\epsilon - 3.883$ ($r^2 = .35$, $n = 5$)

For the pooled data of all solvents:
$\beta_m = 1.460\mu + 0.044\epsilon + 1.401$ ($r^2 = .30$, $n = 30$)

3.3 Solute-solvent Interactions

i) Experimental

a) UV spectroscopic method

UV absorption spectra of HMM in different solvents were recorded using a spectrophotometer (Perkin-Elmer Lambda 5 UV/VIS) with settings of slit 0.25, scan speed 7.5 nm/min and response time 0.5s in order to obtain high resolution spectra. A series of HMM solutions of concentration 40 µg/ml was prepared in various organic solvents as follows: about 2 mg of HMM were weighed out accurately and dissolved in 50ml of the solvents. The errors in weighing have been minimized by using a microbalance (Mettler M5 Microbalance) in an air and humidity controlled room. The solutions in volumetric flasks (A-grade) were prepared in a water bath thermostatically controlled at 20^{0}C so as to minimize the errors in volume expansion. The UV spectrum of each solution was then recorded from wavelength 215 to 235 nm (peak at ~227 nm) using a pair of matched cuvettes with pathlength 0.1 cm. Each sample was examined in duplicate and each time a background correction was run when a different solvent was used.

b) IR spectroscopic method

IR spectra of nearly saturated solutions and suspensions

of HMM in $CHCl_3$ and CCl_4 were determined in an infra-red spectrophotometer. (Perkin-Elmer double beam 297). The HMM samples were prepared by sonicating excess HMM in 1 ml CCl_4 and $CHCl_3$ for a few minutes. The supernatants or suspensions were then injected into an IR solution cell (pathlength 0.1mm) and the IR spectra were recorded from wave-number 3000 to 600 cm^{-1}. Pure solvents were run as the blank. CCl_4 and $CHCl_3$ were chosen not only because they give different crystal habits of HMM (hexagonal compact and needle respectively), but more importantly their IR absorption bands overlap to a minimum with those of HMM. Regarding the latter aspect, most other solvents were not suitable in this study.

c) ^{1}H NMR spectroscopic method

^{1}H NMR spectra of HMM in different solvents were determined using a high resolution NMR spectrometer (Hitachi Perkin-Elmer R-24B). Starting from the saturated concentration, a series of dilutions were used which covered the concentration range of 0.03 - 30% (w/v), depending on the solubility of HMM in the solvents. Tetramethylsilane was used as the internal standard which being chemically inert minimizes the possibility of unwanted solute-solvent interaction. A low temperature (down to -50^0C) spectrum was also done in toluene using a Fourier transform NMR spectrometer (Bruker HX-90) in order to study the temperature dependence of the measurement.

d) Molar Kerr constant measurements

This part of the work was carried out by Dr. Raymond Pierens in the School of Chemistry, University of Sydney using a self-constructed apparatus for Kerr effect measurement (Aroney et al, 1987 and refs. therein). A total of 4 solvents (cyclohexane, dioxane, benzene and hexafluorobenzene) were used. The solvents were distilled and appropriately dried over sodium or molecular sieves.

ii) Results and Discussion

a) UV measurements

The wavelength and the corresponding intensity for the UV absorption maximum of HMM in various solvents are summarized in Table 3.2. It appears that there is a small red shift in the wavelength as the solvents change from nonpolar to polar. However the magnitude of difference of only 2-3 nm makes it difficult to deduce any significant relationship between the shift and the crystal habits. Although the absorption intensity in cyclohexane is apparently lower than that in other solvents, there is no systematic difference in the intensity between the polar and nonpolar solvents. In fact, multiple regression between the intensity and the (i) solvent polarity (dielectric constant μ and dipole moment ϵ) and (ii) solubility parameter (δ) (Martin et al, 1983; Beerbower et

al, 1984) of the solvents were all found to give r^2 values smaller than 0.2, suggesting very weak correlation only.

Table 3.2 The wavelength and the corresponding intensity for the UV absorption maximum of HMM in various solvents (in duplicates)

solvent	absorption peak wavelength (nm)	absorption intensity	
		peak	AUC+
octanol	227.6	0.9818	0.977
	228.0	0.9864	0.980
		(0.9841)++	(0.9785)
butanol	227.5	0.9678	0.967
	227.5	0.9909	1.004
		(0.9794)	(0.9855)
propanol	228.0	0.9832	0.999
	227.1	0.9400	0.947
		(0.9616)	(0.9730)
ethanol	227.6	0.9718	0.978
	227.2	0.9794	0.986
		(0.9756)	(0.9820)
methanol	227.4	0.9851	1.008
	226.8	0.9857	0.983
		(0.9854)	(0.9955)
decane	226.6	1.002	1.008
	226.1	0.979	0.994
		(0.9605)	(1.001)
heptane	224.5	0.962	0.993
	226.2	0.958	0.995
		(0.9600)	(0.994)
hexane	225.3	0.959	0.987
	224.6	0.958	0.990
		(0.9585)	(0.9885)
pentane	224.3	0.971	0.982
cyclo-	225.2	0.949	0.958
hexane	225.2	0.951	0.951
		(0.950)	(0.9545)

+ AUC is the 'cut and weighed' area under the curve from wavelength 215 to 235 nm

++ value in brackets is the mean value of the duplicate.

Results of multiple regression of the intensity on μ, ϵ, and δ:

$$\text{Intensity (peak)} = .01\mu - 7.05\times10^{-5}\epsilon - 9.69\times10^{-4}\delta + .97 \quad (r^2 = .17,\ n = 19)$$

$$\text{Intensity (peak)} = 7.28\times10^{-3}\mu + 1.94\times10^{-5}\epsilon + .96 \quad (r^2 = .14,\ n = 19)$$

$$\text{Intensity (AUC)} = -8.06\times10^{-3}\mu + 5.90\times10^{-4}\epsilon + 4.13\times10^{-4}\delta + .98 \quad (r^2 = .03,\ n = 19)$$

$$\text{Intensity (AUC)} = -6.78\times10^{-3}\mu + 5.51\times10^{-4}\epsilon + .98 \quad (r^2 = .03,\ n = 19)$$

b) IR measurements

Both the IR spectra of HMM in $CHCl_3$ and in CCl_4 are very similar (Fig.3.5 a and b respectively). The absorption bands at wavenumber 2920, 2850, and 2770 cm^{-1} are due to the $(CH_3)_2N-$ groups, and the bands at 1530 and 1390 cm^{-1} are characteristic of the ring substituted s-triazine (Van de varrt-van zutphen et al, 1982). All these absorption bands show no shifts in $CHCl_3$ as compared to those in CCl_4. The results suggested that any interactions between these functional groups of the HMM molecule and the solvent molecule could not be revealed in the present IR study. The suspensions also gave similar results.

c) ^1H NMR measurement

In the ^1H NMR spectrum, HMM shows a single peak at $\delta=3.05\pm0.05$ (Fig.3.6) which corresponds to a total of 18 protons of the six CH_3- groups on the side-chain. Irrespective of the polarity of the solvents, the chemical

Results of multiple regression of the intensity on μ, ϵ, and δ:

$$\text{Intensity (peak)} = .01\mu - 7.05\times10^{-5}\epsilon - 9.69\times10^{-4}\delta + .97 \quad (r^2 = .17,\ n = 19)$$

$$\text{Intensity (peak)} = 7.28\times10^{-3}\mu + 1.94\times10^{-5}\epsilon + .96 \quad (r^2 = .14,\ n = 19)$$

$$\text{Intensity (AUC)} = -8.06\times10^{-3}\mu + 5.90\times10^{-4}\epsilon + 4.13\times10^{-4}\delta + .98 \quad (r^2 = .03,\ n = 19)$$

$$\text{Intensity (AUC)} = -6.78\times10^{-3}\mu + 5.51\times10^{-4}\epsilon + .98 \quad (r^2 = .03,\ n = 19)$$

b) IR measurements

Both the IR spectra of HMM in $CHCl_3$ and in CCl_4 are very similar (Fig.3.5 a and b respectively). The absorption bands at wavenumber 2920, 2850, and 2770 cm^{-1} are due to the $(CH_3)_2N-$ groups, and the bands at 1530 and 1390 cm^{-1} are characteristic of the ring substituted s-triazine (Van de varrt-van zutphen et al, 1982). All these absorption bands show no shifts in $CHCl_3$ as compared to those in CCl_4. The results suggested that any interactions between these functional groups of the HMM molecule and the solvent molecule could not be revealed in the present IR study. The suspensions also gave similar results.

c) ^1H NMR measurement

In the ^1H NMR spectrum, HMM shows a single peak at $\delta=3.05\pm0.05$ (Fig.3.6) which corresponds to a total of 18 protons of the six CH_3- groups on the side-chain. Irrespective of the polarity of the solvents, the chemical

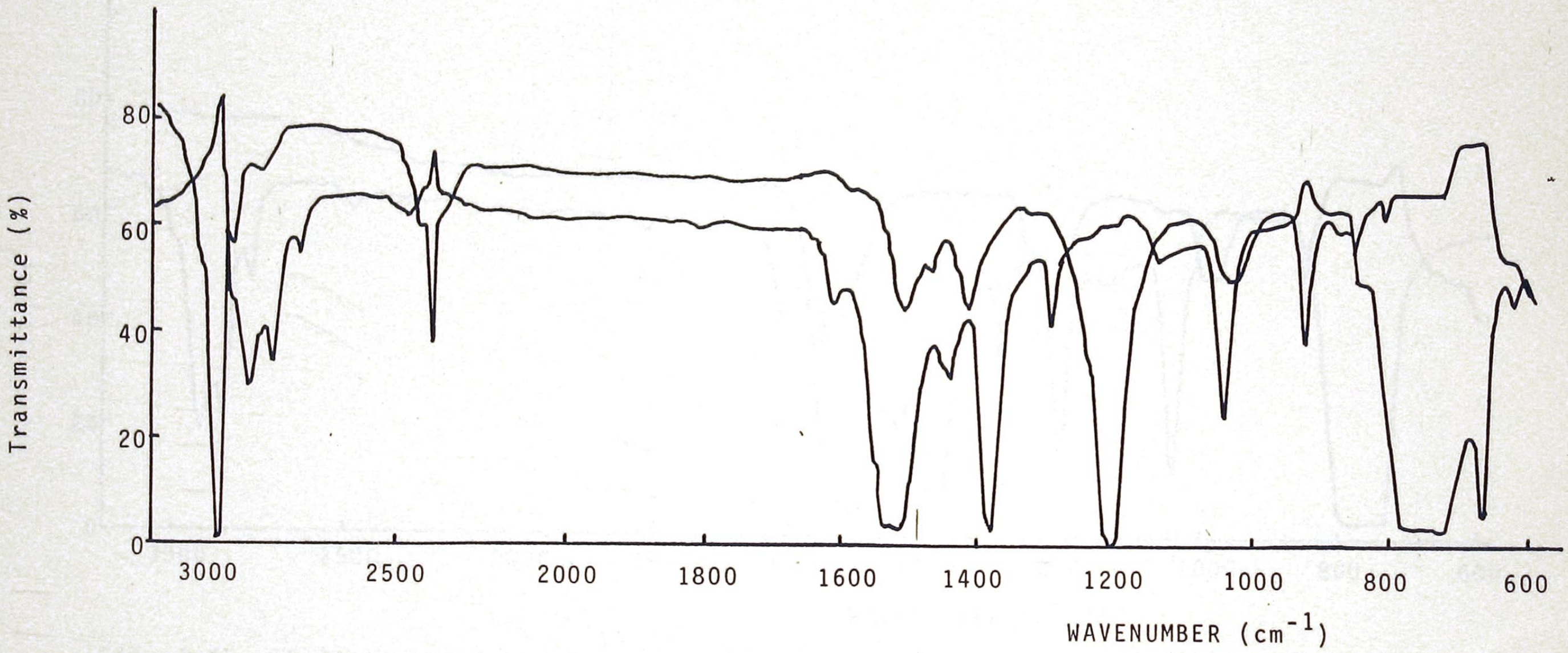

Fig. 3.5a IR Spectrum of HMM in $CHCl_3$
(Upper trace: solvent)

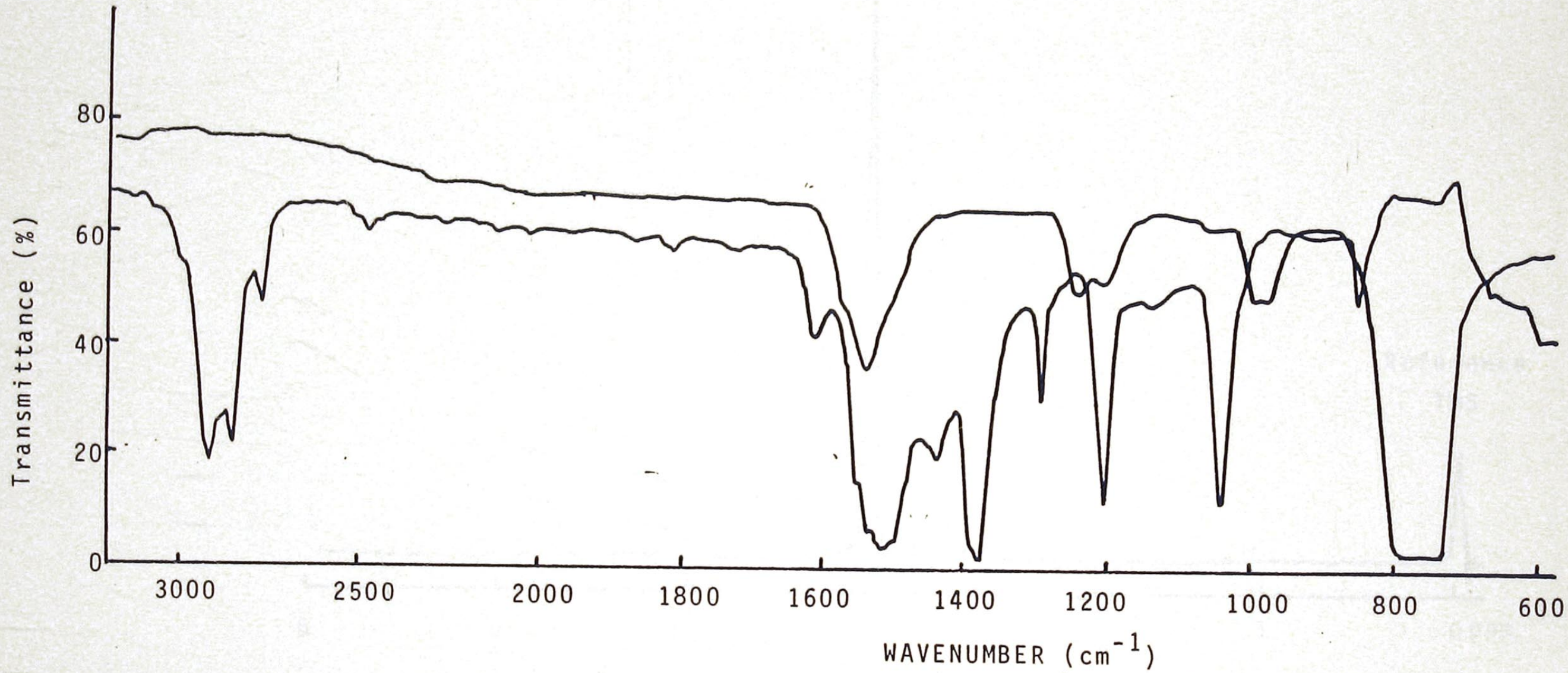

Fig. 3.5b IR Spectrum of HMM in $CHCl_4$
(Upper trace: solvent)

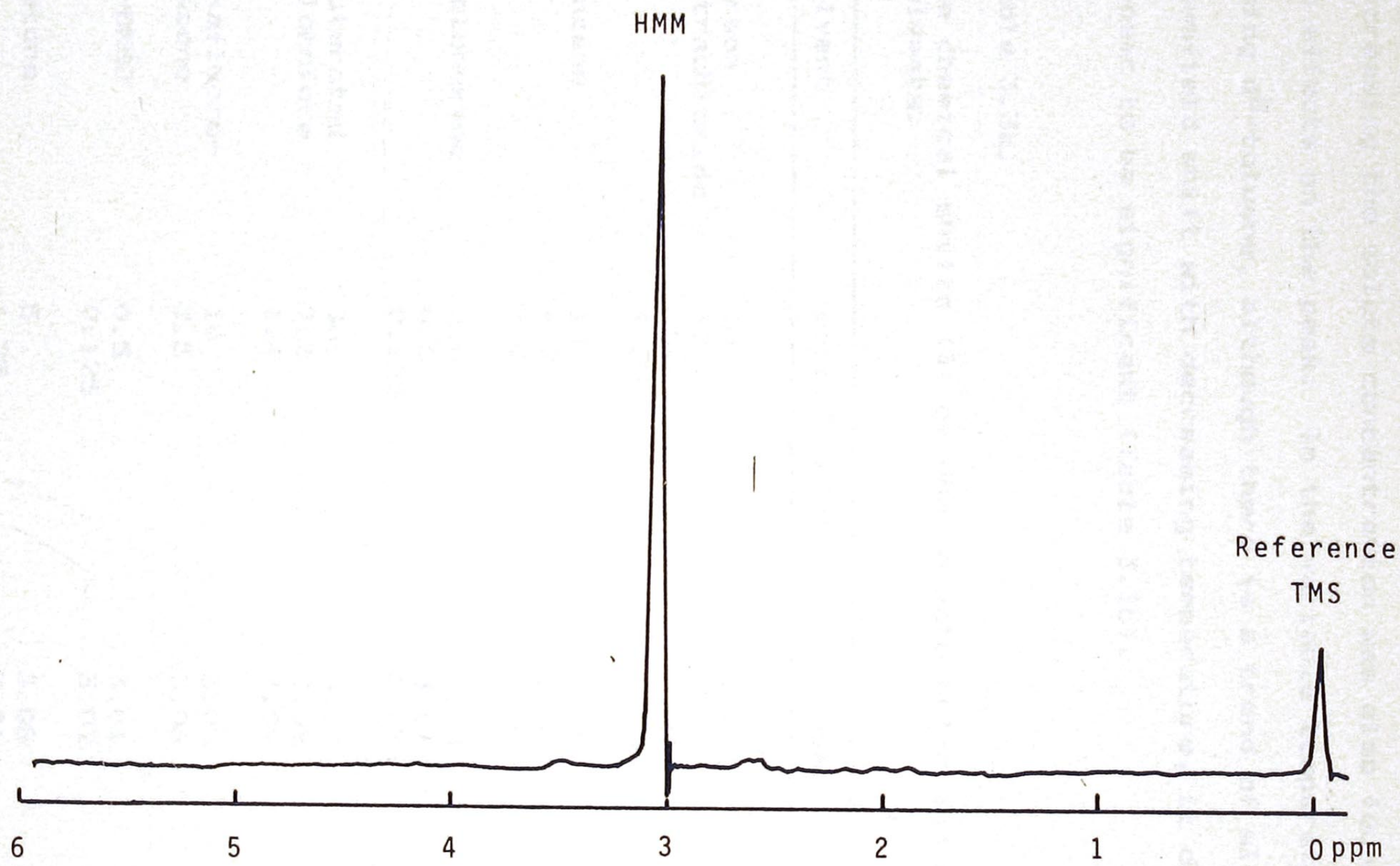

Fig.3.6 ^{1}H NMR Spectrum of HMM

shift remains the same or very similar (Table 3.3a). Increasing the solute concentration was also found to have no effects on the peak. In the variable temperature study using d^8-toluene, although there is a trend of slow downfield shift with decreasing temperature, it does not appear to be significant (Table 3.3b).

Table 3.3a.

The chemical shifts (δ) of HMM in both polar and non-polar solvents.

solvent	conc.(% w/v)	δ(ppm)
carbon tetrachloride	20	3.07
	10	3.07
	5	3.05
	1.25	3.10
benzene	15	3.00
	4.2	3.00
	1.0	3.02
cyclohexane	2.0	3.04
	0.5	3.04
	0.125	3.03
deuterated chloroform	30	3.09
	7.5	3.08
	1.4	3.09
hexafluoro-benzene	10	3.03
	2.5	3.06
d^6-DMSO	0.5	3.01
	0.125	3.02
acetone	5	3.05
	1.25	3.06
	0.03	3.05
pyridine	10	3.10
	1.0	3.08
	0.1	3.09

Table 3.3b. Variable temperature NMR study of HMM in d^8-toluene solution (5% w/v):

temperature (^{0}C)	δ(ppm)
35	2.989
10	2.982
0	2.976
-20	2.969
-50	2.956

Most striking is the absence of strong aromatic-solvent induced shifts (ASIS) which are often found with benzene and hexafluorobenzene and are attributed mainly to a degree of organisation of the magnetically anisotropic benzene molecules about the sensor protons (Armstrong et al, 1973). This suggests that aromatic solvent encounters with the peripheral hydrogen atoms of HMM are relatively weak and overall do not result in the preponderance of shielding or alternatively deshielding HMM/solvent configuration. These rather weak solute-solvent encounters may also be true of HMM in other polar or nonpolar solvents and may explain the lack of observable solvent effects on the various spectra.

d) Molar Kerr measurement

The molar Kerr constants of HMM in various solvents at 298 K extrapolated to infinite dilution are shown in Table 3.4.

Tabe 3.4

solvent	molar Kerr constant $\times 10^{27}$ /m^5 V^{-2} mol^{-1}
cyclohexane	18±1
dioxane	21±1
benzene	18±1
hexafluorobenzene	61±2

Values of the molar Kerr constant for HMM in cyclohexane and dioxane are quite close because both solvents are non-dipolar and the solvating molecules are near isotropically polarisable. However, in benzene it is often found that stereospecific solvation can lead to a time-averaged non-random distribution of the highly anisotropic benzene molecules about the solute and hence to a measured molar Kerr constant which is not that of the "isolated" solute molecule but rather that of the solute-solvent cluster (Armstrong et al, 1973). Such observed solvent effects on the solute molar Kerr constant have been interpreted to obtàin information on the preferred stereospecific solute-solvent encounters. For HMM, however, the molar Kerr constant measured is virtually unchanged from that in cyclohexane which means that the statistical distribution of the solvating benzene molecules is such that the solute polarisability is augmented to the same extent in the direction of the triazine plane of HMM as perpendicular to that plane. This suggests that within a dynamic cluster model, solute-solvent encounters in which the HMM and benzene

planes are parallel are no more or no less favoured than encounters in which the planes are perpendicular. Steric and electrostatic considerations are used to rationalize HMM-solvent interaction. Face-to-face approaches like A in Fig.3.7 result in an enhanced solute anisotropy and hence a greater apparent solute Kerr constant (in the absence of significant charge transfer). Contributions to the cluster from approach such as B with the relatively electrophilic benzene periphery close to the electron rich triazine system or to the exocyclic nitrogens would result in a decreased apparent solute Kerr constant. Angular encounters such as C have far less effect on the solute Kerr constant. Finally, the effect on the solute Kerr constant of incoming benzenes approaching in the plane of HMM (e.g. D or E) would be small as their encounter with nitrogen polar centres is sterically blocked by the peripheral methyl groups of HMM. Thus, as in the spectroscopic studies, no predominant HMM-solvent configuration can be identified. (The distinctive hexafluorobenzene result is discussed in Sec.3.5).

iii) Conclusions

The molar Kerr measurement together with the spectroscopic results as a whole show an absence of solvent effects. It is thus inferred that HMM-solvent interactions in solution are particularly weak and no statistically predominant stereospecific interaction can be identified as responsible for the modification of HMM crystal habits in

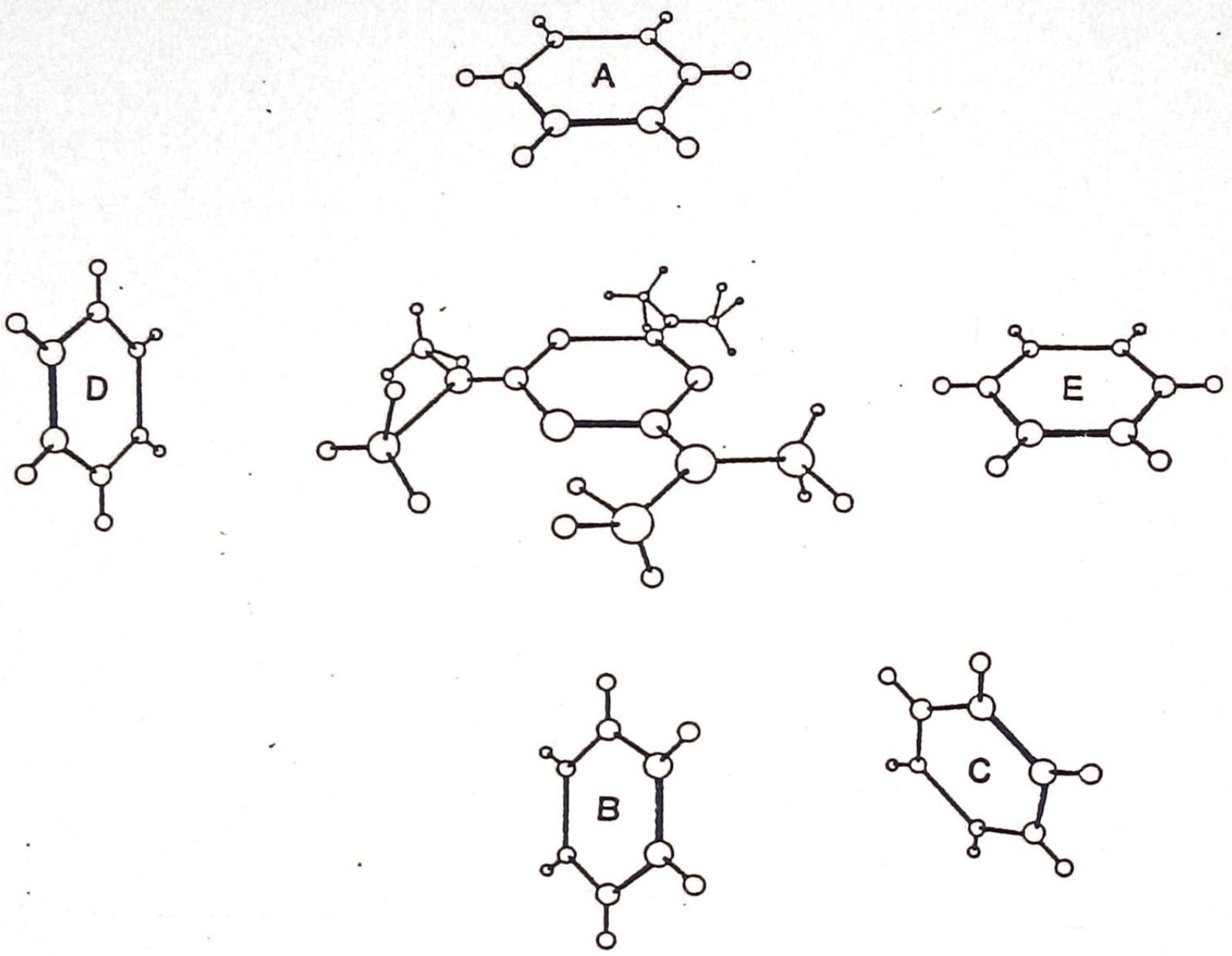

Fig. 3.7 Stereospecific encounters between HMM and solvating aromatic molecules

different solvents.

Future work could be attempted on solvent-solid (crystal face) interactions e.g. by studying the interfacial tensions.

3.4 Growth Kinetics and α-factor Evaluation

i) Experimental

a) Measurement of HMM solubility

In order to obtain information about the solution chemistry of HMM for the growth kinetics and the α-factor evaluation, solubilities of HMM in both a polar and a non-polar solvent at various temperatures were determined. Methanol and cyclohexane, which give needle and compact habit respectively, were used.

Excess HMM in the solvent (Univar, Ajax Chemicals, Sydney) was stirred vigorously inside a stoppered glass-tube (i.d. 60mm) in a water bath by a magnetic stirrer (Chiltern Scientific). The temperature of the bath was controlled by a proportional temperature controller (YSI model 72, Yellow Springs Instrument Co., Yellow Springs, Ohio, U.S.A.) and a cooling unit (CryoCool, Neslab Instruments Inc.). Five predetermined equilibrium temperatures between 10 and 30^{0}C were used. To avoid the asymptotic approach to saturation (James, 1986), the solution was first heated at a temperature of 2^{0}C above the required value for 1 hour before equilibration at the desired temperature. Afterwards sampling was done at a time interval of 6-90 hours (to assure equilibrium solubility value) as follows: The solution was left unstirred for 1 hour to settle the drug particles. Then solution samples were taken by a guarded pipette which has been equilibrated at the same

temperature (the tip of the pipette was connected to a Teflon tubing inside which was a plug of tightly-packed washed glasswool and has been found to give undetectable interference or adsorption at the HMM concentration measured). The sampled solution was transferred and separated into two 50ml volumetric flasks, weighed and diluted appropriately to give the UV absorbance between 0.5 - 1.0. All the dilutions were made at 20^0C to minimize volume expansion effects. The calibration lines of UV absorbance of HMM in methanol and cyclohexane have been found using concentrations of 0.5- 4.0 µg/ml which cover absorbance of range 0.1- 1.0 in a 1 cm cuvette [In methanol: absorbance= 4.098×10^{-3}+ .2496x concentration (µg/ml), n=7, r^2=0.9999; in cyclohexane: absorbance= 4.941×10^{-3}+ .2390x concentration (µg/ml), n=5, r^2=0.9999)].

b) Study of growth kinetics of single crystals

The growth kinetics of single crystals of HMM in methanol and cyclohexane were studied using a growth cell (Fig.3.8) with construction adapted from Maeyashiki et al (1982). The whole set-up is shown in Fig.3.9. The cell was first put under focus on the stage of a microscope (Olympus 220502) and was equilibrated at 20^0C (below the room temperature) for 1 hour by circulating water from a refrigerated bath circulator (Julabo PC-F18 with digital display, temperature accuracy ± 0.02^0C, Julabo Labortechnik GMBH, Schwarzwald, W. Germany). The room temperature was controlled at 24.5 ± 0.5^0C. The

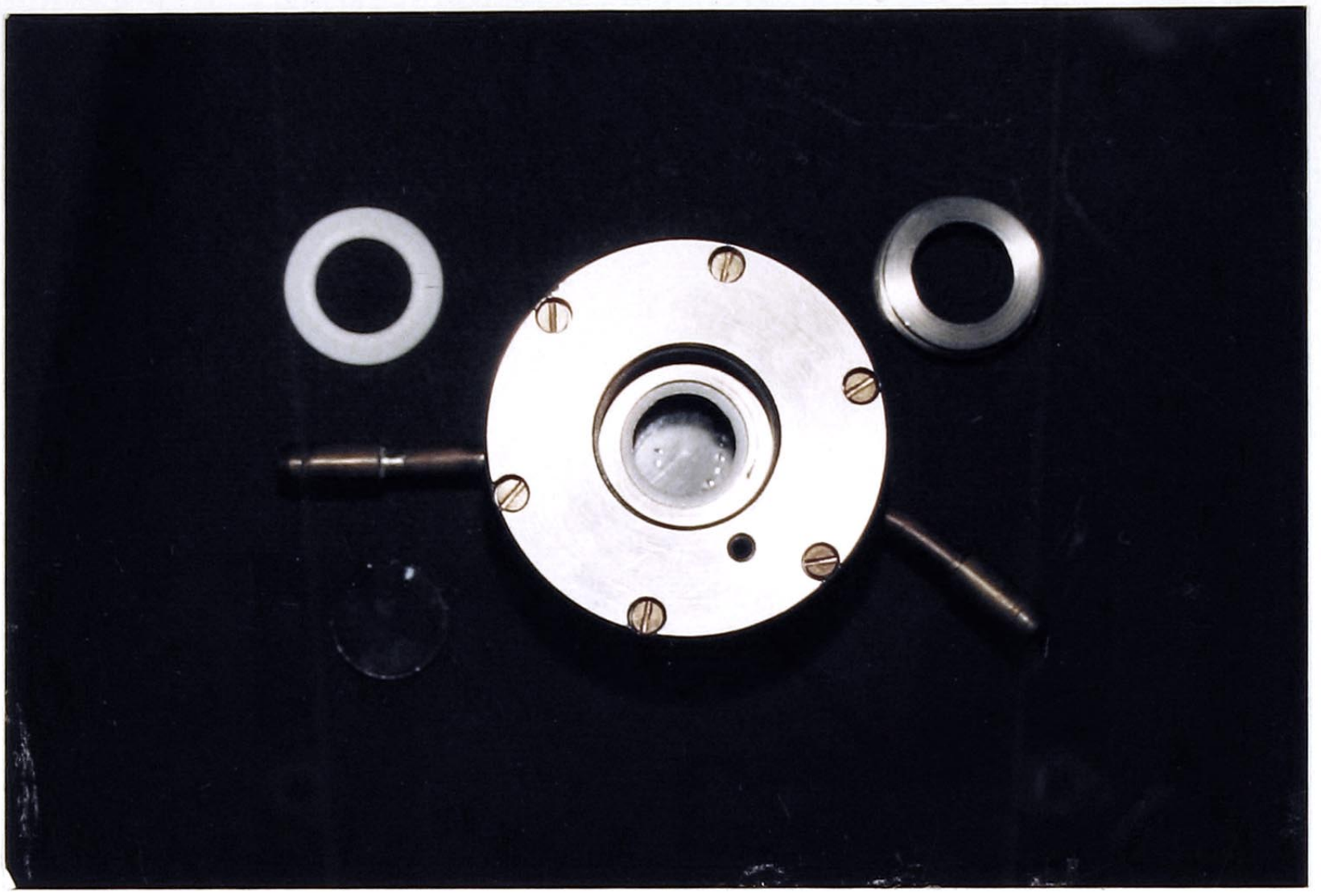

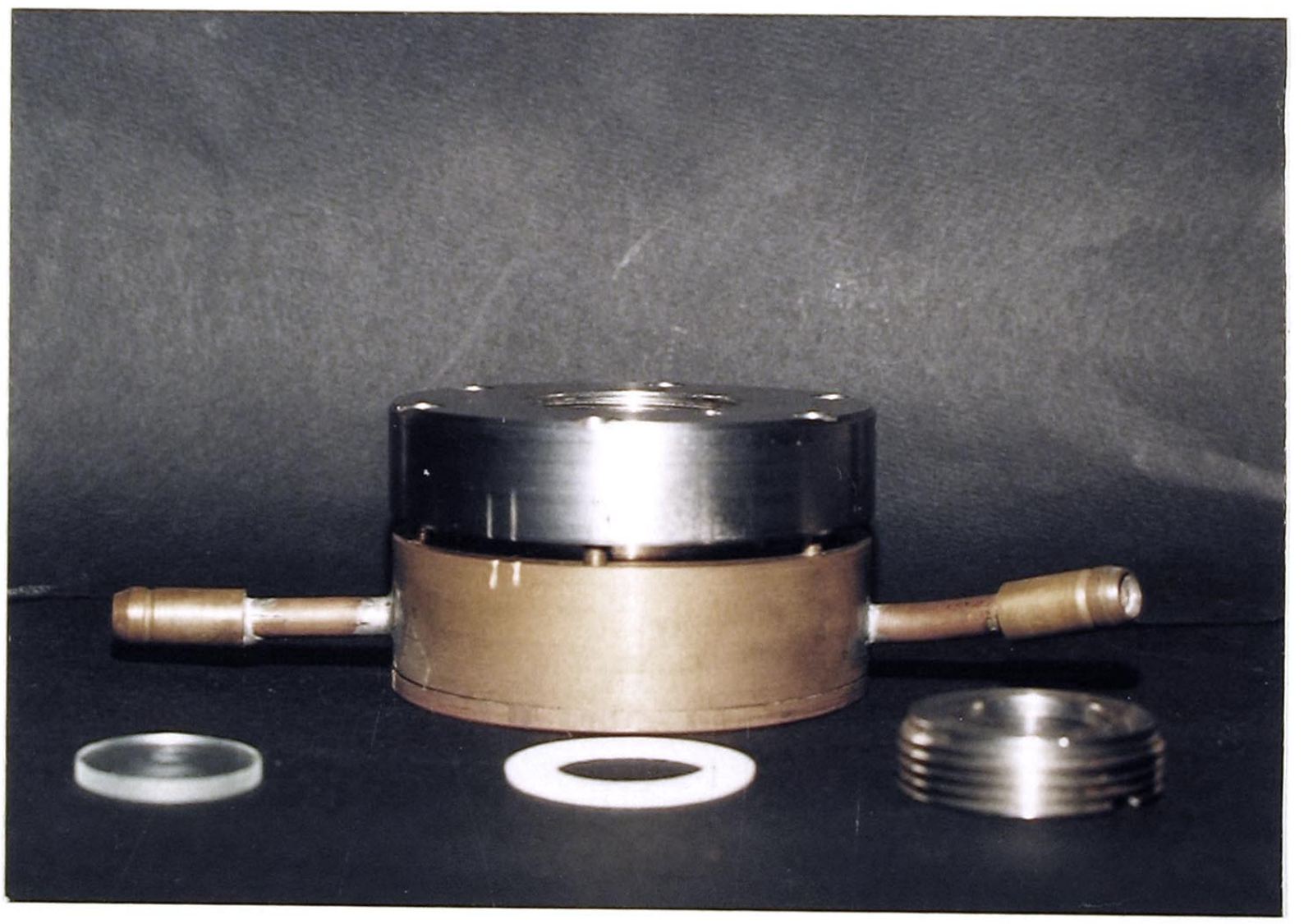

Fig. 3.8 The growth cell for crystal growth kinetics measurement
Top: Top view
Bottom: Lateral view

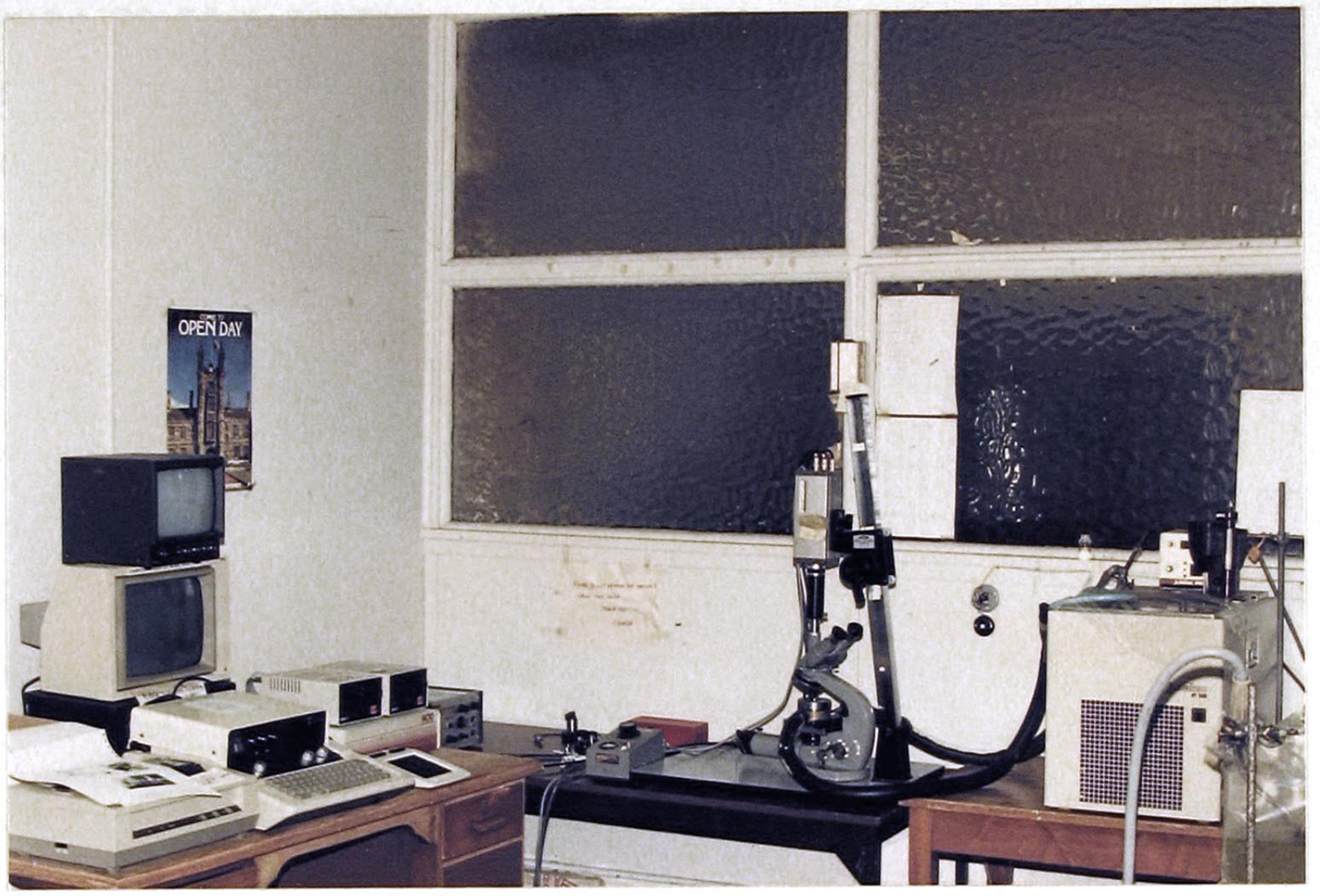

Fig. 3.9 The whole set-up for crystal growth kinetics measurement

temperature of the solution inside the cell was measured to be 20.54 ± 0.15^{0}C by a glass temperature probe (YSI 404) (which was inserted inside through a plug from above). The fluctuation of the solution temperature was found to be within ± 0.15^{0}C which corresponds to an error of less than 5% when an undercooling of 4^{0}C is used as in the present study. Saturated solutions of HMM [as prepared in Sec.a)] which had been equilibrated at 24^{0}C and then left undisturbed for more than 48 hours were used as the stock solutions. 15 ml of the clear supernatant was pipetted into the cell chamber. Due to the undercooling of the solution, spontaneous nucleation took place and the nuclei grew into the seed crystals. Observation was made using an objective lens (M5, Olympus, Tokyo, Japan) of the microscope which was connected to a TV camera. The latter was in turn linked to the image analysis system [see Chapter 1, Sec.1.7.1 iii) for detailed description of the whole system] which recorded the subsequent growth of the seed crystals in the stagnant solution by storing the video (grey) image of the crystals in the computer hard disk at fixed time intervals. The stored images were later enlarged twice to facilitate the editing for measurement. Growth of the length and the breadth, which is the same as growth along the [0001] direction and the [1100] direction or along and normal to the crystallographic c-axis respectively were measured as the L and B in the diagram below:

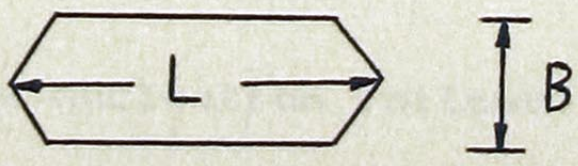

The growth rates were found from the dependence of L and B on time and expressed as R_L (≡ R[0001]) and R_B (≡ R[1100]) respectively.

Estimate of errors in the measurement

The microscope was fitted with a low magnification lens (M5, Olympus) which has a resolution power R calculated by the Abbe formula as 2.5μm [R = λ/2NA, λ: wavelength of the illumination= 500nm, NA: numerical aperture of the lens = 0.1]. Since R is well below the dimension of the crystal, the lens is thus powerful enough to resolve the images. The error in the measurement of the crystal dimension was mainly introduced by editing the image.

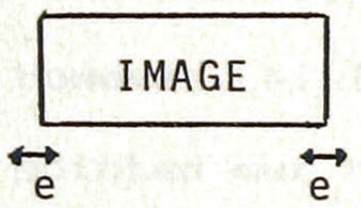

e= max. error in editing, which equals 2 pixels.
Under the experimental conditions and the magnification used, 2 pixels = 3.51 μm. Therefore, the most probable error is $\sqrt{3.5^2 + 3.5^2}$ or just below 5μm which contributes to less than 10% in the measurement (except for time < 5 minutes when the crystal was small, the error < 20%). This magnitude of error seems to be reasonable and has widely occurred in crystal growth literatures (Mullin, 1972).

c) Determination of the supersaturation

Due to the spontaneous nucleation followed by crystal

growth, solute depletion resulted which led to a change in concentration (and thus supersaturation) of the solution in the cell. The decrease in the solute supersaturation with time can be found by measuring the solute concentration under the same experimental conditions as in Sec.3.4 i) b). This was carried out by terminating the experiments at predetermined times. Samples of the cell solution were then taken, weighed, diluted and measured spectrophotometrically as in Sec.3.4 i) a) to determine the solute concentration.

d) Estimation of purely diffusion controlled growth rate

R vs σ curve are usually plotted for studying growth mechanism. However, Nielsen (1984) and Nielsen and Toft (1984) have pointed out that there is little point in discussing empirical growth rate data from the point of view of mechanisms if the data are not first of all analysed to determine whether the growth rate is (volume) transport controlled or surface controlled. This can be identified by calculating the growth rate, R_d, of a purely diffusion controlled mechanism and comparing the values with that measured experimentally. R_d can be estimated by the following expression (Nielsen, 1964; 1980; Nielsen and Christoffersen, 1982):

$$R_d = D\, V_m\, (C-C_s)/\delta$$

D: diffusion coefficient

$\simeq 10^{-5}$ cm^2/s or 10^{-9} m^2/s (Wilke and Chang, 1955; Martin et al, 1983)

Vm : molar volume of HMM = mol. wt./ density

mol. wt. of HMM : 210.27 g/mol;

density : 1.11g/cm^3 (Gonda et al, 1985a)

= 189.43 cm^3/mol or 1.89 x 10^{-4} m^3/mol.

C_s: saturated solute conc. at the cell temperature

C: solute conc. in the cell which in the present study is a function of the time t.

$C - C_s$ can be obtained from the results in Sec.3.4 ii) b) and Table 3.7 a&b as σC_∞

In methanol,

$C - C_s$ = 1.9±0.2 mg/ml or 9.04±0.95 mol/m^3 (at t = 5 mins)

= 0.27±0.09 mg/ml or 1.28±0.43 mol/m^3 (at t = 60 mins)

δ = thickness of the unstirred layer which is a function of the particle radius r (assuming a sphere) and the stirring rate; when the system is motionless (stagnant) δ is approximated by r (Nielsen, 1980)

taking r = half the length L or the breadth B:

L/2 = 40 and 90 μm

B/2 = 25 and 50 μm

(the 2 values for L/2 and B/2 are at t = 5 and 60 mins respectively).

Since R_d is calculated for a single face only, it has to be multiplied by 2 before comparison with the experimental values which was measured for 2 parallel faces. By substitution, values of R_d in methanol can be obtained as follows:

For the length L,

R_d at 5 mins = 10^{-9} x 1.89 x 10^{-4} x (9.04±.95)/(40 x 10^{-6}) x 2

$= (.85\pm.09) \times 10^{-7}$ m/s

or 5.12 ± 0.54 μm/min.

R_d at 60 mins $= 10^{-9} \times 1.89 \times 10^{-4} \times (1.28\pm.43)/(90 \times 10^{-6}) \times 2$

$= (5.39\pm1.81) \times 10^{-9}$ m/s

or $0.32\pm.11$ μm/min.

For the breadth B, similarly, R_d's were found by substituting the appropriate values in the expression for R_d.

In cyclohexane,

$C - C_s = 4.44\pm0.22$ mg/ml or 21.12 ± 1.06 mol/m^3 (at t = 5 mins)

$= 2.13\pm0.10$ mg/ml or 10.14 ± 0.51 mol/m^3 (at t = 60 mins)

L/2 = 60 and 180 μm

B/2 = 40 and 90-140 μm

(the 2 values for L/2 and B/2 are at t = 5 and 60 mins respectively).

Likewise, by substitution, R_d's for the length and the breadth of crystals in cyclohexane were calculated.

e) Evaluation of the α-factor

In the present study, due to the lack of knowledge of the edge energy Υ for HMM crystals, the α-factor was evaluated from the heat of fusion (ΔH_f), density and solubility of HMM at 20^0C, and the heat and entropy of solution (ΔH_s and ΔS_s) using eqns.(3.4), (3.2) and (3.1). Density and ΔH_f were obtained from literature (Gonda et al, 1985). Solubility, ΔH_s and ΔS_s can be obtained from the solution

chemistry of HMM measured in Sec.3.4 i) a).

By means of a van't Hoff's plot of log X vs $1/T \times 10^3$ (X: mole fraction of HMM in the saturated solution at equilibrium temperature T), ΔH_s was found from the slope which equals $-\Delta H_s/2.303\ R$ where R is the gas constant (James, 1986). Similarly, ΔS_s was found from the slope of a plot of lnX vs lnT which equals $\Delta S_s/R$ (James, 1986).

The crystallographic factor ξ of HMM was obtained from the crystal structure (Bullen et al, 1972).

ii) Results and Discussion

a) Solubilities of HMM in methanol and cyclohexane

The apparent equilibrium solubilities of HMM were found to reach within 24-48 hours and the errors in the measurement were less than 1%. The results are summarized in Table 3.5.

Table 3.5

Temperature (^{0}C)	Equilibrium solubility (mg/ml) mean ± s.d.	
	methanol	cyclohexane
10	13.877±0.048 (n=4)	20.557±0.1576 (n=4)
15	16.543±0.002 (n=2)	26.294±0.241 (n=2)
20	19.306±0.136 (n=4)	31.350±0.205 (n=4)
25	23.097±0.063 (n=2)	38.745±0.050 (n=2)
30	26.820±0.075 (n=4)	49.135±0.391 (n=2)

b) Growth kinetics and supersaturation

Three separate runs were carried out in each of the solvents. A total of 12 crystals in methanol and 4 crystals in cyclohexane were measured. The smaller number of the latter corresponded to larger crystal sizes due to the higher growth rate and supersaturation σ.

The increase in size (L and B) of the crystals with time is shown in Fig.3.10 a-f (in methanol) and Fig 3.10 g&h (in cyclohexane). The growth rate is not linear (constant) as the size increment decreased with time due to the decline in supersaturation. The relationship between the crystal size (L and B) and time (t) was best described using $\sqrt{t}$ as the independent variable and fitting into second and/or third degree polynomial equations (r^2 = 0.99):

$$L \text{ or } B = C + C_1 \sqrt{t} + C_2 t + C_3 t^{3/2}$$

Values of C, C_1, C_2, and C_3 are given in Appendix 5. The growth rates of the length and the breadth (R_L and R_B respectively) of the crystal were found from the first derivative of the equation which is

$$R_L \text{ or } R_B = C_1/(2\sqrt{t}) + C_2 + (C_3 \sqrt{t})\ 3/2$$

The results of the triplicate runs are shown in Table 3.6 a-d. All the values in the tables were rounded off from original 4 decimal figures.

Fig.3.10 a-f

Growth of the length (L) and the breadth (B) of the crystals vs time for 3 separate runs (a total of 12 crystals) in methanol. Each number is corresponding to an individual crystal.

Fig.3.10 g-h

Growth of the length (L) and the breadth (B) of the crystal vs time for 3 separate runs (a total of 4 crystals) in cyclohexane. Each number is corresponding to an individual crystal.

Fig.3.10a(Run1)

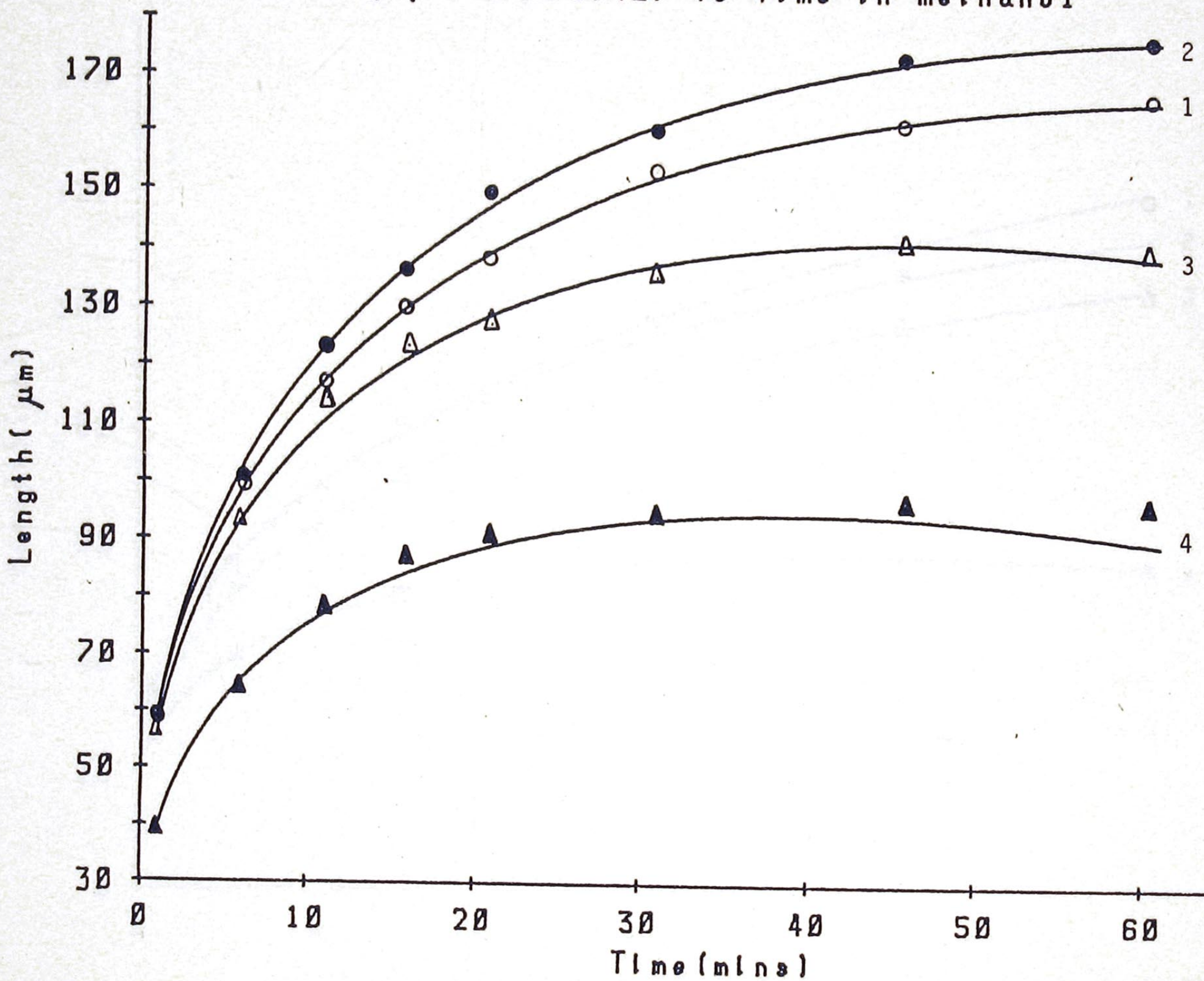

Fig.3.10b(Run1)

Crystal Size(B) vs Time

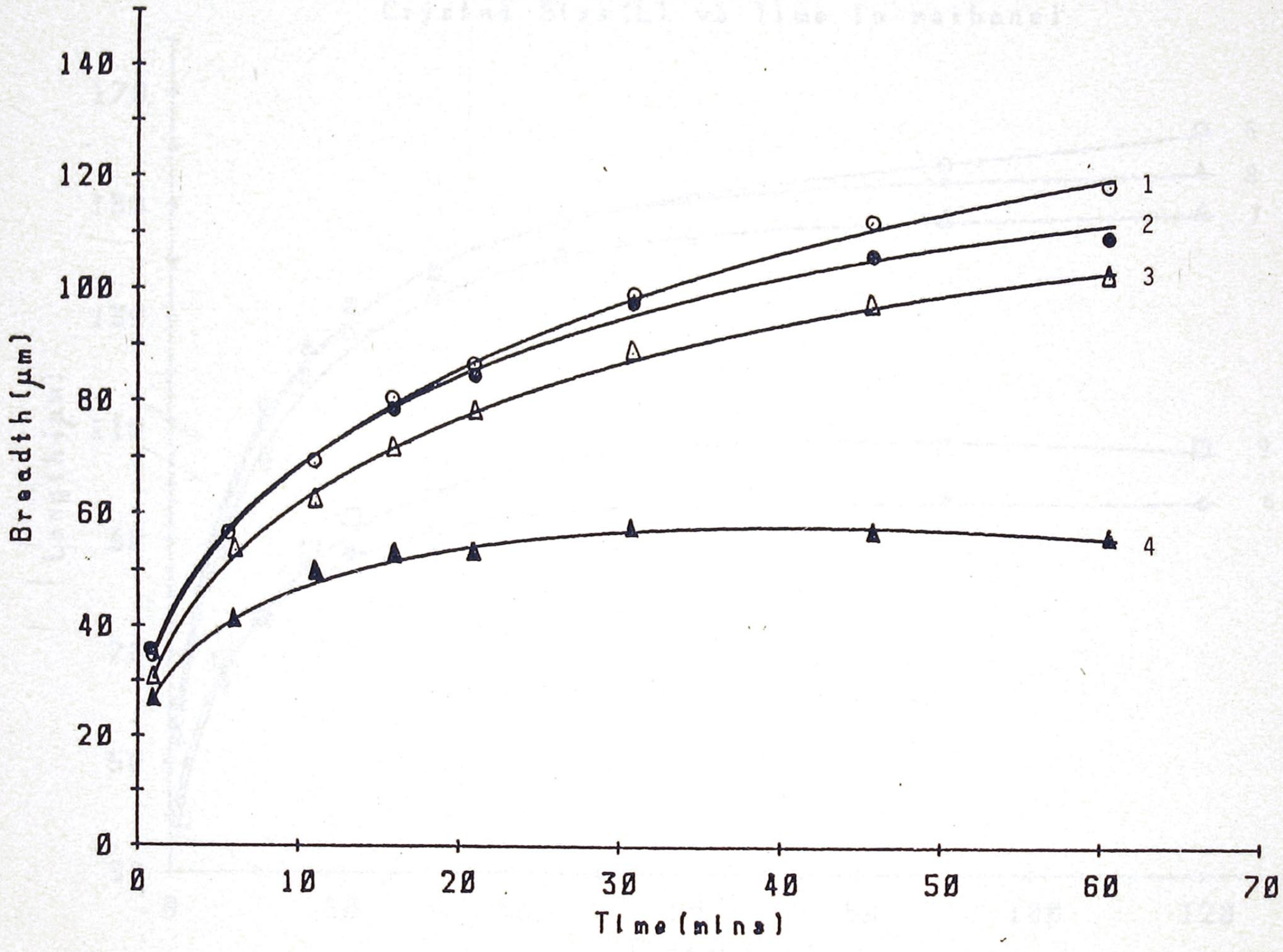

Fig.3.10c(Run2)

Crystal Size(L) vs Time in methanol

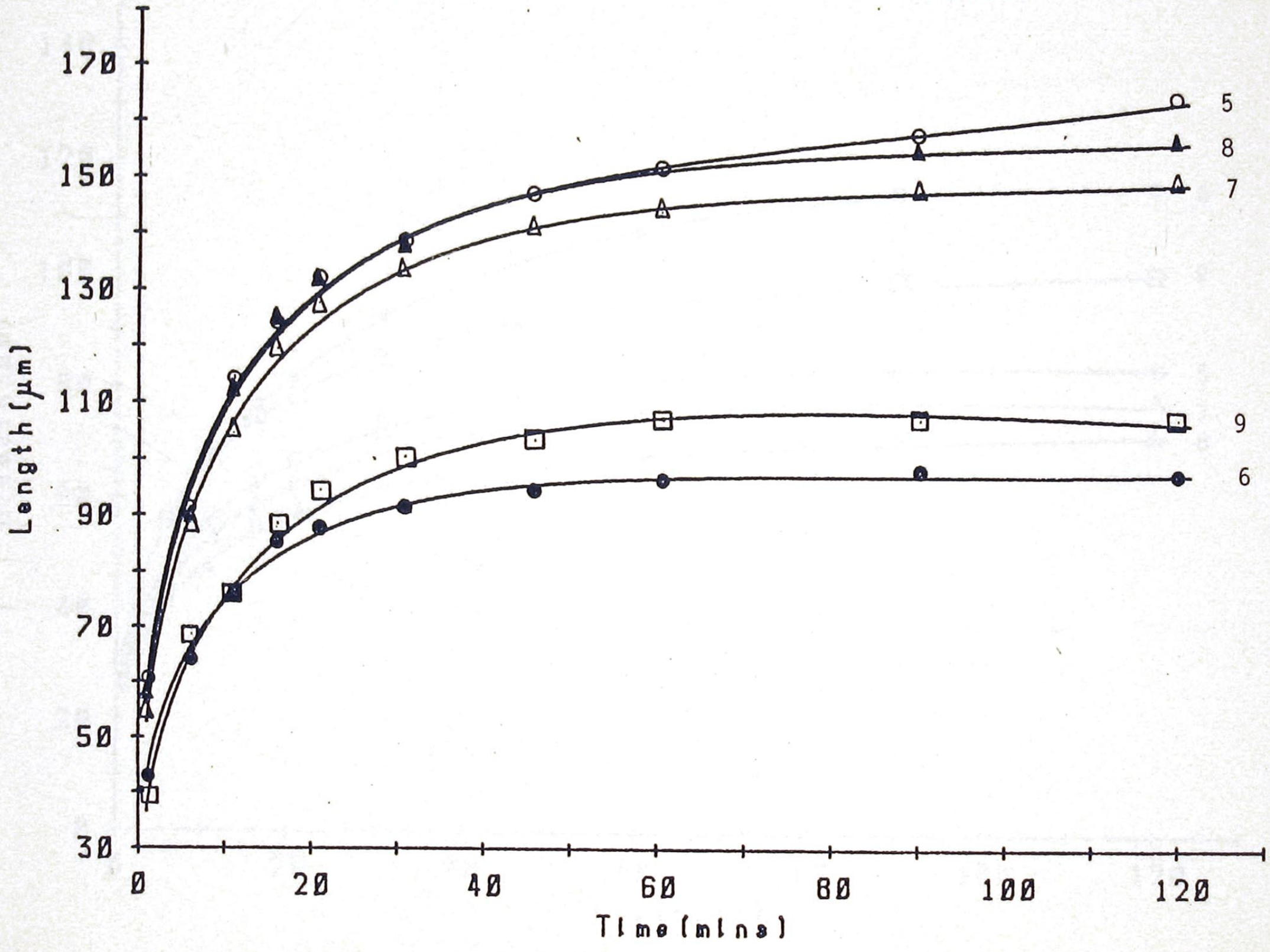

Fig.3.10d(Run2)

Crystal Size(B) vs Time

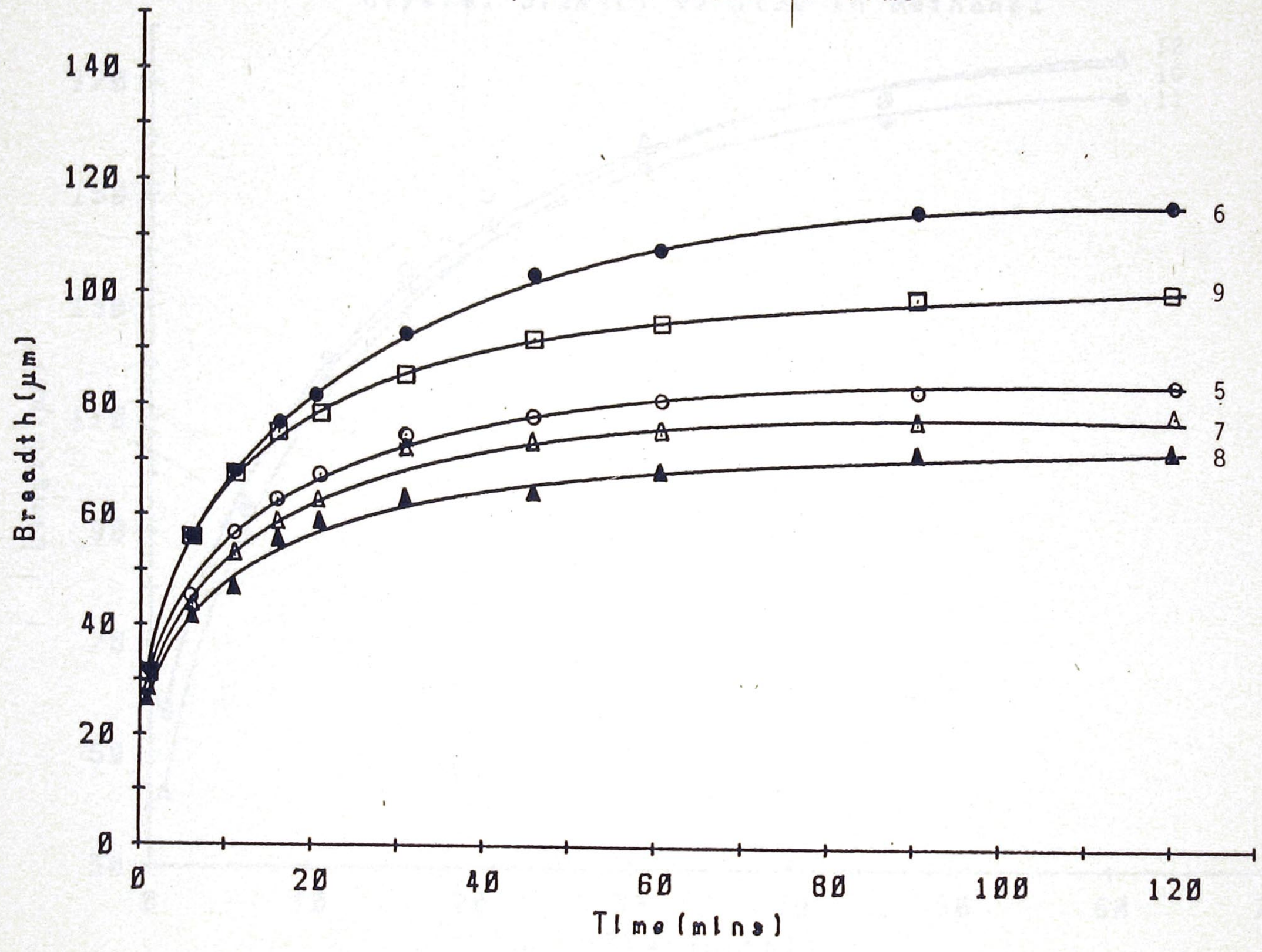

Fig.3.10e(Run3)

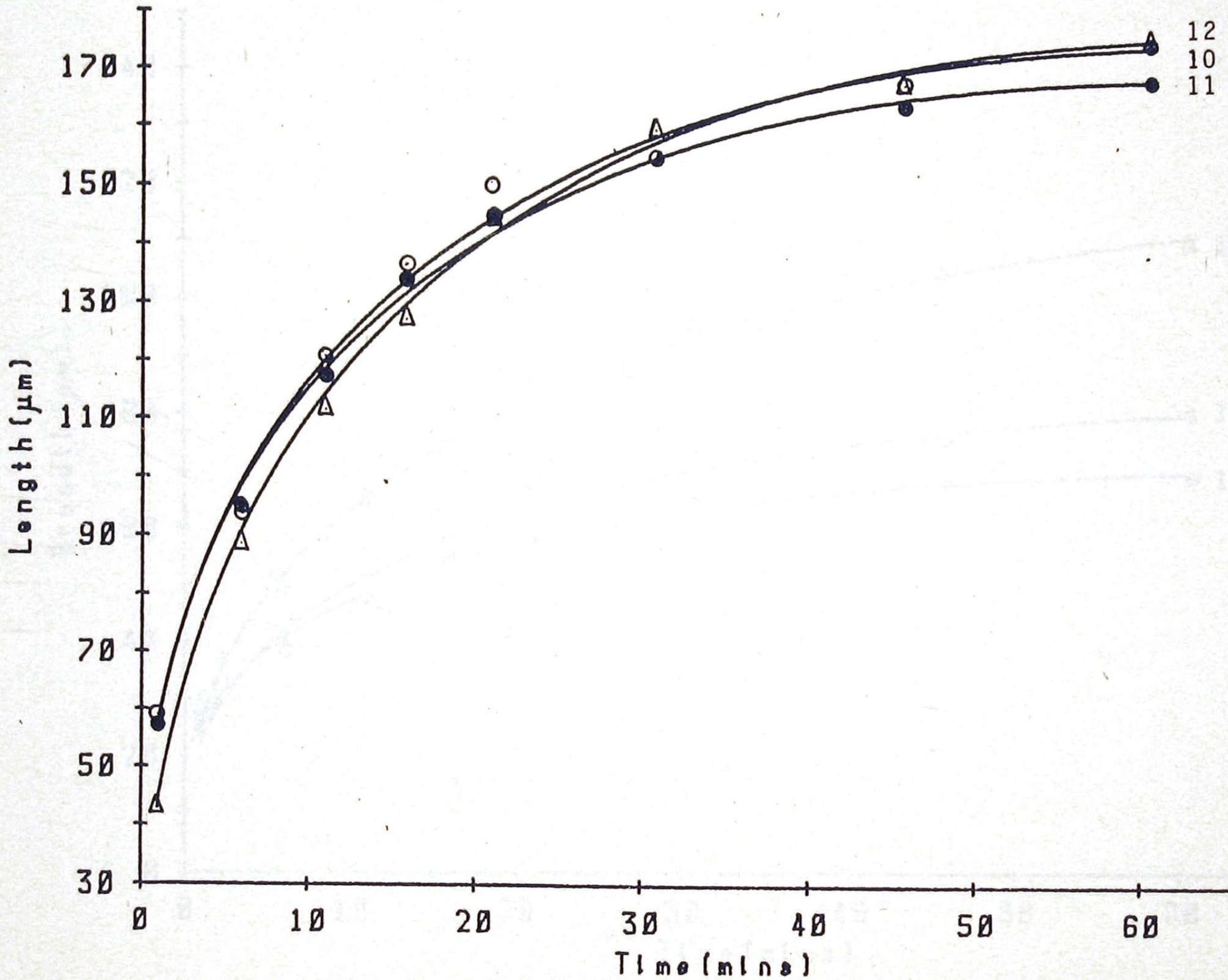

Fig.3.10f (Run3)

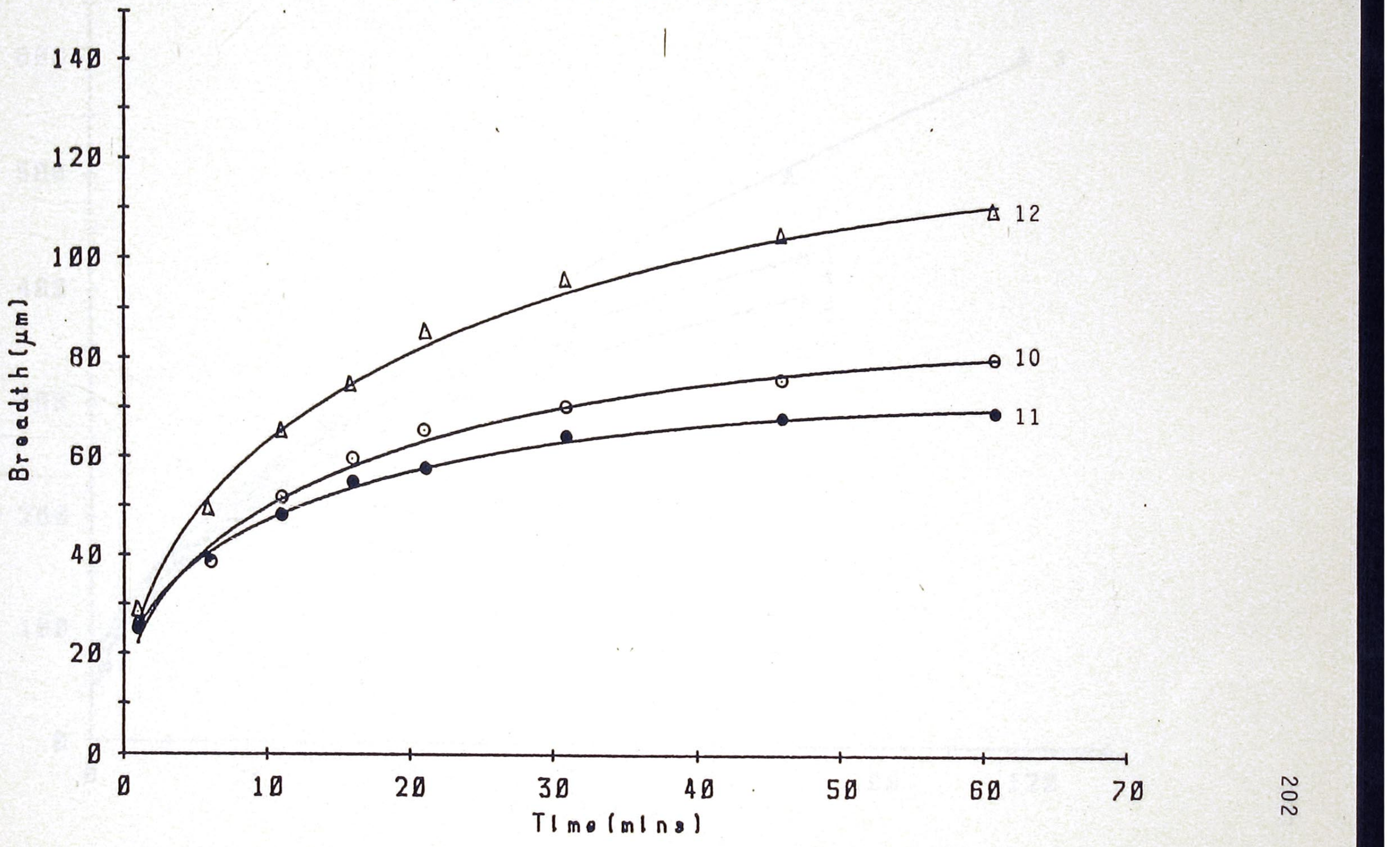

Fig.3.10g(3 Runs)

Crystal Size(L) vs Time in Cyclohexane

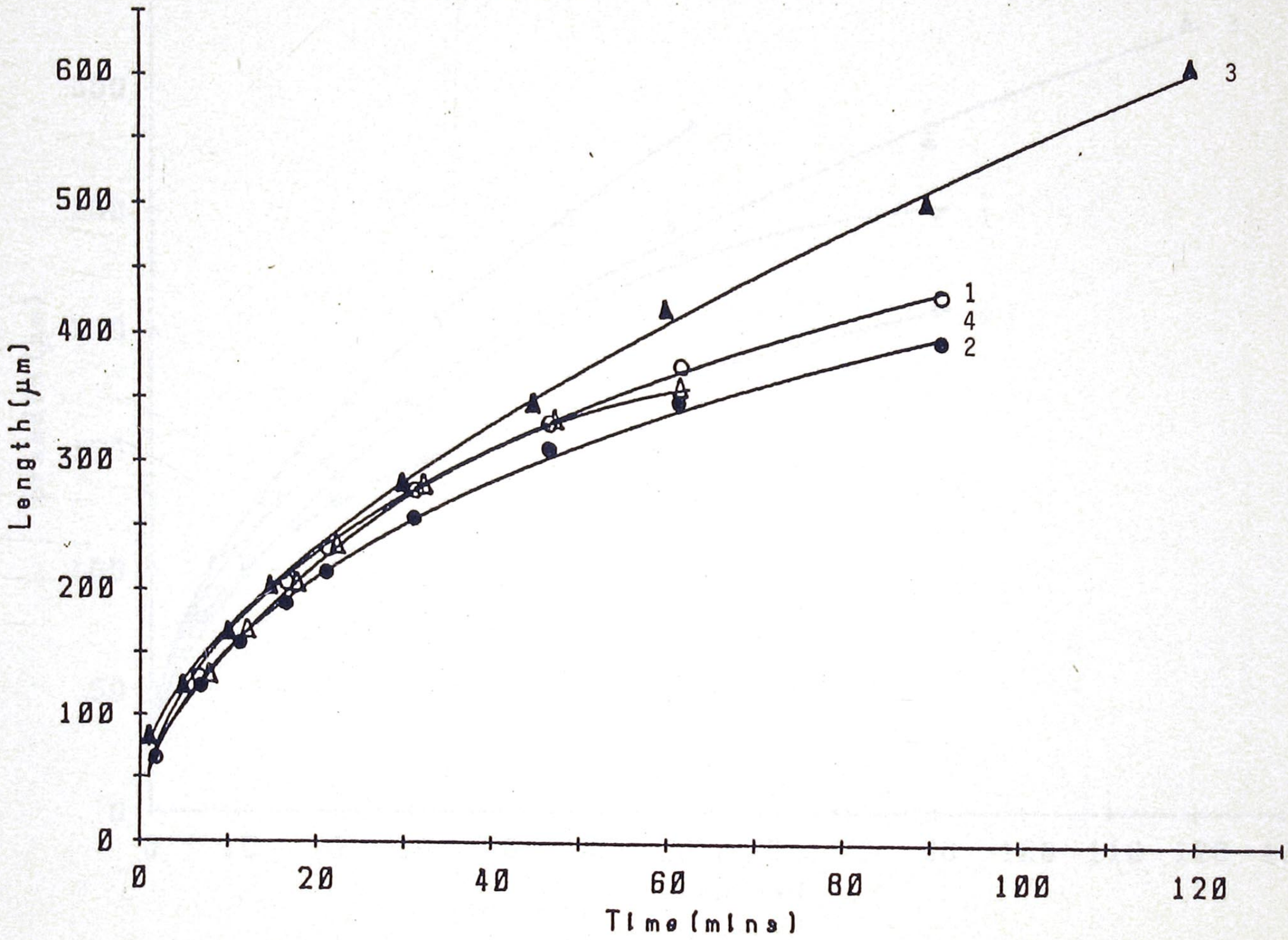

Fig.3.10h(3 Runs)

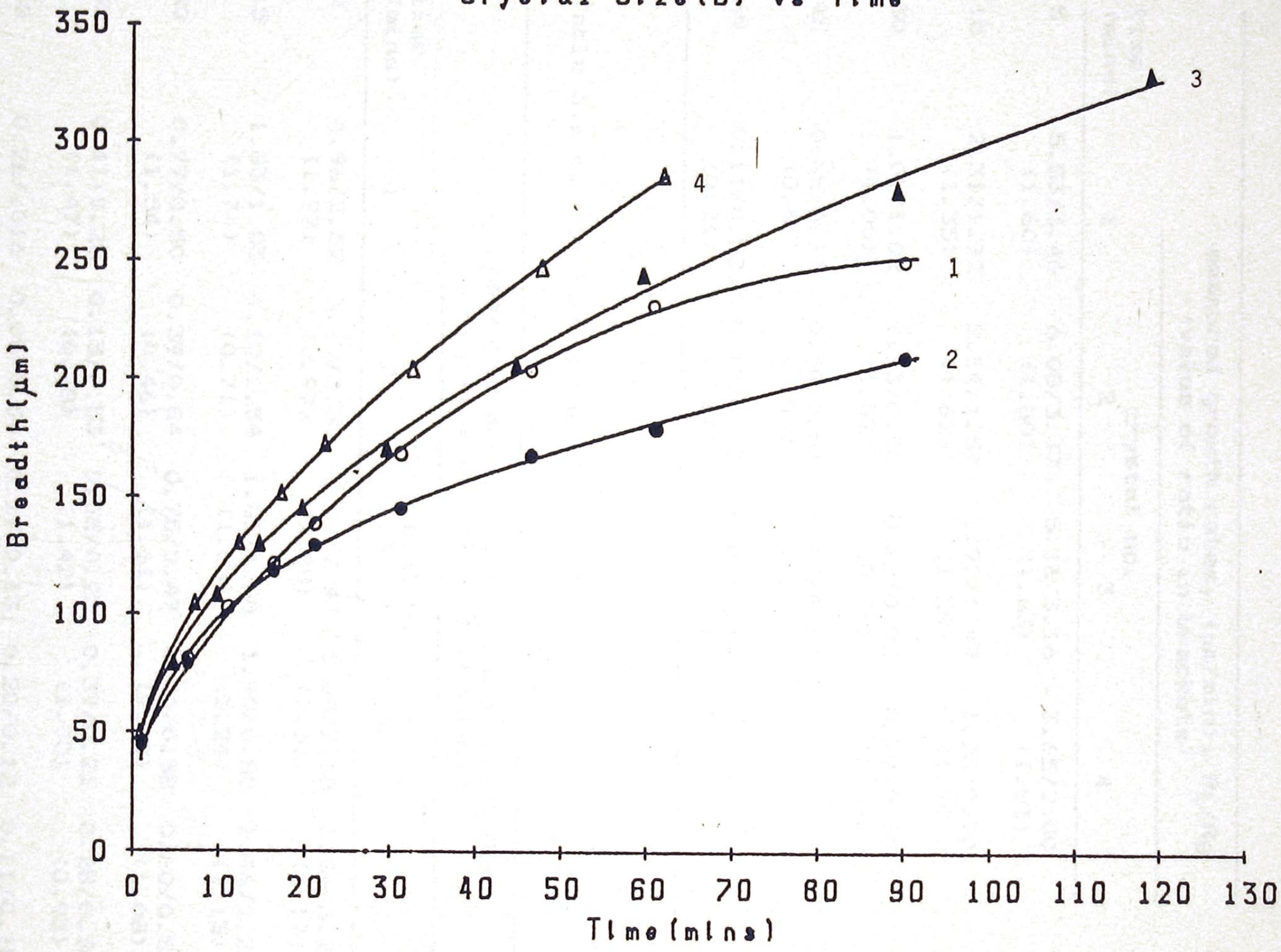

Table 3.6 a. run 1 in methanol

time (mins)	measured growth rates, (μm/min), R_L/R_B (value of ratio in brackets) crystal no. 1	2	3	4
5	5.53/3.46 (1.60)	6.08/3.37 (1.80)	5.16/3.16 (1.63)	3.65/2.00 (1.83)
15	2.31/1.72 (1.35)	2.54/1.57 (1.62)	1.92/1.49 (1.29)	1.25/0.70 (1.79)
30	1.02/1.02 (1.00)	1.13/0.85 (1.32)	0.62/0.82 (0.76)	0.29/0.18 (1.64)
45	0.45/0.71 (0.63)	0.50/0.54 (0.93)	0.05/0.52 (0.10)	–
60	0.11/0.52 (0.21)	0.12/0.35 (0.34)	0.00/0.34 (–)	–

Table 3.6 b. run 2 in methanol

time (mins)	measured growth rates, (μm/min), R_L/R_B (value of ratio in brackets) crystal no. 1	2	3	4	5
5	4.96/2.52 (1.97)	3.19/3.30 (0.97)	5.04/2.43 (2.08)	5.08/2.18 (2.33)	3.84/3.29 (1.17)
15	1.83/1.05 (1.74)	1.10/1.54 (0.71)	1.85/1.00 (1.85)	1.90/0.85 (2.24)	1.46/1.27 (1.15)
30	0.77/0.50 (1.54)	0.39/0.84 (0.46)	0.75/0.47 (1.61)	0.80/0.38 (2.09)	0.60/0.56 (1.08)
45	0.41/0.28 (1.47)	0.15/0.53 (0.28)	0.35/0.25 (1.42)	0.39/0.21 (1.90)	0.28/0.30 (0.93)
60	0.26/.016 (1.61)	0.05/0.34 (0.14)	0.17/0.13 (1.30)	0.20/0.12 (1.65)	0.11/0.18 (0.64)

Table 3.6 c. run 3 in methanol

time (mins)	measured growth rates, (μm/min), R_L/R_B (value of ratio in brackets) crystal no. 1	2	3
5	6.06/2.78 (2.18)	5.84/2.26 (2.58)	6.78/3.82 (1.78)
15	2.54/1.22 (2.08)	2.42/0.97 (2.50)	2.85/1.76 (1.62)
30	1.14/0.60 (1.90)	1.05/0.45 (2.35)	1.28/0.94 (1.37)
45	0.52/0.32 (1.60)	0.44/0.22 (2.04)	0.59/0.57 (1.03)
60	0.15/0.16 (0.92)	0.08/0.08 (1.02)	0.17/0.36 (0.48)

Table 3.6 d. Three runs in cyclohexane

time (mins)	measured growth rates, (μm/min), R_L/R_B (value of ratio in brackets) crystal no. 1 (Run 1)	2 (Run 1)	3 (Run 2)	4 (Run 3)
15	6.10/4.00 (1.52)	5.59/2.69 (2.08)	6.20/3.64 (1.70)	6.79/4.32 (1.57)
30	3.97/2.82 (1.41)	3.65/1.57 (2.33)	4.73/2.56 (1.84)	4.43/3.21 (1.38)
45	3.02/2.00 (1.51)	2.79/1.18 (2.37)	4.08/2.08 (1.96)	2.72/2.73 (1.00)
60	2.43/1.31 (1.86)	2.24/1.00 (2.24)	3.67/1.78 (2.06)	1.32/2.42 (0.51)
95	1.71/0.12 (14.0)	1.59/0.90 (1.76)	3.17/1.42 (2.23)	– –
150	–	–	2.76/1.12 (2.46)	–

The dependence of the solute concentration on time for the HMM solutions in methanol and in cyclohexane was best described by an exponential equation and a second degree polynomial equation respectively:

In methanol,

$C_t - C_\infty = A\ e^{-Bt}$ $\qquad (r^2 = .971)$

A = 2.2939

B = 0.0356

C_t = concentration at time t

C_∞ = concentration at time infinity,

i.e. equilibrium saturated concentration at the lowest cell temperature [$(20.54-.15)^0C = 20.39^0C$]

= 19.815 mg/ml

In cyclohexane,

$C_t - C_\infty = C + C_1 t + C_2 t^2$ $\qquad (r^2 = .981)$

C, C_1, C_2 were found to be 4.6873, −0.04976 and 1.35×10^{-4} respectively.

C_∞ = 32.750 mg/ml

The (relative) supersaturation, σ, at any time t was calculated by the relationship:

$\sigma = (C_t - C_\infty) / C_\infty$

$= A\ e^{-Bt} / C_\infty$ (in methanol)

or $\sigma = (C + C_1 t + C_2 t^2)/C_\infty$ (in cyclohexane)

and are shown in Table 3.7 a and b, and Fig.3.11 a and b respectively. As these experiments show reasonable

Fig.3.11a

Supersaturation vs Time in methanol

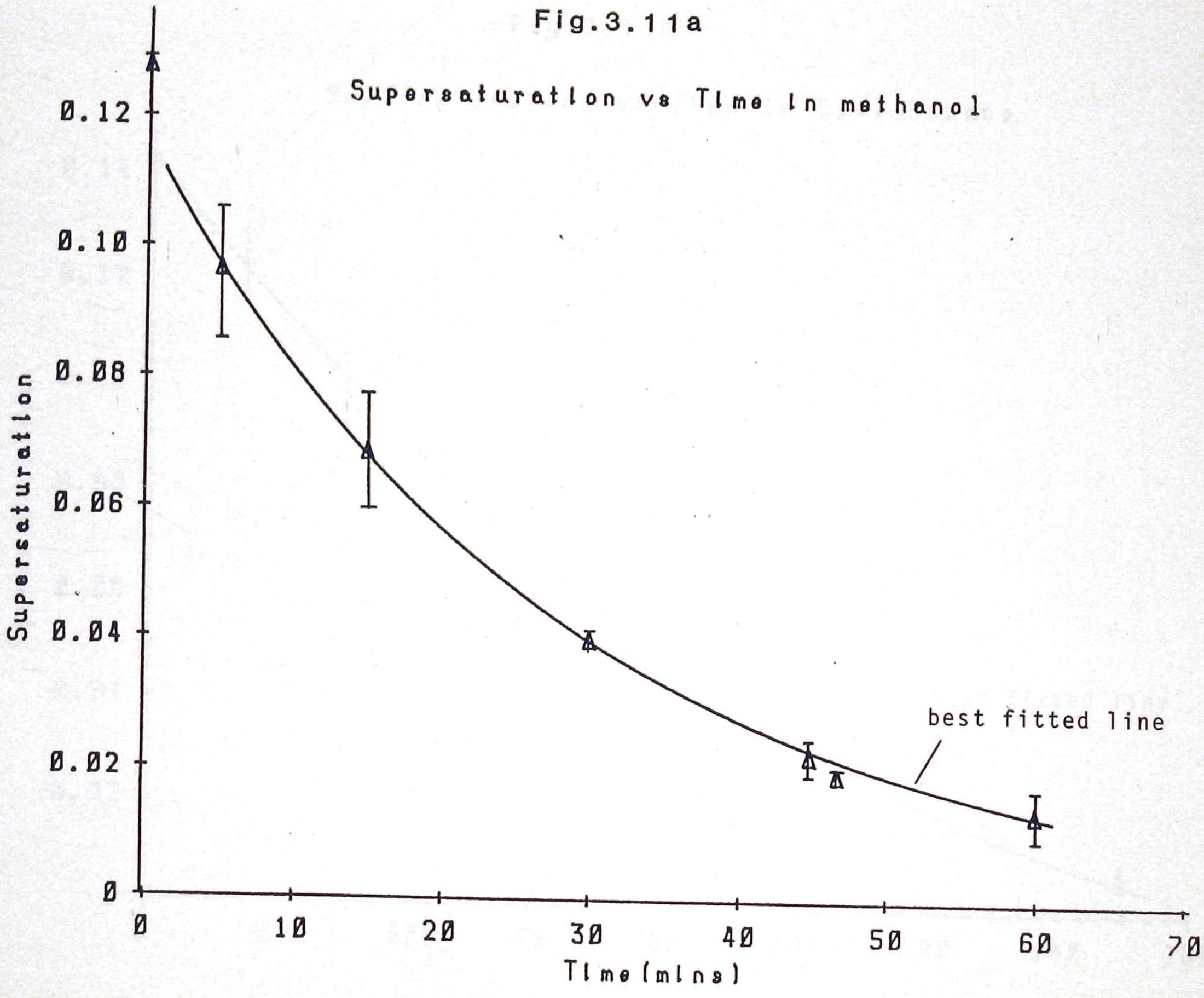

Fig.3.11b

Supersaturation vs Time In Cyclohexane

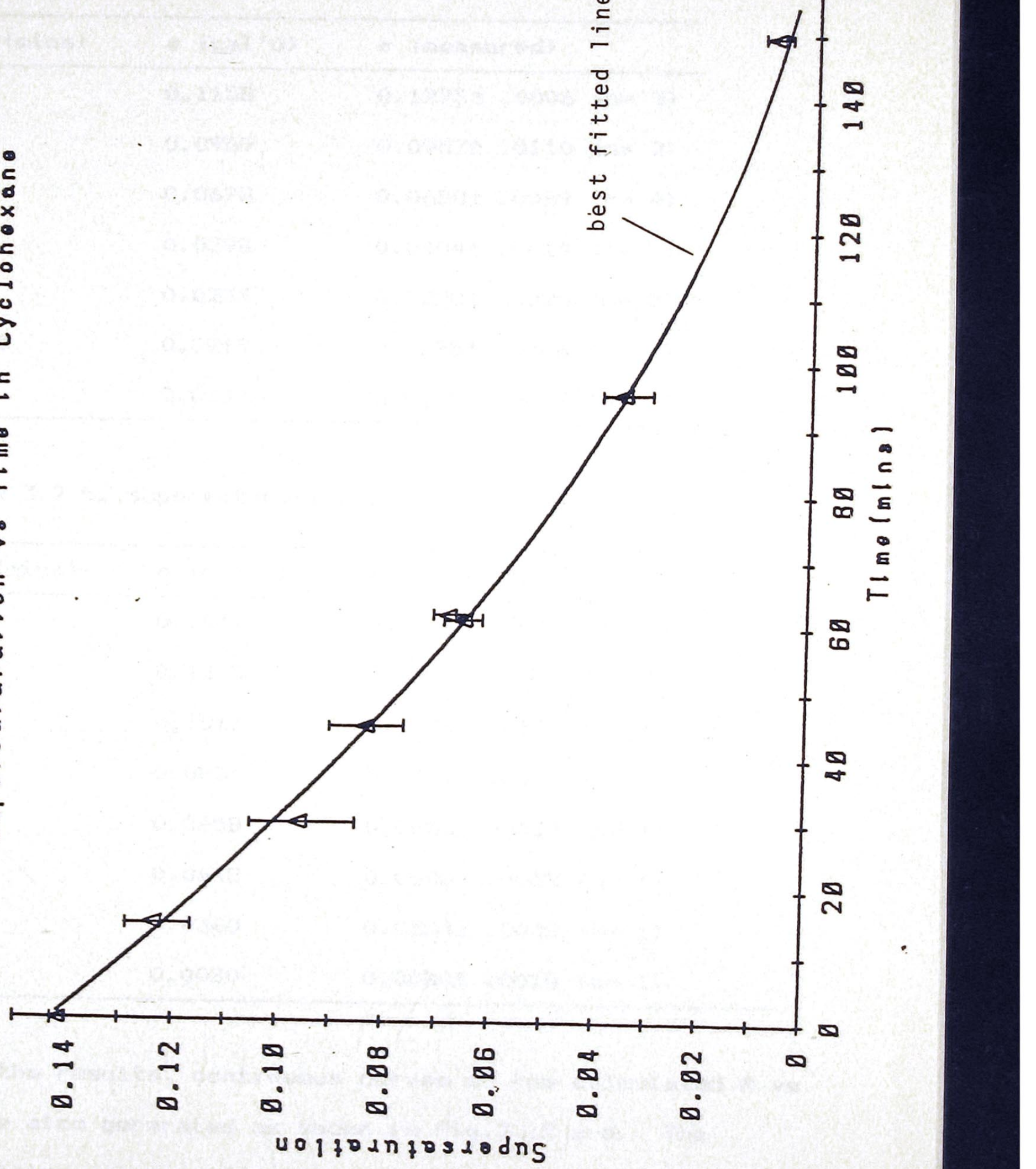

reproducibility, it was justified to use the calculated σ for all growth experiments in the study.

Table 3.7 a. supersaturation in methanol

time(mins)	σ (cal'd)	σ (measured)
0	0.1158	0.1273± .0006 (n= 3)
5	0.0969	0.0957± .0110 (n= 2)
15	0.0678	0.0688± .0089 (n= 4)
30	0.0398	0.0404± .0014 (n= 1)
45	0.0233	0.0220± .0025 (n= 2)
46.75	0.0219	0.0185± .0006 (n= 1)
60	0.0137	0.0135± .0047 (n= 2)

Table 3.7 b. supersaturation in cyclohexane

time(mins)	σ (cal'd)	σ (measured)
0	0.1431	0.1414± .0008 (n= 2)
15	0.1213	0.1234± .0057 (n= 3)
30	0.1013	0.0949± .0107 (n= 1)
45	0.0831	0.0827± .0076 (n= 2)
61	0.0658	0.0656± .0027 (n= 1)
62	0.0648	0.0680± .0032 (n= 1)
95	0.0360	0.0354± .0048 (n= 1)
150	0.0080	0.0080± .0018 (n= 1)

From the results, continuous curves of the calculated R vs σ were also generated as shown in Fig.3.12 a-d. The calculated volume diffusion controlled growth rates, R_d's for the length (i.e. along the c-axis or the [0001] direction) and the breadth (i.e. along the [1100]

Fig.3.12 a-c

Growth rates of the length (———) and the breadth (----) of the crystals vs degree of supersaturation for 3 separate runs in methanol. Each number is corresponding to an individual crystal.

Fig.3.12 d

Growth rates of the length (———) and the breadth (----) of the crystals vs degree of supersaturation for 3 separate runs in cyclohexane. Each number is corresponding to an individual crystal.

Fig.3.12a(Run1)

Growth Rate(R) vs Supersaturation(σ)

in Methanol

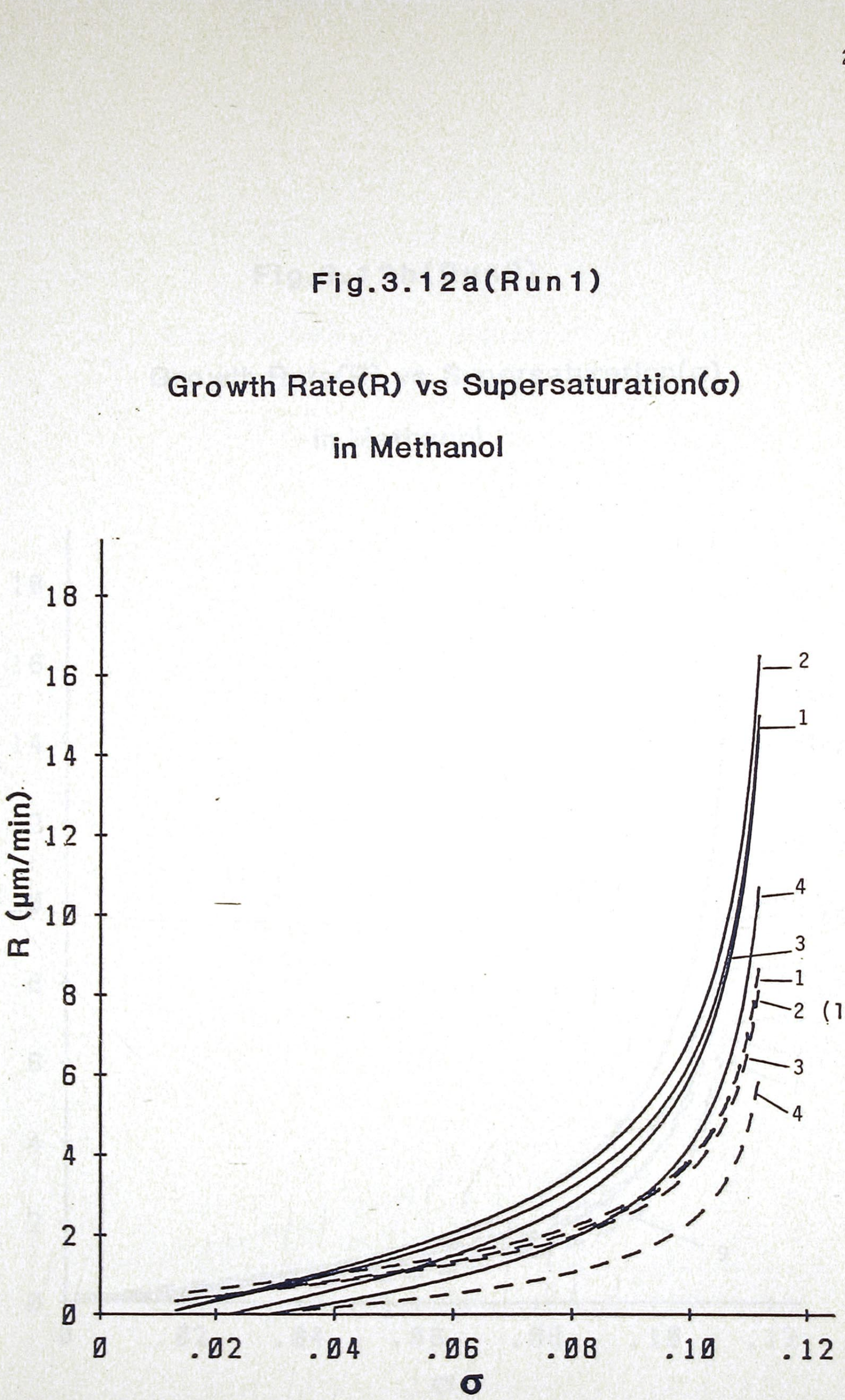

Fig.3.12b(Run2)

Growth Rate(R) vs Supersaturation(σ)

in Methanol

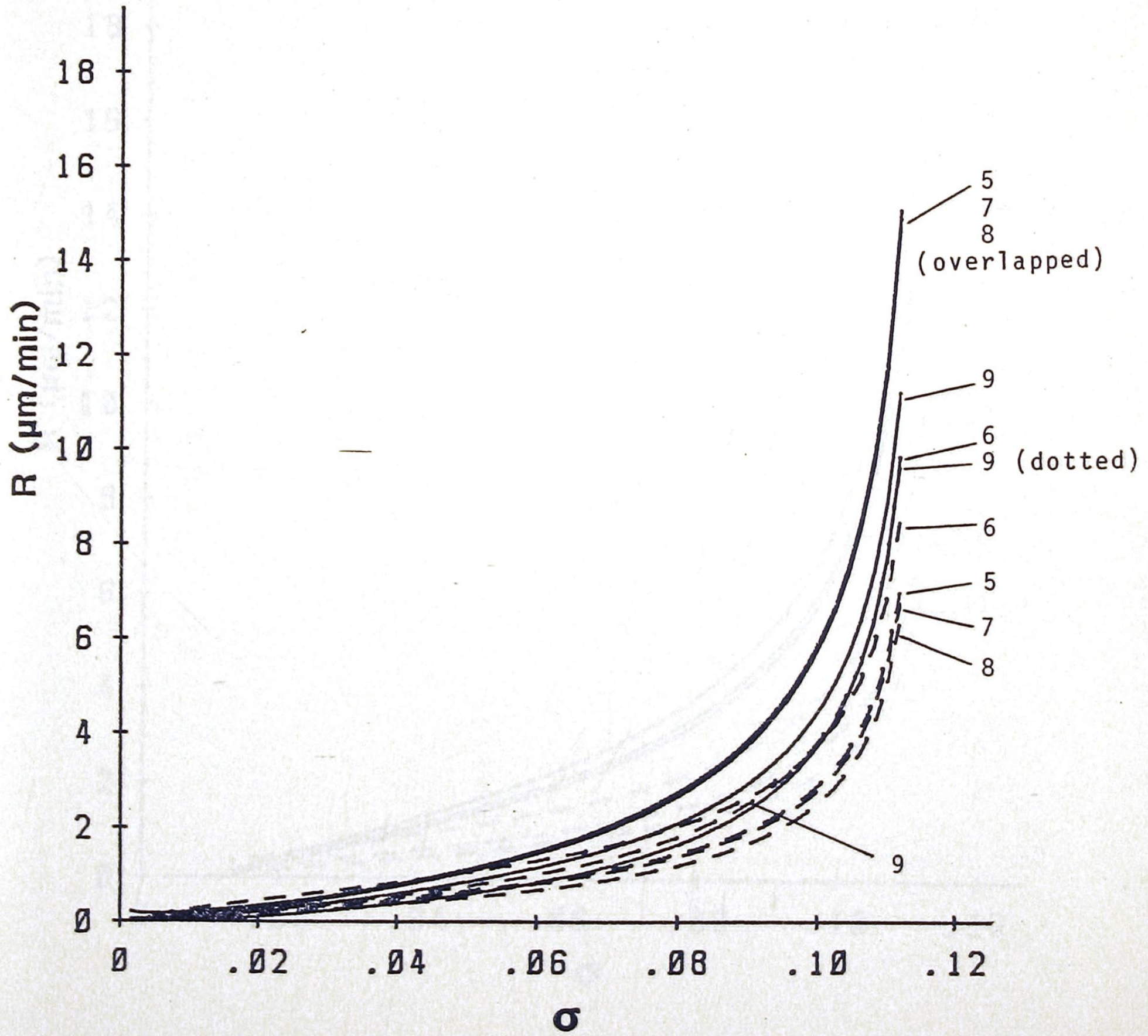

Fig.3.12c(Run3)

Growth Rate(R) vs Supersaturation(σ)

in Methanol

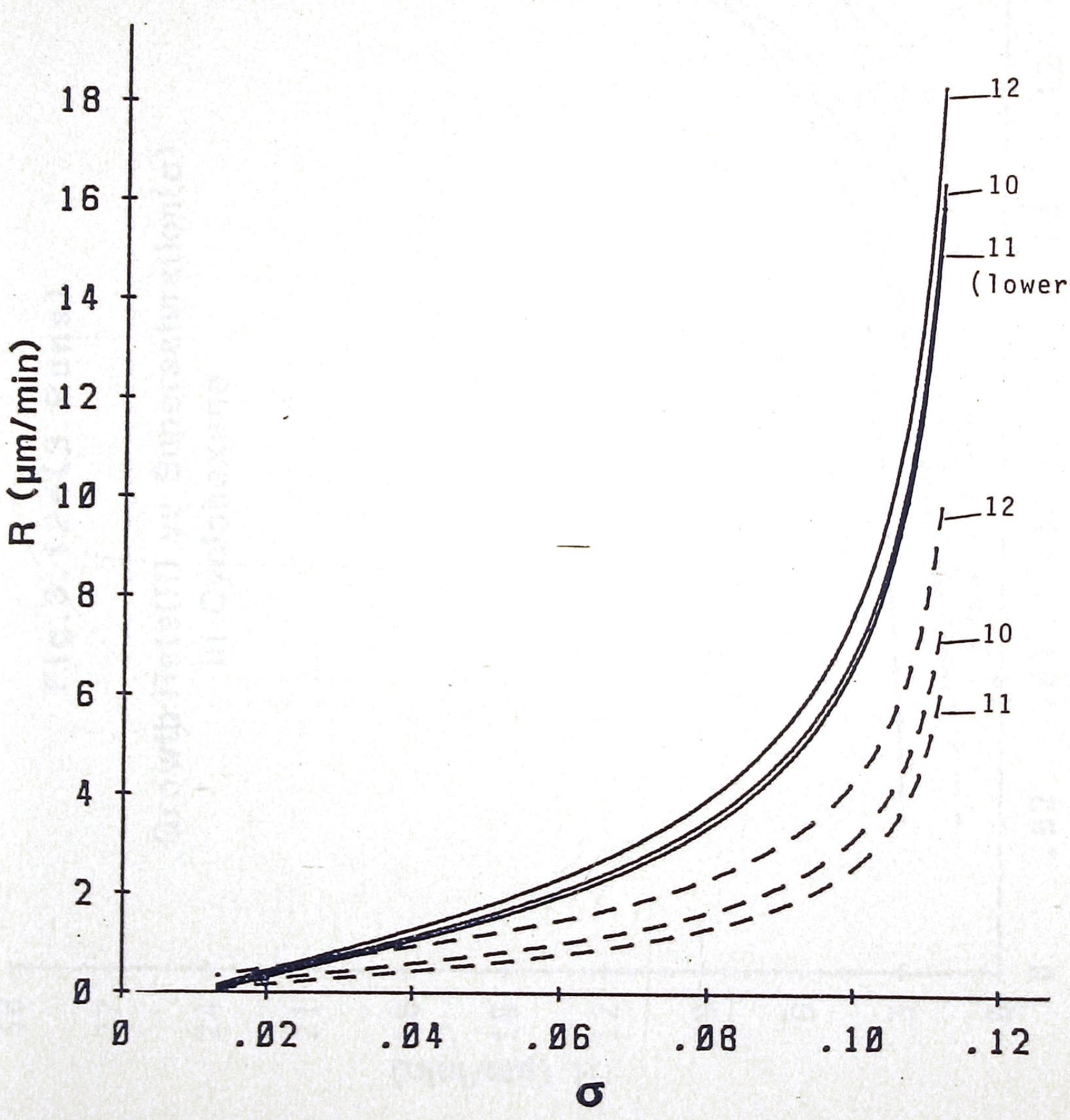

Fig.3.12d(3 Runs)

Growth Rate(R) vs Supersaturation(σ)
in Cyclohexane

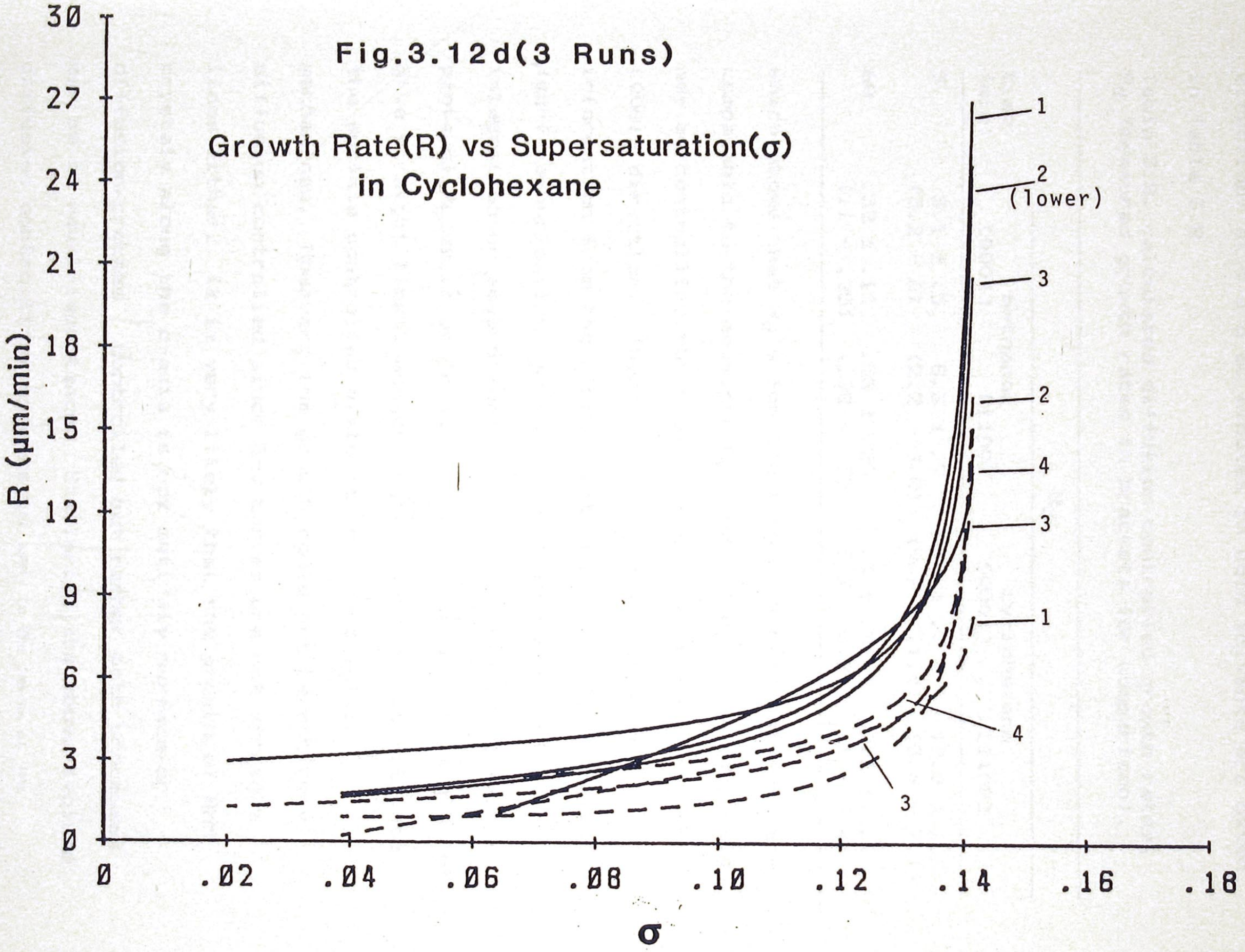

direction) at 5 and 60 minutes in both solvents are given in Table 3.8

Table 3.8. calculated diffusion controlled growth rates, R_d (measured growth rates in brackets for comparison).

time (min)	R_d methanol [0001]	R_d methanol [1100]	R_d cyclohexane [0001]	R_d cyclohexane [1100]
5	5.1 ± .5 (3.2 - 6)	8.3 ± .9 (2.2 - 3.8)	8.0 ± .7 (9.7 - 11.4)	12.0 ± 1.6 (5.6 - 7.1)
60	.32 ± .11 (.1 - .25)	.58 ± .20 (.08 - .52)	1.3 ± .2 (1.2 - 3.7)	2.1 ± 1.1 (1 - 2.4)

which shows that R_d's for the length in both solvents are comparable to the measured R_L, indicating that volume diffusion may be controlling the growth of the length or along the [0001] direction. Therefore further deduction of information from the kinetic data on the surface processes (surface nucleation, screw dislocation and direct integration or adsorption) may be irrelevant. In fact, plots of R_L vs σ^2 or ln ($\sigma^{-5/6}$ R_L) vs 1/ln (σ + 1) did not give straight lines, suggesting that the data do not fit into the surface controlled dislocation or nucleation mechanisms. However, the growth could not be entirely diffusion controlled since R-σ curves are not straight lines either. It is very likely that the growth of HMM crystals along the c-axis is not entirely surface- or diffusion-process controlled but rather both processes may be of equal importance. Similarly, the above (volume diffusion controlling) appears to apply to the growth of the breadth at 60 minutes in both solvents when the supersaturation (σ) is low. However, at 5 minutes when σ

is still high, R_B is consistently lower than R_d in both solvents, ranged from about 2 times in cyclohexane to 3-4 times in methanol. This indicates that surface processes are more important in controlling the growth of the breadth or along the [1100] direction. The kinetics data like that for the length, however, do not conform to any one of the surface mechanisms. Although this may be due to a combination of surface processes, it seems more likely due to the small differences between R_d and R_B which are not sufficiently large to give rise to entirely surface control growth. Therefore, it appears that the observation has been carried out mainly during the diffusion controlled growth except for the initial breadth growth. Fig 3.12 a-d show that in both solvents, R_L's are always larger than R_B's at high σ. This may suggest that at (very) high σ, both solvents should initially give tiny seed crystals with habit of length bigger than breadth , presumably controlled by surface processes otherwise isotropic spheres would have been formed. The seed crystals would have been missed by the low power objective lens because the sizes are likely to be below 50 μm. As the crystals grow in size, volume diffusion slows down (R_d $\propto$ 1/crystal dimension) and becomes more rate determining, thus resulting in more isotropic growth and the compact habit. It thus explains the compact crystal formation in cyclohexane and also some of the results of compact habit obtained in methanol at slow evaporation (presumably low σ). Since diffusion tends to be more important at large crystal size (r) and high σ (Nielsen, 1964), it is quite

easy to understand that in cyclohexane during fast evaportion (high σ) compact crystals form because both r and σ are large. On the other hand, in methanol the seed crystals continue to elongate during fast evaporation in spite of the high σ and large r, indicating that high σ in fact favours elongation (and outweighs the size factor). Such a paradoxical result is explained by the fact that $R_B < R_d$ at high σ, i.e. although the [0001] direction advances by a diffusion controlled mechanism, the growth along the [1100] direction is surface reaction controlled which is even slower. Such an argument is not applicable to growth in cyclohexane during fast evaporation because there is no evidence of elongation. Apparently during fast evaporation the change over of surface control to diffusion control is more rapid in cyclohexane because R_B is only about 2 times lower than R_d at high σ. Elongation in methanol at high σ is also illustrated in Table 3.6 a-c; R_L/R_B keeps increasing systematically with σ in methanol (but not in cyclohexane). This again agrees with the absence of needle habit during fast evaporation from cyclohexane. During slow evaporation (presumably low σ), the formation of needle crystals in methanol is nevertheless still not fully understood from the kinetics data. While the 2-fold difference in R_L and R_B ($R_L/R_B \sim 2 - 0.5$, depending on σ) in cyclohexane agrees very well with the observed compact habit in the slow growth experiments, in methanol R_L/R_B (maximum 2.6 only) quantitatively can hardly form needles with $\beta > 5$ (at least within the σ range in the kinetics measurement), but

rather more compact crystal would be formed. It is possible that during the slow evaporation, σ is still comparatively high which favours diffusion controlled growth along the [0001] direction but the growth along the [1100] direction would be controlled by surface processes, thus favouring elongation along [0001]. The rate of bulk transport of HMM and the change of σ during these experiments would have to be determined in order to verify, or refute, this explanation.

c) α-factor

The plots of log X vs $1/T \times 10^3$ and of ln X vs ln T for HMM in both methanol and cyclohexane are shown in Fig.3.13 and Fig.3.14 (with data shown in Table 3.9 and 3.10) respectively, from which the ΔH_s and ΔS_s were obtained as :

ΔH_s (methanol) = 23.74 ± 0.31 kJ/mol.

ΔH_s (cyclohexane) = 30.97 ± 1.03 kJ/mol.

ΔS_s (methanol) = 81.03 ± 1.08 J/mol.K.

ΔS_s (cyclohexane) = 105.95 ± 3.25 J/mol.K.

Where X is the mole fraction solubility

Table 3.9.

T (K)	$1/T \times 10^3$	mole fraction ($X \times 10^3$) in methanol	cyclohexane
283	3.5334	2.1560	8.3308
288	3.4722	2.5535	10.6927
293	3.4130	2.9870	12.7880
298	3.3557	3.5853	15.8765
303	3.3003	4.1765	20.2633

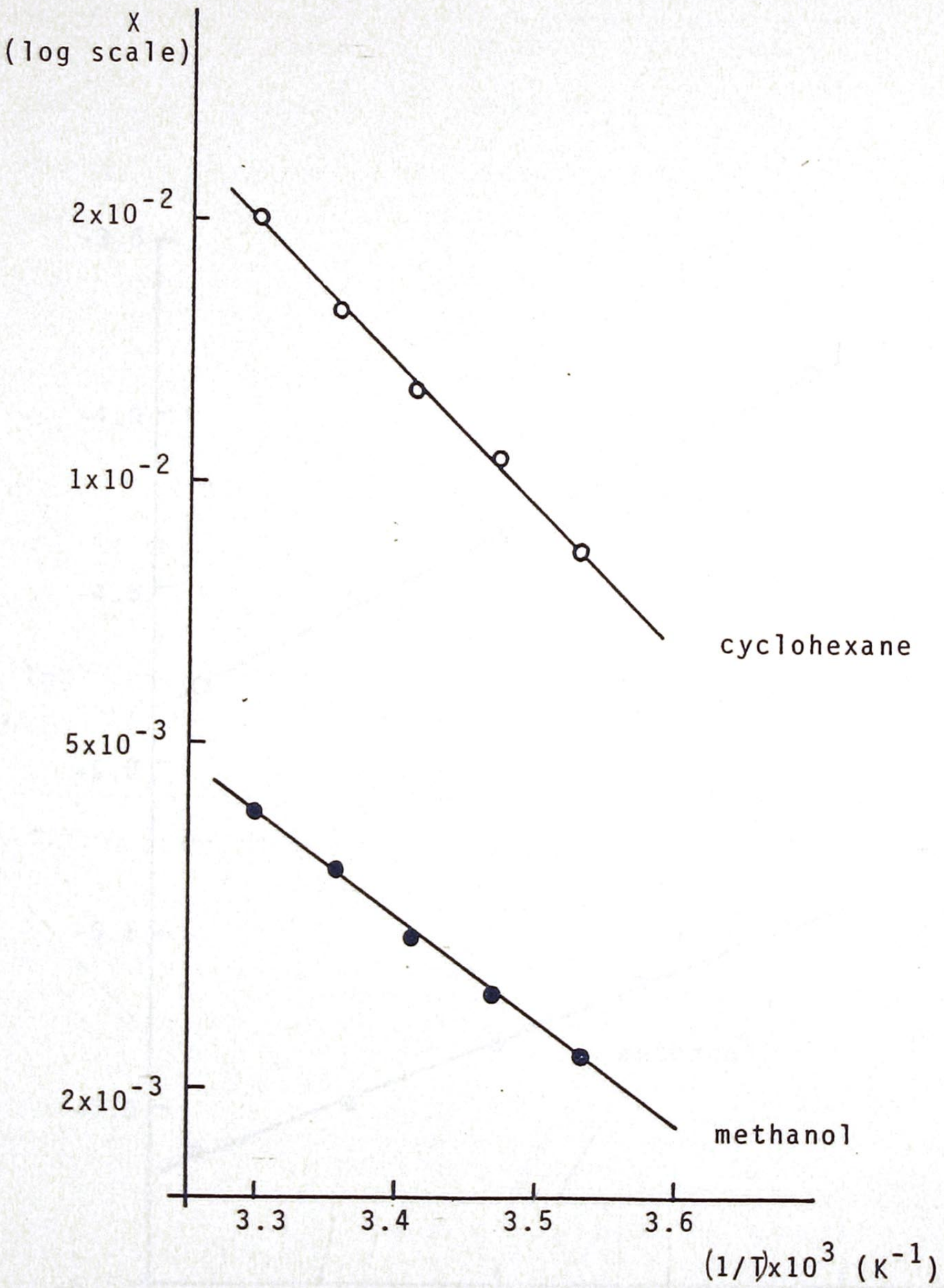

Fig. 3.13 logX (mole fraction solubility of HMM) vs $(1/T)\times10^3$

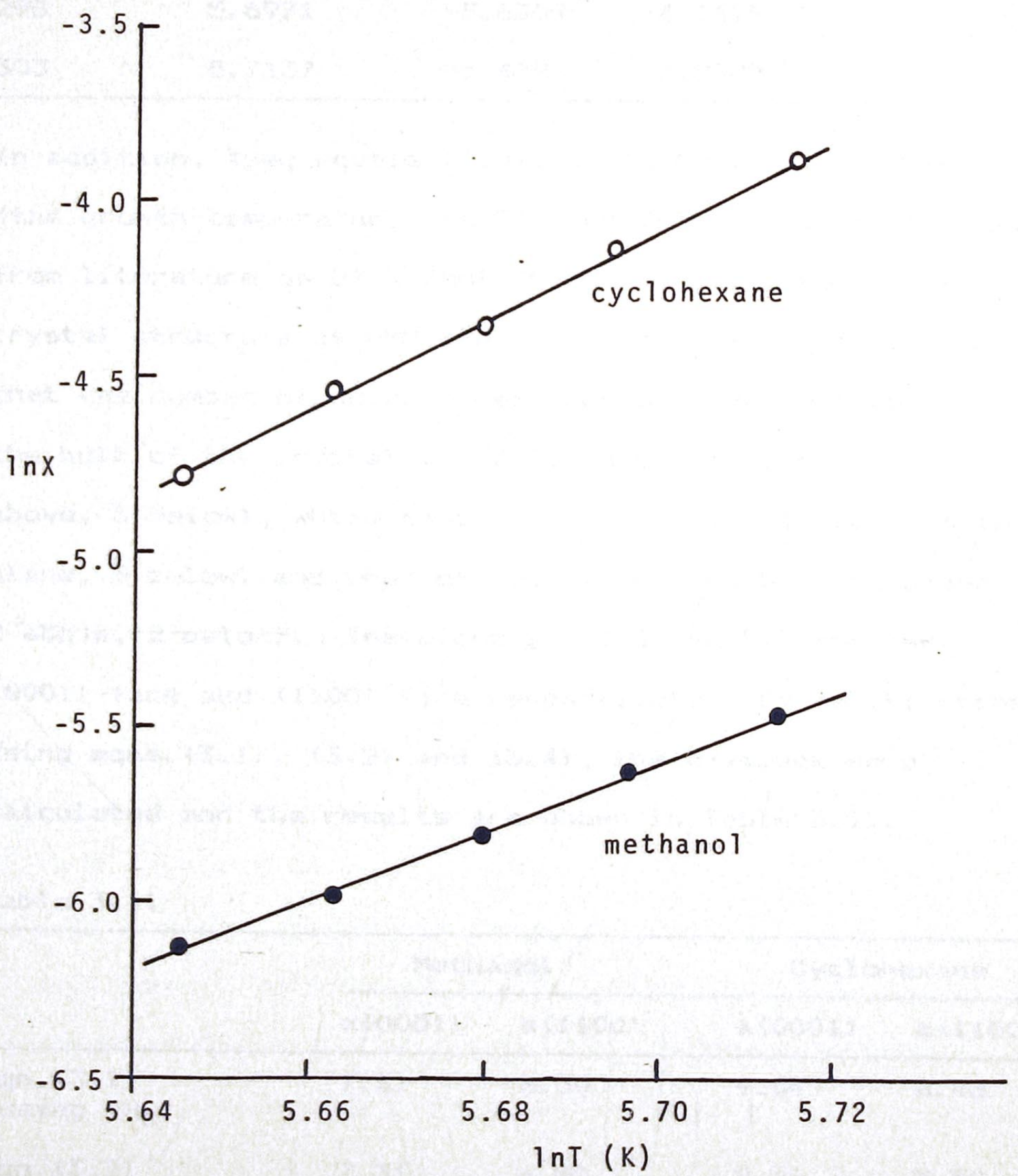

Fig. 3.14 lnX (mole fraction of HMM) vs lnT (temp.)

Table 3.10.

T (K)	ln T	lnX in methanol	lnX in cyclohexane
283	5.6455	-6.1395	-4.7878
288	5.6630	-5.9703	-4.5382
293	5.6802	-5.8135	-4.3593
298	5.6971	-5.6309	-4.1429
303	5.7137	-5.4783	-3.8989

In addition, Xseq equals 19.815/(1.1x1000), T_m is 446K, T (the growth temperature) is 20^0C or 293K and ΔH_f was found from literature as 27 KJ/mol (Gonda et al, 1985a). The crystal structure of HMM (Bullen et al, 1972) revealed that the number of nearest neighbours of HMM molecules in the bulk of the crystal is 12 (6 in the same plane, 3 above, 3 below), while that in the face (0001) is 9 (6 in plane, 3 below) and that of face (1100) is 8 (4 in plane, 2 above, 2 below). Therefore ξ = 3/4 and 2/3 for the (0001) face and (1100) face respectively. By substitution using eqns.(3.1), (3.2) and (3.4), the α-values were calculated and the results are shown in Table 3.11.

Table 3.11

	Methanol		Cyclohexane	
	α(0001)	α(1100)	α(0001)	α(1100)
eqn.(3.1) (using ΔH_s)	7.31	6.50	9.54	8.48
eqn.(3.2) (using ΔS_s)	7.31	6.50	9.56	8.50
eqn.(3.4) (using ΔH_f and Xseq)	8.65	7.69	8.26	7.34

The measured growth rates of the length and the breadth of HMM crystals at high and low σ in both solvents (obtained from Fig.3.12 a-d) are shown in Table 3.12 for comparison with the corresponding α values.

Table 3.12

σ	methanol		cyclohexane	
	R_L+	R_B	R_L	R_B
0.11	8 - 15	4 - 8	< 6	< 4
0.06	~ 2	0.5 - 1.5	~ 2	1 - 2

+: $R_L \equiv R[0001]$; $R_B \equiv R[1100]$

The α values obtained by eqn.(3.4) were overestimates because HMM sublimes on melting, the actual ΔH_f should be < 27 KJ/mol. Nevertheless, the fact that α calculated by eqn.(3.4) for a specific face is lower in cyclohexane than in methanol remains unchanged.

The results show that only the α obtained from eqns.(3.1) and (3.2) gave values which are consistent with the experimentally observed growth rates along [0001] or [1100] direction in the 2 solvents at high σ, i.e. α in methanol ≤ α in cyclohexane corresponding to R_L (or R_B) in methanol ≥ R_L (or R_B) in cyclohexane. However, at lower σ, R_L's in methanol overlap with those in cyclohexane (~ 2μm/min) which contradicts the lower α value in methanol. In such case, the α values predicted by eqn.(3.4) appear to agree better with the observed R_L in the 2 solvents (i.e. similar α values correspond to similar R_L's). The same appears to be the case for R_B at low σ. This suggested that estimation of the values of α-factor in the present study depends on σ. Moreover, all the

calculations show that in methanol α(0001) is higher than α(1100) and this disagrees with the faster growth rate of R_L at high supersaturation and also cannot explain the elongated habit obtained. Such discrepancy between the α and the observed growth rate or habit cannot be explained by the solvent adsorption or orientation effect of the solvent molecules which have been postulated as the main reasons (Davey, 1982; Elwenspoek et al, 1987), because no predominant stereospecific solute-solvent interactions could be identified (Sec.3.3). Assuming a surface controlled growth, it is possible that since both $\alpha > 5$, both faces are smooth and share the same growth mechanism of dislocation. A difference of only around 10% in the α may make no significant change in the actual growth rates. However, recalling the role of volume diffusion in the growth, it seems even more likely that quantitation of the interfacial roughness by α to predict the growth may simply fail in a transport dominated growth.

iii) Conclusions

The results suggest that the formation of compact habit in both polar and nonpolar solvents is controlled by diffusion. Elongation of habit which occurs during fast evaporation from polar solvent is the result of diffusion controlled growth along [0001] direction and surface controlled growth along [1100] direction. Formation of needle crystals in polar solvent during slow evaporation is still not fully understood. A discrepancy was found

between the α-values and the observed growth rates, which may also be due to volume diffusion. The role of bulk transport can be clarified in future work by measuring the kinetics (i) at various temperatures to obtain the activation energy for the growth (diffusion-controlled mechanisms usually give value ~5 kcal/mole, Glasby and Ridgway, 1968); (ii) in an agitated system: a dependence of growth rate on agitation indicates transport controlled mechanism.

3.5 Hexamethylmelamine-Hexafluorobenzene (HMM/HFB) Complex

During the course of studying solute-solvent interaction of HMM, an unexpected new crystal form of HMM was obtained by slow evaporation from a solution in hexafluorobenzene. The crystal habit is flat and needle-like. However, this new form turns opaque immediately after separation from the solution, suggesting that desolvation takes place. The crystals were thus further characterized to confirm their identity.

3.5.1 Characterization

i) Experimental

a) X-ray powder diffraction

The crystals obtained from hexafluorobenzene (HFB) (99%,

Aldrich Chemical Co., Milwaukee, WI, USA) were prepared for X-ray powder diffraction by gentle grinding in an agate mortar. The diffraction pattern was then recorded in the same way as described in Chapter 1, Sec.1.2.2 f. Measurement was also done on the original HMM cyrstals from the supplier for comparison.

b) IR spectroscopy

The IR absorption spectra of the original HMM crystals from the supplier and the crystals obtained from HFB were recorded in the same way as in Chapter 1, Sec.1.2.2 d.

c) Hot-stage microscopy

Crystal samples were prepared by slow drying of a drop of HMM solution in HFB on a microscope slide. The thermal properties of the crystals were then observed under a Kofler hot-stage microscope (Reichert, Wien, Austria) fitted with polarizers using a heating rate of about 4^0C/min.

d) Thermoanalysis (DTA-TG)

Thermoanalytical data were obtained on a combined DTA-TG instrument (Rigaku, Thermoflex M8076) using crystals of freshly filtered HMM from the HFB solution. Transference of the crystals from the Buchner filter to the thermal balance was made in about 20 seconds by which time the

surface of the crystals had become opaque. The sample (7.5mg) was heated from room temperature to approximately 200^{0}C at 10^{0}C/min in a stream of nitrogen (100ml/min).

ii) Results

a) X-ray powder diffraction

Both the original crystals and the crystals from HFB give the same 2θ diffraction angles on the powder diffraction patterns. A representative pattern (of HMM from HFB) is shown in Fig. 3.15.

b) IR spectroscopy

The IR absorption spectrum of the crystals from HFB is very similar to that of the original crystals as illustrated in Fig. 3.16 a & b.

c) Hot-stage microscopy

Changes were observed to take place at around 120^{0}C : The needles disintegrated into much smaller fragments and crystals which then melted and transformed into hexagonal compact form. The latter finally melted at 172-173^{0}C which is characteristic of the parent HMM.

d) DTA-TG

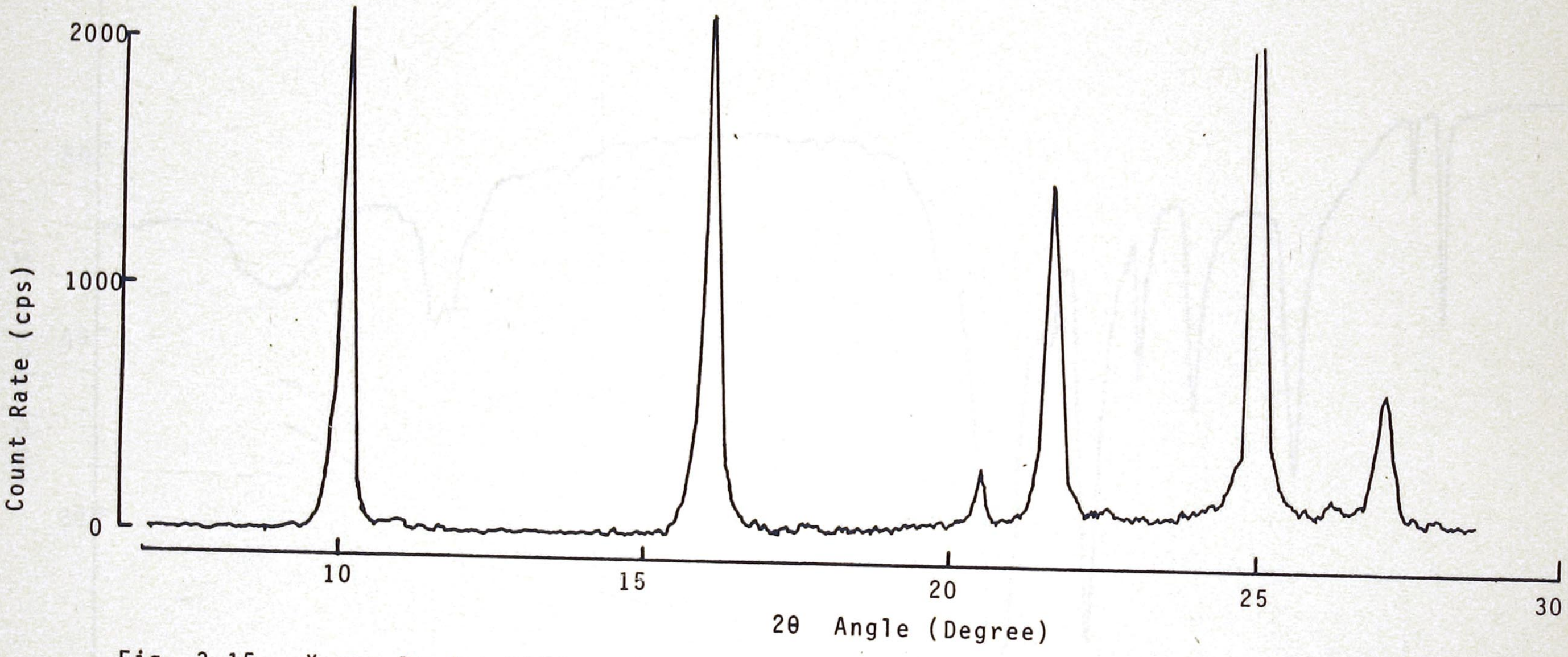

Fig. 3.15 X-ray Powder Diffraction Pattern of HMM Recrystallized from Hexafluorobenzene

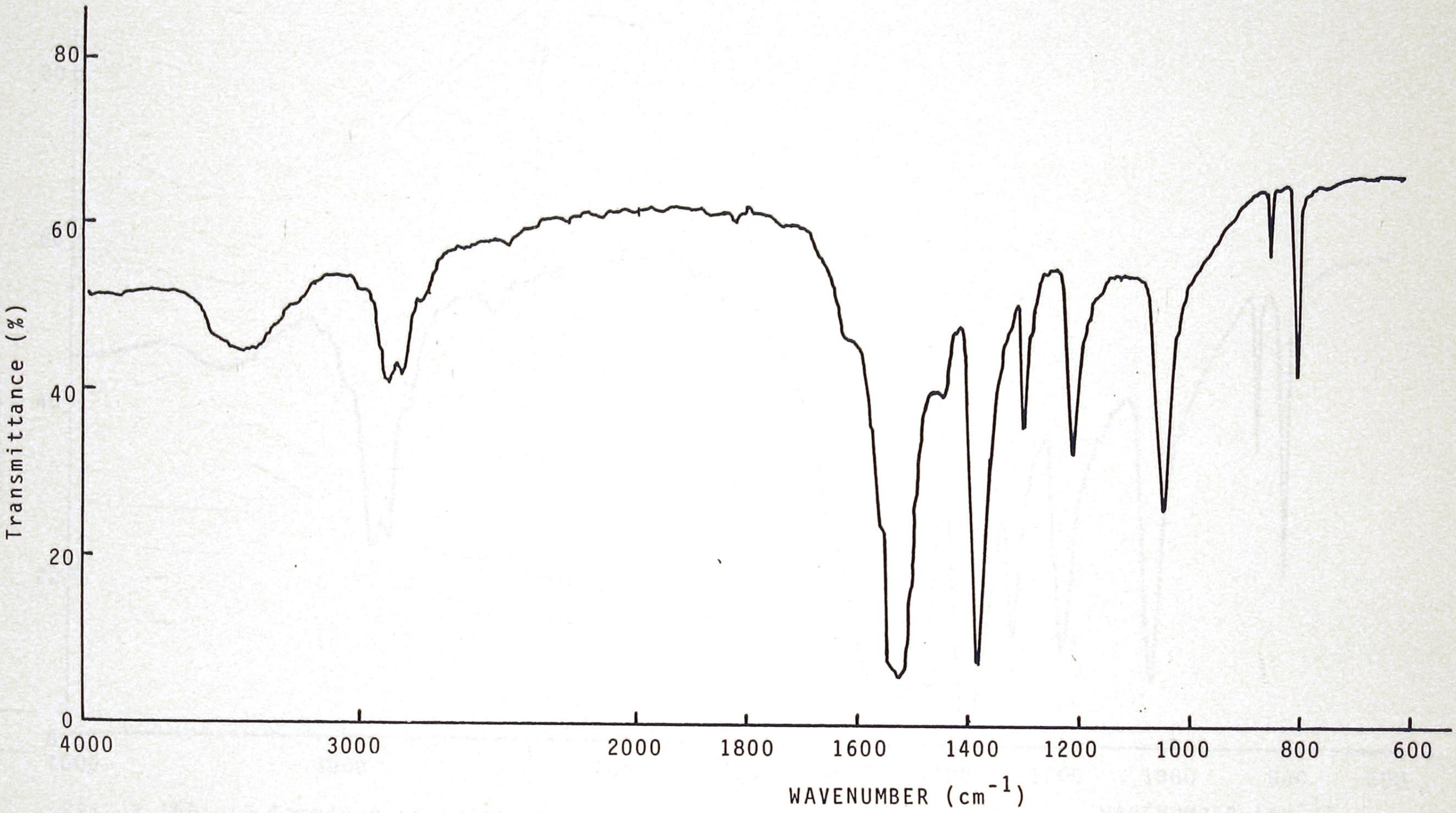

Fig. 3.16a IR Spectrum of HMM recrystallized from hexafluorobenzene

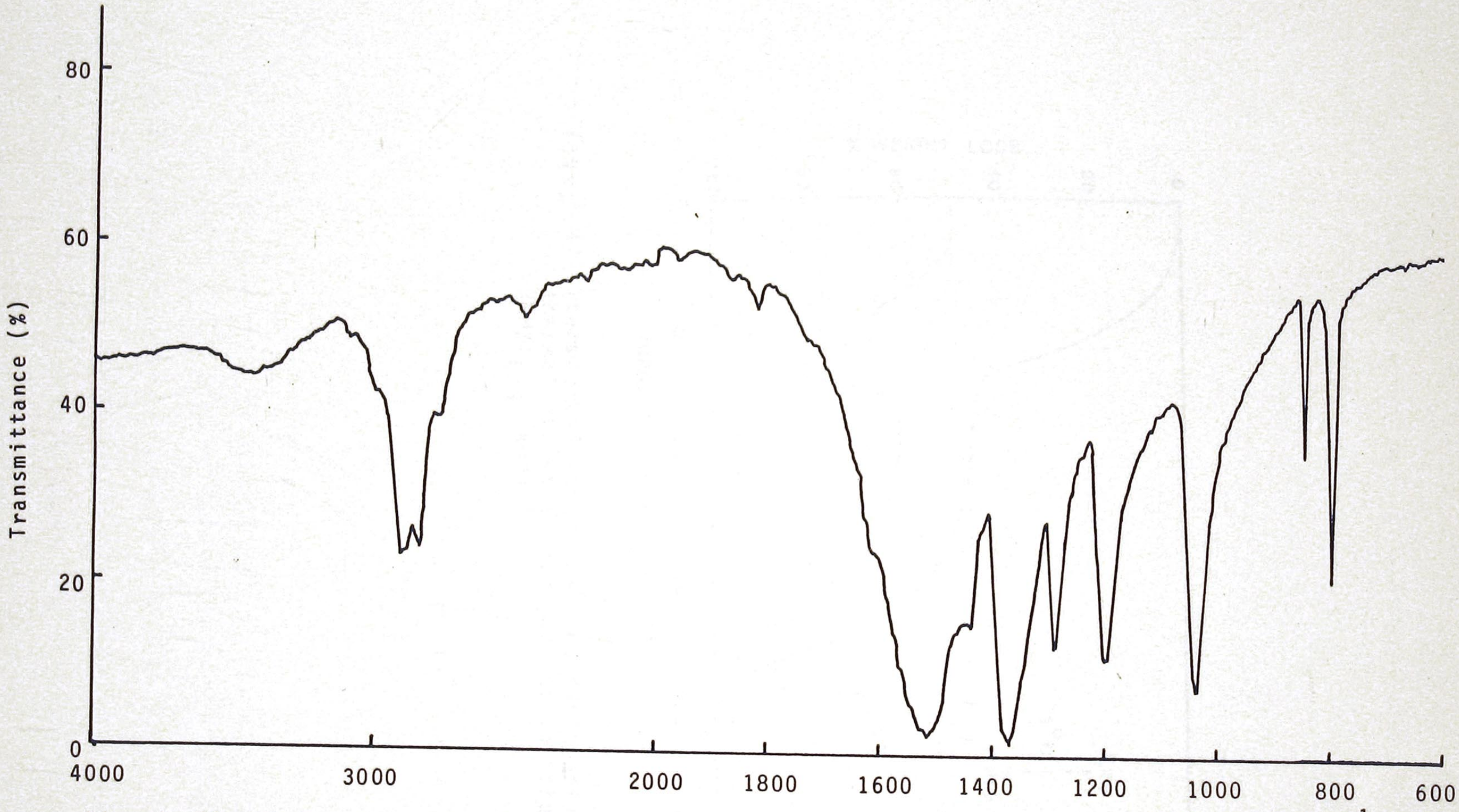

Fig. 3.16b IR Spectrum of original HMM before recrystallization

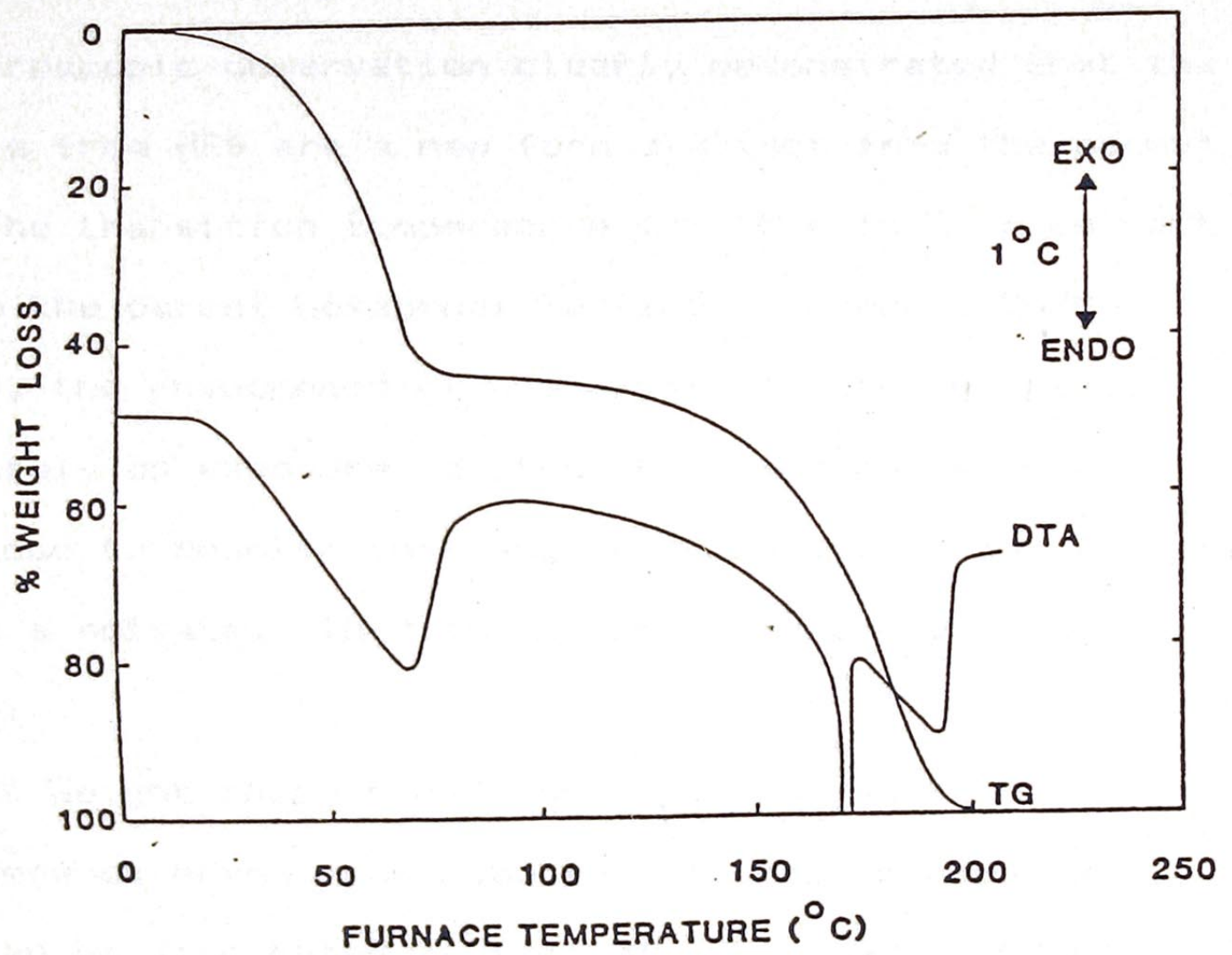

Fig. 3.17 Thermogravimetric (TG) and differential thermal analysis (DTA) curves for the HMM/C_6F_6 adduct

TG and DTA curves are shown in Fig.3.17 with distinct weight and thermal changes.

iii) Discussion

The microscopic observation clearly demonstrated that the crystals from HFB are a new form distinct from the parent HMM. The transition temperature for this form to convert back to the parent hexagonal lattice is around 120^{0}C. However, the phenomenon of the crystals turning opaque immediately on exposure to atmosphere (which is most likely due to desolvation) suggested that this new form is in fact a solvate. This is confirmed by the DTA-TG results:

Distinct weight changes and corresponding endothermic peaks were observed from room temperature to about 80^{0}C which can be attributed to loss of HFB (b.p. 81-82^{0}C). Changes which occurred from 150-200^{0}C were due to the vaporization of HMM. The sharp endothermic peak at about 170^{0}C is due to the fusion of HMM. It should be noted, however, that no distinct changes could be found on the thermal curves at around 120^{0}C corresponding to the transition observed from the microscopy. It is likely that the enthalpy of transition is very small. This may explain the X-ray powder diffraction and IR results of the crystals from HFB which show no difference from that of the parent HMM, presumably polymorphic transition to the stable form has taken place due to the mechanical energy supplied by grinding and compression. From the TG result,

the percentage weight change due to the loss of HFB was found to be about 44% compared to 47% calculated for a 1:1 HMM/HFB adduct. This was further confirmed by the single crystal X-ray diffraction which revealed that in the structure of the HMM/HFB adduct HMM and HFB are alternating in infinite columns parallel to the b axis of the monoclinic unit cell, suggestive of a π-π interaction between the rings (Aroney et al, 1987).

It is thus concluded that the HMM crystals obtained from HFB solution were a 1:1 solvate which is similar to but much less stable than the previously known 1:1 HMM/trinitrobenzene adduct (Williams and Wallwork, 1966).

3.5.2 Solvation Study of HMM/HFB Solvate

In order to gain some insight into the nature of intermolecular interactions in the precursor state to crystallisation, electro-optic and ^{1}H NMR spectroscopic properties of HMM in the solvent HFB were studied.

i) Experimental and Results

The molar Kerr constant and ^{1}H NMR spectroscopic measurements were carried out in Sec.3.3 i) and the results were presented in Sec.3.3 ii).

ii) Discussion

The molar Kerr constant of HMM in HFB is 3 times higher than in other solvents indicating that clustering of HFB molecules about HMM greatly augments the intrinsic solute anisotropy. Thus face to face parellel configuration of HFB solvation of HMM is statistically favoured [Type A, Fig.3.7 & Sec.3.3 ii)d)]. The calculated molar Kerr constant for this configuration of a discreté 1:1 HMM/HFB complex is a little less (numerically 52 c.f. 61) than the observed value. It is possible that in solution HFB associates simultaneously above and below the plane of HMM. The interaction, however, must be weak because the dipole moment of HMM was found to be near zero in HFB solution (Aroney et al, 1987). By contrast, type B approach in Fig.3.7 is not favoured because of the electron repulsion between the negative charge on the centre of the HMM ring and the peripheral fluorine atoms of HFB.

Accepting configuration A as the most probable encounter, the absence of solvent induced chemical shift in the ^{1}H NMR can be rationalised because in such configuration the HMM protons are remote from HFB and are located between the shielding/deshielding regions of HFB. It is important to note that this face to face configuration is similar to that of molecular packing in the HMM/HFB crystal structure (Aroney et al, 1987). The results thus provide direct evidence for the relationship between the stereospecific solute-solvent interaction in solution and the resulting solid crystal form.

APPENDICES

Appendix 1 Publications

Gonda, I. and Chan, H.-K. (1985)
"Model of aerodynamic behaviour of aggregates formed on nebulization of suspensions", J.Pharm. Pharmacol. (Suppl.) 37, 56P.

Chan, H.-K., Hambley, T.W. and Gonda, I. (1986)
"Solid forms and structure of methotrexate", Aust. J. Hosp. Pharm. 16, 66.

Hambley, T.W., Chan, H.-K. and Gonda, I. (1986)
"Crystal and molecular structure of methotrexate", J. Am. Chem. Soc. 108, 2103-2105.

Gonda, I., Chan, H.-K. and Nagai, T. (1986)
"Correlation between the aspect ratio of hexamethylmelamine crystals and solvent polarity", Abstract of the Annual Meeting of the Japanese Pharmaceutical Society, Chiba, Japan, 1986, 2S, 1-5.

Romano, A., Chan, H.-K. and Gonda, I. (1986)
"Tonicity of some commmonly used drug preparations for nebulisation", Aust. J. Hosp. Pharm. 16, 19-21.

Aroney, M.J., Hambley, T.W., Patsalides, E., Pierens, R.K., Chan, H.-K. and Gonda, I. (1987)
"Hexamethylmelamine: a study of solvation and crystallization", J. Chem. Soc. Perkin Trans. II. 1987, 1747-1752.

Chan, H.-K. and Gonda, I. (1988)
"Development of a systematic theory of suspension inhalation aerosols. II. aggregates of monodisperse particles nebulised in polydisperse droplets", Int. J. Pharmaceut. 41, 147-157.

MODEL OF AERODYNAMIC BEHAVIOUR OF AGGREGATES FORMED ON NEBULISATION OF SUSPENSIONS

I. Gonda and H.-K. Chan, Department of Pharmacy, University of Sydney, Sydney, NSW, 2006, Australia.

Formation of aggregates of particles when drug suspensions are aerosolised, was documented (Morén, 1982). Thus, changes in the drug mass median aerodynamic diameter (MMAD) occur, and this is important for airway deposition of aerosols.

Consider a suspension of monodisperse spherical particles, diameter d, aerodynamic diameter $d_{ae}(1)$, concentration c (% v/v) in a volatile liquid. On nebulisation, the probability that a droplet of diameter D contains k drug particles is given by the Poisson probability (Raabe, 1968):

$$P(k,D) = \frac{e^{-n}\, n^{k}}{k!} \quad ; \quad n = \left(\frac{D}{d}\right)^{3} \frac{c}{100}$$

The probability that k particles are found in droplets of any size is

$$P(k) = \int_{D_{min}}^{\infty} P(k,D)\, p(D)\, dD$$

p(D) is a log-normal size distribution with droplet mass median diameter MMD_D and geometric standard deviation σ_D. D_{min} is the diameter of the smallest droplet which can accommodate the aggregate of k particles (Callingham, 1980; Gonda, 1985). It is assumed that, on evaporation of the liquid, the aggregates are spherical and consist of hexagonal close-packed primary particles. The cumulative mass fraction M(i) of aggregates containing up to k=i particles/aggregate is computed as a function of the relative aerodynamic diameter $d^{r}_{ae}(i)$ (Gonda,1985):

$$M(i) = \frac{1}{n} \sum_{k=1}^{i} kP(k); \quad d^{r}_{ae}(i)/d_{ae}(1) = \sqrt[3]{\frac{i}{f(i)}} \sqrt{\frac{K(1)f(i)}{K(i)}}$$

f is the occupied volume fraction and K is the dynamic shape factor (Davies, 1979; Gonda, 1985). The plots of M(i) on probability scale vs. log $d^{r}_{ae}(i)$ are nearly linear. From the graphs, the increase in the drug mass median aerodynamic diameter, $R_1 = MMAD/d_{ae}(1)$, and the apparent geometric standard deviation of MMAD, σ_d, are obtained. The increase of MMAD is calculated also on the assumption of uniform drug distribution throughout the droplets (R_2). It may be concluded (see Table 1) that the statistically-based R_1 is similar to R_2, and that the apparent σ_d of the aggregates is governed by the geometric standard deviation of the droplets σ_D.

Table 1. Dependence of aerodynamic properties of aggregates (R_1, R_2, σ_d) on the concentration of suspension (c) and the droplet size distribution (MMD_D, σ_D).

c	MMD_D/d	σ_D	R_1	R_2	σ_d
0.5	10	1.5	1.61	1.55	1.5
	10	2.0	1.61	1.55	1.9
1.0	10	2.0	2.02	1.95	1.9
	15	2.0	2.95	2.93	1.9
2.0	10	1.5	2.47	2.46	1.5
	10	2.0	2.47	2.46	2.0

Callingham, M (1980) Int. J. Cosm. Sci. 2 : 107-126
Davies, C.N. (1979) J. Aerosol Sci.10: 477-513
Gonda, I. (1985) Int. J. Pharm. (accepted)
Morén, F. (1982) Eur. J. Respir. Dis. 63 (Suppl.119): 51-55
Raabe, O.G. (1968) Am.Ind. Hyg.Assoc. J.29: 439-443

Solid Forms and Structure of Methotrexate

Chan H-K[a] Hambley TW[b], Gonda, I[a] Department of Pharmacy[a] and School of Chemistry[b], The University of Sydney, N.S.W., 2006

Methotrexate (MTX) has been a widely used chemotherapeutic agent. Its efficacy in the treatment of lung cancer may be improved by direct administration into the respiratory tract. We have studied the solid forms of MTX with the view to optimise their aerodynamic properties for aerosol delivery.

The parent MTX (I) supplied by the manufacturer is a powder of anhedral particles. Crystallisation of I from hot water containing 1% Tween 80 yields cubic crystals (II). Recently, spherical particles of MTX (III) were obtained by crystallisation in the presence of β-cyclodextrin (molar ratio 1:1).

All three solid forms of MTX have melting points within the range 185-204°C.[1] The purity and identity of MTX (II) was confirmed by UV, H-NMR and MS.[1] TLC shows the absence of an impurity band present in I. The X-ray powder diffraction of I is different form the patterns of II and III. Thus, II and III may be different habits of the same polymorph which is distinct from I. The solubilities of the forms I and II at 37°C are 0.019 and 0.012 mg/mL, respectively, i.e, reflecting the degree of crystallinity of the materials as expected.

Form II yielded particles of sufficient size and quality for single crystal X-ray diffraction. The tetragonal structure was found to belong to the space group $P4_1\,2_1\,2_0$ with unit cell dimensions a = 10.343(2) and c = 45.521(6)A. The conformation of MTX (II) in the crystal lattice is similar to the proposed structure of dihydrofolate bound to dihydrofolate reductase.[2]

References

1. Stecher PG, ed. The Merck Index. 7th ed. Rathway: Merck & Co Inc, 1960:668.
2. Bolin JT, Filman DJ, Mathews DA, Hamlin RC, Kraut J. Crystal structure of Escherichia coli and Lactobacillus casei dihydrofolate reductase refined at 1.7 A resolution. J Biol Chem 1982; 257:13650-62.

Reprinted from the Journal of the American Chemical Society, 1986, *108*, 2103.
Copyright © 1986 by the American Chemical Society and reprinted by permission of the copyright owner.

Crystal and Molecular Structure of Methotrexate

T. W. Hambley,*† H.-K. Chan,‡ and I. Gonda‡

School of Chemistry and Department of Pharmacy
The University of Sydney
Sydney, New South Wales 2006, Australia

Received November 18, 1985

Methotrexate is a potent inhibitor of the reduction of dihydrofolate to tetrahydrofolate by dihydrofolate reductase (DHFR), an essential step in the synthesis of nucleotide bases, and is consequently a successful and widely used antitumour drug.[1] For some years a major effort has been directed toward the rational design of improved inhibitors of DHFR action.[2] It is believed that the greatly enhanced binding of methotrexate to DHFR compared to that of the natural substrate, dihydrofolate, is associated with protonation of different conformations of these ligands.[3] Thus, a knowledge of the ground-state structure and conformation of both inhibitors and substrates is required for this rational design of new inhibitors to be pursued. Considerable work has gone into establishing the preferred conformations of dihydrofolate reductase ligands by experimental and theoretical methods.[4,5] Despite many attempts to crystallize and structurally characterize such molecules, to date, none has been successful.

We report herein the crystallization and the determination of the crystal structure of methotrexate. The conformation is similar in some respects to that seen for methotrexate bound to DHFR

* To whom correspondence should be addressed.
† School of Chemistry.
‡ Department of Pharmacy.

(1) Chabner, B. A.; Johns, D. G. *Cancer*; Becker, F. F., Ed.; Plenum Press: New York, 1976; pp 363–377.
(2) Gund, P.; Schlegel, H. B. *Ann. N. Y. Acad. Sci.* **1981**, *367*, 510.
(3) Bolin, J. T.; Filman, D. J.; Matthews, D. A.; Hamlin, R. C.; Kraut, J. *J. Biol. Chem.* **1982**, *257*, 13650.
(4) Spark, M. J.; Winkler, D. A.; Andrews, P. A. *Int. J. Quantum Chem., Quantum Biol. Symp.* **1982**, *9*, 321.
(5) Dauber, P.; Osguthorpe, D. J.; Hagler, A. T. *Biochem. Soc. Trans.* **1982**, *10*, 312.

0002-7863/86/1508-2103$01.50/0 © 1986 American Chemical Society

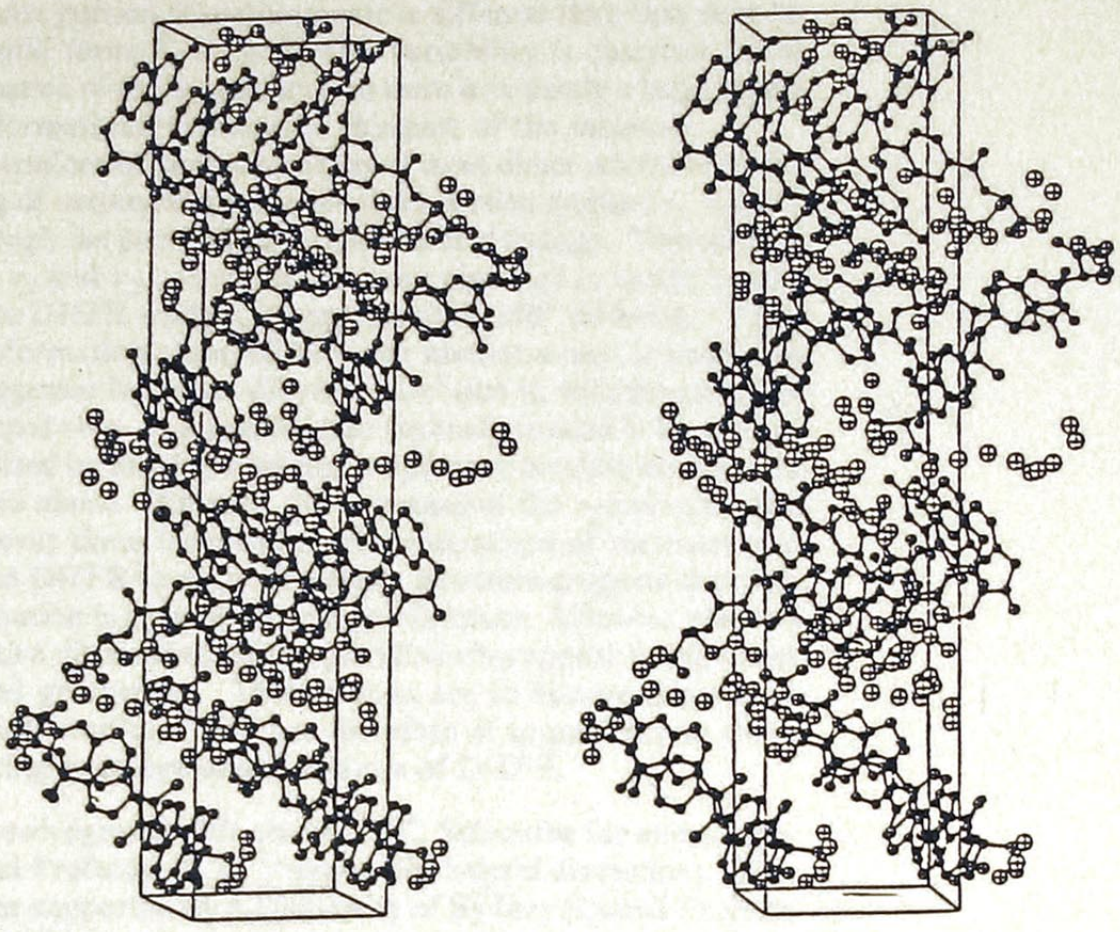

Figure 1. Stereoview of the unit cell of methotrexate.

but is even more similar to the conformation that has been proposed for dihydrofolate bound to DHFR.[3] It is concluded that binding may not impose as much strain on these ligands as had been previously suggested.[4,5] Methotrexate (I) from the manufacturer (Lederle Laboratories, American Cyanamid Co., Pearl River, NY) is a powder that has a low degree of crystallinity as evidenced by broad peaks in X-ray powder diffraction patterns. Recently, while attempting to modify the solid form of methotrexate, we obtained crystals sufficiently large for single-crystal X-ray diffraction: the parent material was dissolved in hot water containing 1% Tween 80 (pH 3.7) and allowed to cool to room temperature. An X-ray powder diffraction pattern of the material thus formed was distinctly different from that of the parent material. However, spectroscopic tests (UV, IR, ^{1}H NMR, and mass spectroscopy) confirmed that the material was methotrexate with solvent of crystallization.

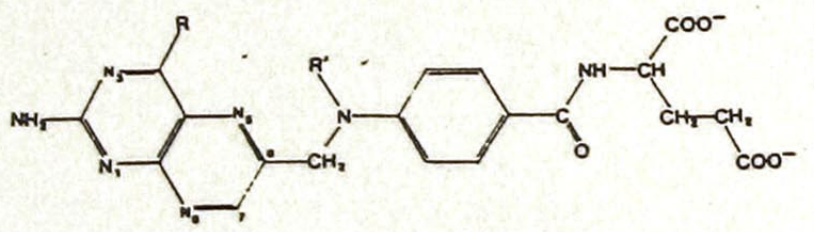

I, methotrexate: R = NH_2, R′ = CH_3
II, dihydrofolate: R = O, R′ = H, C_7 and N_8 positions hydrogenated

A crystal of dimensions 0.20 × 0.10 × 0.10 mm was obtained and found to be tetragonal, space group $P4_12_12$ with a = 10.343 (2) Å and c = 45.521 (6) Å. X-ray diffractometer data were collected using Mo Kα radiation to a 2θ angle of 40°. The structure was solved by direct methods, which revealed the p-aminobenzoyl group, extended by subsequent difference Fourier synthesis, and refined by full-matrix least-squares methods to an R factor (on 983 F, $I > 2.0\sigma(I)$) of 0.083.

The structure consists of layers of hydrophobic and hydrophilic character alternating along the c axis (Figure 1). The hydrophobic layers accomodate the pteridine and benzoyl groups stacked so that they overlay benzoyl and pteridine groups, respectively, of adjacent molecules. The carboxylate groups are disposed into the hydrophilic layers which also accommodate disordered water molecules. The layers are linked by a very strong pair of hydrogen bonds from the two oxygens of the α-carboxylate to N1 and the 2-amino group (N2) of the pteridine (N···O, 2.62 (3) and 2.77 (3) Å). It is interesting that an identical hydrogen bond pair between a carboxylate of an aspartate and the pteridine is observed in the binding of methotrexate to DHFR.[3] The enhanced binding of methotrexate over dihydrofolate (II) is largely due to the ability of methotrexate to form this strong interaction which is in turn due to the greater basicity of N1.[6] It is not possible to establish, with the limited diffraction data currently available, whether N1 is protonated. However, the formation of a hydrogen bond between N1 and an α-carboxylate oxygen atom implies that one of these two atoms is protonated and the pK_a's, which are 5.7 and 2.7, respectively,[7] indicate it is N1 which is protonated. The bond lengths and planarity of the pteridine group are not significantly different than those observed in pteridine itself,[8] though again the resolution of the present structure limits the implications that can be drawn from this similarity. There is a strong hydrogen bond between the 4-amino group and the benzoyl oxygen, also reminiscent of the interaction between this amine and a peptide oxygen of DHFR.[3]

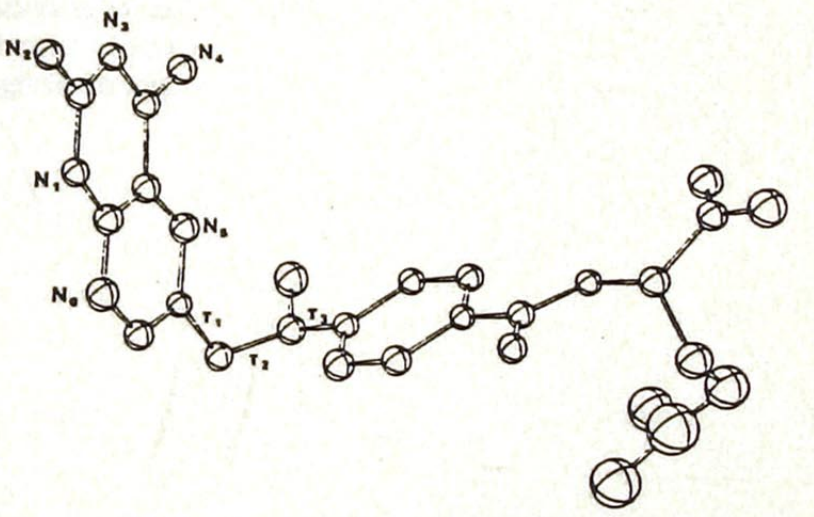

Figure 2. Methotrexate molecule and atom numbering.

The conformation of methotrexate (Figure 2) is best described as two planar groups; the first defined by the 2,4-diaminopteridine

(6) Hood, K.; Roberts, G. C. K. *Biochem. J.* **1978**, *171*, 357.
(7) Cocco, L.; Groff, J. P.; Temple, C., Jr.; Montgomery, J. A.; London, R. E.; Matwiyoff, N. A.; Blakley, R. L. *Biochemistry* **1981**, *20*, 3972.
(8) Shirrell, C. D.; Williams, D. E. *J. Chem. Soc., Perkin Trans. 2* **1975**, 40.

group and the second by the (*p*-aminobenzoyl)-L-glutamate. These planes meet at an angle of 84°. The α-carboxylate lies nearly in the latter plane while the γ-carboxylate is folded back and lies roughly parallel to the same plane. The conformation of the glutamate portion of methotrexate is different than that seen for the bound forms.[3] Considerable variability is observed in the confomation of the bound forms so there is evidently a large degree of conformational freedom in this part of the molecule.

The conformational parameters of most direct relevance to the binding of methotrexate are the three torsion angles (τ_1, τ_2, and τ_3) through the pteridine to *p*-aminobenzoyl linkage. Two of these angles, τ_2 and τ_3, are similar to those observed in methotrexate bound to DHFR while τ_1 is approximately 180° different.[3] Thus, the conformation observed here, for methotrexate, is similar to that suggested for bound dihydrofolate[3] that is, with the pteridine ring flipped over. It is possible that the conformation in the crystal is stabilized by the ring stacking or hydrogen bonding interactions described above. However, the constancy of the τ_2 and τ_3 torsion angles over three independent determinations of methotrexate bound to DHFR[3] and in the present structure suggests that this conformation is a potential energy minimum. Likewise, the two alternative dispositions of the pteridine ring appear to represent preferred geometries. These results are in disagreement with theoretical studies,[4,5] and are therefore of importance to those attempting to design new inhibitors of DHFR.

Acknowledgment. We thank Dr C. Schwalbe for encouragement and Professor H. C. Freeman for helpful discussions. This work was supported by a University of Sydney Special Projects Grant to I.G.

Supplementary Material Available: Tables of least-squares coordinates and thermal parameters for the non-hydrogen atoms of methotrexate (2 pages). Ordering information is given on any current masthead page.

CORRELATION BETWEEN THE ASPECT RATIO OF HEXAMETHYLMELAMINE CRYSTALS AND SOLVENT POLARITY

Univ. Sydney/Dept. Pharmacy — Igor Gonda
Ↄ Hak-Kim Chan
Hoshi Univ./Dept. Pharmaceutics — Tsuneji Nagai

(Purpose) We have noted previously that crystallization of hexamethylmelamine (HMM) at low supersaturation yielded acicular, or compact, crystals depending on the polarity of the solvent.[1] The present study was attempted to investigate a correlation between the aspect ratio of HMM and solvent property.

(Method) HMM was crystallized from 15 solvents at 20°C at very low supersaturation by slow evaporation of the solvent. The aspect ratio of the dry crystals was measured by a computer-assisted image analysis system. The median aspect ratio of HMM, β, was correlated with the dielectric constant (ε) and dipole moment (μ) of the solvents. The data were analysed by multiple regression.

(Results) The multiple regression analysis yielded $\beta = 0.093\varepsilon + 1.976\mu + 0.77$ ($r^2 = 0.704$). It is concluded that there is a high correlation between the crystal habit of HMM and the polarity of the medium used for crystallization. A further confirmation of this hypothesis is provided by the appearance of compact particles when HMM vapour forms crystals by slow homogeneous nucleation from air.

1) J. Pharm. Pharmacol. (suppl), 37, 117 (1985).

Tonicity of Some Commonly Used Drug Preparations for Nebulisation

Romano A. Fois, Hak-Kim Chan, Igor Gonda

The tonicity of eleven commercial preparations of solutions for use in nebulisers in Australia and the United Kingdom was measured. Both the stock solutions and the dilutions suggested by the manufacturers were tested. The majority of these solutions were found to be significantly non-isotonic. The results are discussed in the context of safety and efficacy of these products. Methods for adjusting the tonicity are suggested.

Introduction

Schoeffel et al. reported that hypotonic and hypertonic nebulised solutions can cause a significant fall in forced expiratory volume in one second (FEV_1) in asthmatic subjects.[1] More than 50% of asthmatic patients showed a 20% reduction in FEV_1 after inhalation of less than 2 mL of distilled water, and 3.6% saline was found to have a similar effect.[2] Later, it was suggested that worsening of bronchospasm in some patients using Atrovent® (ipratropium bromide in aqueous solution) could be due to the hypotonic nature of the formulation.[3] We commented briefly on this suggestion at an early stage of our project and proposed a new formulation.[4] It was brought to our attention that Mann et al. in fact recently provided clear clinical evidence about the hypotonicity of the commercial ipratropium bromide solution being the cause of bronchoconstriction in certain asthmatics.[5] A very small drop in FEV_1 was also reported after 'challenge' with hypotonic sodium cromoglycate.[6]

In our studies, the tonicity of preparations used in nebulisers in Australia and the United Kingdom was measured and the results were used to find suitable methods to make these products isotonic.

Romano A. Fois, BPharm
Hak-Kim Chan, BPharm
Igor Gonda, PhD
Department of Pharmacy
University of Sydney, N.S.W. 2006

Address for correspondence:
Igor Gonda
Department of Pharmacy
University of Sydney, N.S.W. 2006

Methods

The osmolality of the stock preparations of each drug was measured by vapour pressure osmometry (Vapour Pressure Osmometer, Knauer, W. Germany) at 37.00 (±0.05)°C.[7] Both this instrument and the cryogenic unit were calibrated with sodium chloride solutions of known osmolality.[8] Next, we measured by the the same method the tonicity of the solutions prepared by dilutions commonly used in hospitals and in some cases recommended by the manufacturers.[9,10]

We then calculated the appropriate quantities of diluents to be added to the stock solutions of the drugs to make the latter isotonic. Our additional criteria were:

1. the sterile diluents could be readily supplied by a hospital pharmacy;
2. the total volume of a unit-dose after dilution should be practicable for typical air-blast nebulisers.

Finally, the tonicity of these preparations was checked by vapour pressure osmometry as well as by the conventional method of freezing point depression (Cryoscopic Unit, Knauer, W. Germany).

Results and discussion

The results are presented in Table 1. All stock solutions tested except the mucolytics acetylcysteine and tyloxapol were found to be hypotonic. In the majority of instances, the commonly used dilutions with isotonic saline still yielded significantly hypotonic solutions (the concentration of isotonic saline

Table 1. Osmolality of stock and diluted solutions for nebulisers expressed as equivalent molality of NaCl at 25°C and dilutions to achieve isotonicity

Drug	Stock solutions (%w/v)	'Usual' dilutions per/mL stock	Equivalent molality of NaCl at 25°C (mol/kg)	Volume of diluent added to 1 mL stock to achieve isotonicity
Salbutamol sulphate (Ventolin® - Glaxo Aust)	0.5	Undiluted 1 mL N/S 2 mL N/S	0.014 0.088 0.125	0.40 mL 3% NaCl
Ipratropium bromide (Atrovent® - Boehringer-Ingelheim)	0.025	Undiluted 1 mL N/S	0.002 0.085	0.43 mL 3% NaCl
Terbutaline sulphate (Bricanyl® - Astra Pharmaceuticals)	1.0	Undiluted 3 mL N/S 7 mL N/S	0.137 0.153 0.157	7.0 mL 0.9% NaCl
Fenoterol hydrobromide (Berotec® - Boehringer-Ingelheim)	0.1	Undiluted 1 mL N/S 3 mL N/S 7 mL N/S	0.005 0.088 0.126 0.142	0.44 mL 3% NaCl
Orciprenaline sulphate (Alupent® - Boehringer-Ingelheim)	2.0	Undiluted 1 mL N/S	0.055 0.108	0.30 mL 3% NaCl
Sodium cromoglycate (Intal® - Fisons)	1.0	Undiluted	0.026	0.37 mL 3% NaCl
Acetylcysteine (Mucomyst® - Mead-Johnson)	20	Undiluted 1 mL WFI 3 mL WFI	1.5 0.68 0.32	7.0 mL WFI
Gentamicin sulphate (Garamycin® - Schering)	4	Undiluted 1 mL 0.9% NaCl	0.108 0.138	0.15 mL 3% NaCl
Tyloxapol (Alevaire® - Winthrop)	0.125	Undiluted	0.531	2.3 mL WFI
Deoxyribonuclease (Deanase® - Consolidated Chemicals Ltd)	Powder 250,000 units	10 mL WFI	Undetectable	10.0 mL 0.9% NaCl
Beclomethasone dipropionate (Becotide Suspension® for nebulisation - Allen & Hanburys)	Suspension 50 µg per mL	Undiluted 1 mL 0.9% NaCl	0.042 0.108	0.33 mL 3% NaCl

Abbreviations:
% w/v = concentration in g/100 mL solution
WFI = water for injection
3% NaCl = aqueous solution containing 3% w/v sodium chloride
0.9% NaCl = normal (isotonic) saline = N/S

at 37°C is 0.162 moles of NaCl/kg of water; i.e. 0.946% w/w).[11] Sodium cromoglycate supplied as 1% w/v for nebulisation is normally used undiluted; the tonicity of this solution corresponded to 1/6 isotonic saline.

The deoxyribonuclease powder, when diluted with water as directed, gave an instrumental response indistinguishable from pure water, presumably due to the high molecular weight of the substance. The beclomethasone dipropionate suspension yielded the same reading whether examined as a whole, or as the liquid part separated by a Millipore filter only. The hypotonicity of this preparation was the result of poor aqueous solubility of the drug.

In contrast, acetylcysteine was strongly hypertonic even when diluted 1:3 with water. We were somewhat surprised initially that the 0.125% w/v solution of the polymeric surfactant tyloxapol was also hypertonic. The explanation lies almost certainly in the buffer added to this preparation by the manufacturer.

The tonicity of all the hypotonic stock solutions, except terbutaline sulphate, was adjusted using a 3% w/w NaCl in water. The terbutaline sulphate was adjusted with isotonic saline as directed by the manufacturers.[10] To achieve isotonicity, 1 mL of 20% w/v acetylcysteine required 7 mL of distilled water and 1 mL of 0.125% w/v tyloxapol needed 2.3 mL of water (Table 1).

The volume of normal saline for the deoxyribonuclease powder would not be crucial in view of the negligible contribution of this biopolymer to tonicity. Vapour pressure osmometry and cryoscopy confirmed that all the adjusted formulations were isotonic with respect to saline within ± 0.01 mol/kg. The good agreement between the measurements at 37°C and near 0°C could be expected in these relatively dilute solutions, in contrast to differences detected at higher solute concentrations.[12]

The following factors which contribute to the therapeutic efficacy may be affected by the concentration of the drug in solutions used for nebulisation:

1. the droplet size distribution leaving the nebuliser;
2. the total amount of drug in the respirable-size droplets;
3. changes in the size of droplets due to evaporation of water from them, or condensation of water upon them.[13] These factors determine the deposition pattern of the aerosol in an individual's airways.

However, as the droplet size distribution from most nebulisers is quite wide, we would not expect

the changes in the deposition pattern to be very significant over the range of concentrations given in Table 1.[14]

It is more likely that the dose-response curve of bronchodilators in sensitive subjects could be favourably shifted if these drugs were nebulised from isotonic solutions because non-isotonic solutions cause an increase in airway resistance in asthmatics.[1,2] However, it is important to note that preferential evaporation of water takes place during nebulisation.[15,16] Thus, an initially isotonic formulation could become significantly hypertonic towards the end of nebulisation for certain designs of generators.[15]

All the nebuliser preparations tested were in use at the time of the study either in Australia, or in the U.K., or both. Gentamicin sulphate used was supplied for parenteral administration (no special formulation for nebulisers seems to exist). We were informed that acetylcysteine available in the U.K. under the name Airbron® (Duncan Flockhart) was equivalent to Mucomyst®. It appears that only Boehringer-Ingelheim have at this stage the intention to present Atrovent solutions as isotonic.

We would like to suggest that there is now sufficient evidence to warrant clinical trials of comparative safety and efficacy of the other products adjusted to isotonicity. Related to this issue is the suggestion of Clay et al. that a minimum of 4 mL fill of nebulisers should be used to optimise their output.[17] In the case of the solutions of very low tonicity (e.g. the preparations of salbutamol, sodium cromoglycate and beclomethasone in Table 1), nearly isotonic solutions could be obtained either by 1:1 dilution with about twice-normal saline, or by dilution with a large excess of normal saline (5-fold or greater dilution should be adequate).

Mucolytic and antibiotic aerosols have been reported to have irritative effects, and it was suggested that co-administration of a bronchodilator could prevent bronchospasm.[18] Perhaps the use of isotonic solutions of these agents could improve their tolerance in sensitive subjects, even without the addition of a bronchodilator.

In fact, in the case of acetylcysteine, the manufacturers have already recommended that dilution with water or isotonic saline may reduce bronchospasm in patients sensitive to the undiluted solution.[9]

We would like to point out that the adjustment of tonicity may only be relevant to large-volume aerosols (i.e. mostly nebulised solutions). Where minute quantities of drugs (typically less than 1 mg of bronchodilators) are administered e.g. in the form of a dry powder in a volatile halocarbon propellant, the effects on the tonicity of the fluids covering the airways will be negligible.

Acknowledgements

The authors would like to thank the Asthma Foundation of N.S.W. for an equipment grant and the University of Sydney for a scholarship to H-K.C. The drugs were kindly supplied by the Departments of Thoracic Medicine and Pharmacy at the Royal Prince Alfred Hospital, Sydney, Sterling-Winthrop Group Ltd. U.K. (Alevaire1®), Consolidated Chemicals Ltd, U.K. (Deanase®) and Glaxo Australia Pty Ltd (Becotide Suspension®). We are grateful to Dr S.D. Anderson for helpful discussions, and to Mrs Nola Strong for typing the manuscript.

® Registered tradename

References

1. Schoeffel RE, Anderson SD, Altouynan REC. Bronchial hyperreactivity in response to inhalation of ultrasonically nebulised solutions of distilled water and saline. Br Med J 1984; 282: 1285-7.
2. Anderson SD, Schoeffel RE, Finney M. Evaluation of ultrasonically nebulised solutions for provocative testing in patients with asthma. Thorax 1983; 38: 284-91.
3. Anonymous. CSM warns on bronchospasm with ipratropium bromide. Pharmaceut J 1984; 233: 171.
4. Fois RA, Gonda I. Atrovent and bronchospasm. Pharmaceut J [Letter] 1984; 233: 437.
5. Mann JS, Howarth PH, Holgate ST. Bronchoconstriction induced by ipratropium bromide in asthma: relation to hypotonicity. Br Med J 1984; 289: 469.
6. Fuller RW, Collier, JG. Sodium cromoglycate and atropine block the fall in FEV, but not the cough induced by hypotonic mist. Thorax 1984; 39: 766-70.
7. Groom CV, Gonda I, Fildes FJT. Prediction of equilibrium aerodynamic diameters for inhalation aerosols. In: 2nd Int Conf Pharm Technol, APGI, Paris, vol. 5, 1980: 124-31.
8. Robinson RA, Stokes HR. Electrolyte solutions. Butterworths, 2nd ed. London, 1959.
9. Roberts RM, ed. Mims Annual 1983. 7th ed. IMS Publishing, Crows Nest (Australia); IMS Publishing, 1983.
10. Association of the British Pharmaceutical Industry. Data Sheet Compendium 1981-82, London: Datapharm Publications Ltd, 1981.
11. Diem K, Lentner C, eds. Documeta Geigy-Scientific Tables, Macclesfield: Geigy Pharmaceuticals, 7th ed. 1975.
12. Gonda I, Kayes JB, Groom CV, Fildes FJT. Characterisation of hygroscopic inhalation aerosols. In: Stanley-Wood N, Allen T, eds. Particle size analysis 1981. Chichester: John Wiley & Sons, 1982: 31-43.
13. Swift DL. Aerosols and humidity therapy: Generation and respiratory deposition of therapeutic aerosols. Am Rev Resp Dis 1980; 122 (Part 2, Suppl): 71-7.
14. Gonda I. Study of the effects of polydispersity of aerosols on regional deposition in the respiratory tract. [Abstract] J Pharm Pharmacol 1981; 33 (Suppl): 52:P.
15. Mercer TT. Production of therapeutic aerosols. Principles and techniques. Chest 1981; 80 (Suppl): 813-17.
16. Ferron GA, Kerrebign KF, Weber J. Properties of aerosols produced with three nebulisers. Amer Rev Resp Dis 1976; 114: 899-908.
17. Clay MM, Pavia D, Newman SP, Leonard-Jones T, Clarke SW. Assessment of jet nebulisers for lung aerosol therapy. Lancet 1983; ii: 592-4.
18. Lourenco RV, Cotromanes E. Clinical aerosols: II. Therapeutic areosols. Arch Intern Med 1982; 142: 2299-308.

Disclaimer: The authors cannot be held responsible if any of the products mentioned in this article are not the same as the products supplied by the manufacturers at the time of the publication.

J. CHEM. SOC. PERKIN TRANS. II 1987

Hexamethylmelamine: a Study of Solvation and Crystallisation

Manuel J. Aroney,* Trevor W. Hambley, Emilios Patsalides, and Raymond K. Pierens
School of Chemistry, University of Sydney, Sydney, New South Wales 2006, Australia
Hak-Kim Chan and Igor Gonda
Department of Pharmacy, University of Sydney, Sydney, New South Wales 2006, Australia

Dielectric, electro-optic, and spectroscopic properties of hexamethylmelamine (HMM) are examined in various solvents. The study is an extension of earlier work relating the dielectric characteristics of solvent to the habit of HMM crystals, a factor of importance to the effectiveness of pulmonary administration of this drug in the treatment of human small-cell lung carcinoma. In solution HMM is confirmed to be non-dipolar though abnormally large atomic polarisation is found. The optical polarisability anisotropy correlates with an extensively delocalised π-system involving the triazine ring and the exocyclic nitrogens. Interactions between HMM and cyclohexane, dioxane, and benzene are weak and not sterically defined—each of these solvents yields predominantly 'compact' crystal forms of HMM. In hexafluorobenzene definitive evidence is provided for strongly favoured stereospecific face-to-face HMM–C_6F_6 interactions. Needle-shaped crystals obtained from this solvent very rapidly become opaque and friable. Thermal analysis indicates an unstable 1:1 HMM–C_6F_6 adduct. This was confirmed by *X*-ray crystal structure determination which showed that HMM and C_6F_6 alternate in infinite columns, suggestive of a π–π interaction between the rings. The study provides an important correlation, based on experiment, between the statistically preferred HMM–C_6F_6 configuration in solution and that found for the crystalline adduct when isolated.

Gonda *et al.*[1–3] have studied the preparation and aerodynamic properties of different crystal forms of hexamethylmelamine (HMM) [2,4,6-tris(dimethylamino)-1,3,5-triazine], (1) a drug active against human small-cell lung carcinoma. Research on the crystal forms was motivated by the need to improve the efficacy of drug action of HMM and to gain information on the toxic potential with the direct pulmonary administration of this drug, a desirable procedure for the reduction of adverse systemic side effects. They noted that crystallisation of HMM from dipolar solvents yielded predominantly acicular crystals while mainly compact crystals were obtained from solvents with zero dipole moments. Both types have a hexagonal crystal lattice but differ in crystal habit. In a study of HMM from fifteen different solvents, Gonda *et al.*[3] have advanced an empirical correlation between the aspect ratio of HMM crystals and the polarity of the solvent used for crystallisation.

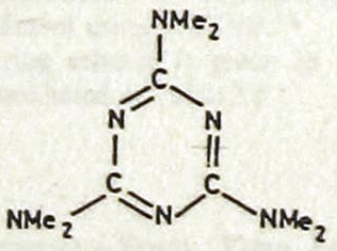

(1)

The present work is concerned primarily with a study of dielectric, electro-optic, and spectroscopic properties of HMM in a variety of solvents to gain some insight into the nature of intermolecular interactions in the precursor state to crystallisation. An unexpected crystal form of HMM from hexafluorobenzene led us to determine the *X*-ray structure of these crystals.

Experimental

Hexamethylmelamine was prepared and characterised as in reference 4. The solvents cyclohexane, dioxane, benzene, and hexafluorobenzene were distilled and appropriately dried over sodium or molecular sieves. Other solvents (reagent grade) were used without purification. Dielectric polarisation, microwave absorption, and electric birefringence measurements were made by techniques previously described.[5–7] Appropriate solvent constants are given in references 5 and 8. The results are summarised in Table 1. ^{1}H N.m.r. data in Table 2 were obtained on a Hitachi Perkin-Elmer R-24B n.m.r. spectrometer at 37 °C; the temperature dependence of ^{1}H n.m.r. measurements were made using a Bruker HX-90 spectrometer. Chemical shifts were extrapolated to infinite dilution, tetramethylsilane being used as internal reference.

Thermoanalytical data were obtained on a combined tga–dta instrument (Rigaku, Thermoflex M8076) using crystals of freshly filtered HMM. Hexafluorobenzene adduct HMM–C_6F_6 (7.5 mg) was heated at 10 °C min^{-1} in a stream of nitrogen (100 ml min^{-1}). Events recorded are fusion and volatilisation.

X-Ray structure determination of the HMM–C_6F_6 adduct proved very difficult since crystals of HMM–C_6F_6 are very unstable when exposed to the atmosphere, shattering and losing all crystallinity within seconds. The decomposition is evidently due to the loss of C_6F_6. To preclude this loss, various coatings were applied to the crystals but many of these absorbed the C_6F_6 leading to decomposition. Mounting in sealed capillaries also resulted in decomposition. Only a heavy coating of epoxy resin was successful in stabilizing the crystals.

Lattice parameters at 21 °C were determined by a least-square fit to the setting parameters of 25 independent reflections, measured and refined on a Enraf-Nonius CAD4F four-circle diffractometer employing graphite-monochromated Mo-K_α radiation.

Crystal Data.—$C_{15}H_{18}F_6N_6$, M_r = 396.3. Monoclinic, space group C_2/m, a = 17.631(6), b = 6.771(1), c = 15.979(3) Å,

Table 1. Molar polarisations, refractions, and molar Kerr constants of HMM in solution at $T = 298$ K and $\lambda = 589.3$ nm

Solvent	$_{\infty}\varepsilon_1$ [a]	β [a]	γ [a]	δ [a]	$_{\infty}P_2$/cm^3 [b]	R_D/cm^3 [b]	$10^{27}\,{}_{\infty}({}_mK_2)$/m^5 V^{-2} mol^{-1} [c]
Cyclohexane	0.52	0.231	0.053	5.2	79 ± 2	64 ± 2	18 ± 1
Dioxane	0.65	0.007	0.137	7.35	81 ± 2	66 ± 2	21 ± 1
Benzene	0.45	0.168	0.025	0.38	77 ± 2	63 ± 2	18 ± 2
Hexafluorobenzene	0.95	−0.502	0.155	1.46	73 ± 2	61 ± 2	61 ± 2

[a] $_{\infty}\varepsilon_1 = \Sigma\Delta\varepsilon/\Sigma w_2$; $\beta = \Sigma\Delta d/d_1\Sigma w_2$; $\gamma = \Sigma\Delta n/n_1\Sigma w_2$; $\delta = \Sigma\Delta B/B_1\Sigma w_2$; where $\Delta\varepsilon$, Δd, Δn, and ΔB are the measured incremental changes from the pure solvent values of the relative permittivities, densities, refractive indices, and Kerr constants, respectively, for solutions having solute weight fractions w_2. [b] From symmetry the molecular electric dipole moment is zero. The difference between $_{\infty}P_2$ and R_D must be due to (field-induced) atomic polarisation of the order of 20% of R_D. [c] The solute electric birefringence is reported as $_{\infty}({}_mK_2)$, the molar Kerr constant of the solute at infinite dilution. SI units are used. The conversion factor from the electrostatic (c.g.s., e.s.u.) system is: 1 m^5 V^{-2} mol^{-1} = 0.8998 × 10^{15} e.s.u. mol^{-1}.

Table 2. Chemical shifts δ_H for protons of HMM in various solvents

Solvent	δ_H/p.p.m.[a]
C_6H_{12}	3.03
CCl_4	3.08
$CDCl_3$	3.09
C_6H_6	3.00
C_6F_6	3.05
Me_2CO	3.05
CD_3OH	3.12

[a] The precision of measurement determined from multiple runs is ±0.01 p.p.m.

$\beta = 91.87(3)°$, $V = 1\,906.6$ Å^3, $Z = 4$, $D_c = 1.380$ g cm^{-3}, μ(Mo-K_α) = 1.20 cm^{-1}, λ(Mo-K_α) = 0.7107 Å, F(000) 1 632 electrons.

Intensity data were collected in the range $1 < \theta < 22.5°$ using an w—θ scan. The scan width and horizontal counter apertures employed were $(1.0 + 0.35 \tan\theta)°$ and $(2.40 + 0.50 \tan\theta)$ mm, respectively. Data reduction and application of Lorentz, polarisation, and decomposition (~6%) corrections were performed using the program SUSCAD.[9] Of the 1 101 independent reflections collected, 555 with $I > 2.5\,\sigma(I)$ were considered, observed, and used in the calculations.

The structure was solved using MULTAN[10] which revealed all atoms of the HMM molecule and six atoms of the C_6F_6. All other atoms were located from subsequent difference maps.

Full-matrix least-squares refinement of an overall scale factor, positional and thermal (anisotropic for full occupancy, isotropic for disordered atoms) parameters converged (all shifts <0.5σ) with R* 0.142, R_w 0.168 and $w = 3.39/[\sigma^2(F_o) + 0.0099\,F_o^2]$. Maximum excursions in a final difference map were +0.5 e Å^{-3} and −0.25 e Å^{-3}. Scattering factors and anomalous dispersion terms used were those supplied in SHELX-76.[11] All calculations were carried out using SHELX-76[11] and plots were drawn using ORTEP.[12]

The atom numbering scheme is given in Figure 1. Final atomic co-ordinates are listed in Table 3.†

Table 3. Positional parameters (× 10^4)*

	x	y	z
N(1)	6 977(10)	0	2 433(17)
C(1)	6 682(13)	0	3 226(19)
N(2)	5 912(13)	0	3 331(12)
C(2)	5 434(12)	0	2 581(13)
N(3)	5 681(10)	0	1 897(10)
C(3)	6 477(14)	0	1 847(19)
N(4)	7 091(12)	0	3 900(16)
C(4)	7 970(15)	0	3 845(18)
C(5)	6 775(14)	0	4 687(13)
N(5)	4 700(12)	0	2 709(13)
C(6)	4 376(15)	0	3 596(17)
C(7)	4 190(19)	0	1 888(26)
N(6)	6 757(11)	0	932(16)
C(8)	6 250(19)	0	224(18)
C(9)	7 496(12)	0	890(17)
F(10)	2 314(15)	0	3 087(16)
F(11)	2 211(15)	0	1 472(21)
F(12)	998(25)	0	586(25)
F(13)	−433(24)	0	1 588(28)
F(14)	−467(19)	0	3 237(26)
F(15)	1 036(20)	0	4 017(20)
C(10)	1 570(22)	0	2 893(23)
C(11)	1 558(16)	0	2 022(22)
C(12)	937(20)	0	1 463(28)
C(13)	268(27)	0	1 901(18)
C(14)	260(14)	0	2 770(17)
C(15)	893(13)	0	3 315(21)
F(10′)	7 611(30)	0	7 782(44)
F(11′)	8 454(49)	0	9 086(50)
F(12′)	10 106(60)	0	8 858(52)
F(13′)	10 613(26)	0	7 556(40)
F(14′)	9 920(29)	0	6 204(31)
F(15′)	8 469(42)	0	5 978(49)
C(10′)	1 488(49)	0	2 651(61)
C(11′)	1 214(93)	0	1 824(75)
C(12′)	581(77)	0	1 283(56)
C(13′)	565(68)	0	2 153(59)
C(14′)	835(74)	0	2 982(80)
C(15′)	1 471(74)	0	3 520(60)

* Primes indicate minor occupancy sites, occupancy = 30%.

Discussion

Molar Kerr Constants.—From *X*-ray crystal structure analysis the molecule of HMM was shown to be planar (apart from the hydrogens) with D_{3h} symmetry.[13] The exocyclic carbon–nitrogen bonds are comparatively short indicating that the 'planar' configuration is stabilised through conjugation between the nitrogen lone pair electrons of the NMe_2 groups and π-orbitals of the ring. Evidence for such electron drift into the triazine ring of HMM is also found in its basic (electron-donor) character towards protons, BF_3 and trinitrobenzene.[4,14] In cyclohexane solution HMM is found to be non-dipolar ($\mu <$ 0.2 C m‡) from absence of measurable microwave absorption in the GHz region. The molar Kerr constant at infinite dilution in

* $R = \Sigma(|F_o| - |F_c|)/\Sigma|F_o|$, $R_w = [\Sigma w(|F_o| - |F_c|)^2/\Sigma w F_o^2]^{1/2}$.

† *Supplementary data* (see section 5.6.3 of Instructions for Authors in the *J. Chem. Soc., Perkin Trans.* 2, 1987, Issue 1). Lists of bond lengths and angles and of thermal parameters have been deposited at the Cambridge Crystallographic Data Centre.

‡ 1 C m = 0.2998 × 10^{30} D.

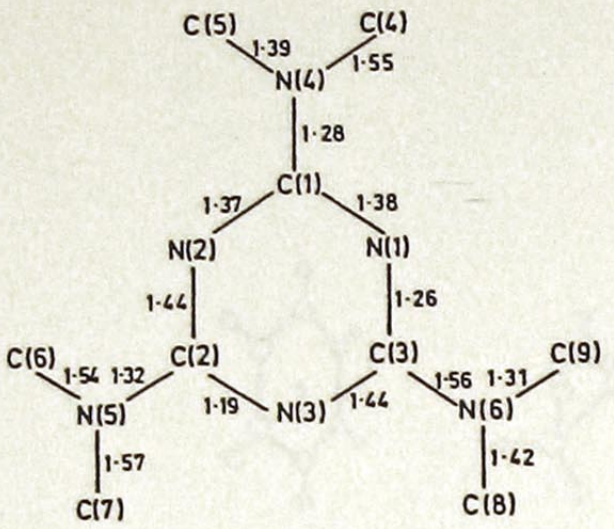

Figure 1. Atom numbering scheme of hexamethylmelamine (1)

cyclohexane is 18×10^{-27} m^5 V^{-2} mol^{-1} from which can be obtained the solute molecular optical anisotropy $\Delta b = (b_1 - b_3)$, using the Le Fèvre modified Langevin–Born expression[5]

$$_mK = L_D P(\Delta b)^2/405\, kT\varepsilon_{oE}P$$

The term b_1 ($= b_2$) refers to the molecular electron polarisability of HMM in the plane of the triazine ring; b_3 is the polarisability perpendicular to that plane; L, $_DP$ ($=_\infty P_2$), k, T, ε_0, and $_EP$ (taken as 0.95 R_D) are in turn Avogadro's number, the molar distortion polarisation, the Boltzmann constant, the absolute temperature, the permittivity of vacuum, and the molar electron polarisation. The polarisability anisotropy 10^{40} Δb* of HMM follows as 5.8 ($\pm$0.2) C m^2 V^{-1} which is somewhat greater than that of triazine 4.8 ($\pm$0.2) C m^2 V^{-1}.[15] The Δb so obtained is little affected ($\pm$0.1) if account were to be taken of the second hyperpolarisability contribution suggested for triazines by Battaglia and Richie.[15]

The effect of change of solvent environment on the molar Kerr constant has been examined. Values of the $_\infty(_mK_2)$ for HMM from solutions in cyclohexane and dioxane are quite close; the solute optical anisotropy 10^{40} Δb from dioxane is 6.3 ($\pm$0.2) C m^2 V^{-1}. Each of these solvents is non-dipolar and the solvating molecules are near isotropically polarisable. In benzene, however, it is often found that stereospecific solvation can lead to a time-averaged non-random distribution of the highly anisotropic benzene molecules about the solute and hence to a measured molar Kerr constant which is not that of the 'isolated' solute molecule but rather that of the solute–solvent cluster.[16] Such observed solvent effects on the solute $_mKs$ have been interpreted to obtain information on the preferred stereospecific solute–solvent encounters. In the case of HMM in benzene the apparent solute $_mK$, and hence the molecular anisotropy of the solute together with its solvent cluster, is virtually unchanged from that in cyclohexane which means that the statistical distribution of the solvating benzene molecules is such that the solute polarisability is augmented to the same extent in the direction of the triazine plane as perpendicular to that plane. This suggests that within a dynamic cluster model, solute–solvent encounters in which the HMM and C_6H_6 planes are parallel are no more or no less favoured than encounters in which the planes are perpendicular. Steric and electrostatic considerations are used to rationalise solute–solvent interactions which are most likely to occur in a stereospecific sense at polar sites within the solute. Face-to-face approaches such as A in Figure 2 would result in an enhanced solute anisotropy and hence a greater apparent solute Kerr constant (in the absence of significant charge transfer). Contributions to the cluster from approaches such as B with the relatively electrophilic benzene periphery close to the electron-rich triazine system or to the exocyclic nitrogens would result in a decreased apparent solute Kerr constant. Angular encounters such as C have far less effect on the solute $_mK$. The effect on the solute $_mK$ of incoming benzenes approaching in the plane of HMM (*e.g.* D or E) would be small as their encounter with nitrogen polar centres is sterically blocked by the ring of methyl groups on the periphery of HMM. Thus no predominant HMM–benzene configuration can be identified. In hexafluorobenzene, however, the $_\infty(_mK_2)$ of HMM is 61×10^{-27} m^5 V^{-2} mol^{-1} clearly indicating that clustering of C_6F_6 molecules about HMM greatly augments the intrinsic solute anisotropy.[8] Thus parallel HMM–C_6F_6 configurations such as A would statistically be favoured. This provides direct experimental evidence to show that in the geometry of C_6F_6 solvation of HMM, A-type face-to-face associations are preponderant. The results correlate with intuitive argument from electrostatics as A represents the close approach of the π-depleted aryl system of C_6F_6 to the electron-rich triazine ring. The interactions must be weak, however, since from microwave absorption the dipole moment of HMM is *ca.* 0 in C_6F_6 solution. By contrast, perpendicular approaches such as B would be destabilised through repulsive interactions between negative charge centres on the plane of HMM and the fluorine atoms on the periphery of C_6F_6. Accepting A as the most probable encounter, the calculated $_mK$ for a discrete 1:1 complex HMM–C_6F_6 with this geometry is calculated to be *ca.* 52×10^{-27} m^5 V^{-2} mol^{-1}, a little less than the observed value. It is possible that in C_6F_6 solution associations A occur simultaneously above and below the plane of HMM. The data of Table 1 relate to dilute solutions but it is pertinent to note that the solute molar Kerr constants appeared to be virtually invariant with increasing solute concentration; in the case of cyclohexane this was to near saturation. Fully saturated solutions could not be studied because of the risk of precipitation in the Kerr cell and concomitant electrical discharge.

^{1}H *N.m.r. Spectra.*—^{1}H N.m.r. shifts δ_H for the HMM protons at high dilution in various solvents are shown in Table 2. Most striking is the absence of strong aromatic solvent-induced shifts which are often found with benzene and hexafluorobenzene and attributed mainly to a degree of organisation of the magnetically anisotropic C_6H_6 or C_6F_6 molecules about the sensor protons.[16,17] This lends support to the suggestion made earlier that aromatic solvent encounters with the peripheral hydrogen atoms of HMM are relatively weak and overall do not result in the preponderance of shielding or alternatively deshielding HMM–solvent configurations. This is supported also by the near constancy of the HMM proton shifts in toluene with variation of temperature (δ 2.96—2.99 for the range −50—35 °C). In the case of configuration A of HMM–C_6F_6 (the statistically favoured encounter from the Kerr effect analysis) the HMM protons are remote from C_6F_6 and are located between the shielding/deshielding regions of C_6F_6, thus resulting in negligibly small solvent induced changes in chemical shift. Little change in the proton shift δ was observed with increasing solute concentration up to near saturation.

Crystallisation of Hexamethylmelamine.—We find in accord with Gonda *et al.*[1–3] that predominantly needle-shaped crystals are formed from the dipolar solvents methanol, chloroform, and acetone while more equidimensional crystals tend to be obtained from cyclohexane, benzene, carbon tetrachloride,

* Polarisabilities are expressed in SI units throughout; the conversion factor from the c.g.s., e.s.u. system is: 1 C m^2 V^{-1} = 0.8988×10^{16} cm^3.

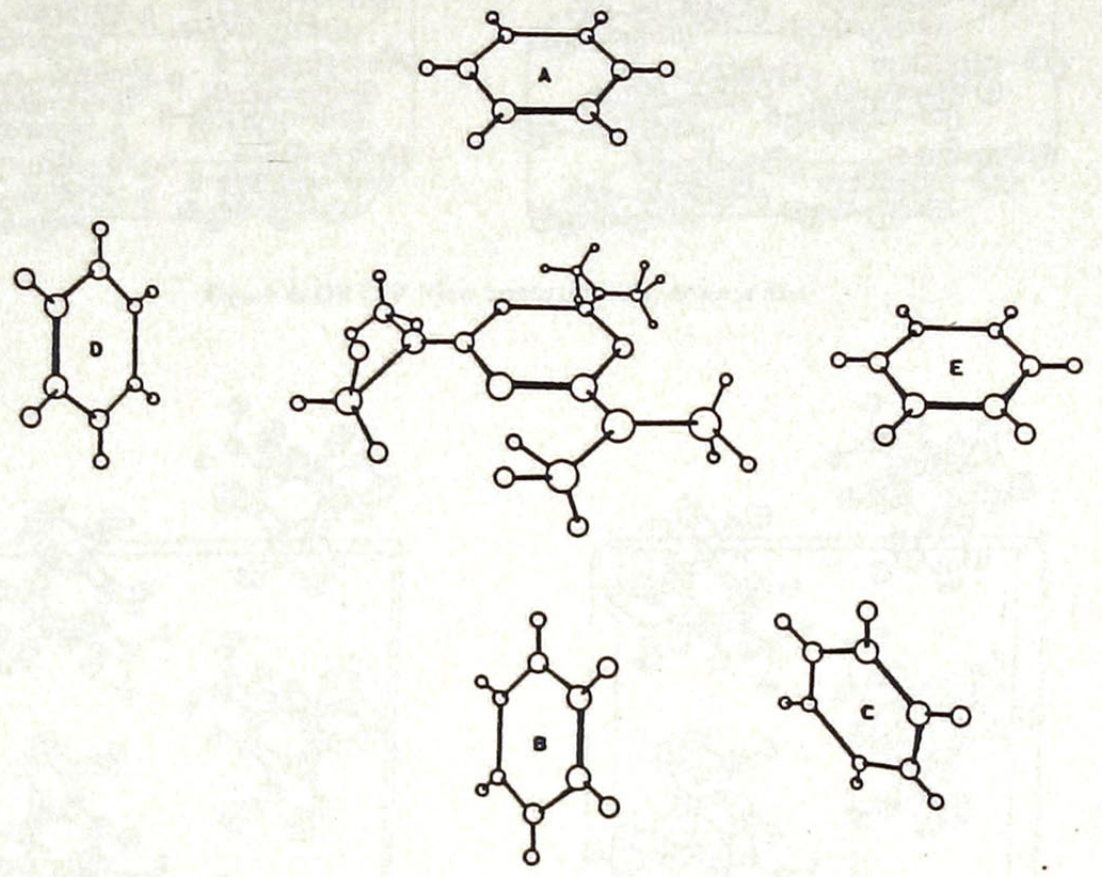

Figure 2. Stereospecific encounters between HMM and solvating aromatic molecules

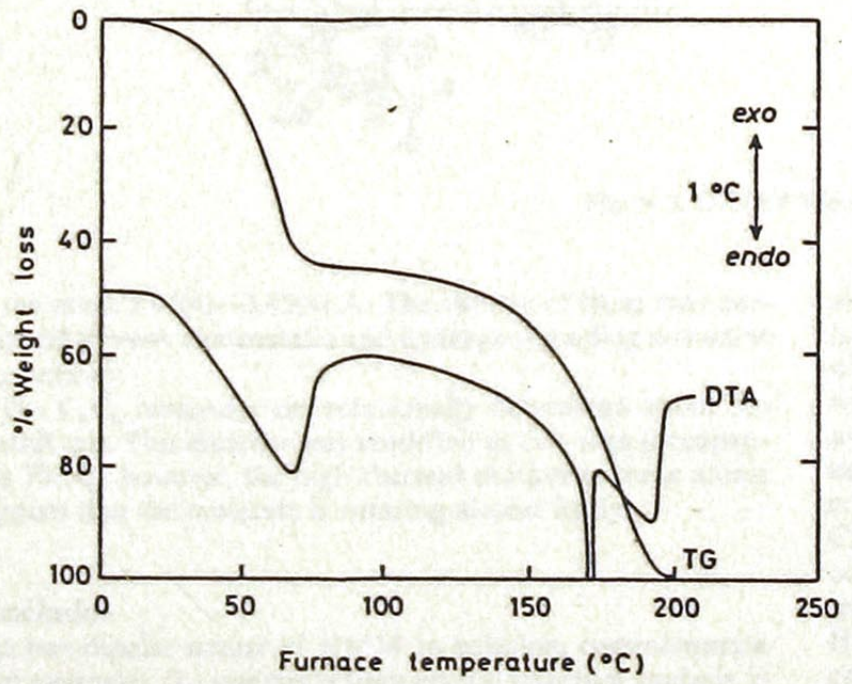

Figure 3. Thermogravimetric (TG) and differential thermal analysis (DTA) curves for the HMM C_6F_6 adduct

and dioxane. Tetrahydropyran which resembles dioxane in geometry and in possessing a C–O–C local dipole appears to yield a mixture of crystal forms. From hexafluorobenzene are obtained long needle-shaped crystals which appears to contravene the relationship between the crystal habit and solvent polarity of reference 3 since this solvent is non-dipolar. The needles were observed to become opaque and friable within seconds of isolation from solution.

Thermal analysis was made of freshly filtered crystals of HMM from hexafluorobenzene. Thermogravimetric (TG) and differential thermal analysis (DTA) curves are shown in Figure 3. Transference of the crystals from the Buchner filter to the thermal balance was made in about 20 s by which time the surface of the crystals had become opaque. The sample was heated (10 °C min^{-1}) from room temperature to approximately 200 °C. Distinct weight changes and corresponding endothermic peaks attributed to loss of C_6F_6 were observed from room temperature to *ca.* 80 °C and for the vaporisation of HMM from 150—200 °C. A sharp endothermic peak at *ca.* 170 °C is due to fusion of HMM. The percentage weight change due to the loss of C_6F_6 was found to be *ca.* 44% compared to 47% calculated for a 1:1 HMM–C_6F_6 adduct. From this it is concluded that the precipitated HMM crystals from C_6F_6 were those of the 1:1 adduct which is similar to but much less stable than the previously known 1:1 HMM–trinitrobenzene adduct.[14]

Crystal Structure of the HMM/C_6F_6 *Adduct.*—The precision of the structure determination was severely limited by a number of factors; all crystals of the adduct obtained diffracted only weakly at higher angles and this problem was exacerbated by the need to coat the crystals with epoxy resin to preclude decomposition. Consequently a data set of limited extent was obtained restricting the type of refinement possible and making location of hydrogen atoms impossible. Secondly, the C_6F_6 molecules are severely disordered, as described below, limiting the accuracy to which they could be modelled. Accordingly, the details of the geometry of the two molecules are not discussed except to note that bond lengths obtained for HMM are in accord with those reported in more precise determinations.[13,14]

The structure consists of planar molecules lying on crystallographically imposed mirror planes at $y = 0$ and $y = \frac{1}{2}$. Molecules of HMM and C_6F_6 alternate in infinite columns parallel to the *b* axis. Thus, the separation between these molecules is equal to half the *b* cell dimension or 3.385(1) A. Such a short contact is suggestive of a π–π interaction between the rings. Within the planes HMM and C_6F_6 alternate parallel to the *a* direction. The lines of molecules in the *a* direction are dislocated by *a*/2 with respect to each other resulting in a close packed arrangement of the columns. Closest contacts within the planes are between *N*-methyl carbon atoms and fluorine atoms

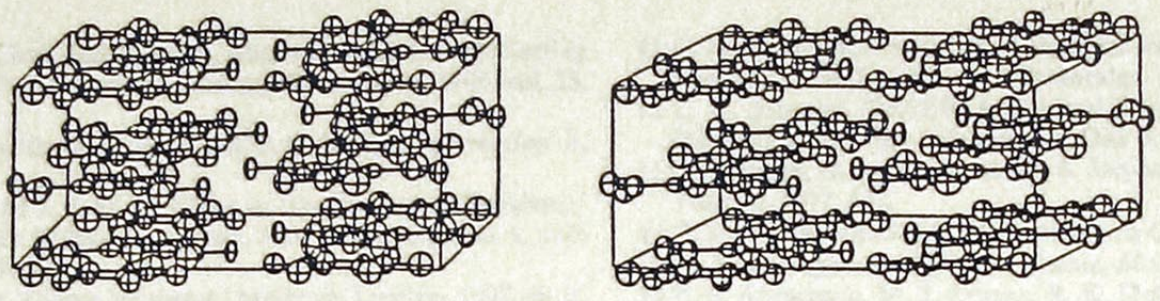

Figure 4. ORTEP View approximately, down *a* axis

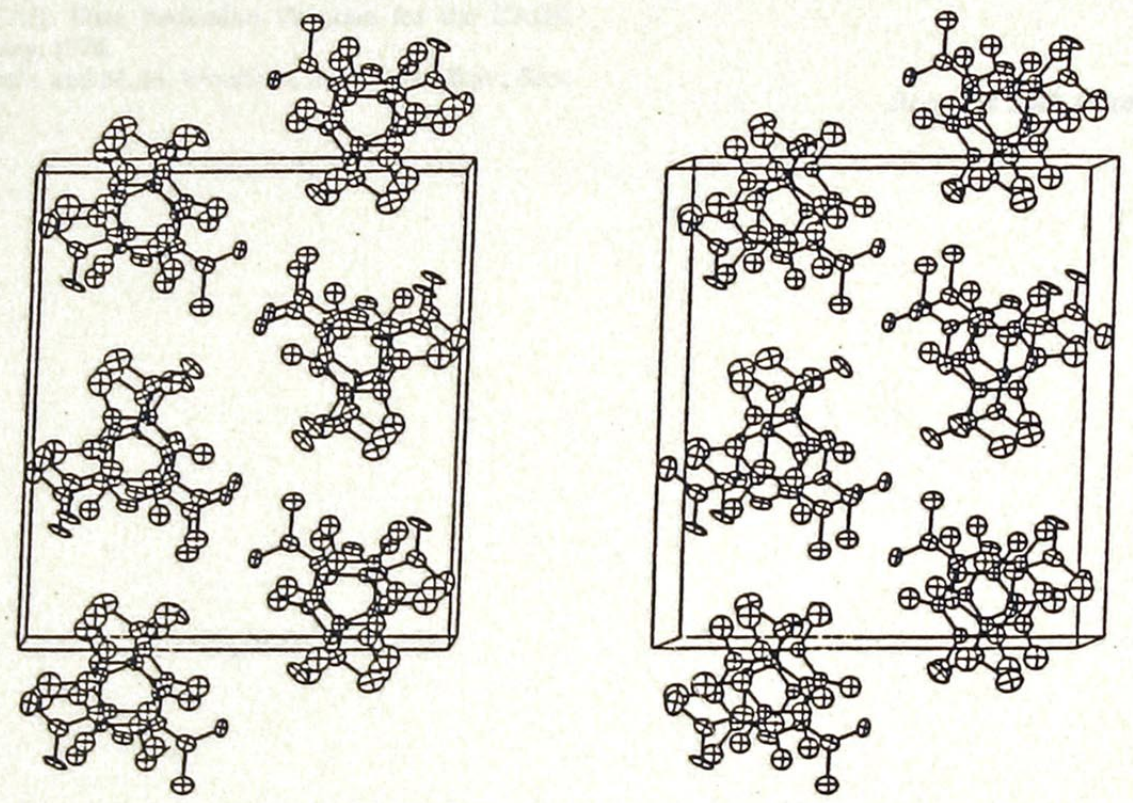

Figure 5. ORTEP View down *b* axis

in the range 2.95(4)—3.45(4) Å. The shorter of these may correspond to weak electrostatic and hydrogen-bonding attractive interactions.

The C_6F_6 molecules are rotationally disordered about the central axis. This disorder was modelled as two sites (occupancies 70:30); however, the high thermal motion of these atoms suggests that the molecule is rotating almost freely.

Conclusion

The non-dipolar nature of HMM in solution, commensurate with molecular D_{3h} symmetry from crystal structure analysis, is verified through the absence of measurable microwave absorption in the GHz region. The disparity between low- and high-frequency field polarisations is attributed to larger than usual field-induced atomic polarisations. The optical polarisability anisotropy of HMM in cyclohexane and in dioxane, derived from electric birefringence measurements, was found to be greater than that of triazine. The large 'in-plane' polarisability correlates with an extended delocalised π-system involving the triazine ring and the exocyclic nitrogens. The apparent solute electric birefringence of HMM in benzene and hence the apparent optical anisotropy of the HMM encapsulated in its benzene solvent cluster is virtually identical to that in cyclohexane. From this and concomitant ^1H n.m.r. evidence, it is inferred that HMM–C_6H_6 interactions are particularly weak and no statistically predominant stereospecific interaction can be identified. In hexafluorobenzene solution, however, the electric birefringence data provide definitive evidence for favoured face-to-face HMM–C_6F_6 encounters. Crystallisation of HMM from hexafluorobenzene yields needle-shaped crystals which very rapidly became opaque and friable. Thermal analysis indicated that the crystals so isolated are those of an unstable 1:1 HMM–C_6F_6 adduct. This was confirmed by *X*-ray crystal structure determination which showed that HMM and C_6F_6 alternate in infinite columns, suggestive of a π–π interaction between the rings. This study provides an important correlation based on experiment, between the statistically preferred HMM–C_6F_6 configuration in solution and that found for the crystalline adduct when isolated.

Acknowledgements

The authors acknowledge with gratitude a grant generously made in support of this work by the Athanase Yenibis Foundation and the award of a postgraduate scholarship by the University of Sydney to H.-K. C. as part of a URG Special Projects Grant to I. G.

References

1 I. Gonda, A. F. A. El Khalik, and A. Z. Britten, *J. Pharm. Pharmacol.* (*suppl.*), 1985, 37, 117.

2 I. Gonda and A. F. A. P. El Khalik, Sixth International Symposium on Inhaled Particles, August 1985, Cambridge, U.K. (to be published in *Ann. Occup. Hyg.*).

3 I. Gonda, H. K. Chan, and T. Nagai, Abstract of the Annual Meeting of the Japanese Pharmaceutical Society, Chiba, Japan, 1986, vol. 25, 1.
4 S. K. Das, T. Gündüz, R. A. Shaw, and B. C. Smith, *J. Chem. Soc. A*, 1969, 1403.
5 C. G. Le Fèvre and R. J. W. Le Fèvre, in 'Techniques of Chemistry,' ed. A. Weissberger, Wiley-Interscience, New York, 1972, vol. 1, part III C, ch. 6, p. 399.
6 R. J. W. Le Fèvre, 'Dipole Moments,' Methuen, London, 1953, ch. 2.
7 S. J. Pratten, M. K. Cooper, M. J. Aroney, and S. W. Filipczuk, *J. Chem. Soc., Dalton Trans.*, 1985, 1761.
8 R. S. Armstrong, M. J. Aroney, R. K. Duffin, H. J. Stootman, and R. J. W. Le Fèvre, *J. Chem. Soc., Perkin Trans. 2*, 1973, 1362.
9 J. M. Guss, SUCAD, Data Reduction Program for the CAD4, University of Sydney, 1976.
10 G. Germain, P. Main, and M. M. Woolfson, *Acta Crystallogr., Sect. A*, 1971, 27, 368.
11 G. M. Sheldrick, SHELX-76, A Program for *X*-ray Crystal Structure Determination, University of Cambridge, 1976.
12 C. K. Johnson, ORTEP, A Thermal Ellipsoid Plotting Program, Oak Ridge National Laboratories, Oak Ridge, 1965.
13 G. J. Bullen, D. J. Corney, and F. S. Stephens, *J. Chem. Soc., Perkin Trans. 2*, 1972, 642.
14 R. M. Williams and S. C. Wallwork, *Acta Crystallogr.*, 1966, 21, 406.
15 M. R. Battaglia and G. L. D. Ritchie, *Mol. Phys.*, 1976, 32, 1481.
16 R. S. Armstrong, M. J. Aroney, R. K. Duffin, H. J. Stootman, and R. J. W. Le Fèvre, *J. Chem. Soc., Perkin Trans. 2*, 1973, 1272.
17 R. D. Bertrand, R. D. Compton, and J. G. Verkade, *J. Am. Chem. Soc.*, 1970, 92, 2702.

Received 30*th October* 1986; *Paper* 6/2107

International Journal of Pharmaceutics, 41 (1988) 147–157
Elsevier

IJP 01385

Development of a systematic theory of suspension inhalation aerosols. II. Aggregates of monodisperse particles nebulized in polydisperse droplets

Hak-Kim Chan and Igor Gonda

Department of Pharmacy, University of Sydney, Sydney N.S.W. (Australia)

(Received 30 July 1986)
(Modified version received 10 July 1987)
(Accepted 21 July 1987)

Key words: Therapeutic aerosol; Aerosolization of suspensions; Aerosol particle size; Formulation effect; Aggregate size distribution; Parameters influence; Statistics of aggregation

Summary

Using the previously developed statistical framework to study the aggregation of primary drug particles in droplets formed on nebulization of suspensions, we have computed the expected size distributions of clusters of monodisperse primary drug particles obtained after drying of log-normally distributed polydisperse aerosol droplet sprays. In systems with a high ratio of droplet to primary particle diameters and relatively high average number of particles per droplet, the cluster size distributions were found to be essentially log-normal with the same geometric standard deviations as the droplets, and the mass median (aerodynamic) diameters were accurately predictable on the basis of assumption of uniform distribution of the solid throughout the liquid phase. In systems where the average number of primary particles per droplet was less than one, the cluster size distributions showed markedly non-linear behaviour on log-normal probability graphs. However, the mass median (aerodynamic) diameters could be still predicted quite reliably assuming uniform distribution of the solid among the fraction of the droplets expected to be occupied by the solid particles (i.e. excluding the empty droplets from the calculations). When the ratio of the droplet to primary particles was small and the concentration of the suspension was high, the size distributions of the aggregates deviated markedly from the log-normal function, particularly when the droplet sprays were narrowly distributed. Calculation of the mass median (aerodynamic) diameters and geometric standard deviations using the uniform distribution assumption could lead to grossly erroneous results in these systems. The reason for this behaviour is that (i) spherical particles cannot fill space completely and (ii) a significant portion of the log-normally distributed droplets is too small to accommodate the number of primary particles which would be computed for these droplets on purely statistical grounds. This 'exclusion' effect, however, becomes marked only at high concentrations which are beyond the range used in current therapeutic aerosols and outside the regions of validity of some of the assumptions of the present theory. Thus, assuming uniform distribution of solid in the droplets of aerosol sprays, it is possible to estimate the significance of formation of solid aggregates arising for purely statistical reasons (i.e. without taking into account any forces of attraction causing flocculation or coagulation). Outside the regions of validity of the assumption of uniform distribution, the full computational model developed in this paper has to be used to find the median size and the shape of the distribution of the solid clusters.

Introduction

Nebulization of suspensions of drug particles is a very common mode of drug delivery into the human respiratory tract. Typically, the primary

Correspondence: I. Gonda, Department of Pharmacy, University of Sydney, Sydney NSW 2006, Australia.

0378-5173/87/$03.50 © 1987 Elsevier Science Publishers B.V. (Biomedical Division)

drug particles have a narrow size distribution with a mass median aerodynamic diameter around 2–3 μm; their concentration is usually in the range (3×10^{-2} to 3% v/v and, on nebulization, they are contained in droplets whose initial mass median diameter is probably 30–40 μm (the basis for these estimates was reviewed in the first paper in this series (Gonda, 1985)). After evaporation of the carrier liquid, the deposition of the drug aerosol in the respiratory tract depends on the aerodynamic behaviour of the resulting drug particles which may be significantly different from the primary drug particles. There could be several reasons (Gonda, 1985) for such behaviour: in the previous paper, we dealt specifically with one of the reasons, namely the situation when large monodisperse droplets of propellant could hold more than one primary drug particle and, on evaporation of the propellant, these particles formed an aggregate (or 'cluster'). Clearly, the aerodynamic diameter of such an aggregate would be greater than that of a single particle. We wish to extend this simple picture, which ignores so far any other causes of aggregation or modified aerodynamic behaviour, to the more realistic model of monodisperse primary drug particles distributed in polydisperse droplets. We have noted previously (Gonda & Chan, 1985) that, over a narrow but reasonable range of formulation parameters, it may be possible to predict an approximate aerodynamic size distribution of the drug aggregates on the assumption that the drug is uniformly distributed in the droplets. In other words, the predicted distribution would be the same as that obtained for a drug completely soluble in the volatile propellant. The present communication investigates the validity of this approximation over a much wider range of formulation parameters.

Theory

We treat a suspension of monodisperse particles with equivalent sphere volume diameters d_e, dispersed in a volatile propellant at a % v/v concentration c. On nebulization, a droplet spray is formed with a size distribution $p(D)$, D being the diameter of individual droplets. The probability $P(k, D)$ that k primary particles are found in a droplet of diameter D is given by the Poisson expression (Raabe, 1968):

$$P(k, D) = \frac{\exp(-n)n^k}{k!} \quad k = 0, 1, \ldots, \infty \qquad (1)$$

where $n = n(D)$ is the average number of particles per droplet of diameter D. The probability that k particles can be found in a droplet of any size is:

$$P'(k) = \int_{D_{min}}^{D_{max}} P(k, D) \cdot p(D)\, dD \qquad (2)$$

If $p(D)$ is the experimentally determined initial distribution of the droplets after nebulization of the suspension, then D_{min} and D_{max} are dictated by the size ranges of the measuring device. The sum of the probabilities is then

$$\sum_{k=0}^{\infty} P'(k) = 1$$

If, however, $p(D)$ is an assumed function defined in the range $0 \leqslant D \leqslant \infty$, it is usual to put $D_{max} = \infty$; it is also necessary to ensure in such theoretical modelling that the diameter of the smallest droplet, D_{min}, is sufficiently large for the droplet to be able to accommodate the cluster of k particles (Callingham, 1980; Gonda, 1985; Gonda and Chan, 1985). In this situation when $D_{min} > 0$ it is found that $\sum_{k=0}^{\infty} P'(k) < 1$ and the probabilities $P'(k)$ must be renormalized:

$$P(k) = \frac{P'(k)}{\sum_{k=0}^{\infty} P'(k)} \qquad (3)$$

Then, clearly, these renormalized probabilities obey the summation condition

$$\sum_{k=0}^{\infty} P(k) = 1 \qquad (4)$$

For experimentally determined $p(D)$, or when $D_{min} = 0$, we have, of course,

$$P'(k) = P(k).$$

The total number of droplets, n_T, formed from a volume V of a suspension is

$$n_T = V/\bar{V}_D \tag{5}$$

where $\bar{V}_D$ is the average volume of a droplet. The total number of droplets containing aggregates of i particles, $n(i)$, is obtained by multiplying the probability of finding such an aggregate in a droplet of any size by the total number of droplets:

$$n(i) = P(i)n_T = P(i)V/\bar{V}_D \tag{6}$$

The mass of an aggregate of i primary drug particles is $m(i)$; the fraction of the total drug mass contained in aggregates of i drug particles is thus

$$F(i) = \frac{m(i)P(i)V/\bar{V}_D}{NgV} \tag{7}$$

where N is the number of primary particles per unit volume of suspension, g is the mass of a primary particle and the aggregate mass is

$$m(i) = ig \tag{8}$$

Eqn. 7 can be rewritten as

$$F(i) = \frac{igP(i)}{Ng\bar{V}_D} = \frac{iP(i)}{\bar{V}_D N} = \frac{iP(i)}{\bar{n}} \tag{9}$$

since the average number of particles per droplet, $\bar{n}$, is equal to the average volume of droplet $\bar{V}_D$ times the number concentration of particles, N:

$$\bar{n} = \bar{V}_D N \tag{10}$$

($\bar{n}$ is in fact the number of particles to be found in a droplet whose volume is equal to the arithmetic average droplet volume). Eqn. 9 is identical to that derived previously for monodisperse droplets (Gonda, 1985), with a proper definition of $\bar{V}_D$ as the average droplet volume (Eqn. 5). The cumulative mass distribution, $M(i)$, as a function of i is then calculated as shown before (Gonda, 1985; Gonda and Chan, 1985):

$$M(i) = \frac{1}{\bar{n}} \sum_{k=1}^{i} kP(k) \tag{11}$$

In order to compute the cumulative mass as a function of 'size', it is necessary to make certain assumptions about the shape of the aggregates. We shall assume the same model as in our previous papers, namely that the aggregates are adequately described as being spherical. It can be shown then (Gonda, 1985) that the equivalent sphere volume diameter $d_e(i)$ and the aerodynamic diameter $d_{ae}(i)$ of an aggregate of i particles are, respectively,

$$d_e(i) = d_e(1)\sqrt[3]{i/f(i)} \tag{12}$$

$$d_{ae}(i) = d_{ae}(1)\sqrt[3]{i/f(i)}\sqrt{K(1)f(i)/K(i)} \tag{13}$$

where $f(i)$ = fraction of volume occupied by the solid; $K(1)$ and $K(i)$ are the dynamic shape factors (Hinds, 1982) for the primary particle and for a spherical aggregate of i such particles, respectively.

The above equations enable us to calculate the cumulative mass distribution $M(i)$ as a function of the equivalent sphere volume diameter $d_e(i)$, or the aerodynamic diameter $d_{ae}(i)$. The model is now in a form which is testable experimentally: $M(i)$ can be obtained from the formulation parameters and $P(k)$'s. The latter can be computed from the experimentally determined $p(D)$ using Eqn. 2. $d_e(i)$ or $d_{ae}(i)$ can be both measured, approximate values of $K(1)$ and $K(i)$ are available in the literature (Hinds, 1982) and $f(i)$ can be deduced, e.g. from microscopic examination of the aggregates.

However, if we wish to carry out a computational investigation, it is necessary to make the model more specific; e.g. the following assumptions can be made (Gonda, 1985; Gonda and Chan, 1985): (1) the primary drug particles are nearly spherical; (2) the aggregates are close-packed hexagonal structures; (3) the droplet size distribution can be described adequately by the log-normal probability function.

Assumptions 1 and 2 which were justified in the first paper in this series lead to the following numerical values (Gonda, 1985):
(i) the volume fractions occupied by the solid in aggregates are

$$f(1) = 1;\ f(i) = 0.741 \text{ for } i \geq 2 \tag{14}$$

(ii) the dynamic shape factors for the aggregates are

$$K(1) = 1,\ K(2) = 1.02 \text{ and } K(i) = 1.10 \text{ for } i \geq 3 \tag{15}$$

(iii) D_{min}, the lower integration limit in Eqn. 2, is calculated as follows: the minimum volume of a droplet containing a spherical aggregate of i particles, V_{min}, must be at least equal to the volume of the aggregate, i.e.,

$$V_{min} = \frac{\pi}{6} D_{min}^3 = \frac{\pi}{6} d_e^3(1) \frac{i}{f(i)} \tag{16}$$

Therefore

$$D_{min} = d_e(1) \sqrt[3]{\frac{i}{f(i)}} \tag{17}$$

Assumption 3 above, i.e., that the droplet size distribution can be approximated by a log-normal probability function, can be justified on empirical grounds (Hinds, 1982). Thus, the distribution at the moment of generation can be characterized by a mass median diameter of the droplets MMD_D, and a geometric standard deviation σ_D. The count median diameter CMD_D is then (Hinds, 1982)

$$CMD_D = MMD_D \exp\left[-3(\ln \sigma_D)^2\right] \tag{18}$$

and the diameter of a droplet of average volume is (Hinds, 1982)

$$\overline{D} = CMD_D \exp\left[1.5(\ln \sigma_D)^2\right] \tag{19}$$

The average droplet volume is (c.f. Eqns. 5 and 10)

$$\overline{V}_D = \frac{\pi}{6} \overline{D}^3 = \bar{n}/N \tag{20}$$

Therefore, the average number of particles per droplet, $\bar{n}$, is

$$\bar{n} = N \frac{\pi}{6} \overline{D}^3 \tag{21}$$

If we express the number concentration N in terms of the % v/v concentration c

$$N = \frac{6c}{100\pi \left[d_e(1)\right]^3} \tag{22}$$

and substitute for $\overline{D}$ in Eqn. 20 from Eqns. 18 and 19, we get

$$\bar{n} = \frac{c}{100} \left[\frac{MMD_D}{d_e(1)}\right]^3 \exp\left[-4.5(\ln \sigma_D)^2\right] \tag{23}$$

Therefore, $\bar{n}$ can be calculated from the basic properties of the droplet size distribution (MMD, σ_D), primary particle size [$d_e(1)$] and the suspension concentration (c), so that $M(i)$ can be obtained according to Eqn. 11. If a population of droplets with a log normal distribution with initial parameters MMD_D and σ_D containing non-volatile solutes evaporates, the resulting dry particles have the same geometric standard deviation σ_d as the droplets and their mass median diameter is proportional to MMD_D and the cube root of their concentration (see the Appendix). The uniform distribution model for nebulized suspensions (Gonda, 1985; Gonda and Chan, 1985) would predict similarly that the geometric standard deviation of the aggregates $\sigma_d = \sigma_D$, and that the mass median diameter of the dry aggregates, MMD_d, corresponds to the diameter of the aggregate which contains the number of particles n_{MMD}, expected in a droplet of median mass. I.e.

n_{MMD} = (vol. of a droplet of median mass) ×
(%v/v concentration)/(vol. of a primary particle)

$$= \frac{\pi}{6} (MMD_D)^3 \frac{c}{100} \Big/ \left[\frac{\pi}{6} d_e^3(1)\right]$$

$$= \left[MMD_D/d_e(1)\right]^3 \frac{c}{100} \tag{24}$$

The n_{MMD} calculated from this equation can be converted to the corresponding mass median diameters MMD_d, or mass median aerodynamic diameters, $MMAD_d$ of the dry aggregates using Eqns. 12 or 13 with $i = n_{MMD}$, $d_e(i) = MMD_d$ and $d_{ae}(i) = MMAD_d$; for non-integer values of n_{MMD}, linear interpolation between two successive values of i can be carried out (Gonda, 1985).

Intuitively, we would expect the uniform distribution model to work satisfactorily for relatively concentrated nebulized suspensions. In dilute systems, the probability of obtaining empty droplets is high, and a better estimate of the mass median (aerodynamic) diameter of the aggregate, MMD_d (or $MMAD_d$) may be obtained by excluding the empty droplets from the considerations. The average number of primary drug particles $n'(D)$ in drug-containing droplets of diameter D can be deduced from Eqn. 1 (Gonda, 1985) as

$$n'(D) = \frac{n(D)}{\sum_{k=1}^{\infty} P(k, D)}$$

$$= \frac{n(D)}{\sum_{k=0}^{\infty} P(k, D) - P(0, D)}$$

$$= \frac{n(D)}{1 - P(0, D)} = \frac{n(D)}{1 - e^{-n(D)}} \qquad (25)$$

Specifically, for $D = MMD_D$, we have

$$n'_{MMD} = \frac{n_{MMD}}{1 - e^{-n_{MMD}}}$$

where

$$n_{MMD} \equiv n(MMD) \text{ and } n'_{MMD} \equiv n'(MMD). \qquad (26)$$

Results and Discussion

Previous studies (Gonda, 1985; Gonda and Chan, 1985) showed that the size distributions of the aggregates calculated according to the above computational model conformed well to the log-normal probability function which is frequently employed to approximate particle size data (Hinds, 1982). For these reasons, we have again plotted the computed values of the cumulative mass fraction (undersize), $100 \times M(i)$, on a probability scale against the relative aerodynamic diameter $d_{ae}(i)/d_{ae}(1)$ (Eqn. 13) on a logarithmic scale (all such plots in this paper show also the scale in units of $d_e(i)/d_e(1)$ (Eqn. 12) for the reader interested in equivalent sphere volume diameters). The ratio R_1, of the mass median aerodynamic diameters of the cluster, $MMAD_d$, to the aerodynamic diameter of the primary drug particle, $d_{ae}(1)$, was obtained, where possible, from the graphs as the interpolated value at $M(i) = 50\%$. Where the $100 \times M(i)$ plot started above 50%, of course, $MMD_d/d_{ae}(1) = 1$ since $MMD_d = d_{ae}(1)$ is the minimum value for the 'aggregate' size that would be measured in practice. Fig. 1 shows the results for $c = 0.5$–2% v/v, $MMD_D/d_e(1) = 10$ and 15 and $\sigma_D = 1.01$–2. Over the range that would be normally accessible in experiments ($100 \times M(i) \cong 10$–90%), the graphs appear reasonably linear, i.e., suggesting logarithmic-normal size distribution of the aggregates; their geometric standard deviation, σ_d, was estimated from (Hinds, 1982; Martin et al., 1983)

$$\sigma_d = \frac{d_{ae}(i) \text{ at } [100 \times M(i) = 84\%]}{MMAD_d} \qquad (27)$$

Where this procedure could not be followed because the cumulative computed values did not reach 84% (see the results below), the formula, (Hinds, 1982; Martin et al., 1983) was used

$$\sigma_d = \frac{MMAD_d}{d_{ae}(i) \text{ at } [100 \times M(i) = 16\%]} \qquad (28)$$

Table 1 shows that the values of σ_d for the systems in Fig. 1 are very well approximated by the geometric standard deviations of the droplets, σ_D. This indicates that the uniform distribution model might represent these systems well. In order to test this possibility, the relative ratio, R_2, of the mass median aerodynamic diameter of the aggregates, $MMAD_d$, to $d_{ae}(1)$ was also calculated according

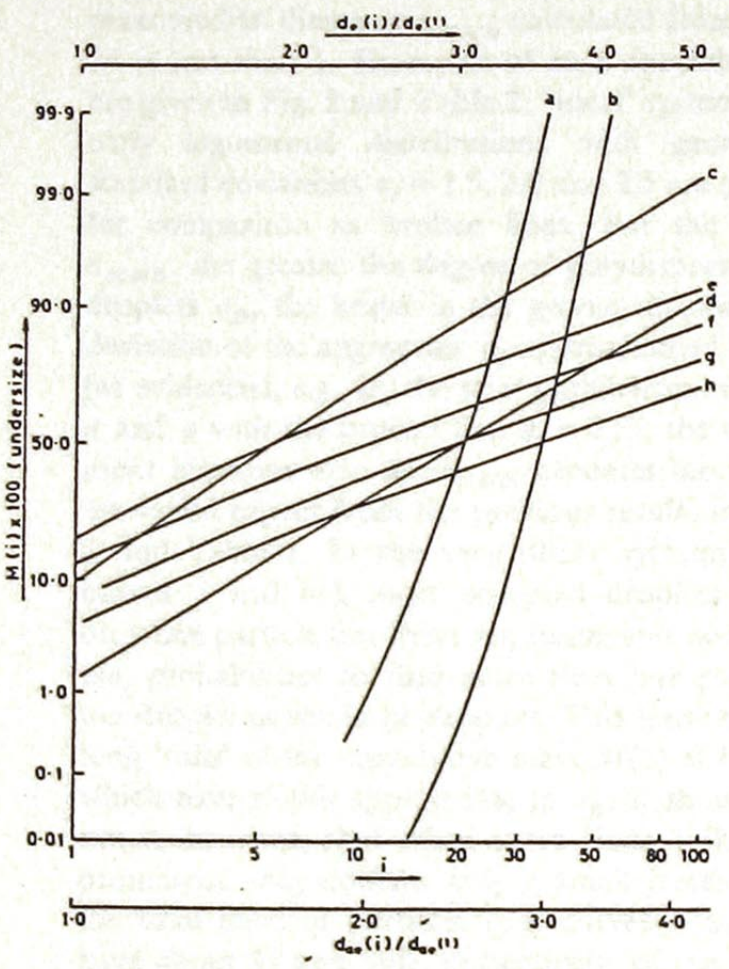

Fig. 1. Percentage cumulative mass fraction (undersize) $M(i) \times 100$, against the number of primary particles per cluster, i, and the relative equivalent volume and aerodynamic diameters, $d_e(i)/d_e(1)$ and $d_{ae}(i)/d_{ae}(1)$, respectively. The formulation parameters for the curves are given in Table 1.

to the uniform distribution model from Eqn. 24 using the procedure explained in the text following that equation. It is evident from the excellent agreement between R_1 and R_2 in Table 1 that the uniform model is, indeed, a very reliable description of the situation for the range of the formulation parameters in Fig. 1. Substitution of the numerical values into Eqn. 24 in fact gives n_{MMD} in the range 5–33.75. For such large n_{MMD}, Eqn. 26 gives $n_{MMD} \cong n'_{MMD}$ because the probability of not finding a solid particle in a droplet size with the mass median MMD_D is very low. Furthermore, the ratio $MMD_D/d_e(1)$ is quite large for these systems, and therefore it is unlikely that there would be too many small droplets which could not accommodate enough solid particles. In other words, the integration limit $D_{min} \cong 0$ in Eqn. 2 and the 'volume exclusion effect' (Callingham, 1980; Gonda, 1985) is not important in these systems. It is thus quite adequate for the purpose of estimation of MMD_d, $MMAD_d$, and σ_d to view the distribution of the solid in the same way as if though it was initially completely dissolved in the carrier liquid. So, $\sigma_d = \sigma_D$ and the median diameters are obtained simply from volumetric relationships, without the need for any computer modelling.

The situation is rather different, however, when

TABLE 1

Numerical relationships between the formulation parameters and the size distribution of the aerosol product for the systems in Fig. 1

Curve in Fig. 1	σ_D [1]	c [2]	$MMD_D/d_e(1)$ [3]	n_{MMD} [4]	R_1 [5]	R_2 [6]	σ_d [7]
a	1.01	2.0	10	20	2.45	2.46	1.08
b	1.01	1.0	15	33.75	2.94	2.93	1.06
c	1.5	0.5	10	5	1.61	1.55	1.5
d	1.5	2.0	10	20	2.47	2.46	1.5
e	2.0	0.5	10	5	1.61	1.55	1.9
f	2.0	1.0	10	10	2.02	1.95	1.9
g	2.0	2.0	10	20	2.47	2.46	2.0
h	2.0	1.0	15	33.75	2.95	2.93	1.9

[1] Geometric standard deviation of droplets.
[2] Percentage v/v concentration.
[3] Ratio of the mass median diameter of the droplets to the diameter of the primary particle.
[4] Average number of particles expected in a droplet of median mass (Eqn. 24).
[5] Ratio of the mass median aerodynamic diameter of the product to the aerodynamic diameter of the primary particle, obtained from the figure.
[6] Same as R_1, but calculated assuming uniform distribution (see text following Eqn. 24).
[7] Geometric standard deviation of the product obtained as explained in the text surrounding Eqns. 27 and 28.

the number of primary particles per droplet of mass median diameter n_{MMD} calculated from Eqn. 24 is less than 1. Examples of such formulations are given in Fig. 2 and Table 2; 'ideal' systems, i.e. truly log-normal distributions with geometric standard deviations $\sigma_d = 1.5$, 2.0 and 2.5 are shown for comparison as broken lines. For the same n_{MMD}, the greater the degree of polydispersity of droplets σ_D, the better is the geometric standard deviation of the aggregates σ_d approximated by σ_D (as evidenced, e.g., by the near parallelism of lines *n* and *o* with the broken line $\sigma_d = 2.5$); the agreement improves also as n_{MMD} becomes larger, as we would expect from the previous results in Fig. 1 and Table 1. In the very dilute systems (e.g. curves *j* and *m*), most occupied droplets have only one particle but there are finite, and observable, probabilities to find more than one particle per droplet in the large droplets. This leads to the long 'tails' of the cumulative mass $M(i)$ at high i which have slopes appropriate to σ_D. It should be noted, however, that when these 'long tails' are prominent, they contain only a small fraction of the total mass of particles (e.g. curves *j* and *m* have about 95 and 90%, respectively, of the mass in the form of individual particles). Effectively, these dilute systems are nearly monodisperse (Raabe, 1968). It is interesting to speculate about

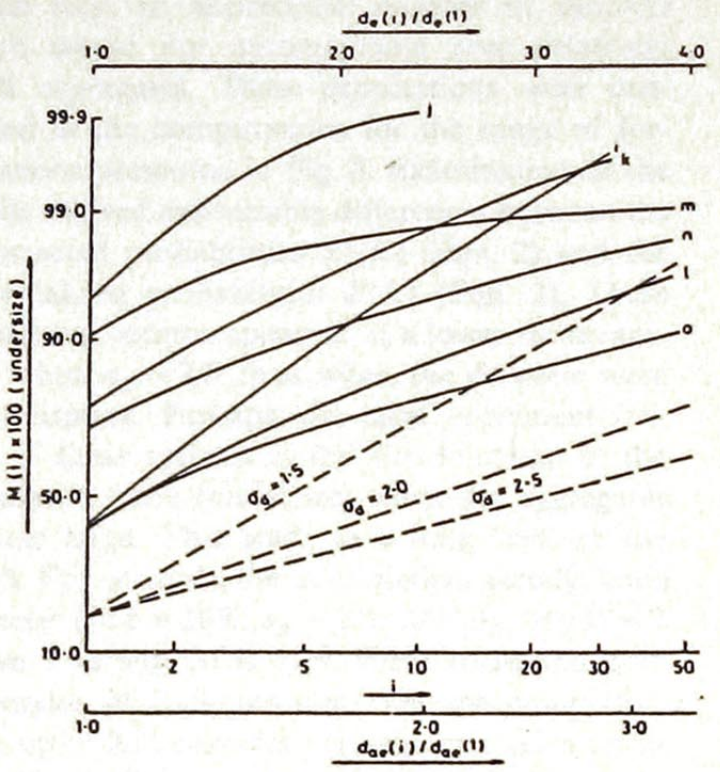

Fig. 2. See legend to Fig. 1 for explanations. The formulation parameters for the curves are given in Table 2. The broken lines show systems which would have geometric standard deviations as indicated.

the conclusion that one might arrive at if such distributions were observed experimentally: microscopic examination of the dry aerosol would reveal (correctly) that there are only a few large

TABLE 2

Numerical relationships between the formulation parameters and the relative mass median aerodynamic diameters of the products for the systems in Fig. 2.

Curve in Fig. 2	σ_D	c	n_{MMD}	n'_{MMD} [1]	R_1	R'_2 [2]	σ_d [3]
i	1.5	0.1	1	1.582	1.08	1.11	1.4
j	2.0	0.001	0.01	1.005	1.00	1.00	–
k	2.0	0.01	0.1	1.051	1.00	1.01	–
l	2.0	0.1	1	1.582	1.10	1.11	1.8
m	2.5	0.001	0.01	1.005	1.00	1.00	–
n	2.5	0.01	0.1	1.051	1.00	1.01	–
o	2.5	0.1	1	1.582	1.10	1.11	2.5

The ratio of the median droplet size to the size of the primary particle, $MMD_D/d_e(1)$, is 10. Other explanations are in the footnotes to Table 1.

[1] Average number of primary particles expected in occupied droplets of median mass (Eqn. 26).

[2] R'_2 is calculated from n'_{MMD} (Eqn. 26), in contrast to R_2 in Table 1 which was obtained from n_{MMD} (Eqn. 24). See text for further details.

[3] The values of σ_d could not be calculated for many of the curves in Fig. 2 using Eqns. 27 or 28. Approximate σ_d can be estimated by comparison with the broken lines.

aggregates present, and that the size distribution is truncated at the lower end at the size of a primary particle. However, devices which fit indirect observations by a continuous curve and extrapolate it as a distribution function from 0 to infinity (as e.g. some light scattering and diffraction instruments) could erroneously predict the presence of a large fraction of particles smaller than the actual primary particles [the reader can imagine this by extrapolating the curves in Fig. 2 to the left toward $d_{ae}(i)/d_{ae}(1)$ less than 1].

Clearly, for $n_{MMD} < 1$, the values of R_2 calculated on the basis of the uniform distribution model from Eqn. 24 (see Table 2) would be meaningless since they would predict for many of the dilute suspension mass median (aerodynamic) diameters of the clusters smaller than those of the primary particles! In these circumstances, the empty droplets must be excluded from the calculation and Eqn. 26 is used instead of Eqn. 24 to obtain R_2' from n_{MMD} by the same procedure as that for obtaining R_2 from n_{MMD} (see text following Eqn. 24). Excellent agreement between the values of R_1 and R_2 can be seen in Table 2. Thus, the uniform distribution model is successful again when it is modified to exclude empty droplets from the calculation of the mass median aggregate size for systems with low average occupancy of median size droplets by the solid particles.

We suspected that the simple uniform distribution approximation may be also inadequate when the volume exclusion effects become important. The type of formulations which would be likely to fall in this category would be those which have a large number of relatively small droplets (low ratio $MMD_D/d_e(1)$ and, or, large σ_D) and a high probability of forming large aggregates (high concentration of the dispersed phase). It was deduced (Gonda, 1985) that in monodisperse droplet systems, the volume exclusion effects for the droplet to primary particle size ratio of 2 would become important at concentrations in excess of 60%. Such concentrated suspensions would be almost certainly outside the validity of assumptions invoked in the introduction. However, it is possible that in polydisperse droplet systems, the volume exclusions begins to operate at much lower concentrations because, for a sufficiently large σ_D, there would exist an appreciable number of droplets which would not accommodate even relatively small aggregates. These expectations were confirmed in the computations for the range of formulations presented in Fig. 3. Examination of the results showed appreciable differences between the uncorrected probabilities $P'(k)$ (Eqn. 2) and the renormalized probabilities $P(k)$ (Eqn. 3). These differences became apparent at a lower concentration when $\sigma_D = 2.0$ than when the droplets were monodisperse. Perhaps, the most prominent feature of these systems is the slow increase in the cumulative mass (undersize) when the aggregates become large. This leads to a long 'tail' in the graph. For example, the mass median aerodynamic diameter for $c = 10\%$, $\sigma_D = 2.0$, $MMD_D/d_e(1) = 2$ (curve s in Fig. 3) is 1.29 which corresponds to aggregates of 2–3 particles. Yet the cumulative mass up to 200 particles per aggregate adds up to only 82.3%. The presence of the 'flat' portion at high cumulative mass is indicative of the fact that

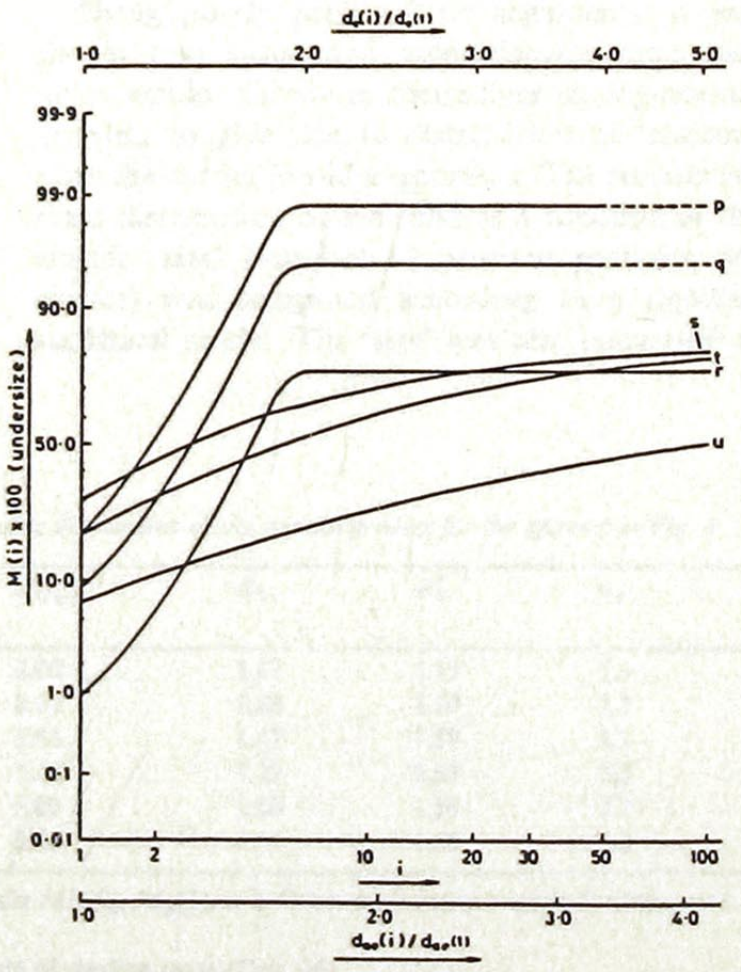

Fig. 3. See Legend to Fig. 1 for explanation. The formulation parameters for the curves are given in Table 3.

the size distribution could be no longer described as approximately log-normal. For the polydisperse systems in Fig. 3 ($\sigma_D = 2.0$), the values of σ_d could not be predicted accurately from σ_D and there are appreciable differences between the values of R_1 and R_2' (Table 3). Therefore the uniform distribution model would be a poor approximation of these systems, particularly if the droplets are polydisperse. The qualitative reasons for this behaviour may be summarized as follows: since the suspensions are relatively concentrated (c.f. Fig. 1 and Table 1), it would be expected on the basis of uniformity that each droplet should contain at least one solid particle. In the nearly monodisperse systems in Fig. 3 and Table 3 ($\sigma_D = 1.01$), this is possible. However, since $MMD_D/d_e(1)$ is only 2, the small droplets in the polydisperse systems cannot accommodate even single solid particles. Consequently, the unnormalized probability of finding a particle in a droplet of any size is less than what we would find in a monodisperse droplet system with $D/d_e(1) = 2$. When the same calculation is carried out for a greater aggregation number, an even bigger fraction of the droplets on the lower side of the droplet size distribution is incapable of accommodating these larger aggregates (c.f. the value of D_{min} in Eqn. 17 as a function of the aggregate number i). Thus, the probabilities of finding large aggregates are truncated by the exclusion of droplets of diameters less than D_{min}. This leads to the 'tailing' of the cumulative mass plots on the log-normal scales as shown in Fig. 3, i.e., the upper part of the calculated $M(i)$ falls below the expected plot for a log-normal distribution derived from the assumption of uniform distribution of the solid among the droplets. This effect is not important in the nearly monodisperse systems in Fig. 3 and Table 3 because more than 5 particles would be required to exceed D_{min} for the ratio $MMD_D/d_e(1) = 2$. Even the most concentrated suspension (curve r) has an average of 5 particles per droplet. The probability of finding droplets greater than the median size is low when $\sigma_D = 1.01$ and therefore the estimates of σ_D and R_2' from the uniform distribution model are quite reasonable (Table 3). Nevertheless, the curves p, q and r in Fig. 3 show that the small, but finite probability of droplets greater than the median sized ones leads to a long tail of low probability clusters with high aggregation numbers i.

Conclusions

Using purely probabilistic arguments, it was shown that suspended monodisperse drug particles would distribute themselves in log-normal droplets to give rise to distribution of 'clusters' after the carrier liquid evaporated. The cumulative mass distribution of the solid as a function of the cluster 'size' (number of primary particles per cluster) was computed according to a rigorous statistical model. The 'size' was also converted to

TABLE 3

Numerical relationships between the formulation parameters and the size distribution of the aerosol product for the systems in Fig. 3

Curve in Fig. 3	σ_D	c	n_{MMD}	n'_{MMD} [1]	R_1	R_2' [2]	σ_d
p	1.01	20.0	1.6	2.00	1.17	1.19	1.1
q	1.01	30.0	2.4	2.64	1.28	1.27	1.1
r	1.01	62.5	5.0	5.03	1.47	1.59	1.1
s	2.0	10.0	0.8	1.45	1.29	1.09	2.3
t	2.0	20.0	1.6	2.00	1.60	1.19	3.9
u	2.0	62.5	5.0	5.03	4.14	1.59	3.0

The ratio of the median droplet size to the size of the primary particle $MMD_D/d_e(1)$, is 2. Other explanations are in the footnotes to Table 1.

[1] average number of primary particles expected in occupied droplets of median mass (Eqn. 26).

[2] R_2' is calculated from n'_{MMD} in a manner analogous to calculation of R_2 in Table 1 from n_{MMD}.

equivalent sphere volume, or aerodynamic diameters assuming sphericity of the primary particles and the clusters, and hexagonal close packing in the aggregates. The computer simulations predict that there would be a significant increase ($\geq 10\%$) in the drug mass median aerodynamic diameter as a result of such an 'aggregation' mechanism at suspension concentrations in excess of 0.1% v/v when the mass median diameter of the droplets is 10 times greater than the diameter of a primary particle. These findings are in agreement with the previous study carried out for monodisperse droplets and they should apply to the type of formulations currently in use (Gonda, 1985). Furthermore, it is shown that for the majority of realistic formulation parameters for therapeutic aerosols, it is possible to estimate the median size of the aggregates and their geometric standard deviation simply from volumetric relationships based on the assumption of uniform distribution of the 'solid' (i.e., usually the drug particles) in the carrier liquid (i.e. the propellant or any other liquid volatile components of the aerosol formulation).

At present, there are no detailed published data on simultaneous droplet and aggregate size analysis. Sakai et al. (1985) studied atomization of several relatively concentrated suspensions. Although they were primarily interested in the effect of suspension concentration on the droplet size, the authors concluded that their observations could be explained by a model in which the concentration of solid particles in each droplet was the same as the concentration in the suspension itself, i.e., their results were consistent with the uniform distribution theory.

Acknowledgements

We are grateful to Lee Bailey for typing this manuscript. This work has been supported by a URG Special Project Grant (administered by the University of Sydney).

Glossary of Symbols

C	% v/v concentration of suspension
CMD_D	count median diameter of droplets
d	diameter of the solid particle after a droplet evaporated
$d_{ae}(i)$	aerodynamic diameter of an aggregate of i particles
$d_e(i)$	equivalent sphere volume diameter of an aggregate of i particles
D	diameter of a droplet
$\overline{D}$	diameter of a droplet of average volume
D_{max}	upper integration limit for droplet size as given e.g. by the size range of the measuring device
D_{min}	lower integration limit for droplet size as given e.g. by the size range of the measuring device
$f(i)$	volume fraction occupied by the solid in aggregates of i particles
$F(i)$	fraction of the total drug mass contained in aggregates of i drug particles
g	mass of a primary particle in suspension
i	number of particles in an aggregate
k	number of particles in a droplet
$K(i)$	dynamic shape factor for an aggregate of i particles
$m(i)$	mass of an aggregate of i particles
$M(i)$	cumulative mass distribution of aggregates as a function of i (i is the number of particles in an aggregate)
MMD_d	mass median diameter of dry aggregates
MMD_D	mass median diameter of droplets
$MMAD_d$	mass median aerodynamic diameter of the dry aggregates
$n = n(D)$	average number of particles per droplet of diameter D
$\bar{n}$	average number of particles per droplet of all sizes including empty droplets
$n'(D)$	average number of particles in drug-containing droplets of diameter D
$n(i)$	total number of droplets containing aggregates of i particles
$n_{MMD} =$ $n(MMD)$	number of particles in an aggregate expected to be formed from a droplet of median mass (including empty droplets in the median calculation)

n'_{MMD} = same as n_{MMD} except that empty droplets are excluded
n'_{MMD}
n_T total number of droplets formed from a volume V of a suspension
N number of primary particles per unit volume of suspension
$p(D)$ initial distribution of droplets after nebulization of the suspension
$P(i)$ probability of finding an aggregate of i particles in a droplet of any size
$P(k)$ renormalized $P'(k)$ to allow D_{min} to be sufficiently large to accomodate a cluster of k particles
$P(k, D)$ probability of finding k particles in a droplet of diameter D
$P'(k)$ probability of finding k particles in a droplet of any size
V volume of a suspension
V_{min} minimum volume of a droplet containing an aggregate of i particles
V_s volume of solid particles after the volatile components evaporated
$\bar{V}_d$ average droplet volume
σ_d geometric standard deviation of dry aggregates
σ_D geometric standard deviation of droplets

Appendix

Imagine a population of droplets with a log-normal distribution characterized by the parameters MMD_D and σ_D containing a non-volatile solute at a concentration c (% v/v). When the solvent evaporates, the remaining solid particle originating from the droplet of diameter D will have a volume V_s.

$$V_s = \frac{\pi d^3}{6} = \frac{\pi D^3}{6}\frac{c}{100} \qquad (A.1)$$

i.e., the solid particle will have a diameter

$$d = D\sqrt[3]{c/100} \qquad (A.2)$$

Since the same proportional relationship exists between all d's and all the diameters of the droplets from which the solid particles originated, the size distribution of the latter is simply shifted by a constant distance on the log-normal probability scale, i.e., it is parallel to the line for the size distribution of the droplets. It follows that the degrees of polydispersity for two parallel curves in such a graph are the same, i.e.,

$$\sigma_d = \sigma_D \qquad (A.3)$$

and

$$MMD_d = MMD_D\sqrt[3]{c/100} \qquad (A.4)$$

References

Callingham, M., A statistical model for predicting the particle distribution of an atomized powder in a liquid mixture. *Int. J. Cosmet. Sci.*, 2 (1980) 107–126.

Gonda, I., Development of a systematic theory of suspension inhalation aerosols. I. Framework to study the effects of aggregation on the aerodynamic behaviour of drug particles. *Int. J. Pharm.*, 27 (1985) 99–116.

Gonda, I. and Chan, H.-K., Model of aerodynamic behaviour of aggregates formed on nebulization of suspensions. *J. Pharm. Pharmacol.*, 37 (1985, Suppl.) 56P.

Hinds, W.C., *Aerosol Technology*, Wiley, New York, 1982, pp. 44–50, 87–90.

Martin, A., Swarbrick, J. and Cammarata, A., *Physical Pharmacy*, 3rd ed., Lea and Febiger, Philadelphia, 1983, pp. 499–500.

Raabe, O.G., The dilution of monodisperse suspensions for aerosolization. *Am. Ind. Hyg. Assoc. J.*, 29 (1968) 439–443.

Sakai, T., Sadakata, M. and Saito, M., Mean diameters and drop size distribution of suspension sprays. *Atom. Spray Technol.*, 1 (1985) 147–164.

Appendix 2

Procedure to locate the random fields of view, f.v., on the filter segment

(i) The number of fields of view, N, along the radius of segment is equal to the length of radius, R, (R=3cm) divided by the breadth of a field of view, B, (B=25μm, Fig.A1)

$$N = R/B = 1200$$

(ii) Therefore the total area of the segment can be approximated by 12 blocks of area (Fig. A1), each block has 100 f.v. along the segment radius.

(iii) To locate the boundaries for the blocks:

E.g., for the 1st block, the top boundary, S_1, is just the lenght of the segment radius, that is at 3cm from the segment apex. The bottom boundary, E_1, is equal to the top boundary subtracted by the distance covered by the breadth of 100 f.v. (D = 100 x 25 μm)

$$E_1 = S_1 - D = 2.75\text{cm}.$$

Of course, the bottom boundary of the 1st block is also the top boundary of the 2nd block.

The boundaries for the remaining 11 blocks can be found in the same way.

(iv) The horizontal length, H.L., of a block is taken as the arc length, A.L., midway between the boundaries.

$$H.L. = A.L. = \theta/360 \times 2\pi r \qquad \text{Eqn. A1}$$

θ= Apex angle of segment
r= radius of the corresponding circle of filter
= mid-way boundary value in Fig. A2.
θ= area of segment/area of circle x 360^0

$\therefore \theta/360$ = area of segment/area of circle

area of segment = Total no. of f.v. x area of 1 f.v.
$= 100{,}000 \times 25 \times 37 \times 10^{-12}\ m^2$
$= 9.25 \times 10^{-5}\ m^2$

area of circle = πr^2
$= 3.1416 \times (3 \times 10^{-2})^2$
$= 2.8 \times 10^{-3}\ m^2$

$\therefore \theta/360 = 3.3 \times 10^{-2}$

E.g., for the 1st block,

H.L. = $\theta/360 \times 2\pi r$

$= 3.3 \times 10^{-2} \times 2\pi \times 2.875$ cm
$= 0.596$ cm

The H.L. for the remaining 11 blocks can be found by substituting the corresponding values of r into Eqn. A1.

(v) The number, N_r, of f.v. in a horizontal row of a block is calculated by dividing the horizontal length of the block by the length of 1 f.v. (which is 37μm, Fig.A1).

$N_r = H.L./L$

E.g., for the 1st block,

$N_r = 0.596/37 \times 10^{-4}$
$\simeq 161$

(vi) The total no. of f.v. in a block, N_t, is therefore:

$N_t = N_r \times 100$ (no. of rows in a block is 100)

E.g. N_t equals 16100 for the 1st block.

(vii) To locate the random fields of view on filter, random numbers are chosen orderly from a 5 digits random number Table (Abramowitz and Stegun, 1970) and subtracted from the nearest cumulative total number of f.v. in Fig.A2. which locates the block (column 2 in Table A1). The residue of subtraction is then divided by N_r of the corresponding block. The quotient is a real number (column 3 in Table A1) which is rounded off to the nearest integer upwards. This integer will indicate the desired row number (coulumn 4 in Table A1) and the decimal remainder after multiplication by N_r of the block will give the exact location along the row (column 5 in Table A1). It has been found that the radius of the segment, 3 cm, corresponded to 29.504 units in the control for the microscope stage. To convert the location on filter to settings of the stage control, the formula,

$LS = (29.504/12)\ [(B-1)+R/100]$

Total number of block is 12
B: the block number
R: the row number in the corresponding block
LS: Settings of stage control to locate the f.v. on filter

is used for control settings along the segment radius. Control settings along a row (column 7 in Table A1) is simply the product of the number of f.v. (column 5 in Table A1) multiplied by the stage control setting for one f.v. (which is 0.03657 units/f.v.).

Finally, it is noteworthy that the dimension of the f.v. at a nominal magnification 3000X was used in all calculations. The SEM pictures were finally taken at a magnification of 7800X and an appropriate fraction of a randomly chosen f.v. was scanned only. However, the random sampling nature remains unaffected.

Examples showing the first two random numbers and the calculated results of their locations on filter and the corresponding settings of the microscope stage are illustrated in Table A1.

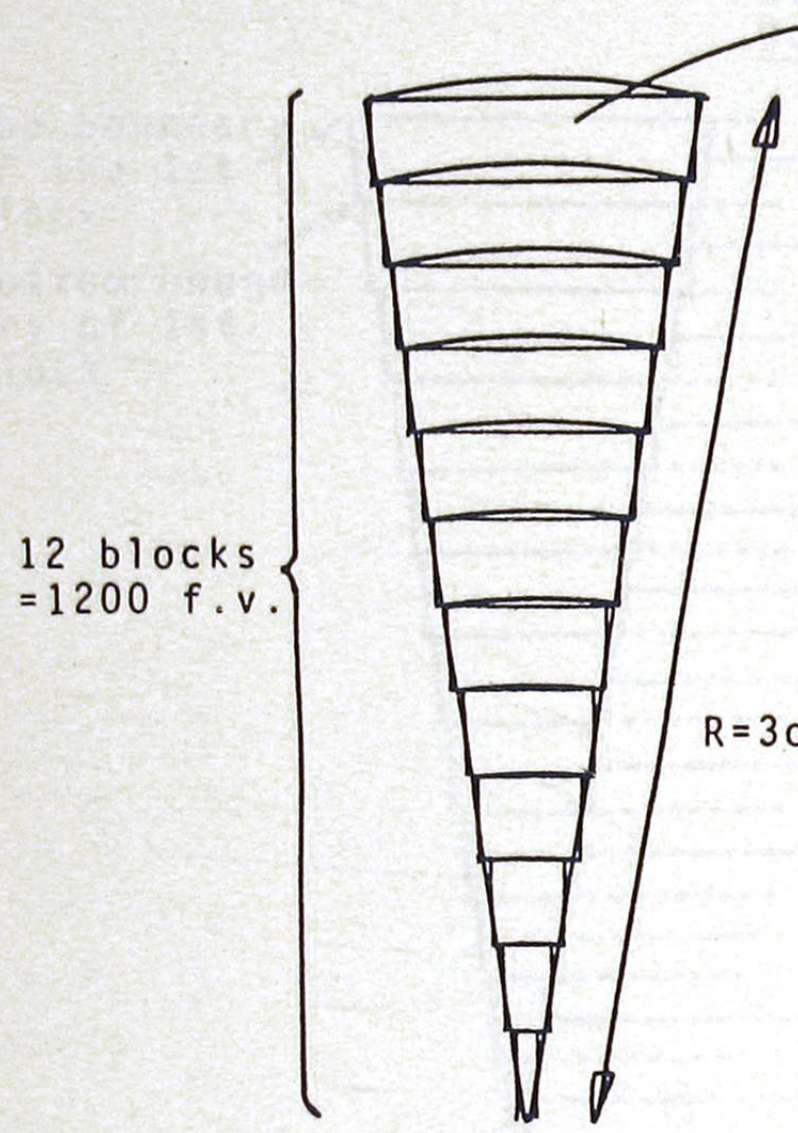

A segment of filter

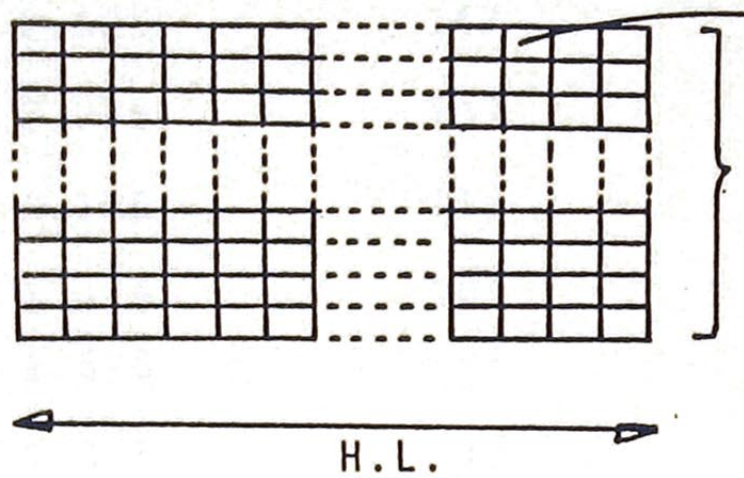

1 Block

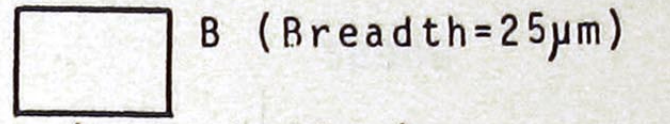

at nominal magnification
of 3000x

1 field of view (f.v.)

Fig. A1

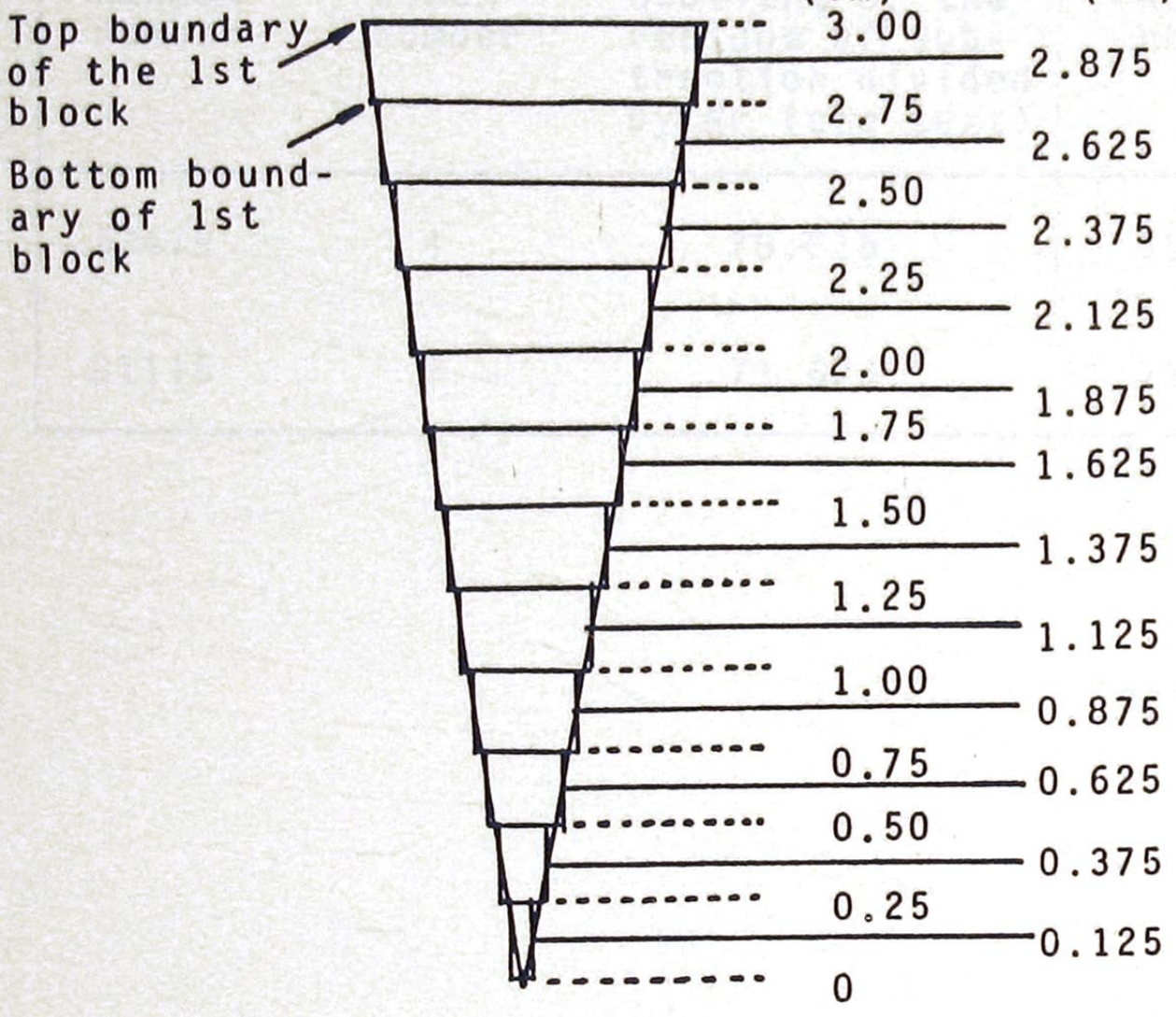

Block Boundary (cm)	Midway Boundary Value (cm)	No. of f.v. Per Block	Total No. f.v. Per Block	Cum. Total No. f.v.
3.00				
	2.875	161	16100	16100
2.75				
	2.625	147	14700	30800
2.50				
	2.375	133	13300	44100
2.25				
	2.125	119	11900	56000
2.00				
	1.875	105	10500	66500
1.75				
	1.625	91	9100	75600
1.50				
	1.375	77	7700	83300
1.25				
	1.125	63	6300	89600
1.00				
	0.875	49	4900	94500
0.75				
	0.625	35	3500	98000
0.50				
	0.375	21	2100	100100
0.25				
	0.125	7	700	100800
0				

Fig. A2

Random number	Block number	Quotient of the residue of subtraction divided by Nr (see text)	Row no.	f.v. number along the row	Control settings of microscope stage	
					along segment radius	along a row
53479	4	78.815	79	96	9.318	3.511
81115	7	71.623	72	48	16.522	1.756

Table *A*.1

Appendix 2

MTX crystal data collection details

crystal system	tetragonal
space group	$\underline{P}4_12_12$
$\underline{a}$, Å	10.355(3)
$\underline{c}$, Å	45.712(5)
$\underline{V}$, Å^3	4902.1
$\underline{D}_{calc}$, g cm^{-3}	1.378
empirical formula	$C_{20}H_{22}N_8O_5$
fw	454.5
$\underline{Z}$	8
$\underline{F}$(000), electrons	2144
absorption coeff., cm^{-1}	6.86
crystal colour	orange
dimensions, mm	0.30x0.15x0.10
crystal habit	prismatic
crystal degradation	<2%
temperature, K	294
diffractometer	Enraf-Nonius CAD4-F
radiation	CuKα, λ 1.5405Å
monochromator	Ni filter
scan mode	ω-0.67θ
2θ range, degrees	1.0-110.0
reflections measured	3555, +$\underline{h}$,+$\underline{k}$,+$\underline{l}$
reflections used ($\underline{I}$>2.5σ($\underline{I}$))	2169
$\underline{R}_{merg}$	0.01
number of variables	370
$\underline{R}$	0.062
$\underline{R}_w$	0.067
w[=g/(σ^2F_o+kF_o^2)], g,k	1.42, 0.0019
shift/esd	<0.2
residual extrema in final difference map	±0.4eÅ^{-3}

Appendix 4

Determination of the crystal orientation by polarizing microscopy

The techniques used in this study are based on the observation of (1) Interference figures and (2) Extinction position.

(1) Interference figures:

When an optically uniaxial crystal is placed between the polarizer and analyzer, together with a high-power objective and a Bertrand lens, an uniaxial interference figure would be obtained. This is formed by the ordinary and extraordinary light rays that travel along different directions while viewed within the crystal. Depending upon whether the crystal rests with its optic-axis (=crystallographic c-axis in HMM) direction (1) perpendicular, (2) at an oblique angle, or (3) parallel to the plane of the polarizer and analyzer, the types of figures resulting from such orientations are respectively called (1) centred optic-axis figures, (2) off-centred optic axis figures and (3) the uniaxial flash figures. For (1) and (2), the interference figures (see Fig.A3) consist of two intersecting black bars (so called isogyres) that form a cross which is concentric with a series of circles representing circular distribution of the interference colour (using white light source). For (3), the flash figure consists of hyperbolic colour curves arranged in four quadrants of the view, with the isogyres appearing at or near the extinction positions. The isogyres move very rapidly when the microscope stage is rotated. For HMM, however, the flash figure is difficult to obtain.

(2) Extinction position

If an optically anisotropic crystal is observed between the polarizer and analyzer during a 360-degree rotation of the stage, there will be four positions, so called extinction positions (at which the crystal's vibration or privileged directions will be parallel to those of the polarizer and analyzer) for which the whole crystal will appear dark and similarly there will be four 'brightest positions' (representing 45 degrees off extinction) for which the brightness will be at the highest intensity. This is the case for HMM crystal placed with its c-axis parallel to the microscopic stage. On the other hand, when an HMM crystal is placed with its c-axis perpendicular to the stage, no extinction positions would be found since in this orientation it behaves optically isotropic and appear completely dark for thin crystals. For thick crystals, it will, however, appears bright due to refraction of light. (unless immersed in an oil with a similar refractive index).

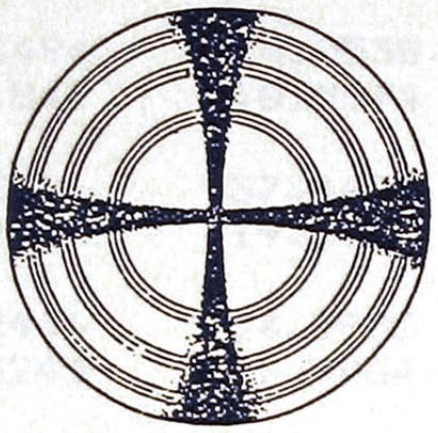

(i)

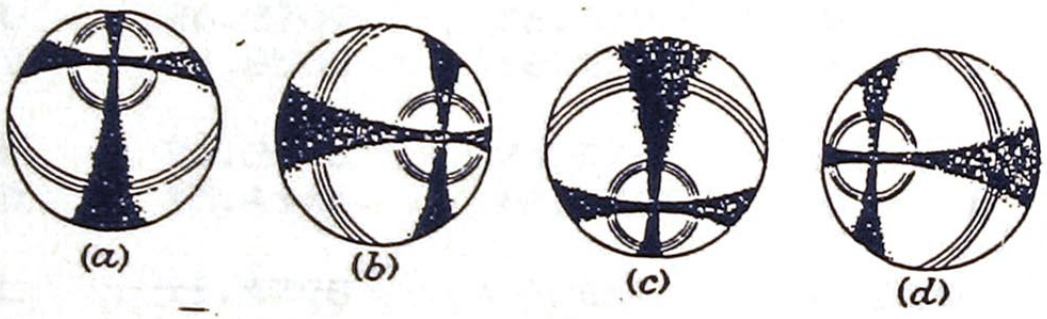

(ii)

Fig. A3 Interference Figures

(i) Centred optic-axis figure

(ii) Off-centred optic-axis figures, (a)-(d) showing the motion of the isogyres across the field of view on rotation of the microscopic stage clockwise.

Appendix 5

Values of C, C_1, C_2, and C_3 in the polynomial equations of dependence of the crystal length (L) and breadth (B) on time:

Methanol (Run 1)

Crystal No.		C	C_1	C_2	C_3
1	L	27.3494	34.0538	-2.0860	-
	B	16.1847	18.5074	-0.6740	-
2	L	24.1486	37.4403	-2.2923	-
	B	16.8965	19.0159	-0.8819	-
3	L	24.2446	34.2985	-2.5081	-
	B	13.5243	17.7464	-0.8043	-
4	L	15.2562	25.3737	-2.0264	-
	B	13.9398	13.7447	-1.0782	-

Methanol (Run 2)

Crystal No.		C	C_1	C_2	C_3
5	L	26.2707	36.5728	-3.6732	0.1350
	B	14.8504	16.2274	-1.1994	0.0268
6	L	20.2126	24.5783	-2.6154	0.0926
	B	15.4144	18.5763	-0.8571	-
7	L	19.4798	36.8603	-3.6110	0.1210
	B	12.7853	15.7967	-1.1961	0.0267
8	L	23.7718	36.4961	-3.4622	0.1127
	B	11.8853	15.1804	-1.3656	0.0438
9	L	11.9680	26.9602	-2.4161	0.0678
	B	10.6366	23.2176	-2.1399	0.0703

Methanol (Run 3)

Crystal No.		C	C_1	C_2	C_3
10	L	21.3606	37.1653	-2.2541	-
	B	6.5611	16.4884	-0.9075	-
11	L	23.1141	36.2086	-2.2568	-
	B	11.6727	13.7323	-0.8071	-
12	L	3.9303	41.5353	-2.5083	-
	B	4.5812	21.7470	-1.0465	-

Cyclohexane (3 Runs)

Crystal No.		C	C_1	C_2	C_3	Run
1	L	-1.2694	56.4677	-1.1877	-	1
	B	30.6076	7.3428	5.2353	-0.3755	
2	L	-0.7537	51.4653	-1.0503	-	
	B	3.0183	38.2109	-3.0241	0.1344	
1	L	34.1729	38.8964	1.1761	-	2
	B	19.0964	28.5175	-0.0407	-	
1	L	43.9931	8.3968	10.6316	-0.8485	3
	B	19.9552	29.1940	0.5498	-	

REFERENCES

Abramowitz, M., and Stegun, I.A. (1970)
"Handbook of Mathematical Functions", Dover Publications, Inc. New York.

Addadi, L., Berkovitch-Yellin, Z., Domb, N., Gati, E., Lahav M., and Leiserowitz L. (1982)
"Resolution of conglomerates by stereoselective habit modifications", Nature 296, 21-26.

Addadi, L., Berkovitch-Yellin, Z., Weissbuch, I., van Mil, J., Shimon, L.J.W., Lahav, M., and Leiserowitz, L. (1985)
"Growth and dissolution of organic crystals with 'tailor-made' inhibitor - implications in stereochemistry and materials science", Angew. Chem. Int. Ed. Engl. 24, 466-485.

Addadi, L. and Weiner, S. (1986)
"Interactions between acidic macromolecules and structured crystal surfaces. Stereochemistry and biomineralization", Mol. Cryst. Liq. Cryst. 134, 305-322.

Altree-Williams, S. and Preston, J.S. (1985)
"Asbestos and other fibre levels in buildings", Ann Occup. Hyg. 29, 357-363.

Ananikyan, T.A., Nalbandyan, A.G., and Nalbandyan H.G. (1985)
"The effect of solution structure on crystal nucleation and growth", J. Cryst. Growth 73, 505-509.

Anonymous (1984)
"CSM warns on bronchospasm with ipratropium bromide", Pharmaceut. J. 233, 171.

Aquilano, D., Rubbo, M., Mantovani, G., Sgualdino, G., and Vaccari, G. (1986)
"Equilibrium and growth forms of sucrose crystals in the {hOl} zone 1. Theoretical treatment of {101}-d form", J. Cryst. Growth 74, 10-20.

Armstrong, R.S., Aroney, M.J. Duffin, R.K., Stootman, H.J. and Le Fevre, R.J.W. (1973)
"Solute-benzene interaction: a nuclear magnetic resonance spectral, dipole moment, and Kerr effect study", J.C.S. Perkin II, 1973, 1272-1275.

Aroney, M.J. (1977)
"The electro-optical Kerr effect in conformational analysis", Angew Chem. Int. Ed. Engl. 16, 663-673.

Aroney, M.J., Hambley, T.W., Patsalides, E., Pierens, R.K., Chan, H.-K. and Gonda, I. (1987)
"Hexamethylmelamine: a study of solvation and crystallization", J.C.S. Perkin II, 1987, 1747-1752.

Beckett, S.T. (1973)
"The evaluation of airborne asbestos fibres using a scanning electron microscope", Ann Occup. Hyg. 16, 405-408.

Beerbower, A., Wu, P.L. and Martin, A. (1984)
"Expanded solubility parameter approach I: naphthalene and benzoic acid in individual solvents". J. Pharm. Sci. 73, 179-188.

Bellamy, L.J. (1975)
"The Infra-red Spectra of Complex Molecules", Chapman and Hall Ltd., London, 3rd Ed., pp 111, 153-154, 239, 283-286.

Bennema, P. and Gilmer, G.H. (1973)
"Kinetics of crystal growth" in "Crystal Growth: An Introduction", ed. by P. Hartman, North-Holland Publishing Co., Amsterdam, Ch. 10, pp 263-327.

Berkovitch-Yellin, Z (1985)
"Toward an ab initio derivation of crystal morphology", J. Am. Chem. Soc. 107, 8239-8253.

Berkovitch-Yellin, Z., Addadi, L., Idelson, M., Leiserowitz, L. and Lahav, M. (1982)
"Absolute configuration of chiral polar crystals", Nature 296, 27-34.

Berkovitch-Yellin, Z., van Mil, J., Idelson, M., Lahav, M., and Leiserowitz, L. (1985)
"Crystal morphology engineering by 'tailor-made' inhibitors: a new probe to fine intermolecular interactions", J. Am. Chem. Soc. 107, 3111-3122.

Black, D. B. and Lovering, E.G. (1977)
"Estimation of the degree of crystallinity in digoxin by X-ray and infrared methods", J. Pharm. Pharmac., 29, 684-687.

Bloss, F.D. (1961)
"An Introduction to the Methods of Optical Crystallography", Holt, Rinehart and Winston, Inc. N.Y. pp 47-150.

Boistelle, R. (1976)
"Survey of crystal habit modification in solution" in "Industrial Crystallization", ed. by J.W. Mullin, Plenum Press, New York.

Bolin, J.T., Filman, D.J., Matthews, D.A., Hamlin, R.C. and Krant, J. (1982)
"Crystal structures of Escherichia coli and Lactobacillus casei dihydrofolate reductase refined at 1.7A^0 resolution", J. Biol. Chem. 257, 13650-13662.

Borecka, B., Sangwal, K., Rak, M., and Lipinski, A. (1983)
"Growth characteristics of p-terphenyl crystals from some organic solvents", J. Cryst. Growth 65, 518-523.

Bourne, J.R. and Davey, R.J. (1976)
"The role of solvent-solute interactions in determining crystal growth mechanisms from solution I. The surface

entropy factor", J. Cryst. Growth 36, 278-286.

Bourne, J.R. and Davey, R.J. (1976 b)
"Solvent effects in the growth of hexamethylene tetramine crystals" in "Industrial Crystallization", Ed. by J.W. Mullin, Plenum Press, New York.

Bourne, J.R. and Davey, R.J. (1978)
"α factors for solution growth with special reference to glyceryl tristearate", J. Cryst. Growth 43, 224-228.

Bourne, J.R., and Davey, R.J., and McCulloch, J. (1978)
"The growth kinetics of hexamethylene tetramine crystals from a water/acetone solution", Chem. Eng. Sci. 33, 199-204.

Broul, M. (1976)
"Influence of Mn(II), Cu(II) and Al(III) ions on size and habit of ammonium sulphate crystals" in "Industrial Crystallization", ed. by J.W. Mullin, Plenum Press, New York.

Brown, T.L. and Stark, K. (1965)
"The effect of aromatic solvents on proton magnetic resonance spectra", J. Phys. Chem. 69, 2679-2683.

Bryant, R.G. (1978)
"NMR relaxation studies of solute-solvent interactions" in "Annual Review of Physical Chemistry", vol. 29, ed. by Rabinovitch, B.S., Schurr, J.M. and Strauss, H.J. pp 167-188.

Buckley, H.E. (1952)
"Crystal Growth", Chapman and Hall, London.

Bullen, G.J., Corney, D.J. and Stephens, F.S, (1972)
"Crystal and molecular structure of hexamethylmelamine [2,4,6-tris(dimethylamino)-1,3,5 - triazine]", J.C.S. Perkin II, 1972, 642-646.

Byrn, S.R. (1982)
"Solid-state Chemistry of Drugs", Academic Press, New York, pp 79-148.

Chamberlin, A.R., Cheung, A.P.K. and Lim, P. (1976)
In "Analytical Profiles of Drug substances, Vol. 5", ed. by K. Florey, Academic Press, N.Y. pp 283-306.

Chan, H.-K., Hambley, T.W. and Gonda, I. (1986)
"Solid forms and structure of methotrexate", Aust. J. Hosp. Pharm. 16, 66.

Cheung, H.T.A., Tattam, B.N., Antonjuk, D.J. and Broadle, D.K. (1985).
"Ammonia and methane chemical ionization mass spectra of methotrexate and its amide and ester analogues", Biomed. Mass Spectrometry, 12, 11-18.

Chow, A.H.-L., Chow, P.K.K., Wang, Z. and Grant, D.J.W. (1985)
"Modification of acetaminophen crystals: influence of growth in aqueous solutions containing p-acetoxyacetanilide on crystal properties", Int. J. Pharmaceut. 24, 239-258.

Chow, K.Y., GO, J., Wang, Z., and Grant, D.J.W. (1985)
"Modification of adipic acid crystals. II. Influence of growth in the presence of oleic acid on crystal properties.", Int. J. Pharmaceut. 25, 41-55.

Comis, R.L. (1981)
"Carcinoma of the lung" in "Cancer and Chemotherapy, Vol. II Introduction to Clinical Oncology", ed. by S.T. Crooke and A.W. Prestayko, Academic Press, N.Y. Ch. 9, pp 147-165.

Daniels, T. (1973)
"Thermal Analysis", Kogan Page Ltd., London, pp 84.

Dauber, P., Osguthorpe, D.J. and Hagler, A.T. (1982)
"Structure, energetics and dynamics of ligand binding to dihydrofolate reductase", Biochem. Soc. Trans. 10, 312-318.

Davey, R.J. (1979)
"The control of crystal habit" in "Industrial crystallization 78", ed. by E.J. de Jong and S.J. Jancic, North Holland Publishing Co., Amsterdam.

Davey, R.J. (1982)
"Solvent effects in crystallization processes" in "Current Topics in Material Science" vol. 8, Ed. by Kaldis, E. pp 431-479.

Davey, R.J. (1986)
"The role of the solvent in crystal growth from solution", J. Cryst. Growth 76, 637-644.

Davey, R.J., Mullin, J.W., and Whiting, M.J.L. (1982)
"Habit modification of succinic acid crystals grown from different solvents", J. Cryst. Growth 58, 304-312.

Davies, C. N. (1979)
"Particle-fluid interaction", J. Aerosol Sci. 10, 477-513.

Davis, S.S. (1978)
"Physico-chemical studies on aerosol solutions for drug delivery I. Water-propylene glycol systems", Int. J. Pharm., 1, 71-83.

Davis, S.S. and Bubb, M.D. (1978)
"Physico-chemical studies on aerosol solutions for drug delivery III. The effect of relative humidity on the particle size of inhalation aerosols.", Int. J. Pharm., 1, 303-314.

Davis, S.S., Elson, G. and Whitmore, J. (1978)
"Physico-chemical studies on aerosol solutions for drug

delivery II. water-propylene glycol-ethanol system.", Int. J. Pharm., 1, 85-93.

De Jong, E.J. and Jancic, S.J. (eds) (1979)
"Industrial Crystallization 78", North Holland Publishing Co., Amsterdam.

Edwards, R.T. (1957)
"Crystal habit of paraffin wax", Ind. Engn. Chem. 49, 750-757.

Eliel, E.L. (1962)
"Stereochemistry of carbon compounds", McGraw-Hill Book Company, Inc. New York, pp 32-43.

Elwenspoek, M., Bennema, P., and Van Der Eerden, J.P. (1987)
"Orientational order in naphthalene crystal-solution interfaces", J. Cryst. Growth 83, 297-305.

Ensminger, W.D. (1984)
"Clinical pharmacology of folate analogs" in "Folate Antagonists as Therapeutic Agents, Volume 2," Ed. by F.M. Sirotnak, J.J. Burchall, W.D. Ensminger, and J.A. Montgomery, Academic Press, Orlando.

Etter, M.C., Jahn, D.A., and Donahue, B.S. (1986)
"Growth and characterization of small molecule organic crystals", J. Cryst. Growth 76, 645-655.

France, W.G. (1944)
"Adsorption and crystal habit modification" in "Colloid Chemistry, Vol. 5", ed. by Alexander, J., Reinhold, N.Y., pp 443-457.

Frondel, C. (1940)
"Effect of dyes on the crystal habit and optics of NaF, LiF, NaCl, KCl, KBr, and KI.", The Am. Mineralogist 25, 91-111.

Fuchs, N.A. (1964)
"The Mechanics of Aerosols", Pergamon Press, Oxford, pp. 37-42.

Garti, N. and Tibika, F. (1980)
"Habit modifications of nitrofurantoin crystallized from formic acid mixtures", Drug Dev. and Ind. Pharmacy 6, 379-398.

Garti, N., Wellner, E. and Sarig, S (1980)
"Stearic acid polymorphs in correlation with crystallization conditions and solvents", Kristall und Technik 15, 1303-1310.

Garti, N., Wellner, E. and Sarig, S. (1982)
"Effect of surfactants on crystal structure modification of stearic acid", J. Cryst. Growth 57, 577-584.

Glasby J. and Ridgway, K. (1968)
"The crystallization of aspirin from ethanol"
J. Pharm. Pharmacol 20, 94S-103S.

Glasser, L.S.D. (1977)
"Crystallography and Its Applications", Van Nostrand Reinhold Co. Ltd., Wokingham, Bershire, England. pp. 125-155.

Go, J., and Grant, D.J.W. (1987)
"Locating the impurity in doped crystals using isotopic double labelling and a column 'flow-through' dissolution cell." Int. J. Pharmaceut. 36, 17-28.

Gonda, I. (1981)
"A semi-empirical model of aerosol deposition in the human respiratory tract for mouth inhalation", J. Pharm. Pharmacol 33, 692-696.

Gonda, I. (1984)
"On 'inversion' of aerosol size distribution data", Aerosol Science and Technology 3, 345-346.

Gonda, I. (1985)
"Development of a systematic theory of suspension inhalation aerosols. I. framework to study the effects of aggregation on the aerodynamic behaviour of drug particles." Int. J. Pharm., 27, 99-116.

Gonda, I., Chan, H.K., Nagai, T. (1986)
"Correlation between the aspect ratio of hexamethylmelamine crystals and solvent polarity", in Abstract of the Annual Meeting of the Japanese Pharmaceutical Society, Chiba, Japan, 1986, 2S, 1-5.

Gonda, I. and Groom, C.V. (1981)
In "Deposition and Clearance of Aerosols in the Human Respiratory Tract" (H. Hanck, ed.) International Symposium (Bad Gleichenberg, Austria, May 22/23, 1981). Organized by IGACM, Part 1, p. 7.

Gonda, I. Kayes, J.B., Groom, C.V. and Fildes, F.J.T. (1982).
"Characterisation of hygroscopic inhalation aerosols" in "Particle Size Analysis 1981" (Eds. N. Stanley-Wood and T. Allen), J. Wiley, Chichester, England, pp. 31-43.

Gonda, I. and Khalik, A.F.A.E. (1985)
"On the calculation of aerodynamic diameter of fibers", Aerosol Science and Technology 4, 233-238.

Gonda, I. and Khalik, A.F.A.E. (1985b)
"Aerodynamic properties of different crystal forms of hexamethylmelamine" in the Sixth International Symposium on Inhaled Particles, August 1985, Cambridge, U.K. (to be published in Ann. Occup. Hyg., 1988).

Gonda, I., Khalik, A.F.A.E. and Britten, A.Z., (1985a)

"Crystal forms of hexamethylmelamine (HMM)", J. Pharm. Pharmacol. (suppl.), 37, 117P.

Gonda, I, Khalik, A.F.A.E. and Britten A.Z., (1985c) "Hexamethylmelamine aerosols prepared in an evaporation-condensation generator", Int. J. Pharm. 27, 255-265.

Grant, D.J.W. and York, P. (1985) "A disruption index for quantifying the solid state disorder induced by additives or impurities. II. Evaluation from heat of solution", Int. J. Pharmaceut. 28, 103-112.

Grant, D.J.W. and York, P. (1986) "Entropy of processing: a new quantity for comparing the solid state disorder of pharmaceutical materials", Int. J. Pharmaceut. 30, 161-180.

Griffiths, W.D., Patrick, S. and Rood, A.P. (1984) "An aerodynamic particle size analyser tested with spheres, compact particles and fibers having a common settling rate under gravity", J. Aerosol Sci. 15, 491-502.

Griffiths, W.D. and Vangham, N.P. (1986) "The aerodynamic behaviour of cylindrical and spheroidal particles when settling under gravity", J. Aerosol Sci. 17, 53-65.

Groom, C.V. and Gonda, I. (1980) "Cascade impaction: the performance of different collection surfaces", J. Pharm. Pharmacol. 32 (suppl.), 93P.

Groom, C.V. (1981) "Effects of relative humidity on inhalation aerosols", Ph.D. Thesis, Department of Pharmacy, University of Aston in Birmingham, Chapter 4.

Hahn, D.A. (1983) "Hexamethylmelamine and pentamethylmelamine: an update", Drug Intell. Clin. Pharm. 17, 418-424.

Haleblian, J.K. (1975) "Characterization of habits and crystalline modification of solid and their pharmaceutical applications", J. Pharm. Sci. 64, 1269-1288.

Hambley, T.W., Chan, H.-K. and Gonda, I. (1986) "Crystal and molecular structure of methotrexate", J. Am. Chem. Soc. 108, 2103-2105.

Harris, R.J., Jr., and Fraser, D.A. (1976) "A model for deposition of fibers in the human respiratory system", Am. Ind. Hyg. Assoc. J. 37, 73-89.

Hartman, P. (1969) "The dependence of crystal morphology on crystal

structure" in "Growth of Crystals vol.7", Ed. by N.N. Sheftal, pp. 3-18.

Hartman, P. (1973)
"Structure and morphology" in "Crystal Growth: An Introduction", Ed. by P. Hartman, North-Holland Publishing Co., Amsterdam, pp. 367-402.

Hartman, P. (1980)
"The attachment energy as a habit controlling factor II. Application to anthracene, tin tetraiodide and orthorhombic sulphur", J. Cryst. Growth 49, 156-165.

Hartman, P. (1980)
"The attachment energy as a habit controlling factor III. Application to corundum", J. Cryst. Growth 49, 166-170.

Hartman, P. and Bennema, P. (1980)
"The attachment energy as a habit controlling factor I. Theoretical considerations", J. Cryst. Growth 49, 145-156.

Hering, S.V. and Friedlander, S.K., Collins, J.J. and Richards, L.W. (1979)
"Design and evaluation of a new low-pressure impactor. 2", Environmental Science and Technology 13, 184-188.

Huang, C.-M., Kerker, M., Matijevic, E. and Cooke, D.D. (1970)
"Aerosol studies by light scattering VII: preparation and particle-size distribution of linolenic acid aerosols", J. Coll. Interface Sci. 33, 244-254.

Human, H.J., Van Der Eerden, J.P., Jetten, L.A.M.J., and Odekerken, J.G. M. (1981)
"On the roughening transition of biphenyl: transition of faceted to non-faceted growth of biphenyl for growth from different organic solvents and the melt", J. Cryst. Growth 51, 589-600.

James, K.C. (1986)
"Solubility and Related Properties", Marcel Dekker, Inc. New. York.

Jancic, S.J., and de Jong, E.J. (eds) (1982)
"Industrial Crystallization 81", North Hollands Publishing Co., Amsterdam.

Jancic, S.J., and de Jong, E.J. (eds) (1984)
"Industrial Crystallization 84", Elsevier Science Publishers B.V., Amsterdam.

Johnson, D.L. (1986)
"Aerodynamic behaviour of non-spherical, orthotropic aerosols under viscous settling conditions", J. Aerosol Sci. 17, 426-430.

Johnson, D.L., Leith, D., Reist, P.C. (1987)
"Drag on non-spherical, orthotropic aerosol particles", J.

Aerosol Sci. 18, 87-97.

Kasper, G. and Shaw, D.T. (1983)
"Comparative size distribution measurements on chain aggregates", Aerosol Sci. Technol. 2, 369-381.

Kawashima, Y., Handa, T., Takeuchi, H., Okumura, M., Katou, H. and Nagata, O. (1986a)
"Crystal modification of phenytoin with polyethylene glycol for improving mechanical strength dissolution rate and bioavailability by a spherical crystallization technique", Chem. Pharm. Bull. 34, 3376-3383.

Kawashima, Y., Handa, T., Takeuchi, H. and Okumura, M. (1986b)
"Effect of polyethylene glycol on the size of agglomerated crystals of phenytoin prepared by the spherical crystallization technique", Chem. Pharm. Bull. 34, 3403-3407.

Kawashima, Y., Okumura, M. and Takenaka, H. (1982)
"Spherical crystallization: direct spherical agglomeration of salicylic acid crystals during crystallization", Science, 216, 1127-1128.

Kawashima, Y., Okumura, M., Takenaka, H. and Kojima, A. (1984)
"Direct preparation of spherically agglomerated salicylic acid crystals during crystallization", J. Pharm. Sci. 73, 1535-1538.

Khalik, A.F.A.E. (1984)
"Generation and Characterization of Hexamethymelamine Aerosols", Ph.D. Thesis, Department of Pharmacy, University of Aston in Birmingham.

Khamskii, E.V. (1976)
"Some problems of crystal habit modification" in "Industrial Crystallization" (J.W. Mullin, ed.) Plenum Press, New York.

Kleber, W. and Raidt, H. (1963)
"Uber den einfluß des losungsmittels auf die exogene symmetrie von salol", Z. Phys. Chem. 222, 1-14.

Kuhnert-Brandstatter, M. (1966)
"Identification of organic substances after L. Kufler" in the "Commentary on the Austrian Pharmacopoeia, 9th Edition", Scientia Pharmaceutica (Heft 2/1966, jg. 34, S. 147-166).

Laszlo, P. (1967)
"Solvent effects and nuclear magnetic resonance" in "Progress in Nuclear Magnetic Resonance Spectroscopy" Ed. by Emsley, J.W., Feeney, J. and Sutcliffe, L.H. vol. 3, Pergamon Press, Oxford. pp. 231-402.

Lippmann, M. (1985)

"Respiratory tract deposition and clearance of aerosols" in "Aerosols: Research, Risk Assessment and Control Strategies", proceedings of the second U.S.-Dutch International Symposium, Williamsburg, Virginia, The United States. S.D. Lee, T. Schneider, L.D. Grant, and P.J. Verkerk (Editors).

Lippmann, M., Yeates, D.B., and Albert, R.B. (1980) "Deposition, retention, and clearance of inhaled particles", British J. of Industrial Medicine, 37, 337-362.

Maeyashiki, Y., Okada, M., and Sato, K., (1982) "Influence of polymorphism on growth of stearic acid single crystal in solution", Jap. J. Appl. Physics, 21, L781-L782.

Malem, H., Henry, D., Ward, M., Smith, W.H.R., and Gonda, I. (1981) "Early experience with a vertical spinning-disc nebuliser", The Lancet 2, 664-666.

Martin, A., Swarbrick J., and Cammarata, A (1983) "Physical Pharmacy", 3rd Ed., Lea and Febriger, Philadephia, pp. 477.

McCarthy, C.J., Riley, G.S. and Rees, J.E. (1983) "Rounding of crystals by periodic temperature cycling", J. Pharm. Pharmacol. 35 (suppl.), 2P.

McRae, E.G. (1957) "Theory of solvent effects on molecular electronic spectra. Frequency shifts", J. Phys. Chem. 61, 562-572.

Michaels, A.S. and Colville, A.R. Jr. (1960) "The effect of surface active agents on crystal growth rate and crystal habit", J. Phys. Chem. 64, 13-19.

Mitchell, R.I. and Pilcher, J.M. (1959) "Improved cascade impactor for measuring aerosol particle sizes in air pollutants, commercial aerosols, cigarette smoke", Industrial and Engineering Chemistry 51, 1039-1042.

Moss, G.F., Jones, K.M., Ritchie, J.T. and Cox J.S.G. (1971) "Plasma levels and urinary excretion of disodium cromoglycate after inhalation by human volunteers", Toxicolgy and Applied Pharmacology 20, 147-156.

Mullin, J.W. (1972) "Crystallization", Butterworths, London.

Mullin, J.W. (ed) (1976) "Industrial Crystallization", Plenum Press, New York.

Myers, A.B. and Birge, R.R. (1980) "The effect of solvent environment on molecular electronic oscillator strengths", J. Chem. Phys. 73, 5314-5321.

Nielsen, A.E. (1964)
"Kinetics of Precipitation", Pergamon Press, Oxford.

Nielsen, A.E. (1980)
"Transport control in crystal growth from solution",
Croatica Chem. Acta 53, 255-279.

Nielsen, A.E. (1984)
"Electrolyte crystal growth mechanisms", J. Cryst. Growth
67, 289-310.

Nielsen, A.E. and Christoffersen, J. (1982)
"The mechanisms of crystal growth and dissolution" in
"Biological Mineralization and Demineralization", Ed. by
G.H. Nancollas, Springer-Verlag, Berlin, pp. 37-77.

Nielsen, A.E. and Toft, J.M. (1984)
"Electrolyte crystal growth kinetics", J. Cryst. Growth
67, 278-288.

Palmes, E.D., Wang, C-S., Goldring, R.M. and Altershuler,
B. (1973)
"Effect of depth of inhalation on aerosol persistence
during breath holding", J. Appl. Physiol. 34, 356-360.

Polli, G.P., Grim, W.M., Bacher, F.A. and Yunker, M.H.
(1969)
"Influence of formulation on aerosol particle size", J.
Pharm. Sci. 58, 484-486.

Raabe, O.G. (1968)
In "Fission product inhalation program annual report
1967-68", R.O. McClellan and F.C. Rupprecht (eds),
Lovelace Foundation for Medical Education and Research,
Albuequerque, NM, pp. 165-171.

Randerath, K. (1966)
"Thin-Layer Chromatography", Academic Press, New York.
P.18.

Rao, A.K. and Whitby, K.T. (1978a)
"Non-ideal collection characteristics of inertial
impactors- I. Single-stage impactors and solid particles",
J. Aerosol Sci. 9, 77-86.

Rao, A.K. and Whitby, K.T. (1978b)
"Non-ideal collection characteristics of inertial
impactors-II. Cascade impactors.", J. Aerosol Sci. 9,
87-100.

Rao, C.N.R. (1963)
"Chemical Application of Infrared Spectroscopy" Academic
Press, N.Y.
pp. 577-584.

Rao, C.N.R. (1975)
"Ultra-violet and Visible Spectroscopy", Butterworths,
England, 3rd ed. pp. 17, 206-209.

Sano, A., Kuriki, T., Handa, T., Takeuchi, H. and Kawashima, Y. (1987)
"Particle design of tolbutamide in the presence of soluble polymer or surfactant by the spherical crystallization technique: improvement of dissolution rate", J. Pharm. Sci, 76, 471-474.

Saska, M. and Myerson, A.S. (1983)
"The theoretical shape of sucrose crystals from energy calculations", J. Cryst. Growth 61, 546-555.

Sato, K. and Boistelle, R. (1984)
"Stability and occurrence of polymorphic modifications of stearic acid in polar and nonpolar solutions", J. Cryst. Growth 66, 441-450.

Schoeffel, R.E., Anderson, S.D., and Altouynan, R.E.C. (1984)
"Bronchial hyper-reactivity in response to inhalation of ultrasonically nebulised solutions of distilled water and saline", Br. Med. J. 282, 1285-1287.

Schroeder, J., Skudlarska, W., Szczepanik, A., Sikorska, E., and Zielinski, S. (1976)
"The influence of surface-active agents on gypsum crystallization in phosphoric acid solutions" in "Industrial Crystallization" Ed. by J.W. Mullin, Plenum Press, London.

Scottys, J., Lisowski, Z., Knapczyk, J. (1984)
"X-ray diffraction study of the crystallinity index and the structure of the microcrystalline cellulose", Acta Pharm. Tech. 30, 174-180.

Sheaffer, A.W. (1987)
"Drag on modified rectangular prisms", J. Aerosol Sci. 18, 11-16.

Sheldrake, R. (1981)
"A New Science of Life", Blond & Briggs Ltd., London.

Spark, M.J., Winkler, D.A. and Andrews, P.R. (1982)
"Conformational analysis of folates and folate analogues", Int. J. Quantum Chem., Quantum Biol. Symp. 9, 321-333.

Staniforth, J.N. (1984)
"Particle engineering of a direct compression excipient", Int. J. Pharm. Tech., & Prod. Mfr., 5, 1-12.

Stober, W., (1972)
In "Assessment of Airborne Particles", ed. by T.T. Mercer, P.E. Morrow and W. Stober, C.C. Thomas Publ., Springfield, Ill, pp 249-288.

Suryanarayanan, R. and Mitchell, A.G. (1985)
"Evaluation of two concepts of crystallinity using calcium gluceptate as a model compound", Int. J. Pharmaceut. 24,

1-17.

Sutton, P.A., Cody, V. and Smith, G.D. (1986)
"Crystal structure of methotrexate tetrahydrate", J. Am. Chem. Soc. 108, 4155-4158.

Tarjan, I. and Matrai, M. (1972)
"Laboratory Manual on Crystal Growth", Akademiai Kiado, Budapest, Hungary.

Task Group on Lung Dynamics (1966)
"Deposition and retention models for internal dosimetry of the human respiratory tract", Health Physics, 12, 173-207.

Timbrell, V. (1965)
"The inhalation of fibrous dusts", Ann. N.Y. Acad. Sci. 132, 255-273.

Timbrell, V. (1972)
In "Assessment of Airborne Particles", ed. by T.T. Mercer, P.E. Morrow and W. Stober, C.C. Thomas Publ., Springfield, Ill, pp 290-330.

Timbrell, V. (1982)
"Deposition and retention of fibers in the human lung", Ann. Occup. Hyg. 26, 347-369.

Torgesen, J.L. and Strassburger, J. (1964)
"Growth of oxalic acid single crystals from solution: solvent effects on crystal habit", Science 146, 53-55.

United States Pharmacopeia XIX (1975),
United States Pharmacopeial Convention, Inc., Rockville, M.D. p. 315.

Van de vaart-van zutphen, H.P.C., Smulders, C.F.A., Renema, J. and Hulshoeff, A. (1982)
"Hexamethylmelamine and hexamethylmelamine hydrochloride", Pharmaceutisch Weekblad Scientific Edition, 4, 25-31.

Van Enckevort, W.J.P. (1984)
"Surface microtopography of aqueous solution grown crystals", Prog. Crystal Growth and Charact. 9, 1-50.

Verdaguer, S.V. and Clemente, R.R. (1986)
"Crystal growth of KDP from boiling solutions in the presence of impurities", J. Cryst. Growth, 79, 198-204.

Watson, D.H. (1954)
"The solvent effect on crystal growth", in "Proc. 3rd Intl. Conf. Electron Microscopy", London, 497-500.

Wells, A.F. (1946)
"Crystal habit and internal structure-I", Phil. Mag. 37, 184-199.

Wells, A.F. (1949)
"III. Abnormal and modified crystal growth", Disc. Farad.

Soc., 5, 197-201.

Weijnen, M.P.C., Van Rosemalen, G.M., and Bennema, P. (1987)
"The adsorption of additives at the gypsum crystal surface: a theoretical approach II. Determination of the surface coverage required for growth inhibition", J. Cryst. Growth 82, 528-542.

Weissbuch, I., Shimon, L.J.W., Addadi, L., Berkovitch-Yellin, Z., Weinstein, S., Lahav, M, and Leiserowitz, L. (1985a)
"Stereochemical discrimination at organic crystal surfaces 1: the systems serine/threonine and serine/allothreonine", Israel J. Chem. 25, 353-361.

Weissbuch, I., Berkovitch-Yellin, Z., Leiserowitz, L. and Lahav, M. (1985b)
"Stereochemical discrimination at organic crystal surfaces 2: the effect of the molecular structure and conformation of dipeptides additives on the morphology of glyclyglycine crystals", Israel J. Chem. 25, 362-372.

Weissbuch, I., Zbaida, D., Addadi, L., Leiserowitz, L. and Lahav, M. (1987)
"Design of polymeric inhibitors for the control of crystal polymorphism. Induced enantiomeric resolution of racemic histidine by crystallization at 25^{0}C", J. Am. Chem. Soc. 109, 1869-1871.

Wilke, C. R., and Chang, P. (1955)
"Correlation of diffusion coefficients in dilute solutions", A.I. Ch. E. Journal, 1, 264-270.

Winchell, A.N. (1954)
"The optical properties of organic compounds", Second ed., Academic Press, New York, pp 243.

Williams, D.H. and Fleming, I. (1966)
"Spectroscopic Methods in Organic Chemistry", McGraw-Hill Publishing Co. Ltd., London, pp. 86-88.

Williams, R.M. and Wallwork, S.C. (1966)
"Molecular complexes exhibiting polarization bonding. VI. the crystal structure of the 2,4,6-tri(dimethylamino)-1,3,5-triazine-s-trinitrobenzene complex", Acta Cryst. 21, 406-412.

Wollmann, H. and Braun, V. (1983)
"Die anwendung der differenzthermoanalyse in der pharmazie", Pharmazie 38, H.1, 5-21.

York, P. and Grant, D.J.W. (1985)
"A disruption index for quantifying the solid state disorder induced by additives or impurities. I. Definition and evaluation from heat of fusion", Int. J. Pharmaceut. 25, 57-72.

Zaharko, D.S. and Dedrick, R.L. (1984)
"Pharmacokinetics of methotrexate in animals and man" in
"Folate Antagonists as Therapeutic Agents, vol. 2", ed. by
Sivotnak, F.M., Burchall, J.J., Ensminger, W.D. and
Montgomery, J.A., Academic Presss, Orlando, pp 97-163.